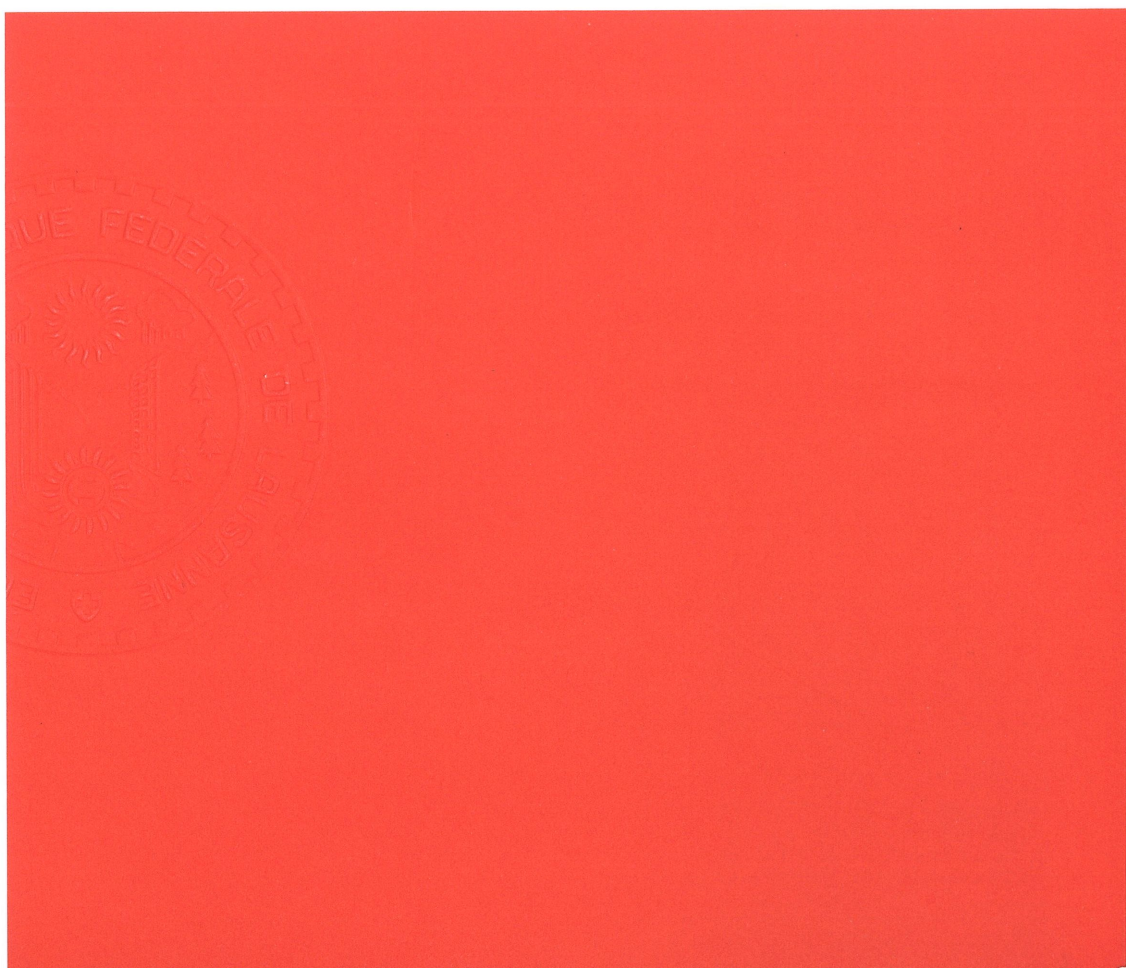


**Max TIRASSA**

The transfer of forces through rough surface contact in  
concrete



# The transfer of forces through rough surface contact in concrete

THIS IS A TEMPORARY TITLE PAGE  
It will be replaced for the final print by a version  
provided by the registrar's office.

Thèse n. 7804 2020  
présentée le 29 Juin 2020  
à la Faculté de l'environnement naturel, architectural et construit  
laboratoire de construction en béton  
programme doctoral en génie civile et environnement  
École Polytechnique Fédérale de Lausanne  
pour l'obtention du grade de Docteur ès Sciences  
par

Max Tirassa

acceptée sur proposition du jury :

Dr Anastasios Vassilopoulos, président du jury  
Prof. Aurelio Muttoni, directeur de thèse  
Dr Miguel Fernández Ruiz, directeur de thèse  
Dr Guillaume Anciaux, rapporteur  
Dr Juan Sagaseta, rapporteur  
Prof. Frank J. Vecchio, rapporteur

Lausanne, EPFL, 2020  
Version : 22 juillet 2020

The logo of the École Polytechnique Fédérale de Lausanne (EPFL), consisting of the letters 'EPFL' in a bold, black, sans-serif font.



# Acknowledgements

The work presented in this thesis was performed over the last four and a half years at the Structural Concrete Laboratory IBETON at EPFL. This institution offered me a harmonious and supportive environment, which allowed me to work with dedication and live happily. I will always remember with fondness the calm and welcoming kindness of the people and communities of EPFL, Lausanne, Vaud, and Switzerland in general. They made this wonderful place my home.

The research project was funded by the Swiss National Science Foundation through research grant 200021\_169649. I am very appreciative of the generous support received.

I would like to acknowledge the members of my jury, Dr Guillaume Anciaux from EPFL, Dr Juan Sagaseta from the University of Surrey, Dr Anastasios Vassilopoulos from EPFL (jury president), and Prof. Frank J. Vecchio from the University of Toronto. Their comments and remarks were food for thought and helped me to improve the thesis manuscript.

There are many more people who I want to thank for supporting me over the course of this project. The first are certainly my supervisors, who guided me along the way.

Prof. Aurelio Muttoni allowed me to start this adventure, gave important input and insights while always reminding me of the greater picture. He inspired me with his hands-on passion for designing quality structures and his teachings will be one of the foundations of my engineering knowledge.

The guidance and support of Dr Miguel Fernández Ruiz were essential as well. He provided essential inputs, lots of enthusiasm, and encouraged me in investigating various research paths. He was quick to find and address aspects that needed improvement and followed me all along the model's development. I could not have asked for a better guide and will always remember Miguel as a great role-model.

I had the pleasure to collaborate with Dr Guillaume Anciaux and Mohit Pundir from the LSMS laboratory at EPFL. Our discussions helped in focusing various aspects of this research, and their view on several issues was enriching and insightful.

The experimental campaign represents an important part of this thesis, and it was made possible thanks to the technical team of the GISGE unit at EPFL. The technicians helped preparing set-ups and specimens, taught me countless practical skills, and supported me with

---

suggestions and custom-made tools all along the way. Dear A. Krkic, F. Perrin, L.F. Dubugnon, G. Rouge, G. Guignet, S. Despont and S. Demierre, you are the best technicians I could ask for. Merci beaucoup!

Several others helped achieving the experimental campaign as well: The team at the LMC laboratory at EPFL, and in particular L. Sofia and A. Costarella, assisted me in some of the castings and tolerated my prolonged use of their facilities to grade aggregates. Dr S. Kohler and the LMAF laboratory at EPFL gave me access to their microscope for scanning the specimen surfaces. M. Sonderegger and A. Trifunović helped me with part of the laboratory work. The team of *walter+bai ag* contributed in developing the set-ups and improving the test program. M. Bugnon at the *Gravière de la Claire-aux-Moines SA* helped me with some of the castings.

Working on this thesis would not have been the same without my colleagues from the IBETON laboratory, with its warm atmosphere spurring productive working and interesting conversations. My senior colleagues were great models and inspirations: M.R. Backes, F. Brantschen, F. Cavagnis, I.S. Drakatos, J. Einpaul, F. Niketic, D. Tasevski, P. Valeri, thank you very much for all the insights and recommendations! My junior colleagues helped me a lot as well and will do the IBETON-name great honour. Dear, R. Cantone, E. Corres Sojo, D. Hernández Fraile, X. Malja, F. Moccia, F. Monney, M. Pejatovic, Q. Yu, I will miss you a lot!

IBETON wouldn't be the same without its heart and soul Y. Bühl, who helped me in many different ways with great patience and kindness. Thank you a lot Yvonne!

Many thanks also go to Dr O. Burdet, who was essential for the set-up development and provided countless useful suggestions and recommendations.

There are many other people I encountered at IBETON, like Dr M. Corrado, H. Saso, Dr J. Sorensen, and E. Veloso Dos Santos. They all gave interesting insights and useful inspirations, and I'm grateful for having met them. Similarly, I'm thankful for the many people at EESD and other EPFL labs with whom I shared interesting discussions and great moments. Thank you very much!

Several people encouraged and supported me at the very beginning of this journey. My gratitude goes to all of them, and in particular G. Gruben, Prof. T. Iori, Prof. S. Mornati, Prof. S. Poretti, Prof. Z. Rinaldi and Prof. S. Stucchi.

The person who motivated me most, both at the beginning and all along the path, is certainly the architect of my life, Korinna Zinovia Weber, who deserves all my admiration and gratitude. Her presence at my side is the best support I could have wished for.

Finally, I thank my family and my parents Elisabeth Mairhofer and Romolo Tirassa. It is their support, teachings and values which allowed me to start and master this exciting journey. Their education was truly the greatest gift they could give me. Thank you.

*Lausanne, July 2020*

Max Tirassa

# Foreword

The transfer of forces through cracked concrete surfaces and through concrete-to-steel interfaces is one of the most instrumental aspects ruling the response of structural concrete. Its implications are for instance found in the shear strength of beams, the friction between concrete surfaces or the transfer of forces by bond. Such phenomenon has been investigated under different perspectives since the early developments of structural concrete, showing a high complexity. Despite these efforts, many difficulties have been found to provide an accurate characterization of the various phenomena implied and to provide a unified perspective to the various situations where interface stresses may develop. As a consequence, this situation has led to development of specific empirical approaches and models for particular cases, in many cases without a clear connection or consistent hypotheses amongst them.

The present thesis of Mr Tirassa is aimed at presenting a general approach to the phenomenon of the transfer of forces through concrete surfaces. To that aim, a series of innovative tests is presented, allowing to track the interface stresses for given kinematics. These measurements are performed both for concrete-to-concrete and steel-to-concrete rough surfaces, providing also a detailed characterization of the actual surface roughness. On this basis, the work of Mr Tirassa shows that the contact forces developed under different contact scenarios and surface properties can be described in a unified manner, on the basis of a set of simple and mechanically-based assumptions. The results show consistent predictions when they are also applied to other related cases implying the transfer of forces in cracked concrete. This work contributes thus to the state-of-the-art in the understanding of the phenomenon, but also opens a promising approach to assess the capacity of rough concrete surfaces under different scenarios.

This thesis has been funded by the Swiss National Science Foundation, whose support is greatly acknowledged.

*Lausanne, May 2020*

Prof. Aurelio Muttoni

Dr Miguel Fernández Ruiz



# Summary

Aggregate interlocking is a phenomenon occurring when the opposite sides of a concrete crack slide relative to each other. Due to surface roughness, protruding material from one crack-side can engage with the opposite one and thus exchange forces. This affects the load-carrying capacity for structures where the failure is determined by the development of large cracks, like beams and slabs without transverse reinforcement. In such cases, aggregate interlocking contributes significantly to the various shear-transfer actions, allowing forces to traverse cracks.

Aggregate interlocking has been studied for several decades, leading to various experimental and theoretical approaches. However, a number of aspects remain unclear, like the development of new cracks from the initial one and the influence of certain concrete properties on the interlocking forces (e.g. aggregates, crack surface roughness). The present research project comprises three scientific publications focusing on the fundamentals of interlocking and force transfer across concrete cracks and other interfaces related to concrete structures. It is based on the results of an extensive experimental campaign performed with an arrangement allowing to apply precise kinematics upon material discontinuities. The tested specimens include pre-cracked concrete prisms subjected to simultaneous crack opening and sliding and steel-to-concrete interfaces characterized by simple geometries (spheres and rebar-surfaces). Particular attention is given to the roughness properties of the tested cracks and interfaces, several of which were scanned at high resolution.

The experimental results are used to develop a new model for estimating aggregate interlocking forces as a function of crack kinematics. The model is based on the approach originally introduced by Li and Maekawa (1987) with the *Contact Density Model* and allows estimating the contact properties using 2D crack-profiles. Depending on the crack width, two contributions to force transfer are considered. For contacts occurring in wide cracks, contact forces are calculated using an elastic-plastic material law, whereas for small crack opening the effect of residual material soundness is considered. The model can be applied on surfaces corresponding to tests with various failure modes, thus considering different levels of roughness.

Finally, the bond between steel rebar-ribs and concrete is investigated using steel-to-concrete interface specimens, and several similarities with aggregate interlocking are discussed. The previously introduced model is extended to the case of interlocking rebar-ribs, where it can estimate the bond and confinement stresses and the decrease in bond strength for cases where

## Summary

---

cracks develop parallel to the rebars.

The thesis ends with an extensive appendix containing details on the performed tests which can be of interest for future researchers.

**Keywords:** aggregate interlocking, concrete cracks, mechanical modelling, surface roughness, shear transfer, bond

# Résumé

L'engrènement des granulats est un phénomène engendré par un glissement relatif des deux lèvres d'une fissure dans le béton. Due à la rugosité de la surface, des forces sont transmises par engrènement. Ceci affecte la résistance de certaines structures ou le comportement globale est influencé par la présence d'importantes fissures, comme pour les poutres et les dalles sans armature transversale. Dans ces cas, il a été montré que l'engrainement des granulats contribue considérablement aux différents modes de transmission de l'effort tranchant, permettant ainsi de transférer des forces à travers les fissures jusqu'aux appuis.

L'engrainement des granulats a été étudié depuis plusieurs décennies dans la littérature avec différentes approches expérimentales et théorétiques. Néanmoins, certains aspects restent peu clairs, comme le développement possible de nouvelles fissures ou l'influence de certaines propriétés du béton sur les forces d'engrainement (par exemple les agrégats ou la rugosité de la surface de la fissure). Cette thèse, constituée principalement de trois publications scientifiques, porte sur les aspects fondamentaux du transfert des forces à travers les fissures en béton. Elle est basée sur les résultats d'un vaste programme expérimental, élaboré avec une nouvelle machine d'essai capable d'appliquer des déplacements précis sur des fissures. De plus, les échantillons testés comprennent aussi des interfaces acier-béton caractérisés par des géométries simples (comme des sphères ou les nervures d'une barre d'armature). Une attention particulière a été dédiée à la rugosité des fissures et des interfaces, dont plusieurs ont été scannés avec une haute résolution.

Les résultats expérimentaux sont utilisés pour proposer un nouveau modèle sur l'estimation des forces d'engrainements en fonction des cinématiques d'une fissure. Il est basé sur l'approche introduite avec le *Contact Density Model* de Li et Maekawa (1987) et permet d'estimer les caractéristiques des contacts en fonction des cinématiques appliquées en considérant les profils géométriques 2D de la fissure. En fonction de l'ouverture de la fissure, deux contributions au transfert des forces sont considérées. Pour des contacts dans des grandes fissures, les efforts sont trouvés sur la base d'une loi élastique-plastique, alors que pour des petites fissures la possible présence d'une résistance résiduelle du matériel est prise en compte. Le modèle peut être appliqué à des surfaces correspondant à des essais avec différents modes de rupture, permettant ainsi de considérer plusieurs niveaux de rugosité.

Enfin, l'adhérence entre les nervures des aciers d'armatures et le béton est investiguée au moyen d'échantillons spéciaux, et plusieurs similitudes avec l'engrainement des granulats

## Résumé

---

sont discutés. Le modèle introduit précédemment est étendu au cas de l'armature, ou il peut être utilisé pour estimer l'intensité relative des forces d'adhérence et de confinement, ainsi que la réduction de l'adhérence pour le cas où des fissures sont parallèles aux barres d'armature.

La thèse se termine avec un appendice, qui détaille les essais achevés et pourrait être intéressant pour de futurs chercheurs.

**Mots clé :** engrainement des granulats, fissures dans le béton, modélisation mécanique, rugosité de la surface, effort tranchant, adhérence

# Zusammenfassung

Die Kornverzahnung ist ein Phänomen, das in Betonrissen auftritt, wenn die beiden Rissseiten auf unterschiedliche Weise verschoben werden. Aufgrund der natürlichen Rauheit der Rissoberflächen können die gegenüberliegenden Seiten in Kontakt treten und somit Kräfte übertragen. Bei Bauteilen wie beispielweise Betonträger und -decken ohne Querkraftbewehrung wird das strukturelle Versagen massgeblich von der Entwicklung einzelner Risse bestimmt, sodass die Kornverzahnung einen signifikanten Beitrag zur Querkraft-Übertragung leistet. Das Phänomen ermöglicht es Kräften, die Riss-Diskontinuität zu überbrücken und zu den Auflagern zu gelangen.

Im Laufe der letzten Jahrzehnte wurden verschiedene Ansätze für die Beschreibung und Modellierung der Kornverzahnung entwickelt. Dennoch bestehen weiterhin mehrere Unklarheiten, wie die Entstehung neuer Risse ausgehend vom anfänglichen Rissbild oder der Einfluss verschiedener Betoneigenschaften auf die Verzahnungskräfte (z.B. verwendete Zuschlagskörner, Rauheit der Rissoberfläche). Die vorliegende Dissertation beinhaltet drei wissenschaftliche Publikationen, die verschiedene Aspekte der Kraftübertragung durch Verzahnung analysieren. Grundlage der Arbeit sind die Ergebnisse einer umfangreichen experimentellen Untersuchung, bei der präzise Rissöffnungen und Verschiebungen auf Betonrisse angewandt wurden. Zusätzlich wurden die Grenzflächen zwischen Beton und Stahlflächen mit einfachen Geometrien getestet, wie Halbkugeln und profilierte Bewehrungsstäbe. Besondere Aufmerksamkeit ist der Rauheit der Risse und Oberflächen gewidmet, die teilweise in hoher Auflösung digital erfasst wurden.

Die experimentellen Ergebnisse dienen der Entwicklung eines neuen Modelles zur Schätzung der Verzahnungsspannungen in Betonrissen unter Berücksichtigung der Rissöffnung und Verschiebung. Das Modell basiert auf dem Ansatz, der ursprünglich von Li and Maekawa (1987) für das *Contact Density Model* entwickelt wurde. Es ermöglicht eine Schätzung der Kontakteigenschaften durch Verwendung von 2D Rissprofilen. Abhängig von der Rissbreite werden zwei Beiträge zur Kraftübertragung berücksichtigt. Bei breiten Rissen werden die Kontaktspannungen mit einem elastisch-plastischen Materialgesetz gefunden, während bei kleinen Rissbreiten der Einfluss der verbleibenden Materialfestigkeit berücksichtigt wird. Durch Beachtung der Oberflächenrauheit kann das Modell auf Rissoberflächen angewandt werden, die beim Testen unterschiedliche Versagensarten aufwiesen.

Schliesslich wird mittels spezieller Probekörper der Verbund zwischen profilierten Beweh-

## Zusammenfassung

---

rungsstäben und dem umliegenden Beton untersucht und Ähnlichkeiten zur Kornverzahnung erläutert. Das zuvor beschriebene Modell wird auf den Fall der Bewehrungsstäbe erweitert, sodass die Intensität der Verbunds -und Umschnürungsspannungen analysiert werden kann. Ausserdem ist eine Schätzung der reduzierten Ausreissfestigkeit im Falle von Stahlbewehrung mit paralleler Rissbildung möglich.

Am Ende der Thesis befindet sich ein umfangreicher Anhang mit Details zu den vollzogenen Tests, die für zukünftige Forscher von Interesse sein können.

**Schlagwörter:** Kornverzahnung, Betonrisse, mechanisches Modell, Oberflächenrauheit, Querkraftübertragung, Verbund

# Riassunto

L'ingranamento degli inerti è un fenomeno riguardante le strutture in calcestruzzo, che si manifesta quando i due lati di una fessura scorrono l'uno rispetto all'altro. A causa della rugosità superficiale, del materiale sporgente da un lato può entrare in contatto con il lato opposto, trasmettendo degli sforzi. Questo fenomeno influenza la capacità portante di strutture per le quali il collasso è caratterizzato dallo sviluppo di ampie fessure, come travi e solette senza armatura trasversale. In questi casi, l'ingranamento degli inerti contribuisce considerevolmente alla trasmissione del taglio, permettendo agli sforzi di oltrepassare le zone di discontinuità materiale.

Il tema è indagato da vari decenni, con diversi approcci sperimentali e teorici documentati nella letteratura scientifica. Nonostante ciò, alcuni aspetti rimangono poco chiari, come il potenziale sviluppo di nuove fessure a partire da una iniziale o l'effetto delle proprietà del calcestruzzo. Questa tesi contiene tre pubblicazioni scientifiche volte all'indagine di vari aspetti riguardanti la trasmissione di sforzi per ingranamento nelle discontinuità delle strutture in calcestruzzo. L'indagine è basata sui risultati di una vasta campagna sperimentale svolta con un allestimento capace di imporre cinematiche precise su singole fessure, come apertura e scorrimento simultanei. Inoltre, sono state studiate delle interfacce acciaio-calcestruzzo caratterizzate da geometrie semplici, come calotte o le superfici di barre d'armatura nervate. È stata dedicata particolare attenzione alla rugosità delle superfici testate, diverse delle quali sono state scansionate ad alta risoluzione.

I risultati sperimentali sono utilizzati per lo sviluppo di un nuovo modello volto alla stima degli sforzi per ingranamento in funzione della cinematica della fessura analizzata. Questo modello è basato sull'approccio originariamente introdotto nel *Contact Density Model* di Li e Maekawa (1987) e permette di stimare l'entità del contatto considerando una serie di profili 2D della fessura. Vengono considerati due contributi, dipendenti dall'apertura della fessura considerata. Per grandi aperture le forze di contatto sono determinate utilizzando una legge costitutiva elastica-plastica, mentre per piccole aperture viene considerato l'effetto della resistenza residuale del calcestruzzo.

Infine, viene investigata l'aderenza tra barre d'armatura nervate ed il calcestruzzo, discutendo le similitudini con il fenomeno dell'ingranamento degli inerti. Il modello precedentemente introdotto è esteso al caso delle barre d'armatura, per le quali è possibile stimare gli sforzi di aderenza, quelli di confinamento e la riduzione della resistenza allo strappo per casi in cui

## Riassunto

---

delle fessure si sviluppano parallelamente alle barre d'armatura.

A conclusione della tesi vengono forniti dati e dettagli sulle prove sperimentali svolte, come fonti per analisi e futuri studi.

**Parole chiave:** ingranamento degli inerti, fessure nel calcestruzzo, modellazione meccanica, rugosità superficiale, trasmissione sforzo di taglio, aderenza acciaio-calcestruzzo

# Contents

<b>Acknowledgements</b>	<b>i</b>
<b>Foreword</b>	<b>iii</b>
<b>Summary (English, Français, Deutsch, Italiano)</b>	<b>v</b>
<b>1 Introduction</b>	<b>1</b>
1.1 Context of the present study . . . . .	1
1.1.1 Cracking in reinforced concrete . . . . .	1
1.1.2 Description and significance of aggregate interlocking . . . . .	3
1.2 Overview of state of the art . . . . .	4
1.2.1 Experimental investigations . . . . .	4
1.2.2 Modelling approaches . . . . .	6
1.3 Aims and objectives . . . . .	7
1.4 Thesis methodology and contributions . . . . .	9
<b>2 Set-ups and preliminary tests</b>	<b>15</b>
2.1 Specimens . . . . .	15
2.2 Set-ups and testing procedure . . . . .	17
2.3 Concrete properties . . . . .	19
2.4 Tensile properties of concrete components . . . . .	21
2.5 Preliminary Mixed-Mode Tests . . . . .	23
2.5.1 Types of responses . . . . .	24
2.5.2 Test results . . . . .	25
2.5.3 Discussion of test results . . . . .	27
<b>3 Review of fundamental assumptions of the Two-Phase Model for aggregate interlocking in cracked concrete using numerical methods and experimental evidence</b>	<b>33</b>
3.1 Introduction . . . . .	34
3.2 Two-Phase model . . . . .	37
3.3 Experimental programme . . . . .	40
3.3.1 Test-Setup . . . . .	40
3.3.2 Tests with concrete specimens . . . . .	44
3.3.3 Test with mortar specimens . . . . .	45

## Contents

---

3.4	Review and extension of the Two-Phase model . . . . .	48
3.4.1	Review of original formulation according to Walraven . . . . .	48
3.4.2	Two-Phase model enhancement: surface alterations . . . . .	53
3.4.3	Two-Phase model enhancement: elasto-plastic deformation of matrix . . . . .	55
3.5	Discussion . . . . .	60
3.6	Conclusions . . . . .	61
<b>4</b>	<b>Influence of cracking and rough surface properties on the transfer of forces in cracked concrete</b>	<b>69</b>
4.1	Introduction . . . . .	70
4.1.1	Scales of roughness . . . . .	71
4.1.2	Experimental investigations . . . . .	72
4.1.3	Theoretical approaches . . . . .	74
4.1.4	Aims of the present work . . . . .	74
4.2	Experimental programme . . . . .	75
4.2.1	Test set-up . . . . .	75
4.2.2	Specimens . . . . .	75
4.2.3	Test results . . . . .	78
4.2.4	Surface roughness . . . . .	79
4.3	Consistent modelling of transfer of forces through cracked concrete . . . . .	85
4.3.1	Model outline . . . . .	85
4.3.2	Contact events . . . . .	86
4.3.3	Penetrating segments . . . . .	86
4.3.4	Contribution of residual strength . . . . .	88
4.3.5	Model results . . . . .	90
4.4	Conclusions . . . . .	93
<b>5</b>	<b>An interlocking approach for the rebar-to-concrete contact in bond</b>	<b>105</b>
5.1	Introduction . . . . .	106
5.2	Experimental programme . . . . .	107
5.2.1	Interface surfaces of rebars . . . . .	109
5.2.2	Main experimental results . . . . .	112
5.3	Modelling of bond by consideration of surface interlocking . . . . .	115
5.3.1	Model description . . . . .	115
5.3.2	Model results . . . . .	119
5.4	Application to bond under cracked conditions . . . . .	122
5.5	Conclusions . . . . .	123
<b>6</b>	<b>Conclusions and Outlook</b>	<b>129</b>
6.1	Main conclusions . . . . .	129
6.2	Outlook and future works . . . . .	131
	<b>Appendix 1: Results at maximum shear stress for concrete cracks</b>	<b>135</b>

A1.1 Special specimens . . . . .	138
<b>Appendix 2: Detailed results for concrete cracks</b>	<b>141</b>
<b>Appendix 3: Detailed results for rebar-to-concrete interfaces</b>	<b>201</b>
<b>Appendix 4: Results at maximum shear stress from literature</b>	<b>211</b>
<b>Appendix 5: Interface stresses in cracked concrete: testing for review of its fundamentals</b>	<b>217</b>
A5.1 Cracks and Aggregate Interlocking . . . . .	218
A5.2 Test Setup . . . . .	219
A5.3 Results of Group 1 - Mode I on small specimens . . . . .	221
A5.4 Results of Group 2 - Mixed-Mode . . . . .	225
A5.5 Conclusions and Outlook . . . . .	225
<b>Appendix 6: Modern experimental research techniques for a consistent understanding of aggregate interlocking</b>	<b>227</b>
A6.1 Introduction . . . . .	227
A6.2 Experimental Setup . . . . .	229
A6.3 Experimental programme . . . . .	230
A6.4 Discussion of test results . . . . .	233
A6.5 Conclusions . . . . .	236
 <b>Curriculum Vitae</b>	 <b>239</b>



# 1 Introduction

This thesis presents the results of a research program focusing on the force transfer across concrete cracks and interfaces by means of their surface roughness. The phenomenon is referred to as *aggregate interlocking* and has been a subject of studies for several decades. This introduction presents the topic and some fundamental concepts related to it. It also provides an overview of the state of the art, including a summary of notable insights, approaches and models from the literature. Finally, the significance of aggregate interlocking for the design of concrete structures and the scientific contributions of the present thesis are outlined.

Some of the figures in this chapter are adapted from articles also published elsewhere [28, 34–37].

## 1.1 Context of the present study

### 1.1.1 Cracking in reinforced concrete

Reinforced concrete is a composite material that is widely used for construction due to its low cost and adequate durability. Its main component is concrete, resulting from the mixture of cement, water, sand, and aggregates. Concrete has a high compressive resistance, but is also characterized by low resistance and brittle behaviour when subjected to tension [12]. The material is thus prone to cracking and must usually be enhanced with steel reinforcement bars, thus obtaining reinforced concrete. These rebars can carry tensile forces and, if suitably arranged, confine to the aforementioned cracks, thus significantly improving the structural performance of the composite material.

Despite the presence of steel reinforcement, ordinary concrete structures develop cracks already at the serviceability limit state. The influence of such cracks must thus be taken into account for design purposes. Moreover, it is sometimes preferable to avoid certain reinforcement layouts (for example transverse reinforcement in concrete slabs) due to constructive and economic constraints. Therefore, cracks are sometimes only partially confined and can

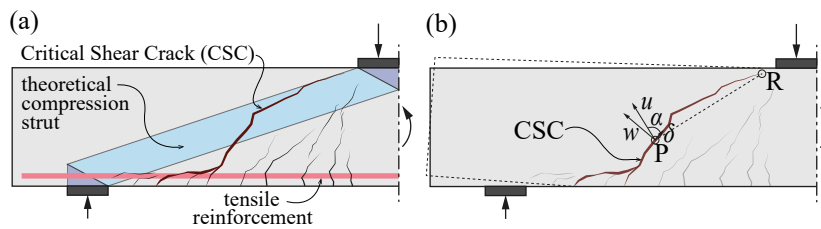


Figure 1.1 – Beam without transverse reinforcement failing in shear: (a) location of Critical Shear Crack and theoretical strut carrying shear; and (b) local kinematics at a generic point of the Critical Shear Crack

influence the overall structural behaviour as zones of material discontinuity. In certain structures, cracks with insufficient confinement can suddenly propagate, leading to brittle failure. A typical example are beams without transverse reinforcement, which behave similar to reinforced concrete slabs [24], a widely used constructive element. In order for such members to resist bending moments, it is necessary to place sufficient longitudinal reinforcement. This is relatively simple and cost-effective, as the rebars can be easily placed at the bottom of the formwork. However, the shearing action can require the further addition of transverse shear reinforcement, which is more challenging and labor-intensive to put in place. Consequently, designers often prefer to increase shear resistance by incrementing the slab thickness, thus increasing the amount of resources needed for construction. A better understanding of the shear carrying capacity of concrete without shear reinforcement (and of the developing cracks) is thus necessary to limit the amount of employed resources and the overall costs, without reducing the required structural safety.

The shear resistance of concrete beams without transverse reinforcement was studied with numerous experimental campaigns, where the development of several bending cracks in the tensile zone was observed [4, 22, 32]. As loads increase, a single crack propagates to traverse the beam, going from one of the supports towards the centre and becoming dominant for the structural behaviour (Figure 1.1a). To enable the loads to traverse this crack and reach the supports, researchers found evidence for several shear carrying mechanism. These mechanisms must thus be understood to determine the maximum shear carrying capacity of the structure. Among the shear carrying mechanisms, aggregate interlocking was identified as one of the most important ones [5, 30, 32]. For example, aggregate interlocking plays an important role in the Critical Shear Crack Theory (CSCT) developed by Muttoni and Fernández Ruiz [22]. They noticed a relationship between the strength of beams and the load-carrying capacity of the main crack, called the Critical Shear Crack (CSC). This is due to the fact that the CSC propagates into the theoretical compression strut carrying the loads to the support (Figure 1.1a), thus limiting the member's capacity to transfer forces.

### 1.1.2 Description and significance of aggregate interlocking

Aggregate interlocking occurs when the two sides of a concrete crack (like the previously mentioned Critical Shear Crack for beams without transverse reinforcement) slide relative to each other. Due to the non-uniform nature of the material, such cracks are characterized by a rough interface with many zones of protruding material. For ordinary concrete mixes, this can be single aggregates, which tend to detach at their interface with the cement matrix as cracks propagate around them [14, 41]. Aggregates are thus often considered to be a major contributor to the overall crack surface roughness, leading to the name *aggregate interlocking*. Several codes account for the increased capacity for shear transfer of rougher cracks considering the maximum aggregate size [8, 31]. However, other factors have been shown to influence the concrete roughness as well, as for example the material strength [1, 15], and concrete cracks maintain a certain level of roughness even in cases where no large aggregates are present. Depending on the material properties (e.g. high strength concrete, lightweight aggregates [1], strong adhesion between matrix and aggregates [29]), increased inter-aggregate fracture can reduce the roughness, which remains thus a topic of debate in the literature.

Depending on the overall structural behaviour, a single crack can open following various paths. It is initiated when concrete reaches its tensile resistance and damage starts accumulating in a narrow zone called *crack* or *Fracture Process Zone* [12]. Thereafter, the crack-lips can be subjected to different *Modes* [25]. In *Mode I*, the crack opens perpendicular to its overall plane of an amount  $w$ , with the resultant of the transferred stresses being normal to it, as shown in Figure 1.2a. After formation, new kinematics become possible. For example, one crack-side can slide of an amount  $\delta$  relative to the other one, a modality called *Mode II* and illustrated in Figure 1.2b. Other behaviours are possible as well, and in general various modes occur at the same time.

In the case of beams without transverse reinforcement failing in shear, detailed measurements have shown that the Critical Shear Crack typically propagates in Mode I and then opens further in Mixed-Mode I+II (referred to as *Mixed Mode* in the following, see Figure 1.1b and Figure 1.2c) [5]. Due to the crack roughness, the relative sliding of two crack lips in Mode II or Mixed-Mode can cause contact between the opposite sides. Shear forces are thus exchanged across the discontinuity by aggregate interlocking. These forces contribute to the ultimate shear carrying capacity of the beam, thus making the understanding of aggregate interlocking instrumental for designing and assessing such structures.

In addition to beams without transverse reinforcement and slabs, aggregate interlocking also plays an important role in other concrete structures characterized by a significant crack development. Some notable examples are footings [23], panels subjected to shear [39], flat-slabs subjected to punching [10], construction joints in concrete structures (where the zone of weakness can behave similar to a crack) and beams reinforced with external plates [38]. Finally, the phenomenon has several similarities with that of bond between concrete and steel

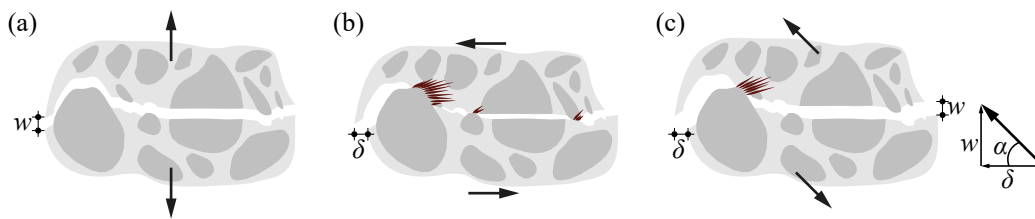


Figure 1.2 – Crack kinematics: (a) Mode I; (b) Mode II; and (c) Mixed-Mode I+II

reinforcement bars, where the protruding ribs can interlock with the surrounding concrete and thus enable a combined structural response.

## 1.2 Overview of state of the art

Aggregate interlocking has been studied since the 1960s, resulting in various experimental campaigns and modelling approaches [7, 11, 15, 16, 18, 20, 21, 25, 27, 32, 40]. In this section, the results and insights of some notable works are summarized, providing an overview of the current knowledge on the topic. This introduces the discussion of several remaining open questions, which are addressed in the following chapters.

### 1.2.1 Experimental investigations

Typical experimental campaigns on aggregate interlocking are performed using concrete specimens with a geometry suitable to generate a fracture plane, upon which Mode II or more complex kinematics are applied. Several specimen shapes and loading conditions are reported in the literature, with some notable examples illustrated in Figure 1.3. The specimens are characterized by the presence of notches to properly localize cracking. Although they differ considerably in size and shape, the tested crack plane typically measures between one and ten times the maximum aggregate size  $D_{\max}$ . The loading procedures and associated boundary conditions vary as well, and in some cases reinforcement is added in areas where cracking is undesired. Despite these differences, the reported results are relatively consistent, as discussed in later chapters (see also Appendix 4).

A specimen type which is frequently chosen for experiments on aggregate interlocking are “push-off” specimens, as those of Paulay and Loeber [26] and Walraven et al. [42] represented in Figure 1.3. These specimens present a series of practical advantages, as they are easy to produce, allow for relatively large crack planes and can be tested in common uniaxial machines. However, the arrangement also has several drawbacks, like difficulties in precisely introducing the initial crack and controlling the crack kinematics.

When the specimens are loaded undamaged, several diagonal cracks develop (instead of a single crack plane), and high forces are measured [13]. Rather than a single crack, such tests concern a zone of diffused cracking and the results can be significantly influenced by

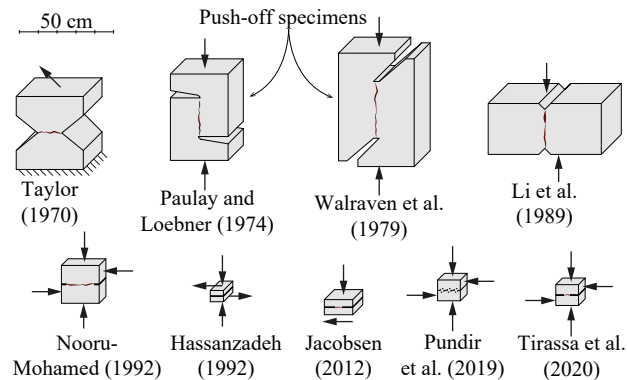


Figure 1.3 – Comparison of geometries and loading condition for specimens from the literature and the present research [11, 16, 19, 25, 26, 28, 32, 36, 42]

variations in the boundary conditions. Therefore, in most cases a single crack is introduced prior to testing, as shown for the examples of Figure 1.3. However, due to set-up limitations in the case of push-off specimens, these cracks are usually produced by splitting rather than in direct tension, and therefore tend to open and propagate in a relatively uncontrolled manner. This can potentially lead to a reduction of the residual tensile resistance in cracks with small openings and thus influence the interlocking forces (refer to the model presented in Chapter 4). A second drawback of push-off specimens is the difficulty in controlling crack kinematics. The uni-axial set-up is used to shear the crack plane, while the crack opening cannot be controlled precisely. Tests are thus often performed under approximately constant normal forces (provided by yielding rebars which cross the widening interface), by adapting the crack opening step-wise or by letting it dilate freely.

Regardless of these drawbacks, push-off specimens are frequently used [15, 26, 29, 42] and the results are relatively consistent with those obtained using different specimen shapes. For example, an early paper by Paulay and Loeber [26] reports the results of 44 push-off tests, showing that smaller crack openings correspond to larger aggregate interlocking forces. Interestingly, no influence of the maximum aggregate size  $D_{\max}$  was observed for the employed concrete mixes, an aspect debated by many following researchers and further discussed in Chapter 4. The same study also reports a change in behaviour due to the differential settling of wet concrete and the associated variations in concrete properties (weaker material close to the surface due to bleeding [9]). This is indicative of the phenomenon's complexity, characterized by numerous parameters which can influence the interlocking behaviour.

The work of Walraven [40–42] is also based on results obtained testing push-off specimens. It resulted in the development of the *Two-Phase Model*, which influenced several approaches for shear transfer in reinforced concrete beams [6, 38] and concrete structures in general [8, 10, 27, 39]. A detailed discussion of this model can be found in Chapter 3.

The introduction of more modern testing equipment enabled the development of set-ups with jacks acting in two perpendicular directions. Compared to push-off specimens, this allows for the introduction of tensile cracks (rather than splitting ones) and facilitates the application of

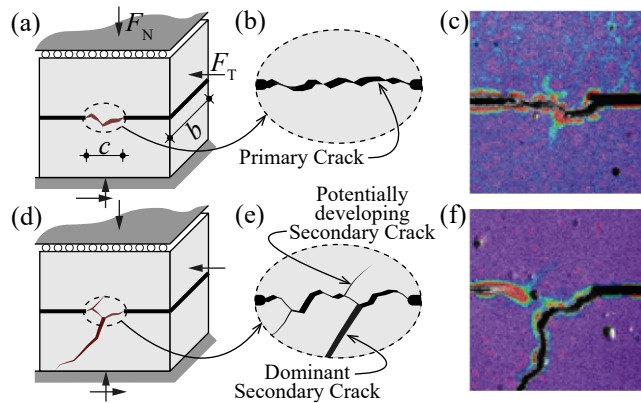


Figure 1.4 – Typical cracking patterns: (a) specimen with Primary Crack; (b) detail of Primary Crack; (c) DIC image of Primary Crack; (d) specimen with Dominant Secondary Crack; (e) detail with Primary Crack and a Secondary Crack developing from it; and (f) DIC image of Primary Crack with Dominant Secondary Crack

precise kinematics upon them. Such set-ups are usually more complex and require additional space, leading to a reduction in specimen sizes (Figure 1.3). Early examples are the works of Nooru-Mohamed [25] and Hassanzadeh [11]. By avoiding the use of steel reinforcement in the specimens, their researches focus increasingly on the development of single cracks as a function of complex loading paths. Possibly due to rather small notch depths, both researchers report difficulties in obtaining planar cracks and the consequent development of new cracks generating from the initial one during testing. These cracks are commonly called *Secondary Cracks* to distinguish them from the *Primary Crack* initially introduced in the plane identified by the specimen notches (see Figure 1.4). Secondary cracks significantly influence the specimen's behaviour and often result in a different failure mode. Such cracks can also be observed in tests of full-scale concrete structures [5].

Another work on aggregate interlocking of particular relevance is that of Jacobsen [16]. It consists of 20 tests where precise Mixed-Mode kinematics were consistently applied on double-notched specimens pre-cracked in Mode I. These kinematics correspond to those observed in certain types of full-scale structures [5, 10] (see for example Figure 1.1b for the case of concrete beams without transverse reinforcement). The kinematic parameters chosen in [16] were thus taken as a reference for the experiments reported in this thesis.

### 1.2.2 Modelling approaches

The previously discussed experimental campaigns led to the development of several models, aimed at estimating the interlocking forces which can be transferred across concrete cracks. Two major aspects concern most approaches and are addressed in various ways. The first is how to estimate the number, depth and size of contacts between the two crack sides as a function of the concrete properties and the crack kinematics. A second issue are the assumptions to calculate the intensity and direction of the exchanged forces as a function of

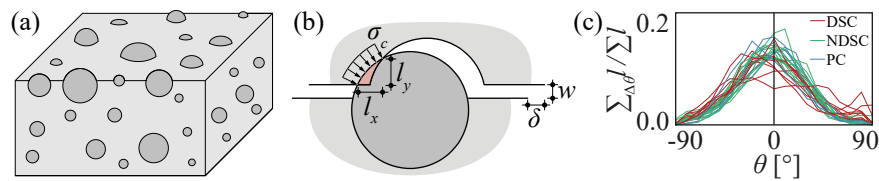


Figure 1.5 – Modelling approaches from literature: (a) crack idealization in Two-Phase Model; (b) contact in Two-Phase Model; and (c) distribution of segments steepness for surfaces from present research (see Chapter 4)

said contact properties.

For example, the previously mentioned *Two-Phase Model* by Walraven [40–42] approximates the roughness of concrete cracks by considering the statistical distribution of aggregates protruding from a flat plane. These aggregates are approximated as rigid spheres (Figure 1.5a), thus enabling a calculation of the contact under consideration of the crack kinematics (Figure 1.5b). A perfectly plastic constitutive law is assumed for each contact, allowing to determine the interlocking stresses.

Another influential approach is introduced with the *Contact Density Model* by Li and Maekawa [18, 19]. In this case, the crack roughness is taken into account considering several 2D-profiles (consisting of a series of segments) extracted from concrete crack surfaces. These profiles are used to determine an overall contact density function, which approximates the distribution of segments based on their steepness and is assumed as characteristic of the considered material (see Figure 1.5c for examples of such distributions). It is thus possible to account for the fact that concrete cracks are mostly flat, with a limited amount of steep protruding zones. A simple geometric approach allows finding the patches which are in contact with the opposite crack-side for given kinematics. An elastic-perfectly plastic constitutive law is then used to determine the contact forces. The original model was adapted and extended for various material properties and crack kinematics [1–3], for example by adapting the chosen contact density function. Slight adjustment of this function, most notably in the range determining the relative amount of steep segments ( $50^\circ$  to  $90^\circ$ ), can significantly influence the results. Additional information on the Contact Density Model can be found in Appendix B of Chapter 4.

### 1.3 Aims and objectives

Although aggregate interlocking has been studied for several decades, a series of aspects remain unclear. In this section, some major remaining issues are presented to introduce the further analysis of the following chapters.

- **Concrete properties and crack roughness:** To determine the contact properties (e.g. size, penetration depth, material confinement) for given crack kinematics, it is necessary to account for the crack roughness. However, the surfaces of concrete cracks have

complex shapes with fractal properties [17], so that the scale of analysis is mostly chosen for practical reasons. Considering the surface at a high level of detail is unpractical for most applications, as it significantly increases complexity and computational times. The measured roughness is thus approximated using various approaches [16, 18, 41]. There remains, however, great uncertainty in relating the material properties of concrete (e.g. material strength, aggregate sizes and resistances) with the roughness of corresponding crack surfaces. Many models, especially for full-scale structures, adopt simplified approaches, often using the maximum aggregate size as the main parameter defining the surface roughness [5, 8, 22, 30, 31, 39]. However, some studies report a limited influence of the maximum aggregate size [26] or variations in roughness as a function of the aggregate properties [29]. It thus remains unclear how to relate material properties and the associated surface roughness for the calculation of interlocking stresses.

- **Secondary cracking:** The development of secondary cracks is a further element of uncertainty. Cracks in concrete structures grow as loading increases, and in some cases new cracks can cause significant changes in the load-transfer mechanisms, potentially leading to failure. This is partially accounted for in finite-elements models using approaches based on rotating cracks. Nevertheless, the causes and influence of secondary cracking remain unclear, with some studies even taking specific measures to avoid tests resulting in this failure mode [16].
- **Cohesive properties of cracks:** Concrete cracking is a complex phenomenon, and the development of cracks occurs progressively. In a displacement controlled tensile test, the stress  $\sigma$  normal to the crack plane initially increases following an elastic path. Close to the peak load, this tensile stress becomes non-linear and finally gradually decreases during the softening phase [12] (typical load-displacement curves for tensile tests are shown in Figure 2.7). Hillerborg [12] explained this behaviour introducing the concept of a *Fracture Process Zone*. According to his *Fictitious Crack Model*, a great number of micro-cracks start to develop in concrete subjected to increasing tensile stresses. They localize in zones of weakness, generating a Fracture Process Zone characterized by material damage, while also maintaining some residual tensile resistance (as observed during the softening phase) until significant crack openings are reached (approximately 0.2 mm). The Fracture Process Zone can be conceptualized as a zone of diffused cracking with some remaining material bridging the two sides. Alternatively, it can be simplified as a crack possessing a residual tensile strength, which can be distinguished from a full crack with no cohesion.

For simplicity, in this thesis the term *crack* indicates zones of localized damage regardless of the crack opening. The term will therefore refer both to Fracture Process Zones capable to transfer tensile stresses and to full cracks without any residual material soundness.

As discussed previously, in some research projects on aggregate interlocking (and particularly for push-off specimens) cracks are introduced in an uncontrolled manner

by splitting, thus potentially removing all material soundness. This approach can be questioned, as cracks in full-scale structures can have some residual tensile strength influencing the aggregate interlocking behaviour.

- **Contact forces:** When a contact between two crack lips is identified, models for aggregate interlocking need to estimate the intensity and direction of the resulting forces. However, it remains unclear how to determine local parameters like the friction coefficient, the material's resistance and confinement or its behaviour for increasing penetrations. For example, some models assume the contact force as perpendicular to the contact plane [19], while others consider the presence of friction [40].
- **Extension to bond:** Bond between steel rebars and concrete allows for their combined response and is an important aspect of reinforced concrete structures. It is activated when the ribs on the rebar surface penetrate into the surrounding material, a phenomenon with clear similarities to aggregate interlocking. Nevertheless, no unified mechanical approach has yet emerged to treat both phenomena in a similar manner.

## 1.4 Thesis methodology and contributions

This thesis presents new insights on various aspects related to the interlocking of surfaces in concrete structures:

- The results of an extensive experimental programme on concrete cracks engaging in aggregate interlocking are presented. This new evidence is needed due to the limited amount of tests on cracks subjected to realistic kinematics available in the literature. Moreover, modern measuring techniques like Digital Image Correlation (DIC) were only used in few research projects [16] and can help tracking the crack development. The reported tests were thus conducted using a set-up capable of applying precise bi-axial kinematics in accordance to [16], consisting mostly of Mode I followed by Mixed Mode, and were monitored using DIC.
- Tests characterized by the development of dominant secondary cracking were sometimes neglected in previous research programmes. However, the phenomenon is also observed in full-scale concrete structures, where it can significantly influence the behaviour at failure. The present investigation thus includes the results of tests with secondary crack propagation and considers them for the development of a mechanically based model.
- Several crack surfaces obtained from the tests are scanned at high resolution to study the roughness as a function of the material properties. Different concrete mixes are considered to study how the maximum aggregate size and the concrete strength influence the surface roughness and the capability for force transfer by aggregate interlocking.

- In addition to tests on concrete cracks, special steel-to-concrete interlocking tests on surfaces consisting of half-spheres were also performed. These surfaces simplify the analysis of contacts, allowing to focus on the exchanged contact forces. In particular, the experimental evidence complies with the geometrical hypotheses of the Two-Phase Model [41], thus enabling an evaluation of its assumptions regarding the material and contact properties.
- A new mechanically based model for the transfer of forces in concrete cracks is presented. It is based on the approach of Li and Maekawa [18, 19], and additionally accounts for the possible development of secondary cracks and the influence of residual material soundness for cracks with small openings.
- The model is finally extended to the case of bond and interlocking between ribbed steel rebars and concrete. Several similarities with aggregate interlocking are identified and discussed, thus introducing a unified approach for both interlocking problems.

The thesis contains several scientific articles addressing the previous points. It is structured as follows:

- **Chapter 2** focuses on the experimental approach, describing the set-ups developed for the test-campaign and some early experiments performed in the frame of this research project. The results of tensile tests on small scale concrete specimens are presented, which show how the various components of concrete (matrix, aggregate interfaces, aggregates) behave differently when subjected to tension. Moreover, preliminary Mixed Mode experiments are compared to models from the literature, showing good agreement. The chapter is based on the following conference papers, which can also be consulted in Appendices 5 and 6 in their entirety:

Tirassa M., Fernández Ruiz M., Anciaux G., Muttoni A. (2017). Interface Stresses in Cracked Concrete: Testing for Review of Its Fundamentals. In *2017 fib Symposium: High Tech Concrete: Where Technology and Engineering Meet*, pp. 740–748. Maastricht, Netherlands. (doi: 10.1007/978-3-319-59471-2\_87)

Tirassa M., Fernández Ruiz M., Muttoni A. (2018). Modern experimental research techniques for a consistent understanding of aggregate interlocking. In *Proceedings of the 12th fib PhD Symposium in Civil Engineering*, pp. 723–730. Prague, Czech Republic. (url: [infoscience.epfl.ch/record/257222](http://infoscience.epfl.ch/record/257222))

- **Chapter 3** contains a review of the hypotheses of the Two-Phase Model by Walraven [40–42]. It is based on the results of interlocking experiments performed on interfaces between concrete and steel spheres, which correspond to the geometry assumed by Walraven. These insights are used to develop a model aimed at reproducing the test results with a precise calculation of the contacts occurring due to interface sliding. The chapter was previously published as the following scientific publication [28]:

Pundir M., Tirassa M., Fernández Ruiz M., Muttoni A., Anciaux G. (2019). Review of fundamental assumptions of the Two-Phase model for aggregate interlocking in cracked concrete using numerical methods and experimental evidence. *Cement and Concrete Research*, 125:105855. (doi: 10.1016/j.cemconres.2019.105855)

- **Chapter 4** deals with aggregate interlocking in the case of concrete cracks subjected to Mixed-Mode kinematics. The experimental results of several specimens, including their surface geometry, are summarized and analysed, and a mechanically based model for estimating the interlocking forces is presented. The chapter consists of a paper accepted for publication as follows [36]:

Tirassa M., Fernández Ruiz M., Muttoni A. (2020, in press). Influence of cracking and rough surface properties on the transfer of forces in cracked concrete. *Engineering Structures*.

- **Chapter 5** reports the results of interlocking experiments between rebar-ribs and concrete material. The model of Chapter 4 is extended to the case of rebars, thus addressing similarities between the phenomena of bond in cracked conditions and aggregate interlocking, and introducing a unified approach. The chapter consists of a paper submitted for review as follows [35]:

Tirassa M., Fernández Ruiz M., Muttoni A. (2020). An interlocking approach for the rebar-to-concrete contact in bond.

The thesis ends with **Chapter 6**, which contains a summary of the main conclusions and an outlook for future research. The final **Appendix** can be of particular interest for researchers interested in aggregate interlocking, as it reports detailed data and test results for all performed experiments, some of which are not included in the previously mentioned papers. This data is also available for download on Zenodo [33].

## Bibliography

- [1] Bujadham, B. and Maekawa, K. (1992a). Qualitative studies on mechanisms of stress transfer across cracks in concrete. *Proc. of JSCE*, 451(V-17):265–275.
- [2] Bujadham, B. and Maekawa, K. (1992b). The universal Model for Stress Transfer across cracks in Concrete. *Proc. of JSCE*, 451(V-17):277–287.
- [3] Bujadham, B., Mishima, T., and Maekawa, K. (1992). Verification of the universal stress transfer model. *Proc. of JSCE*, 451(V-17):289–300.
- [4] Cavagnis, F, Fernández Ruiz, M., and Muttoni, A. (2015). Shear failures in reinforced concrete members without transverse reinforcement: An analysis of the critical shear crack development on the basis of test results. *Engineering Structures*, 103:157–173.

- [5] Cavagnis, F, Fernández Ruiz, M., and Muttoni, A. (2017). An analysis of the shear-transfer actions in reinforced concrete members without transverse reinforcement based on refined experimental measurements. *Structural Concrete*, 19(1):49–64.
- [6] Cavagnis, F, Fernández Ruiz, M., and Muttoni, A. (2018). A mechanical model for failures in shear of members without transverse reinforcement based on development of a critical shear crack. *Engineering Structures*, 157:300–315.
- [7] Divakar, M. P, Fafitis, A., and Shah, S. P. (1987). Constitutive Model for Shear Transfer in Cracked Concrete. *Journal of Structural Engineering*, 113(5):1046–1062.
- [8] fib (International Federation for Structural Concrete) (2013). *fib Model Code for Concrete structures 2010*. Ernst & Sohn, 402 p, Germany.
- [9] Giaccio, G. and Giovambattista, A. (1986). Bleeding - Evaluation of its effects on concrete behaviour. *Materials and Structures*, 19(4):265–271.
- [10] Guidotti, R. (2010). *Poinçonnement des planchers-dalles avec colonnes superposées fortement sollicitées*. Ph.D. Thesis, EPFL, Lausanne, Switzerland.
- [11] Hassanzadeh, M. (1992). *Behavior of Fracture Process Zones in Concrete Influenced by Simultaneously Applied Normal and Shear Displacements*. Ph.D. Thesis, Lund University, Sweden.
- [12] Hillerborg, A. (1983). Analysis of one single crack. In *Fracture Mechanics of Concrete (Developments in civil engineering)*, pages 223 – 249. Wittmann, Folker H., Amsterdam, Netherlands.
- [13] Hofbeck, J., Ibrahim, I., and Mattock, A. (1969). Shear transfer in reinforced concrete. *ACI Journal Proceedings*, 66(2):119–128.
- [14] Hsu, T. T. C. and Slate, F. O. (1963). Tensile Bond Strength Between Aggregate and Cement Paste or Mortar. *ACI Journal Proceedings*, 60(4):465–486.
- [15] Huber, T., Huber, P., and Kollegger, J. (2019). Influence of aggregate interlock on the shear resistance of reinforced concrete beams without stirrups. *Engineering Structures*, 186:26–42.
- [16] Jacobsen, J. S. (2012). *Constitutive Mixed Mode Behavior of Cracks in Concrete: Experimental Investigations of Material Modeling*. Ph.D. Thesis, Technical University of Denmark, Kongens Lyngby, Denmark.
- [17] Lange, D. A., Jennings, H. M., and Shah, S. P. (1993). Relationship between Fracture Surface Roughness and Fracture Behavior of Cement Paste and Mortar. *Journal of the American Ceramic Society*, 76(3):589–597.
- [18] Li, B. and Maekawa, K. (1987). Contact density model for cracks in concrete. In *IABSE reports*, volume 54, pages 51–62, Delft.

- [19] Li, B., Maekawa, K., and Okamura, H. (1989). Contact density model for stress transfer across cracks in concrete. *Journal of the Faculty of Engineering, The University of Tokyo*, 40(1):9–52.
- [20] Mattock, A. and Hawkins, N. (1972). Shear transfer in reinforced concrete – recent research. *Pci Journal*, 17.2:55–75.
- [21] Millard, S. and Johnson, R. (1984). Shear transfer across cracks in reinforced concrete due to aggregate interlock and to dowel action. *Magazine of Concrete Research*, 36(126):9–21.
- [22] Muttoni, A. and Fernández Ruiz, M. (2008). Shear Strength of Members without Transverse Reinforcement as Function of Critical Shear Crack Width. *ACI Structural Journal*, 105(2):163–172.
- [23] Muttoni, A., Fernández Ruiz, M., and Simões, J. T. (2018). The theoretical principles of the critical shear crack theory for punching shear failures and derivation of consistent closed-form design expressions. *Structural Concrete*, 19(1):174–190.
- [24] Muttoni, A. and Fernández Ruiz, Miguel, M. (2010). Shear in slabs and beams: should they be treated in the same way? In *fib Bulletin 57*, pages 105–128. fib (International Federation for Structural Concrete), Lausanne, Switzerland.
- [25] Nooru-Mohamed, M. B. (1992). *Mixed-Mode Fracture of Concrete: An Experimental Approach*. Ph.D. Thesis, Delft University of Technology, Sweden.
- [26] Paulay, T. and Loeber, P. J. (1974). Shear Transfer By Aggregate Interlock. *ACI Special Publication*, 42:1–16.
- [27] Presvyri, S. (2019). *Aggregate Interlock: Extending the aggregate interlock model to high strength concrete*. Ph.D. Thesis, Delft University of Technology, Sweden.
- [28] Pundir, M., Tirassa, M., Fernández Ruiz, M., Muttoni, A., and Anciaux, G. (2019). Review of fundamental assumptions of the Two-Phase model for aggregate interlocking in cracked concrete using numerical methods and experimental evidence. *Cement and Concrete Research*, 125:105855.
- [29] Sagaseta, J. and Vollum, R. L. (2011). Influence of Aggregate Fracture on Shear Transfer Through Cracks in Reinforced Concrete. *Magazine of Concrete Research*, 63(2):119–137.
- [30] Sherwood, E. G., Bentz, E. C., and Collins, M. P. (2007). Effect of aggregate size on beam-shear strength of thick slabs. *ACI Structural Journal*, 104(2):180.
- [31] Swiss Society of Engineers and Architects (2013). *SIA Code 262 for Concrete Structures*. Zurich, Switzerland.
- [32] Taylor, H. P. J. (1970). *Investigation of the Forces Carried Across Cracks in Reinforced Concrete Beams in Shear by Interlock of Aggregate*. Number 42.447 in Technical report (Cement and Concrete Association). London, United Kingdom.

- [33] Tirassa, M. (2020). Experimental data for 'The transfer of forces through rough surface contact in concrete'. type: dataset, doi: 10.5281/zenodo.3894516.
- [34] Tirassa, M., Fernández Ruiz, M., Anciaux, G., and Muttoni, A. (2017). Interface Stresses in Cracked Concrete: Testing for Review of Its Fundamentals. In *2017 fib Symposium High Tech Concrete: Where Technology and Engineering Meet*, pages 740–748. Maastricht, Netherlands.
- [35] Tirassa, M., Fernández Ruiz, M., and Muttoni, A. (2020). An interlocking approach for the rebar-to-concrete contact in bond. [*Submitted for review*].
- [36] Tirassa, M., Fernández Ruiz, M., and Muttoni, A. (2020, in press). Influence of cracking and rough surface properties on the transfer of forces in cracked concrete. *Engineering Structures*.
- [37] Tirassa, M., Fernández Ruiz, Miguel, and Muttoni, A. (2018). Modern experimental research techniques for a consistent understanding of aggregate interlocking. In *Proceedings of the 12th fib PhD Symposium in Civil Engineering*, pages 723–730, Prague, Czech Republic.
- [38] Ulaga, T. (2003). *Betonbauteile mit Stab-und Lamellenbewehrung: Verbund-und Zuggliedmodellierung*. Ph.D. Thesis, ETH Zurich, Switzerland.
- [39] Vecchio, F. J. and Collins, M. P. (1986). The modified compression-field theory for reinforced concrete elements subjected to shear. *ACI Journal*, 83(2):219–231.
- [40] Walraven, J. C. (1980). *Aggregate Interlock: a Theoretical and Experimental Analysis*. Ph.D. Thesis, Delft University of Technology, Sweden.
- [41] Walraven, J. C. (1981). Fundamental Analysis of Aggregate Interlock. *ASCE Journal of the Structural Division*, 107(11):2245–2270.
- [42] Walraven, J. C., Vos, E., and Reinhardt, H. W. (1979). Experiments on shear transfer in cracks in concrete. Part I. Technical report, Delft University of Technology, Faculty Civil Engineering and Geosciences.

## 2 Set-ups and preliminary tests

This chapter describes the test set-ups, concrete mixes and testing procedures which were used throughout this research project. It also presents the results of several preliminary tests, including Mode I tests on small concrete specimens. The chapter's content is a summary (with some additions and modifications) of the following two conference papers [9, 10]:

Tirassa M., Fernández Ruiz M., Anciaux G., Muttoni A. (2017). Interface Stresses in Cracked Concrete: Testing for Review of Its Fundamentals. In *2017 fib Symposium: High Tech Concrete: Where Technology and Engineering Meet*, pp. 740–748. Maastricht, Netherlands. (doi: 10.1007/978-3-319-59471-2\_87)

Tirassa M., Fernández Ruiz M., Muttoni A. (2018). Modern experimental research techniques for a consistent understanding of aggregate interlocking. In *Proceedings of the 12th fib PhD Symposium in Civil Engineering*, pp. 723–730. Prague, Czech Republic. (url: [infoscience.epfl.ch/record/257222](http://infoscience.epfl.ch/record/257222))

The original version of these papers can be consulted in Appendices 5 and 6. For both articles, Max Tirassa planned and carried out the experimental program and analysed the obtained data under the supervision of the other authors.

### 2.1 Specimens

The specimens used in this research project mostly consisted of double notched specimens made out of concrete and produced following the procedure shown in Figure 2.1. Several concretes with varying characteristics were prepared, and the material was used to cast bars (unreinforced beams) laying horizontally and measuring approximately 1000 · 250 · 200 mm. After a curing period under sealed conditions of minimum 28 days, the bars were demoulded and processed to obtain the test specimens. Using a circular saw, slices of thickness  $b$  (usually approximately 50 mm) were cut, and from each slice several specimens (typically two) were made using a water-jet cutting machine. That way it was possible to introduce notches of

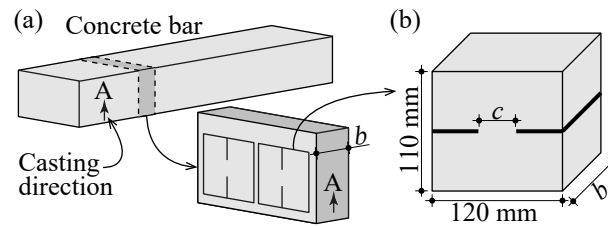


Figure 2.1 – Specimen production: (a) concrete bar and slice; and (b) double notched specimen

varying depth, thus obtaining specimens with crack planes measuring  $c \cdot b$  (see Figure 2.1b). Unless otherwise specified, the specimens were 120 mm long and 110 mm high. These measurements, as well as the specimen width  $b$ , were chosen in accordance with constraints relating to the first of the set-ups presented in Section 2.2.

In wet concrete, rising water can accumulate under large aggregates due to bleeding and thus influence the matrix-to-aggregate interface, reducing its tensile resistance [3]. To minimize the influence of this phenomenon on the test results, specimens were oriented with the crack plane perpendicular to the casting direction (unless otherwise specified, see Appendix 1). That way, the zones of weakness were located on the sides of aggregates, thus reducing their influence on the initial crack development and resulting in a more average material response.

The front side of most specimens was prepared for surface measurements using Digital Image Correlation (DIC) which allow for detailed tracking of the developing cracks (Appendix 2 reports DIC pictures of the crack-patterns for numerous tests). The surface was painted white and a pattern of small black dots was sprayed randomly on this background to achieve good optical contrast (Figure 2.2c). Two cameras were placed in front of each specimen at approximately 30 cm of distance and took pictures at regular time intervals. For typical tests with crack initiation in Mode I and followed by Mixed-Mode loading (with an initial loading speed of  $0.1 \mu\text{m}/\text{sec}$ , which was increased after the peak in shear force), a picture was taken every 10 seconds during the Mode I phase, to capture the instant of crack-localization with relative precision. During the much longer Mixed-Mode phase, the time interval was increased to 100 seconds, as the crack pattern developed slowly with the exception of the sometimes occurring sudden propagation of a secondary crack. Most tests were monitored with 4 Megapixel cameras of the company “Manta”, although in some cases cameras with higher resolution were used. The pictures were analysed using the commercial software “Vic3D” by the company “Correlated Solutions”, which allowed to obtain data on displacements and strains on the specimen surface, thus identifying even small cracks. The theoretical precision was of approximately  $1/32$  of the pixel size, with each pixel having a side length of about 0.08 mm). In practice, when considering pictures taken before testing, the typical level of noise for displacements in static conditions measured less than approximately 0.01 mm.

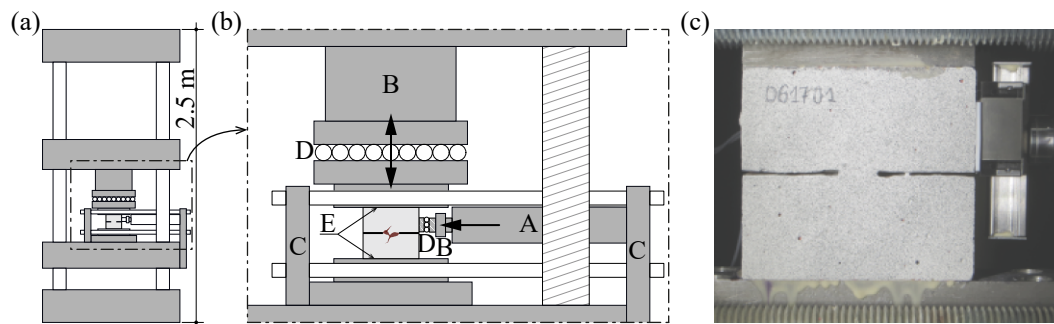


Figure 2.2 – (a) Test set-up with 500 kN electromechanical machine “Zwick”; (b) detail of testing area (A-horizontal jack, B-load cell, C-holding plate, D-slider, E-gluing planes); and (c) double-notched specimen ready for testing

## 2.2 Set-ups and testing procedure

Tests were performed with one of two test set-ups capable of pre-cracking the specimens in Mode I and to subject the resulting crack to Mixed-Mode kinematics. The first set-up consisted of a 500 kN electromechanical machine by the company “Zwick” acting in the vertical direction. A 50 kN hydraulic jack was added for imposing horizontal displacements (Figure 2.2a-b). Specimens were glued to steel plates as shown in Figure 2.2c, so that the lower half was fixed, while low friction-roller slides allowed the upper specimen part to translate freely. The described arrangement worked well, allowing for precise control of the crack kinematics, but presented limitations in terms of maximum horizontal loads. This was mainly due to the slide allowing for vertical displacements, which was small due limited available space and could only be charged up to 19 kN.

A second set-up, called “Triroc”, was used for some tests in later phases of the research project to carry out tests with higher horizontal load (Figure 2.3). It consisted of a stiff steel frame, with two hydraulic jacks capable of applying larger loads (approximately 1000 kN vertically and 300 kN horizontally).

Both set-ups worked similarly, being able to introduce a crack between the specimens notches and displacing one of the resulting specimen halves vertically and horizontally. The crack was introduced by applying a tensile force in the vertical direction and slowly increasing the width  $w$  of the obtained crack. This force is indicated with  $F_N$ , as it is normal to the crack plane, and corresponds to a normal stress  $\sigma$  (positive for tension). The set-ups could also apply compression ( $\sigma < 0$ ) to limit the opening  $w$  as a function of the desired crack kinematics. The horizontal jacks could push sideways, thus making the crack slide by an amount  $\delta$  and applying a tangential force  $F_T > 0$  associated to a shear stress  $\tau > 0$ . These operations were performed in a closed-controlled loop, to relate the measured values of crack opening and sliding with each other and follow pre-defined Mixed-Mode or Mode II kinematics.

The crack opening and sliding were measured using a novel arrangement consisting of two pairs of custom-made 2D-gauges glued on the back of the specimen as shown in Figure 2.4.

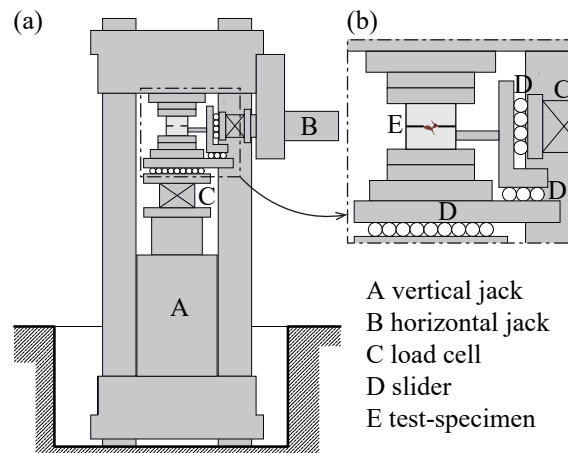


Figure 2.3 – (a) Test set-up with hydraulic jacks “Triroc”; and (b) detail of testing area

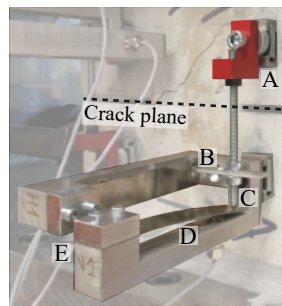


Figure 2.4 – 2D-gauge used to measure applied kinematics: A-steel pin fixed on upper specimen half; B-element pushing horizontally on blade; C-element pushing vertically on blade; D-curved steel blade with strain gauge on its back; and E-support element for blades fixed on lower specimen half

Each of them consisted of two steel blades, with a strain gauge glued on the back and placed perpendicularly to each other (one vertically and the other horizontally). They were fixed on one half of the specimen, while a steel pin pushing on the two perpendicular blades at the same time was glued on the other half (the distances between the glueing points was of approximately 50 mm, see elements A and E in Figure 2.4). The change in curvature of each blade was registered by the strain gauge and converted into a displacement measurement. Finally, the signal of the two vertical gauges were averaged to obtain the crack opening  $w$ , while the two horizontal gauges indicated the amount of crack sliding  $\delta$ . The test control was programmed so that when the displacement of the horizontal jack resulted in sliding at the crack, additional opening of the crack was allowed in accordance to the predefined kinematics.

Table 2.1 – Mix design and compressive resistance of castings

Series #	Cement	$D_{\max}$ [mm]	Water [kg/m <sup>3</sup> ]	Cement [kg/m <sup>3</sup> ]	Aggregates [kg/m <sup>3</sup> ]	$f_{c,28}$ [MPa]
01 02 03	CEMII A-LL42.5R	16	172	310	1955	32.8 30.6
04 05	white CEMII A-LL42.5N	8	204	316	1809	29.8 25.7 24.7
06 07 3101	CEMII A-LL42.5N	8	177	321	1853	30.1 37.1 28.9
08		4	Mortar “Weber mur 920”			8.1 7.7 8.4
09 3103	CEMII A-LL42.5N	16	165	330	1880	60.0 56.5 63.6
3102	CEMII B-M-T-LL42.5N	16	195	340	1817	40.4 37.6 37.8
3105	CEMII A-LL42.5N	2	250	500	1500	42.2 42.9 49.4
15 3104	CEMII A-LL42.5N	2	250	500	1500	41.2 37.1 39.8

## 2.3 Concrete properties

Various concrete mixes were employed, and the mix designs and material properties are summarized in Table 2.1. The table also reports the cylinder compressive resistance after 28 days  $f_{c,28}$ . This resistance was typically measured using 300 mm high cylinders with a diameter of 150 mm. In some cases, smaller cylinders with height 200 mm and diameter 100 mm were employed, and the obtained values were reduced with a correction factor equal to 0.92, as in [12]. In the following, tests will be normalized and modelled using a value  $f_c$  corresponding to the day of testing and calculated according to *fib* Model Code [2] as a function of the number of days since casting. Figure 2.5 reports the results of the cylinder tests as well as the calculated concrete strength development curve for various castings.

The force transfer capacity of concrete cracks is often assumed to be influenced by the sizes and strengths of the aggregates used in the concrete mix [2, 13]. However, due to their great variability, it is difficult to precisely characterize the employed aggregates and assess how their properties influence the crack roughness. Particular attention was thus dedicated to the properties of the aggregates used for this study. Figure 2.6 presents pictures of the employed material and the corresponding granulometric curves (where available). The petrographic properties are reported in Table 2.2. Some castings were performed using ordinary components (like for series 01-03), while for others the components were adapted to ensure a visual distinction between aggregates and cement matrix. For castings 04-05 this was achieved using dark and uniformly coloured aggregates, mixed with light coloured sand and white cement. For casting 06-07 red pigment was added to the mix in order to colour the cement matrix.

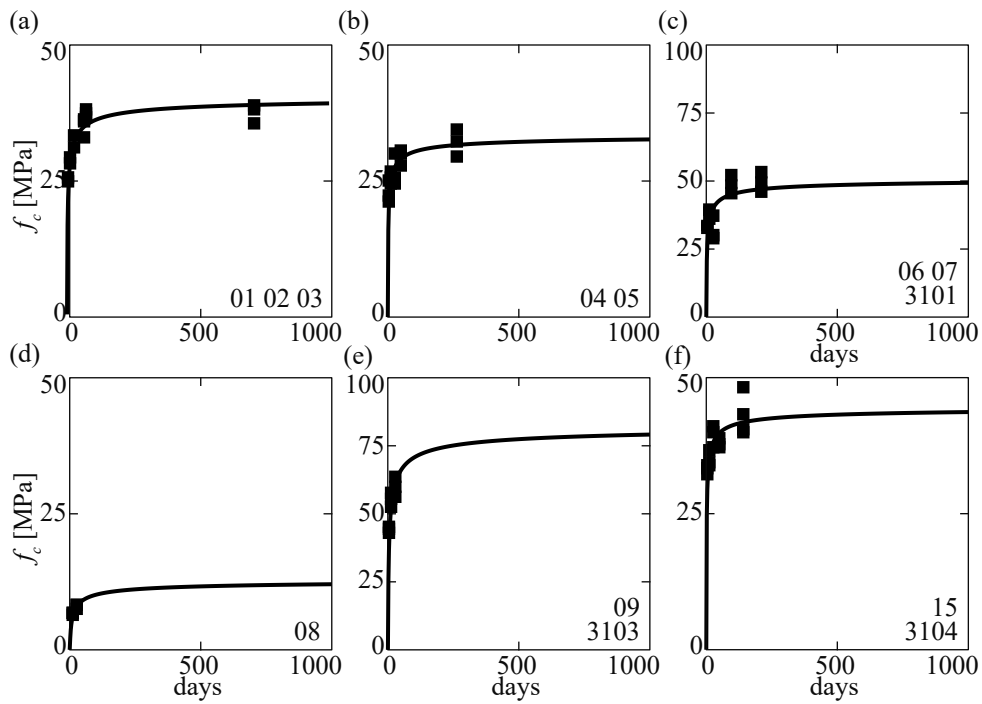


Figure 2.5 – Development of cylinder concrete compressive strength: (a) series 01 02 03; (b) series 04 05; (c) series 06 07 3101; (d) series 08; (e) series 09 3103; and (f) series 15 3104

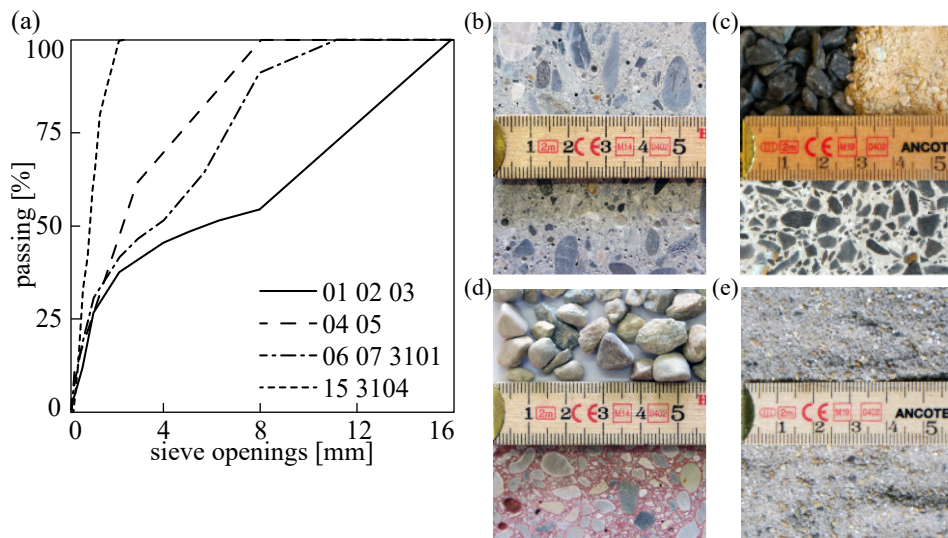


Figure 2.6 – Employed aggregates: (a) granulometric curves for various castings; (b) concrete for casting 01 02 03; (c) concrete, aggregates and sand for casting 04 05; (d) concrete and aggregates for casting 06 07 3101; and (e) sand for casting 15 3104

## 2.4. Tensile properties of concrete components

Table 2.2 – Aggregate properties for various castings (hardness according to [11])

Series	$D_{\max}$ [mm]	Type [11]	Origin	Petrography
01 02 03	16	Hard gravel	Rhone river Riddes (CH)	limestone ~30% granitoids ~30% sandstone ~20% quartzites ~20%
04 05	8	Medium-hard gravel	Quarry Villeneuve (CH)	limestone ~95%
06 07 3101	8	Medium-hard gravel	Gravel pit Savigny (CH)	limestone ~85%
15 3104 3105	2	Hard sand	Quarry (DE)	quartz ~80%

## 2.4 Tensile properties of concrete components

Concrete is a heterogeneous material, and its various components (cement matrix, aggregates and the interface between them) behave differently when subjected to cracking. For example, tests performed by Hsu and Slate [6] show that the tensile resistance at the interface between aggregates and the surrounding cement matrix is generally lower compared to the tensile resistance of the matrix itself, although influenced by numerous factors. To investigate this aspect, the “Zwick” set-up was used to test 38 small specimens in tension focusing on the local material properties of the various components of concrete. The specimens were part of series 01 (see Table 2.1) and measured 40 mm in length and height, while  $b$  was 10 mm (Figure 2.7). Two notches of varying depth determined the fracture plane. To analyse the material variability, some of the specimens were randomly cut out of 10 mm thick concrete plates with various orientations. Others were cut from specific positions, so that single aggregates or the interface between aggregates and matrix were placed next to the critical section (see details in Figure 2.7b and d). It should be noted that, with respect to the orientation to the casting direction discussed in Section 2.1 and unlike the typical Mixed-Mode specimens used throughout the rest of the thesis, for these Mode I tests the crack plane was usually not perpendicular to the casting direction. The randomly selected specimens had a critical surface of approximately 20 mm · 10 mm, while for the others the depth of the notches was chosen considering the size of the aggregate.

After testing in simple tension, the fracture surfaces were visually inspected to determine if a particular mode of fracture (crack through matrix, crack at aggregate interface or crack through aggregate) was predominant. The tests were thus categorized and compared. In 11 cases, the fracture surface developed through the concrete matrix. In 8 cases it mostly developed at the interface of one or several aggregates. In 3 cases the crack went mostly through an aggregate (these cases included breaking of different kinds of stone). In the remaining cases, the obtained crack was irregular or the fracture surface did not show a predominant fracture type.

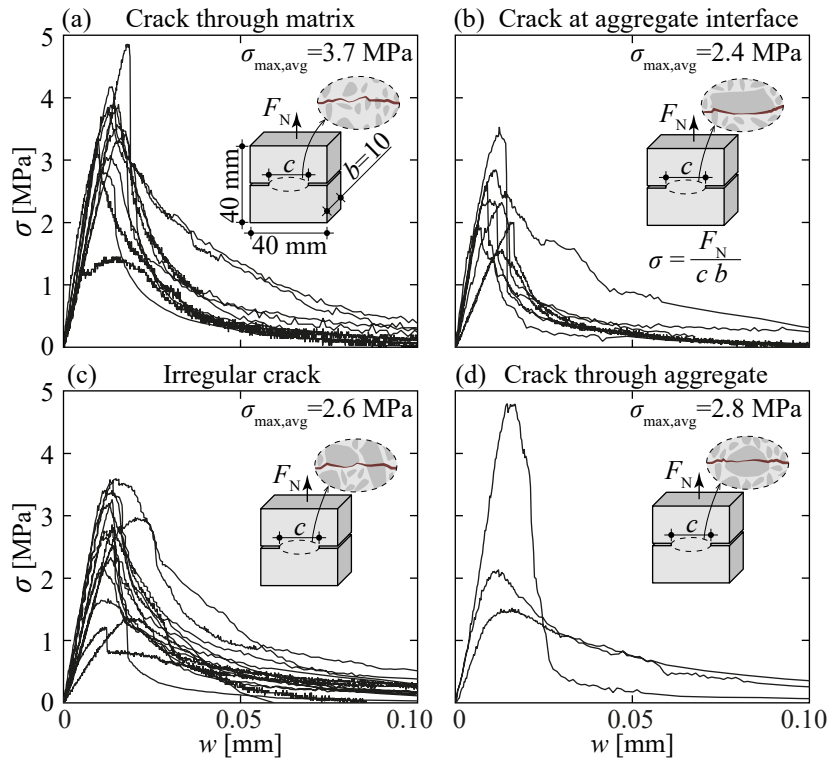


Figure 2.7 – Results for small-scale tensile tests (series 01), classified by crack surface components

The load-displacement curves are plotted in Figure 2.7. It shall be noted that the values on the horizontal axis represent the displacement of the testing machine and thus include the deformation of the set-up. The small size of the specimen and the low maximum load (about 1 kN) do not allow the use of strain gauges, since their tensile stiffness and resistance would become important compared to those of the specimen. The stress  $\sigma$  is calculated dividing the force  $F_N$  by the surface determined by the notches, measuring  $c \cdot 10$  mm. The results show that the set-up is capable of capturing the different behaviour of cracks in the matrix or at the interface with aggregates. The recorded data is subjected to a considerable amount of scatter, but can be indicative of average material parameters for the different crack types. These parameters can then be used in connection with numerical analyses. It should be noted that in the case of cracks passing at the aggregate interface or through an aggregate, the maximum tensile stress  $\sigma_{\max}$  is potentially influenced by the fact that a minor part of the fracture surface develops through the cementitious matrix as the notches would not stop exactly at the beginning of the aggregate (see for example Figure 2.9e).

The tests also show that DIC-Data can be used to track the evolution of the crack path during testing. For example, there is particularly high scatter in the 3 tests with the crack going through the aggregate (Figure 2.7d): One test reached a very high tensile strength of about 5 MPa, while the other two broke at about 2 MPa. This is connected to the fact that different aggregate types were concerned, and the different behaviour is visible in the DIC analysis. Figure 2.8 and

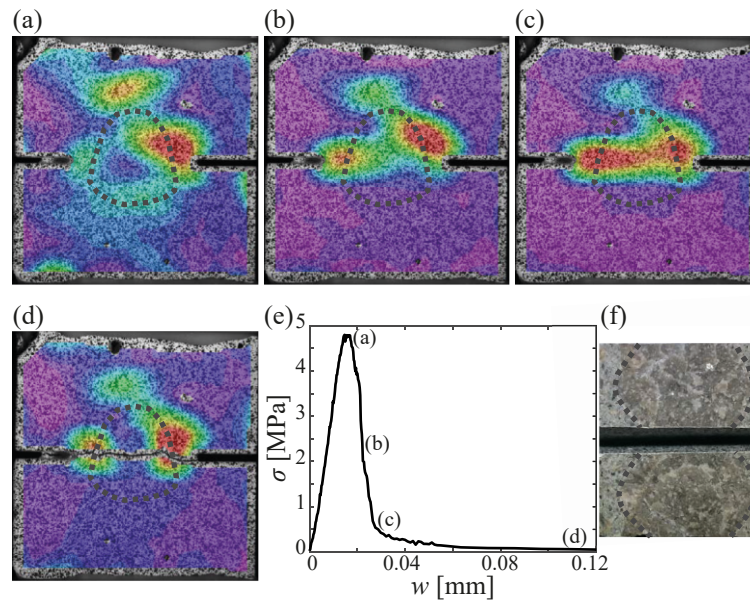


Figure 2.8 – Experiment 012802, crack through aggregate (approximate shape of aggregate shown dashed): (a)–(d) principal tensile strains on specimen surface; (e) displacement-stress graph; and (f) fracture surface

Figure 2.9 compare two of the tests. It can be noted that in test 012802 (Figure 2.8), the areas with most tensile deformation are those located in zones around the aggregate for most of the test. Only late on the softening branch, the crack develops through the aggregate (Figure 2.8c). The specimen is thus subjected to significant stress redistribution, indicating an overall higher resistance. For specimen 012702 (Figure 2.9), however, the main strains develop through the aggregate from the beginning.

## 2.5 Preliminary Mixed-Mode Tests

To compare the set-up of the current research project with results reported in the literature, a series of preliminary Mixed-Mode tests was carried out. As performed by Jacobsen [7], each test starts with a Mode I phase to produce a crack of a predefined initial opening  $w_0$ . Then, the test continues in Mixed-Mode with a constant opening angle  $\alpha$  (see Figure 1.2c), while the applied forces are monitored constantly. The average normal stresses in the region between notches are defined as:

$$\sigma = \frac{F_N}{c \cdot b} \quad (2.1)$$

where  $F_N$  is the measured normal/vertical load (with tension being positive) and  $b$  the specimen thickness (typically 50 mm for Mixed-Mode tests). Similarly, the average shear stress is defined as:

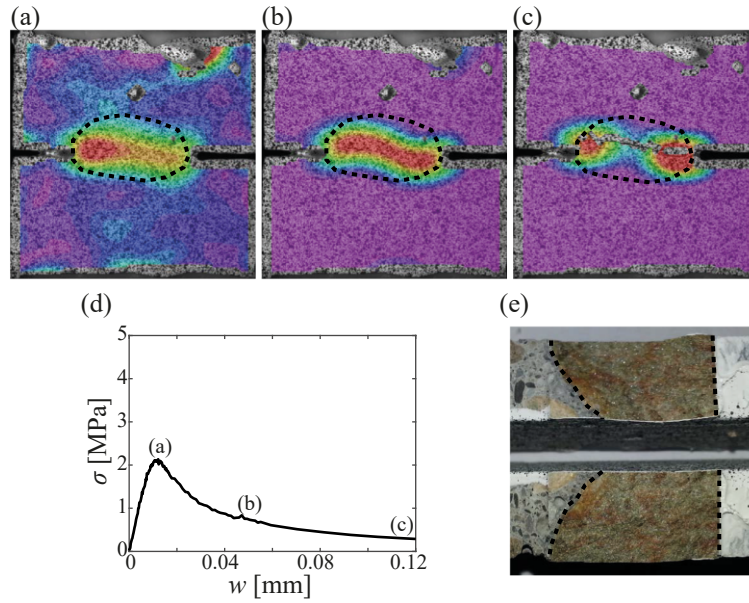


Figure 2.9 – Experiment 012702, crack through aggregate (approximate shape of aggregate shown dashed): (a)–(c) principal tensile strains on specimen surface; (d) displacement-stress graph; and (e) fracture surface

$$\tau = \frac{F_T}{c \cdot b} \quad (2.2)$$

where  $F_T$  is the measured tangential/horizontal force. Two different concrete mixes have been used for the preliminary tests, numbers 02 and 06 (refer to Table 2.1). The parameters for the applied kinematics have been chosen in accordance with [7], and can be found in Table 2.3.

### 2.5.1 Types of responses

The Mode I tensile phase ends once the measured value of  $w$  reaches a predefined value  $w_0$ . At that moment, the fracture process zone normally yields a well-defined crack in-between the notches. During the Mixed-Mode phase, the crack can develop in one of the following ways (see Figure 2.10):

- *Primary/Interface Crack* (PC): No additional (significant) cracks develop and strains localize in the crack originated in Mode I.
- *Non-Dominant Secondary Cracking* (NDSC): One or several secondary cracks develop, but they do not propagate through the whole specimen. Most of the imposed displacements localize thus in the Primary Crack.
- *Dominant Secondary Crack* (DSC): A new crack develops, often starting from the tip of a notch, and progresses in a brittle (unstable) manner.

## 2.5. Preliminary Mixed-Mode Tests

Table 2.3 – Preliminary tests, classified by the imposed kinematics; the first two digits of the specimen number indicated the casting, see Table 2.1; the width  $c$  is reported in [mm] in brackets for each test, for definition see Figure 2.1b; PC, NDSC and DSC indicated tests with Primary Cracking, Non-Dominant Secondary Cracking or Dominant Secondary Cracking respectively

$\alpha \backslash w_0$	0.015 mm	0.025 mm	0.040 mm	0.100 mm
40°	021701 (22.0 DSC) 061802 (19.0 NDSC)	061501 (19.0 NDSC)	061602 (22.0 PC)	061502 (25.0 PC)
45°	022002 (19.0 NDSC)	021601 (19.0 NDSC) 061401 (19.5 PC)	061701 (19.0 NDSC)	021702 (28.0 NDSC) 060402 (29.5 NDSC)
50°		020804 (34.5 NDSC)		
55°		021402 (34.5 NDSC) 061402 (25.0 NDSC)	061801 (25.0 PC)	061601 (28.0 NDSC)
60°	022001 (25.0 PC)	021602 (24.5 PC)		

Figure 2.10 shows instances of cracking patterns as determined using DIC. The different types of cracking are further analysed and discussed in Chapter 4.

### 2.5.2 Test results

In this section, the stresses derived from the preliminary tests will be presented. Figure 2.11 shows tests for concrete 02 and Figure 2.12 reports the results for specimens of concrete 06. In each plot, one parameter defining the kinematics is set as constant while the other is progressively varied. The plots do not present the initial Mode I phase since  $\delta \approx 0$ . Peak values are marked with a square. As the Mixed-Mode phase starts,  $\delta$  increases and the shear stress  $\tau$  grow notably. At the same time,  $\sigma$  changes from tensile to compressive stresses, going from positive to negative values. The averages of the maximum tensile strengths reached during the Mode I phases were:

- $f_{ctm,02} = 3.7$  MPa (standard deviation 0.54) for casting 02 (which corresponds well to the average result for small-scale tensile tests with cracks going through the matrix, as shown in Figure 2.7a)
- $f_{ctm,06} = 4.1$  MPa (standard deviation 0.65) for casting 06

The plots show consistent results between the two concrete types: for the same initial opening, tests with lower displacement angles yield higher normal and shear loads. Similarly, for the same opening angle, tests with lower initial openings develop higher normal and shear loads.

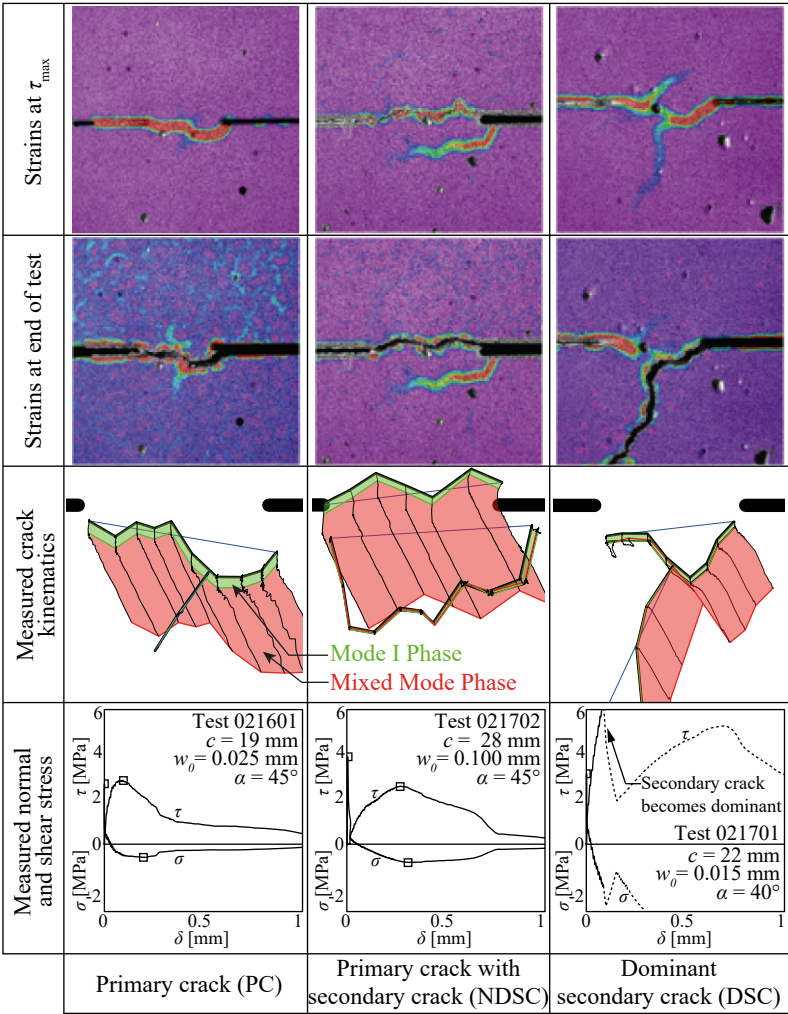


Figure 2.10 – Examples of specimen responses and cracking patterns (based on DIC-analyses)

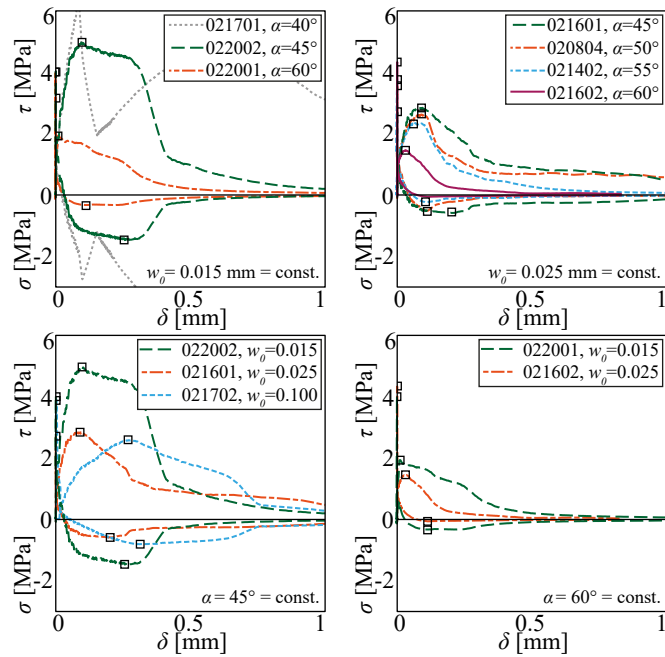


Figure 2.11 – Tests with concrete of casting 02; in each plot one parameter is maintained constant (indicated in the lower right corner) while the other one is progressively varied

### 2.5.3 Discussion of test results

#### Remarks on notch size

Cutting notches into specimens in order to obtain a single concentrated crack is common practice for these types of tests. Yet, the criteria to select the notch depth and size and the associated parameter  $c$  are not normally homogeneous nor justified. However, this has significant influence on the crack development and therefore on the test results. For example if very small notches are performed (high values of  $c$ ), most tests will be characterized by strong secondary cracking [5, 8]. In reference [7], the researcher reports that preliminary testing started with a value of  $c$  which was subsequently decreased in order to reduce the amount of tests dominated by secondary cracking. Once a given notch depth is set, secondary cracking became more dominant for flatter kinematics (small openings and small angles). For the present study, different notch depths have been investigated. It was noted that if the notches are sufficiently large (low values of  $c$ ), it is possible to avoid secondary cracks even for rather flat kinematics. On the other hand, for large values of  $c$ , secondary cracking was occurring even for kinematics with little shear displacement. It seems thus, that the notch depth is an important parameter, which governs the specimen response and the development of secondary cracks.

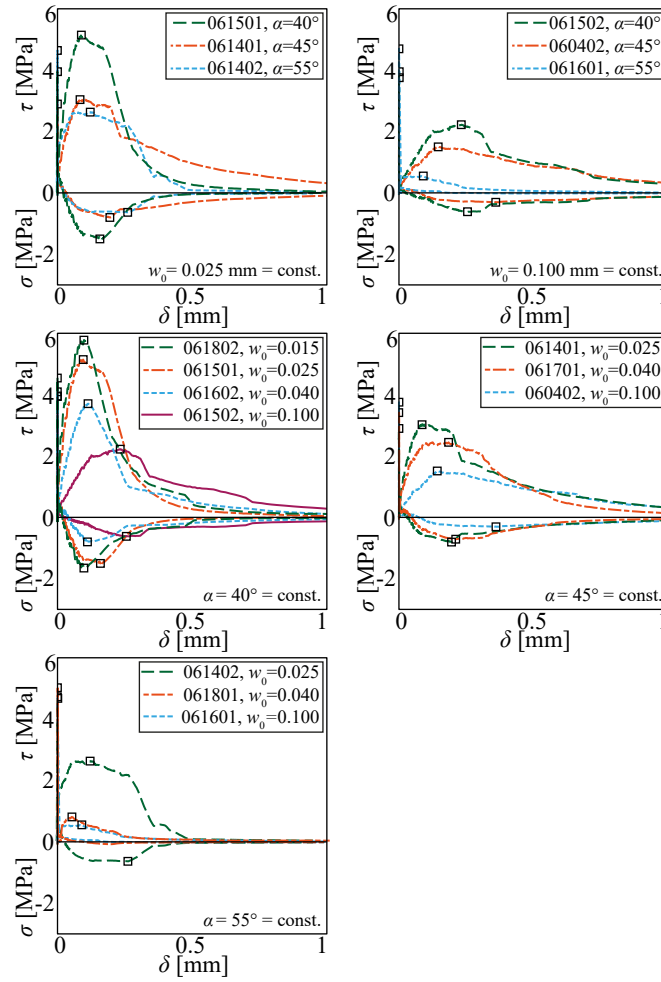


Figure 2.12 – Tests with concrete of casting 06; in each plot one parameter is maintained constant (indicated in lower right corner) while the other one is progressively changed

### Remarks on displacement application

During calibration tests of the experimental set-up (not corresponding to the tests discussed herein), it was noted that when the displacement was not applied in a constantly smooth manner, but with small ramps, secondary cracking developed in a more dominant manner. This can indicate that for testing programmes in the literature with no closed-loop control or where this aspect was not properly addressed, the results and cracking patterns can significantly differ.

### Summary and comparison of experimental results

The maximum values of  $-\sigma$  and  $\tau$  obtained for the preliminary tests are plotted as data points in Figure 2.13. The figure clearly shows that for a given initial opening, the maximum stress progressively decreases for larger opening angles. No significant difference in behaviour between castings 02 and 06 can be observed despite their very different aggregate size. The results reported in [7] are indicated as well, and their behaviour is consistent to the tests of the present study. In addition to the experiments, the estimates of the strength provided by the following two models are also indicated:

- The Two-Phase Model by Walraven [14]; this model only considers Mode I opening followed by pure Mode II sliding. Therefore, the global kinematics (until  $w = 2$  mm) applied to the specimens has been subdivided into 401 steps to follow the Mixed-Mode kinematics closely
- The empirical closed-form formulas provided in [1], which are based on the Two-Phase Model by Walraven as well, but additionally consider modifications to follow Mixed-Mode kinematics more precisely [4] (see also Appendix A of Chapter 4)

For each of the models two curves are plotted next to each other in Figure 2.13, as the material parameters were adjusted in accordance to the characteristics of both castings 02 and 06.

### Conclusions from preliminary Mixed-Mode tests

This sections presents the results of a preliminary experimental investigation on aggregate interlocking. Several tests with two different types of concrete and several different imposed kinematics are presented. The following conclusions can be taken:

- The forces measured during the tests consistently show that specimens subjected to low initial crack openings and to low angles of displacement develop higher aggregate interlocking stresses than specimens with higher initial openings or angles of displacement
- The tests are consistent with similar tests reported in the literature

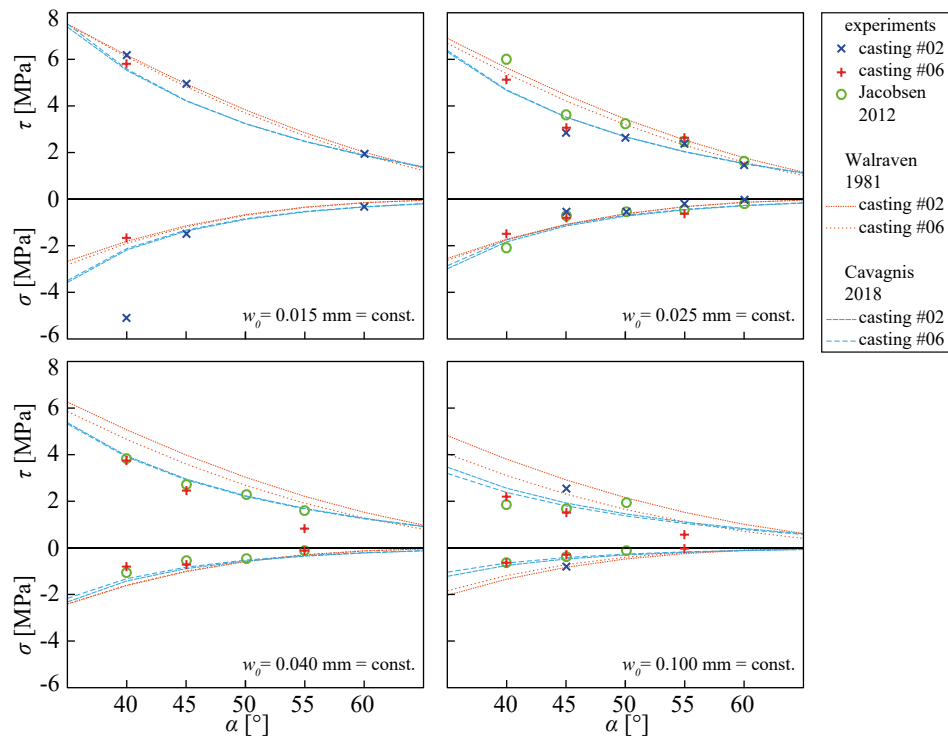


Figure 2.13 – Maximum values of  $-\sigma$  and  $\tau$  for all tested concretes, including experimental results [7] and model estimates from the literature [1, 14]

- The test results are consistent with the Two-Phase Models presented in [14] and [1] despite the various theoretical limitations of such models
- Different cracking patterns have been observed, notably the development of a single primary crack going from notch to notch and the possible additional development of a secondary crack developing diagonally from the primary crack. Some qualitative observations on the influence of the testing procedure on the type of cracking are given, notably that it is easier to obtain primary cracks in specimens with larger notches

## Bibliography

- [1] Cavagnis, E, Fernández Ruiz, M., and Muttoni, A. (2018). A mechanical model for failures in shear of members without transverse reinforcement based on development of a critical shear crack. *Engineering Structures*, 157:300–315.
- [2] fib (International Federation for Structural Concrete) (2013). *fib Model Code for Concrete structures 2010*. Ernst & Sohn, 402 p, Germany.
- [3] Giaccio, G. and Giovambattista, A. (1986). Bleeding - Evaluation of its effects on concrete behaviour. *Materials and Structures*, 19(4):265–271.

- [4] Guidotti, R. (2010). *Poinçonnement des planchers-dalles avec colonnes superposées fortement sollicitées*. Ph.D. Thesis, EPFL, Lausanne, Switzerland.
- [5] Hassanzadeh, M. (1992). *Behavior of Fracture Process Zones in Concrete Influenced by Simultaneously Applied Normal and Shear Displacements*. Ph.D. Thesis, Lund University, Sweden.
- [6] Hsu, T. T. C. and Slate, F. O. (1963). Tensile Bond Strength Between Aggregate and Cement Paste or Mortar. *ACI Journal Proceedings*, 60(4):465–486.
- [7] Jacobsen, J. S. (2012). *Constitutive Mixed Mode Behavior of Cracks in Concrete: Experimental Investigations of Material Modeling*. Ph.D. Thesis, Technical University of Denmark, Kongens Lyngby, Denmark.
- [8] Nooru-Mohamed, M. B. (1992). *Mixed-Mode Fracture of Concrete: An Experimental Approach*. Ph.D. Thesis, Delft University of Technology, Sweden.
- [9] Tirassa, M., Fernández Ruiz, M., Anciaux, G., and Muttoni, A. (2017). Interface Stresses in Cracked Concrete: Testing for Review of Its Fundamentals. In *2017 fib Symposium High Tech Concrete: Where Technology and Engineering Meet*, pages 740–748. Maastricht, Netherlands.
- [10] Tirassa, M., Fernández Ruiz, Miguel, and Muttoni, A. (2018). Modern experimental research techniques for a consistent understanding of aggregate interlocking. In *Proceedings of the 12th fib PhD Symposium in Civil Engineering*, pages 723–730, Prague, Czech Republic.
- [11] VSS Swiss Association of Road and Transportation Experts (2005). *SN670115 - Gesteinskörnungen: Qualitative und quantitative Mineralogie und Petrographie*. Zurich, Switzerland.
- [12] Walkner, R. (2014). *Critical review of EC 2 regarding punching and proposal for improvement the design approach*. PhD thesis, Leopold-Franzens-Universität Innsbruck, Austria.
- [13] Walraven, J. C. (1980). *Aggregate Interlock: a Theoretical and Experimental Analysis*. Ph.D. Thesis, Delft University of Technology, Sweden.
- [14] Walraven, J. C. (1981). Fundamental Analysis of Aggregate Interlock. *ASCE Journal of the Structural Division*, 107(11):2245–2270.



# 3 Review of fundamental assumptions of the Two-Phase Model for aggregate interlocking in cracked concrete using numerical methods and experimental evidence

This chapter contains an analysis of the Two-Phase-Model as originally proposed by Walraven [32]. It was previously published in a scientific journal [24]:

Pundir M., Tirassa M., Fernández Ruiz M., Muttoni A., Anciaux G. (2019). Review of fundamental assumptions of the Two-Phase model for aggregate interlocking in cracked concrete using numerical methods and experimental evidence. *Cement and Concrete Research*, 125:105855. (doi: 10.1016/j.cemconres.2019.105855)

Max Tirassa planned and carried out the experimental campaign and analysed the obtained data under the supervision of the third, fourth and fifth authors. He collaborated with the first author on drafting the article manuscript, focusing on the introduction (Section 3.1) and the description of the experimental programme (Section 3.3). The model formulation described in Section 3.2, its implementation and extension (Section 3.4 and Section 3.5) were performed by the first author under supervision of the fifth one and do not represent a contribution of Max Tirassa.

## Abstract

Aggregate interlocking allows transferring shear and normal stresses through open cracks, and is considered to significantly contribute to the force transfer in cracked concrete. The complex phenomenon depends on the roughness of cracked surfaces, where material protruding

### Chapter 3. Review of fundamental assumptions of the Two-Phase Model for aggregate interlocking in cracked concrete using numerical methods and experimental evidence

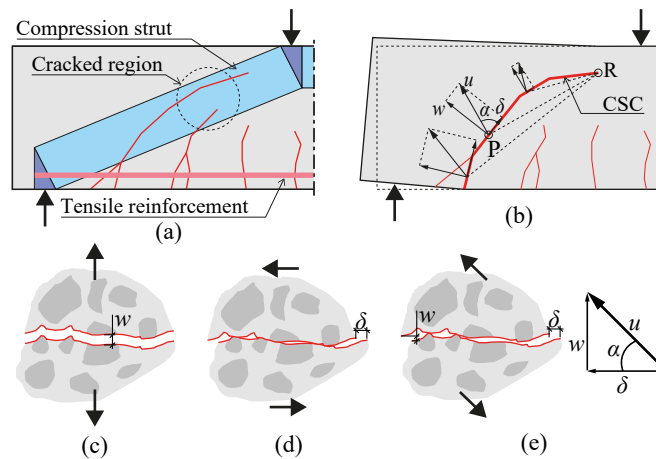


Figure 3.1 – (a) Cracks developing through the compression strut in a concrete beam without shear reinforcement; (b) Crack pattern before shear failure (c) Mode I kinematics; (d) Mode II kinematics (e) Mixed Mode kinematics.

from one side may engage with the opposite one. Two-Phase models were established in the 1980's by Walraven to estimate the force transfer, distinguishing between cement matrix and spherical aggregates. The approach leads to good results but has several shortcomings. In this paper, the fundamental assumptions are reviewed using specific numerical and experimental investigations. Special tests respecting the geometrical assumptions are presented and the results compared with numerically calculated estimates. The model is extended to address some shortcomings and investigate the physical nature of the main parameters. Positive aspects of Two-Phase Models and a number of limitations are highlighted, allowing a consistent step forward in the understanding of aggregate interlocking.

**Keywords:** concrete; cracks; shear transfer; mechanical modelling; aggregate interlocking; Two-Phase model;

## 3.1 Introduction

Concrete is characterised in tension by a low resistance and a small deformation capacity. Unless specific measures are adopted (such as pre-stressing to compensate external actions or providing joints to limit the imposed deformations due to structural and thermal effects), concrete is generally cracked both at serviceability and ultimate limit states. To provide the necessary resistance, reinforcement can be arranged in regions where tension occurs for static reasons (e.g. in the tension side of a bending beam), but the transfer of compression and shear stresses is performed in many cases through cracked regions, which developed due to previous actions. This is for instance shown in Figure 3.1, where cracks with a flexural origin (and controlled by the tensile reinforcement) progress and eventually develop inside the location of the theoretical compression strut carrying shear.

The ability of transferring shear and compression stresses through cracks in concrete is governed by the crack opening and sliding as well as the surface properties of the concrete (surface roughness, aggregate and matrix strengths). As shown in the example of Figure 3.1b, the kinematics of the lips of the crack generally imply both opening (Mode I kinematics, Figure 3.1c) and sliding (Mode II kinematics, Figure 3.1d) components. Hence, the kinematic angle  $\alpha$  depends on the relative position of the centre of rotation which is located approximately at the tip of the shear crack [3, 4, 19]. Such general kinematics (Figure 3.1e) are usually referred to as Mixed Mode kinematics. Also, it is interesting to note that different kinematics normally develop along a crack and this yields potentially to different capacities to transfer shear and normal forces. The resulting contact forces at the cracked surface (engagement of aggregates and rough surfaces) as a function of the acting kinematics, is usually defined as the aggregate interlocking capacity [7, 17, 26, 32]. Investigated in an intensive manner since the 1960s, a number of mechanical approaches have been developed, particularly during the 1980s [6, 11, 17, 30, 32] but also more recently [2, 14]. These approaches gave a comprehensive outlook of the phenomenon and allowed to calculate the interface forces based on the mechanical parameters of concrete. In general, they can be classified depending on the approach followed to model the continuum, which allows to distinguish two general strategies.

The first, referred to as the *Homogeneous models*, assume that concrete is made of a single homogeneous material, with rough surface profiles taken into account in the shear resistance calculations [14, 17]. The second, referred to as the *Two-Phase model*, originally proposed by Walraven [32] and with later modifications [12, 29], accounts for heterogeneity of concrete (considering aggregates and mortar), however with a rather simple surface profile. Both approaches predict eventually the resisting force  $F_R$  as the following ensemble average,

$$\langle F_R \rangle = \iint \Phi(\mathcal{A}, N) \cdot N \mathbf{F}(\mathcal{A}) d\mathcal{A} dN \quad (3.1)$$

where  $\Phi(\mathcal{A}, N)$  is the joined probability density of having one contact patch  $\mathcal{A}$ , such a contact patch being among  $N$  other patches and  $\mathbf{F}(\mathcal{A})$  is the force produced by such a contact patch. This equation, which will be re-derived in section 3.2, is central to *Two-Phase models* aiming at predicting shear stress/force resistance of a concrete crack. While  $\Phi$  describes the stochastic part coming from the random distribution of aggregates, the force  $\mathbf{F}(\mathcal{A})$  is usually computed with a purely geometrical treatment [32].

In this paper, we will focus only on the *Two-Phase models* as originally proposed by Walraven [32] and used in many works to model shear [4] or punching cases [12, 20]. Additional hypotheses are introduced in their works in order to find semi-analytical forms of the probability density ( $\Phi$ ) and the transmitted force ( $F$ ). These hypotheses can be divided into two categories: geometrical and material. The geometrical hypotheses state that the crack surface profile is planar with spherical aggregates protruding partially from it. Figure 3.2 presents such an approach. The probability density  $\Phi$  can be derived as a function of both the packing density of the concrete and of the distribution of aggregate sizes (through a grading curve as

**Chapter 3. Review of fundamental assumptions of the Two-Phase Model for aggregate interlocking in cracked concrete using numerical methods and experimental evidence**

Symbol	Description	Physical Dimension
$a$	contact area for a single patch	area
$\theta$	inclination angle	-
$N$	number of contact patches	-
$A$	total contact area	area
$A_{sp}$	horizontal projection of all spheres	area
$\mathbf{X}$	material point position vector	-
$\{\mathbf{e}_x, \mathbf{e}_y, \mathbf{e}_z\}$	orthonormal basis	-
$\tau$	contact stress field	force/area
$F_N$	total normal force	force
$F_T$	total shear resistance force	force
$H$	Hurst exponent	-
$F_R$	total resistance force	force
$\sigma_{pu}$	plastic stress threshold	force/area
$\mu$	friction coefficient	-
$\mathcal{A}$	physical space where interlock occurs	length <sup><math>d-1</math></sup>
$u$	crack opening	length
$w$	crack opening along crack plane	length
$\delta$	crack sliding along perpendicular to crack plane	length
$\rho^N(a, \theta)$	joined probability density function of contact patch of area $a$ and an inclination angle $\theta$	-
$\varphi(N)$	probability density function of number of contact patches	-
$\Phi(a, \theta, N)$	joined probability density	-
$\alpha$	crack opening angle respective to crack plane	-
$D_{steel}$	diameter of steel spheres	length
$D_{max}$	maximum aggregate size in concrete mix	length
$f_c$	cylinder compressive strength of concrete	force/area
$f_{cm,28}$	average cylinder compressive strength at 28 days	force/area
$f_{c,Test Day}$	cylinder compressive resistance on day of test	force/area
$f_{c,ref}$	reference compressive strength (30 MPa)	force/area
$\eta_{f_c}$	brittleness factor	-
$f_{cp}$	equivalent plastic resistance	force/area

Table 3.1 – Symbols and notations

in [10]). In [32], the material hypotheses state that the deformation is undertaken mostly by the matrix, so that it is idealized as perfectly-plastic whereas aggregates are considered as rigid. Lastly, in the original formulation of Walraven, the surface profile is un-physically assumed to remain unchanged after being in contact. There are two material free-parameters for this model: a plastic stress threshold  $\sigma_{pu}$ , and a friction coefficient  $\mu$ .

This approach generally provides reasonable estimates of the maximum normal and tangential stresses [28], but is less accurate in the post-peak phase where it tends to overestimate the transferred forces [4]. Moreover, the assumption of perfectly spherical and rigid aggregates may be very unrealistic depending on the type of aggregates effectively used. Finally, the physical nature of the free-parameters  $\sigma_{pu}$  and  $\mu$  remains unclear, as they are difficult to measure directly and were likely adapted to better fit experimental results.

The aim of this paper is to better understand the consistency of the *Two-Phase model* approach and particularly of the physical interpretation of the parameters  $\sigma_{pu}$  and  $\mu$ . An extension of the model will be suggested by introducing the induced surface alterations, which will allow accurate semi-analytic predictions of shear stress resistance. This new model will be strengthened by a number of tailored experiments, comprising concrete with various aggregate sizes, and various loading kinematics. Furthermore, the new model being an extension of Walraven's model uses only a few material parameters ( $\sigma_{pu}$ ,  $\mu$ ) as well as parameters ( $\beta_y$ ,  $\beta_z$ ) to predict the complex mechanical mechanism (elasto-plastic deformation, degradation of matrix material) at the crack interface. Being simple and purely geometric in nature, the model does possess some limitations which are discussed in detail in later sections.

This paper starts in Section 3.2 by reviewing and reformulating the *Two-Phase* problem, which will describe the necessary mathematical concepts. Section 3.3 describes the experimental setup, which is designed to remain as close as possible to the hypotheses of the presented models. In Section 3.4.1, the *Two-Phase model* is extended to predict shear stress resistance for a 3D geometry. New predictions made by this model will be compared with experimental results, which allow to highlight the situations where the original model does not work accurately. Then, a new semi-analytical model acknowledging the surface alterations due to contact and the elasto-plastic behaviour of the problem is introduced in Section 3.4.2 and Section 3.4.3. With such an approach, a fine agreement with experiments will be demonstrated. Finally, Section 3.5 discusses the implications and perspectives brought by this model, especially in view of making predictions for complex crack roughness, therefore involving a statistical treatment.

## 3.2 Two-Phase model

*The content of this section was developed and implemented by Pundir M. under the supervision of Anciaux G.. It does not represent a contribution of Tirassa M..*

In this section, Walraven's approach [32] is reviewed, starting with the derivation of its central

**Chapter 3. Review of fundamental assumptions of the Two-Phase Model for aggregate interlocking in cracked concrete using numerical methods and experimental evidence**

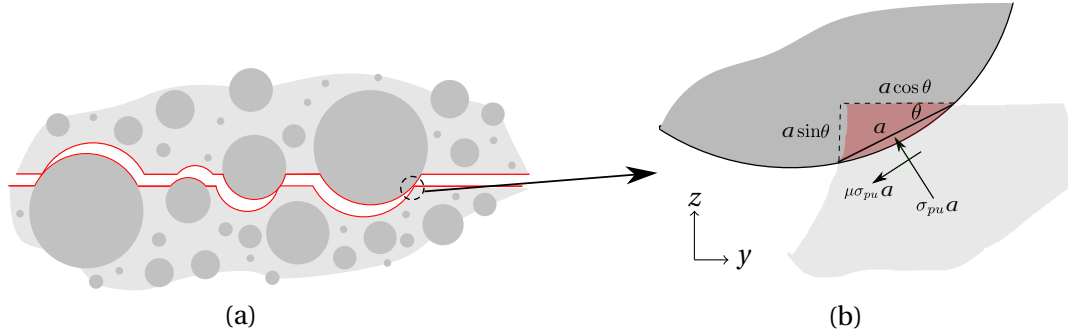


Figure 3.2 – (a) Idealised crack surface based on *Two-Phase model's* hypotheses. (b) Detail of an aggregate coming in contact with mortar. The red zone marks the region where mortar is being plasticised.

equation (3.1). To do so, the resisting force  $\mathbf{F}_R$  is calculated as the sum of all the forces acting along the contact area  $A$  on the crack surface, which provides the general definition:

$$\mathbf{F}_R = \int_A \tau(\mathbf{X}) \mathbf{n} dS \quad (3.2)$$

where  $\tau$  refers to the contact stress field and  $\mathbf{n}$  the unit vector field normal to the surface. The contact area  $A$  can be decomposed into  $N$  smaller contacting patches  $(a_i)_{i=1..N}$  such that  $\sum_i^N a_i = A$ . The average contact force produced by these patches can be linked to the total force with:

$$\bar{\mathbf{F}} = \frac{1}{N} \sum_i^N \underbrace{\int_{a_i} \tau(\mathbf{X}) \mathbf{n} dS}_{\mathbf{F}_i} \implies \mathbf{F}_R = N \cdot \bar{\mathbf{F}} \quad (3.3)$$

Assuming numerous contact patches and a faithful statistical representation,  $\bar{\mathbf{F}}$  can be expressed with a probability density integral:

$$\bar{\mathbf{F}} = \frac{1}{N} \sum_i^N \mathbf{F}_i = \int \rho^N(\mathcal{A}) \cdot \mathbf{F}(\mathcal{A}) d\mathcal{A} \quad (3.4)$$

where  $\rho^N(\mathcal{A})$  is the joined probability density of having a contact patch  $\mathcal{A}$ , knowing that there are  $N$  patches in total. On the other end,  $\mathbf{F}(\mathcal{A})$  is the force produced by a contact patch. When the probability density for the number of contact patches ( $\varphi$ ) is provided, the expectation of

the resistance force (3.1) can be obtained by combining equations (3.3) and (3.4):

$$\langle \mathbf{F}_R \rangle = \iint \underbrace{\varphi(N) \rho^N(\mathcal{A})}_{\Phi(\mathcal{A}, N)} \cdot N \mathbf{F}(\mathcal{A}) d\mathcal{A} dN. \quad (3.5)$$

In this equation,  $\Phi$  reflects the stochastic nature of surface topologies produced during concrete cracking, as well as the current level of opening and shear displacements. In order to obtain a formal expression, Walraven employed a 2D geometry where the crack surface is nominally flat with perfectly circular protruding aggregates, globally following a specified density and a specified distribution of radii (Fuller curve). Also, the opening and shear displacements were assumed to be homogeneous throughout the entire crack surface. In a 2D setup, any contact patch  $\mathcal{A}$  is simply characterised with a contact area  $a$  and an inclination angle  $\theta$  leading to:

$$\langle \mathbf{F}_R \rangle = \iiint \Phi(a, \theta, N) \cdot N \mathbf{F}(a, \theta) da d\theta dN. \quad (3.6)$$

Also, thanks to this simple geometry, the resistance force  $\mathbf{F}(a, \theta)$  can be geometrically constructed. For a given opening displacement  $w$  and shear displacement  $\delta$ , the interlocking situation is as shown in Figure 3.2. The overlapping volume between mortar and aggregates (shown in red colour on the Figure) allows to define a contacting plane resulting from plastic deformation, and to associate it with a contact area and an inclination angle  $(a, \theta)$ . Therefore the force produced becomes the following line integral

$$\mathbf{F}(a, \theta) = \int_0^a \underbrace{\tau(l, \theta) \mathbf{n}}_{\boldsymbol{\tau}^P} dl \quad (3.7)$$

where the stress  $\boldsymbol{\tau}^P$  is naturally decomposed into a normal contribution preventing interpenetration and a tangential component resulting from Coulomb friction forces

$$\boldsymbol{\tau}^P(l, \theta) = p(l) \begin{bmatrix} 1 & \mu \\ -\mu & 1 \end{bmatrix} \begin{pmatrix} \sin(\theta) \\ \cos(\theta) \end{pmatrix} = p(l) \begin{pmatrix} \sin(\theta) + \mu \cdot \cos(\theta) \\ \cos(\theta) - \mu \cdot \sin(\theta) \end{pmatrix} \quad (3.8)$$

where  $p$  is the normal load field and  $\mu$  is the Coulomb friction coefficient. Under a perfectly-plastic assumption,  $p$  becomes the constant  $\sigma_{pu}$  and we obtain the following expression:

$$\mathbf{F}(a, \theta) = a \cdot \sigma_{pu} \begin{pmatrix} \sin(\theta) + \mu \cdot \cos(\theta) \\ \cos(\theta) - \mu \cdot \sin(\theta) \end{pmatrix} \quad (3.9)$$

With the final equation that Walraven produced being

$$\langle \mathbf{F}_R \rangle = \sigma_{pu} \iiint a N \begin{pmatrix} \sin(\theta) + \mu \cdot \cos(\theta) \\ \cos(\theta) - \mu \cdot \sin(\theta) \end{pmatrix} \Phi(a, \theta, N) da d\theta dN. \quad (3.10)$$

## Chapter 3. Review of fundamental assumptions of the Two-Phase Model for aggregate interlocking in cracked concrete using numerical methods and experimental evidence

---

Actually, Walraven's equation is written in the form

$$\langle F_R \rangle = \iint \Psi(D, h) F(D, h) dD dh. \quad (3.11)$$

where the probability density  $\Psi$  and the force  $F(D, h)$  are resulting from an integration of the variable  $N$  followed by a change of variable  $(a, \theta) \rightarrow (D, h)$ , where  $D$  represents aggregate diameters and  $h$  represents the elevation (distance to crack plane) at which aggregates are cut. This comes from the manner Walraven used to derive this expression (by using Fuller's curve and density constraints). Therefore, the probability for the number of contact patches is not appearing, even though it is taken into account to obtain the analytical expressions reported in [32].

Several remarks can be pointed out on Walraven's model. First, it is only a 2D model with purely circular aggregates, leading to possible errors, in computing  $F(D, h)$ , coming from the limitations of the geometry description. Second, the actual cracked surfaces have profiles with a roughness generally characterised by a Hurst exponent  $H$ , which ranges from 0.6-0.8 for naturally occurring rough surfaces [23, 27]. The Hurst exponent  $H_{\text{ideal}}$  for the surface profile considered in *Two-Phase model* is found out to be in the range 1.0-1.1 (for further detail refer to Appendix A). This oversimplification of cracked surfaces leads to possible errors in the probability density  $\Psi$  which accounts for the number of contact patches. Third, there are only two parameters in the model characterising the matrix (assumed to be homogeneous), namely the plastic stress threshold  $\sigma_{pu}$  and the friction coefficient  $\mu$ . These values are usually determined by fitting the experimental values. Last, the assumed constitutive behaviour is perfectly-plastic.

The aim of the presented work is to analyse in depth the interlock elasto-plastic mechanical response, which is modelled by the function  $F(a, \theta)$  in equations (3.1) and (3.6). To that end, a 3D geometry made with few spherical aggregates of the same radius will be employed, therefore discarding any stochastic contribution. In the next section, the employed experimental setup will be introduced, immediately followed by the achieved experimental results. A novel predictive model will be presented in latest sections.

### 3.3 Experimental programme

#### 3.3.1 Test-Setup

To validate the *Two-Phase model*, 23 experiments respecting its two main geometrical hypotheses (globally planar cracks and rigid, spherical aggregates) were carried out. To this purpose, three steel half-spheres of identical diameter were fixed every 30 mm to one of the sides of a polished steel cuboid. The spherical shape was selected to match the idealized aggregates of the Two-Phase model. To average the material local variability, three spheres were used for each test. In addition, the distance between spheres (spaced 7 to 10 times the sphere

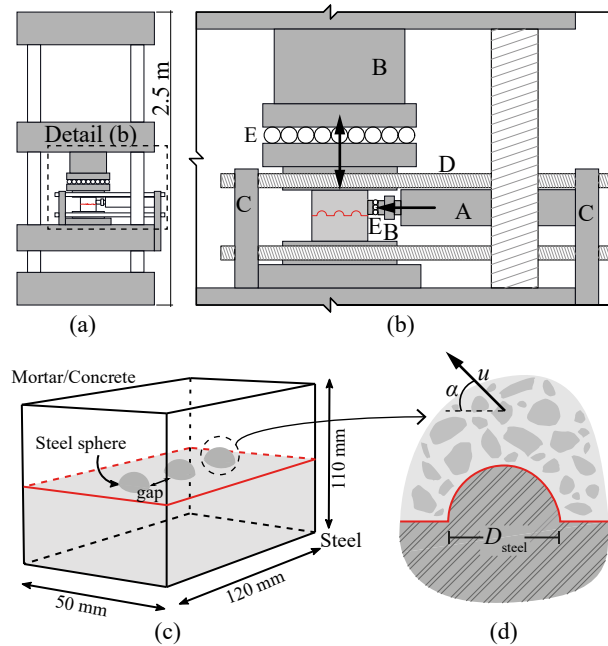


Figure 3.3 – (a) Schematic representation of test setup (b) Detail of test setup: A - horizontal jack; B - load cell; C - holding plates; D - holding bars; E - sliders (c) Schematic representation of typical specimen (d) Section through a sphere

radius) was set to limit the potential interaction between the contact regions, to reproduce again in a close manner the basic assumptions of the Two-Phase Model. All steel parts were made with S235JR+C steel, in order to avoid any potential rupture of the sphere (as would potentially occur for lightweight or weak aggregate [1]). The specimens were identical except for the diameters of the three half-spheres  $D_{steel}$ , which measured 6 or 8 mm depending on the specimen. A formwork was then fixed to the cuboid in order to cast concrete or mortar on top of the surface with the three half-spheres. The final specimens consisted thus of a steel part and a cement-material part and were 120 mm wide, 110 mm high and 50 mm thick, as shown in Figure 3.3c. The casting was done using five different mixes with varying the maximum aggregate size  $D_{max}$ , as reported in Table 3.2. Series 3101, 3102 and 3103 were made using concrete, while series 3104 and 3105 were produced with a mortar mix similar to the one prescribed by EN 196-1 [5].

Figure 3.4 provides some additional information on the aggregates used for the different castings. The gravel used for #3102 consisted prevalently (>90%) of limestone classified as medium-hard according to the Swiss code SN670115 [31]. Castings #3101 and #3103 contained mainly aggregates made of medium-hard limestone (~85%, see aggregate curves in Figure 3.4 and details in [28], casting #06). Finally, ordinary quartz-sand with a granulometry similar to the one of the standard-sand prescribed by EN 196-1 [5] was used for the mortar specimens (see Figure 3.4c).

After casting, the specimens were cured under sealed conditions for at least 28 days (typi-

**Chapter 3. Review of fundamental assumptions of the Two-Phase Model for aggregate interlocking in cracked concrete using numerical methods and experimental evidence**

	Series #				
	3101	3102	3103	3104	3105
$D_{\max}$ [mm]	8	16	16	2	2
Water [kg/m <sup>3</sup> ]	177	195*	165	500	500
Cement [kg/m <sup>3</sup> ]	321	340*	330	1000	1000
Cement Type	CEMII	CEMII	CEMII	CEMII	CEMII
	A-LL42.5N	B-M-T-LL42.5N	A-LL42.5N	A-LL42.5N	A-LL42.5N
Aggregates [kg/m <sup>3</sup> ]	1853	1817*	1880	3000	3000
$f_{cm,28}$ [MPa]	40.2	38.7	61.1	38.3	44.3
$f_{c,Test\ Day}$ [MPa]	43.7	43.0	63.8	39.6	49.6

Table 3.2 – Mix designs for the used concrete castings.  $f_{c,Test\ Day}$  is estimated in accordance to MC 2010 [9] (values marked with an asterisk refer to values from a comparable casting)

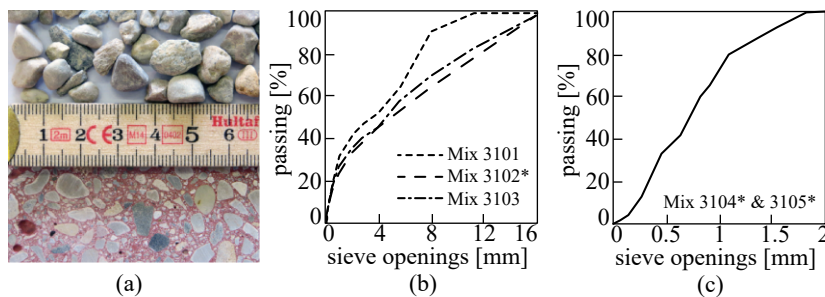


Figure 3.4 – (a) Aggregates employed for castings 3101 and 3103 (b) Granulometric curves for concrete castings (c) Granulometric curve for mortar castings (values marked with an asterisk refer to values from a comparable casting)

### 3.3. Experimental programme

Concrete Specimens			Mortar Specimens		
#	$D_{\text{steel}}$ [mm]	$\alpha$ [°]	#	$D_{\text{steel}}$ [mm]	$\alpha$ [°]
310101	8	30	310401	6	30
310102	6	25	310402	6	20
310103	6	25	310403	6	15
310104	8	25	310404	8	20
310201	6	25	310405	8	25
310202	6	20	310406	8	30
310204	8	25	310502	6	25
310301	8	25	310503	6	15
310302	8	30	310504	8	15
310303	6	0*	310505	8	20
310304	6	25	310506	8	30
310305	0	90*			

Table 3.3 – Test specimens, spheres diameter and applied kinematics; the asterisks indicate tests with special kinematics as described in the text

cally around 6 weeks) and then de-moulded and prepared for testing. Devices measuring crack opening and sliding across the interface between steel and concrete were fixed on the specimen, which was then glued on the steel plates of a 500 kN electro-mechanical testing machine, shown in Figure 3.3a and described more extensively in reference [28]. The machine was capable to impose displacements in the vertical direction of the specimen, equivalent to a Mode I opening. Through the addition of a 50 kN hydraulic jack in horizontal position it was also possible to push sideways on the upper half of the specimen, in order to apply Mode II kinematics to the analysed interface. Low-friction linear guides allowed for movement of the upper part of the specimen during testing, and load cells enabled the measurement of the applied vertical and horizontal forces. Using a control unit with a closed-controlled loop it was possible to coordinate the displacements applied in the two directions, and to apply predefined Mixed Mode kinematics on the crack. These kinematics were characterized by a constant opening angle  $\alpha$  as shown in Figure 3.1e, which was one of the main test parameters in addition to the material properties and the half-sphere diameter  $D_{\text{steel}}$ . A summary of the performed tests is given in Table 3.3, where the first four digits of the specimen name indicate the concrete or mortar mix. The table includes two specimens tested with special kinematics:

- Specimen 310305 had no spheres crossing the steel/concrete interface and was tested in Mode I to verify if adherence between the two materials was present. The maximum tensile force which was measured was about 20 N. Thus, the adherence between the planar surfaces can be considered as existent but negligible compared to the force measured during the other tests. This result is further confirmed by the Mode I phase of test 310303 which leads to similar results.
- Specimen 310303 was tested following Mode I kinematics until an initial crack opening

### Chapter 3. Review of fundamental assumptions of the Two-Phase Model for aggregate interlocking in cracked concrete using numerical methods and experimental evidence

---

$w_{\text{init}}$  of 0.5 mm was reached; then pure Mode II was applied at constant crack opening ( $\alpha = 0^\circ$ ). During this second phase, the measured forces increased until they reached the load limit of the setup and the experiment had to be stopped. At that instant both the vertical and the horizontal load measured about 16 kN. After removal of the specimen it could be seen that the high forces had caused the steel spheres to plastically deform at their tips. This shows that, without dilatation, aggregate interlocking forces can reach very high values and the local stresses may reach the plastic steel resistance, invalidating the geometrical assumption of perfect spheres.

#### 3.3.2 Tests with concrete specimens

The 12 concrete specimens were cast using three different mixtures (Table 3.2, the specimens with mortar will be detailed later): Series 3101 and 3102 had a similar compressive strength but varied in maximum aggregate size, while the concrete of series 3103 had a 50% higher resistance. Moreover, a red pigment was added to the mix 3101, allowing to better distinguish crushed sand and aggregates (Figure 3.8). Figure 3.5 reports the measured forces for all Mixed Mode tests, normalized as follows:

$$\frac{\tau}{f_{cp}} = \frac{F_T}{3A_{sp}f_{cp}} \quad \text{and} \quad \frac{\sigma}{f_{cp}} = \frac{F_N}{3A_{sp}f_{cp}}, \quad (3.12)$$

where  $F_T$  is the measured tangential force,  $F_N$  is the measured normal force,  $A_{sp} = \pi D_{\text{steel}}^2/4$  is the area of the horizontal projection of a sphere and  $f_{cp}$  is the equivalent plastic compressive resistance of the material accounting for the material brittleness in compression and for the fact that the plastification is a gradual process (with regions in the softening phase while others attain the material strength [8, 18]). According to Model Code 2010 [9], this value can be estimated as:

$$f_{cp} = \eta_{f_c} f_c, \quad \text{where} \quad \eta_{f_c} = \left( \frac{f_{c,\text{ref}}}{f_c} \right)^{\frac{1}{3}} \leq 1 \quad (3.13)$$

A suitable value for  $f_{c,\text{ref}}$  is 30 MPa [8, 9]. Each test is plotted as four curves in a graph with four axes, to better show the relationship between the measured values of  $\tau$ ,  $\sigma$ ,  $\delta$  and  $w$ .

Some curves, like the ones relative to the shear stress of tests 310202, 310304, 310101 and 310104, follow a clear trajectory: they start with a stiff, almost linear ascending phase, followed by a non-linear phase as they approach the maximum shear load  $\tau_{\text{max}}$  and end with a gradual softening phase. Others however do not behave so consistently and present some scatter.

For example, during test 310102 the shear force started to increase again after the first peak load. In other cases, like for test 310301, the maximum shear force is not clearly defined and a large plateau is recorded. Finally, for test 310302 the shear force decreases very rapidly after the peak load, before it reverts to the typical rate of other tests.

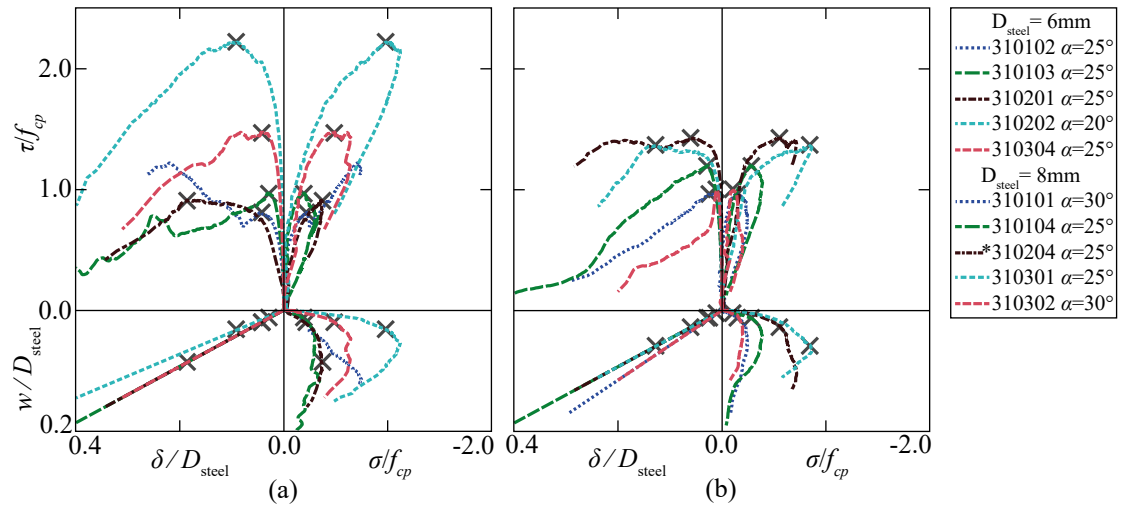


Figure 3.5 – Experimental results for interlocking tests between concrete and steel spheres (a)  $D_{\text{steel}} = 6 \text{ mm}$  (b)  $D_{\text{steel}} = 8 \text{ mm}$

Such randomness can be potentially attributed to the heterogeneous nature of the concrete material: when the steel spheres mostly interact with the cement matrix and small sand particles, the behaviour is clear and consistent. However, when the spheres enter in contact with a large aggregate, a more random behaviour can be observed, depending on the size, shape and hardness of the aggregate. For example, Figure 3.8 (e) shows the surface of the aforementioned specimen 310102 after the test. A large aggregate (length  $>10 \text{ mm}$ ) has been clearly revealed by one of the spheres scraping off the surrounding material.

With respect to the behaviour of specimen 310204, the results are not considered valid for larger displacements as two parts of the device measuring the crack opening and sliding entered in contact, influencing the force transfer and resulting in the pronounced force plateau. The test is thus marked with an asterisk in Figure 3.5.

The values of  $\tau$  and  $\sigma$  occurring when  $\tau = \tau_{\text{max}}$  are marked with an X in Figure 3.5. Note that this does not correspond to the maximum value of  $\sigma$ , as the normal force usually reaches its peak only after the maximum tangential force is measured. According to the approach of Walraven ( $\mu$  is constant) this can only be explained by a change in the angle of the plasticized region with respect to the crack plane (Figure 3.2). These peak values are compared to each other in Figure 3.6, where they are plotted as a function of the applied angle  $\alpha$ . The plot shows a clear trend, as the peak forces decrease consistently with increasing Mixed-Mode angle regardless of the various used materials.

### 3.3.3 Test with mortar specimens

In order to limit the random material response observed for the concrete specimens (direct contact of spheres and aggregates), 11 mortar specimens were additionally tested. The mix-

**Chapter 3. Review of fundamental assumptions of the Two-Phase Model for aggregate interlocking in cracked concrete using numerical methods and experimental evidence**

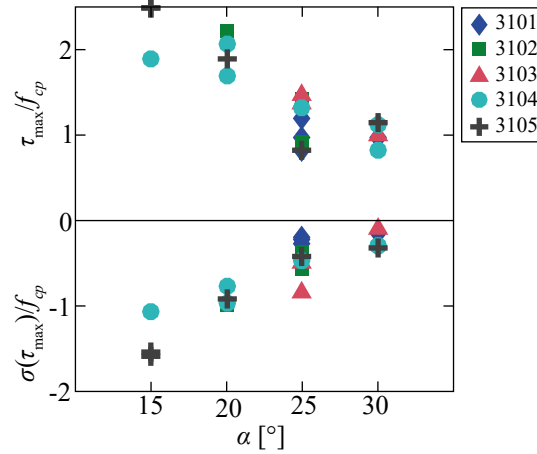


Figure 3.6 – Normalized stresses occurring at  $\tau_{\max}$  as a function of  $\alpha$

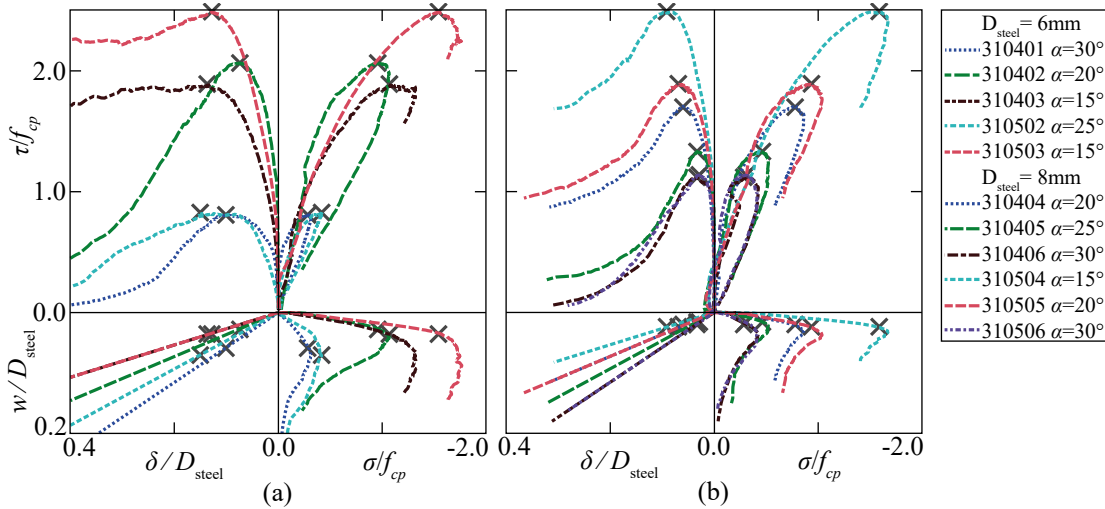


Figure 3.7 – Experimental results for interlocking tests between mortar and steel spheres (a)  $D_{\text{steel}} = 6 \text{ mm}$  (b)  $D_{\text{steel}} = 8 \text{ mm}$

design for the material was prepared according to EN 196-1 [5], using ordinary sand with  $D_{\max} = 2 \text{ mm}$ . Series 3105 had a higher compressive resistance on the test-day compared to series 3104 and typically resulted in higher forces. As shown in Figure 3.7, the curves are better defined than the ones for the concrete specimens, generally showing one clearly identified force peak followed by the softening phase. The trends observed for the concrete specimens remain visible. An exception is presented by tests 310403 and 310503 ( $D_{\text{steel}} = 6 \text{ mm}$ ,  $\alpha = 15^\circ$ ), where the forces remain relatively high even after the peak force. A similar response in terms of  $\tau_{\max}$  and  $\sigma_{\max}$  was observed as for concrete specimens (see Figure 3.7) with a delayed occurrence of  $\sigma_{\max}$  with respect to  $\tau_{\max}$ .

### 3.3. Experimental programme

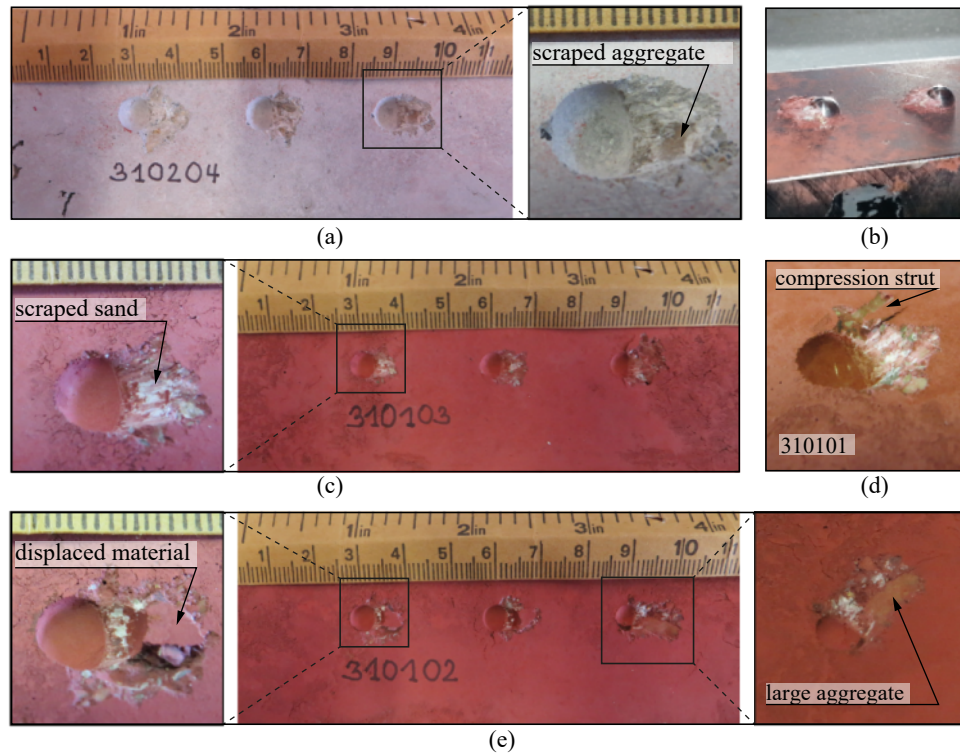


Figure 3.8 – Pictures of tested specimens: (a) Concrete surface of specimen 310204 after testing: the void due to the presence of the steel sphere and the damage due to the applied kinematics are visible. A scraped aggregate is visible in the damaged zone; (b) Steel block after testing: crushed concrete material is visible on one side of the spheres; (c)-(d) Concrete surface after testing: A red pigment was added to mix 3101 making the crushed, white material clearly visible; (e) Concrete surface of specimen 310102 after testing: on the left, cohesive material pushed away by one of the spheres; on the right a large aggregate is visible next to one of the voids, possibly explaining the anomalous softening behaviour of this test;

### 3.4 Review and extension of the Two-Phase model

*The content of this section was developed and implemented by Pundir M. under the supervision of Ancaux G.. It does not represent a contribution of Tirassa M..*

#### 3.4.1 Review of original formulation according to Walraven

The interpretation of the described tests with steel spheres is made by assuming that the distance between spheres is sufficient to avoid any interaction between them. Therefore, a single sphere will be numerically modelled and a proper normalisation will be used to make the comparison with experiments. Starting from the *Two-Phase model* governing equation (3.1), the probability density function  $\Phi$  is now discrete since randomness was fully removed, therefore leading to the simplified shear resistance equation expressed after projection to the direction  $\mathbf{e}_y$ :

$$\langle F_T \rangle = 3F(\mathcal{A}(w, \delta, D_{\text{steel}})) \quad (3.14)$$

where  $\mathcal{A}$  is the region of space where contact/interlocking occurs. Similar to experimental results, the total shear resistance force  $\langle F_T \rangle$  is normalised by  $3A_{sp}f_{cp}$  where  $A_{sp} = \pi D_{\text{steel}}^2/4$  and  $f_{cp}$  is the equivalent plastic resistance. In a 2D setup,  $\mathcal{A}$  can be represented by the area  $a$  and the inclination  $\theta$ , which is not possible anymore for the more general 3D case.  $\mathcal{A}$  is expressed as a function of the opening vector  $(w, \delta)$ . The purpose of this section is two-fold. First an expression for  $\mathcal{A}(w, \delta, D_{\text{steel}})$  is provided in the case of a spherical aggregate. Secondly a perfectly-plastic constitutive behaviour will be used to compare with the experimental results. Few modifications are required to adapt the *Two-Phase model* to the investigated case. By definition, we have in the perfectly-plastic case:

$$\begin{aligned} F(\mathcal{A}) &= \int_{\mathcal{A}} \boldsymbol{\tau}^P(\mathbf{X}) \cdot \mathbf{e}_y dS = \sigma_{pu} \int_{\mathcal{A}} (\mathbf{n}(\mathbf{X}) + \mu \mathbf{t}(\mathbf{X})) \cdot \mathbf{e}_y dS \\ &= \sigma_{pu} \underbrace{\int_{\mathcal{A}} \mathbf{n}(\mathbf{X}) \cdot \mathbf{e}_y dS}_{A_y^n} + \sigma_{pu} \mu \underbrace{\int_{\mathcal{A}} \mathbf{t}(\mathbf{X}) \cdot \mathbf{e}_y dS}_{A_y^t} \end{aligned} \quad (3.15)$$

where  $\sigma_{pu}$  is the plastic threshold stress and is constant.  $\mathbf{n}(\mathbf{X})$  and  $\mathbf{t}(\mathbf{X})$  are the direction vectors for normal and frictional forces respectively. The surfaces  $A_y^n$  and  $A_y^t$  are the projected contact areas along  $\mathbf{e}_y$  direction, following the convention of Walraven, now extended for 3D.

Comparatively to the projected equation (3.9) in 2D, we now have to determine the contact patch  $\mathcal{A}$  before calculating the integral in (3.15). Such a contact patch can be identified geometrically, as Walraven does in the 2D case. To this end, let us consider a rigid sphere of diameter  $D$ , as seen in Figure 3.9a. The crack opening displacement is applied to a second spherical surface of same diameter, representing the opposite mortar/concrete face (represented in red on Figure 3.9b). The region of overlapping/interlock between these two spheres

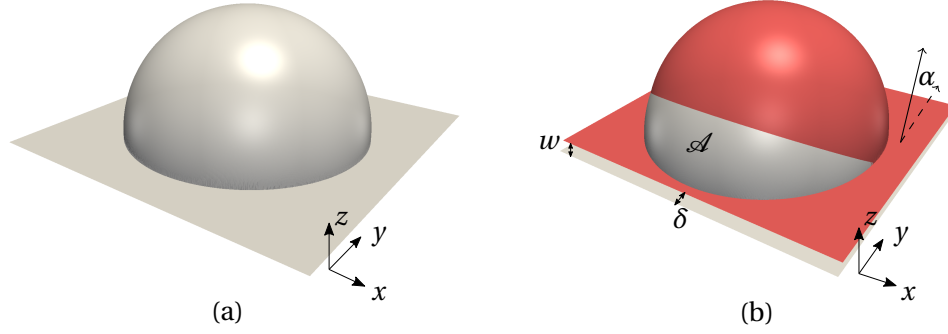


Figure 3.9 – (a) Bottom sphere in an interlock-situation (b) Crack-opening between bottom sphere (gray) and upper sphere (red) for a given shear opening  $\delta$  and a vertical opening  $w = \delta \tan \alpha$ . The interlocking contact patch  $\mathcal{A}$  is the remaining gray region, visible because the bottom surface stays above the upper surface in this configuration.

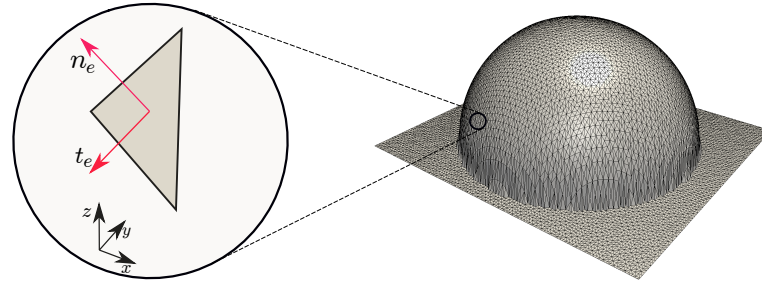


Figure 3.10 – A spherical aggregate discretized into finite elements. The zoom view shows the normal and tangential vector acting on a finite element

is therefore remaining gray and measures  $\mathcal{A}$ .

The integration over the contact patch  $\mathcal{A}$  is computed by discretizing the surface into  $N^{el}$  finite elements, each with an area  $a_e$ , a normal  $\mathbf{n}_e$  and a tangent vector  $\mathbf{t}_e$  as shown in Figure 3.10. The tangent vector  $\mathbf{t}_e$  is defined as the unit vector mutually orthogonal to the normal  $\mathbf{n}_e$  and a vector of the tangent plane normal to  $\mathbf{e}_y$ , i.e.  $\mathbf{t}_e \propto (\mathbf{e}_y \wedge \mathbf{n}_e) \wedge \mathbf{n}_e$ . Thus the expression of the projected contact areas along  $\mathbf{e}_y$  becomes:

$$A_y^n = \sum_{e=1}^{N^{el}} a_e \mathbf{n}_e \cdot \mathbf{e}_y \quad \text{and} \quad A_y^t = \sum_{e=1}^{N^{el}} a_e \mathbf{t}_e \cdot \mathbf{e}_y \quad (3.16)$$

Figure 3.11 shows the evolution of the projected contact areas ( $A_y^n$  and  $A_y^t$ ), normalised by their respective  $A_{sp}$  as a function of normalised shear displacement for various displacement angles and sphere diameters. The material parameters  $\sigma_{pu}$  and  $\mu$  remain free parameters and are obtained by fitting the experimental results obtained in Section 3. The numerical model is thus fitted to each experimental result separately, using the method of least squares. Each fitting yields values of  $\sigma_{pu}$  and  $\mu$  which are recorded and later cross compared (refer

### Chapter 3. Review of fundamental assumptions of the Two-Phase Model for aggregate interlocking in cracked concrete using numerical methods and experimental evidence

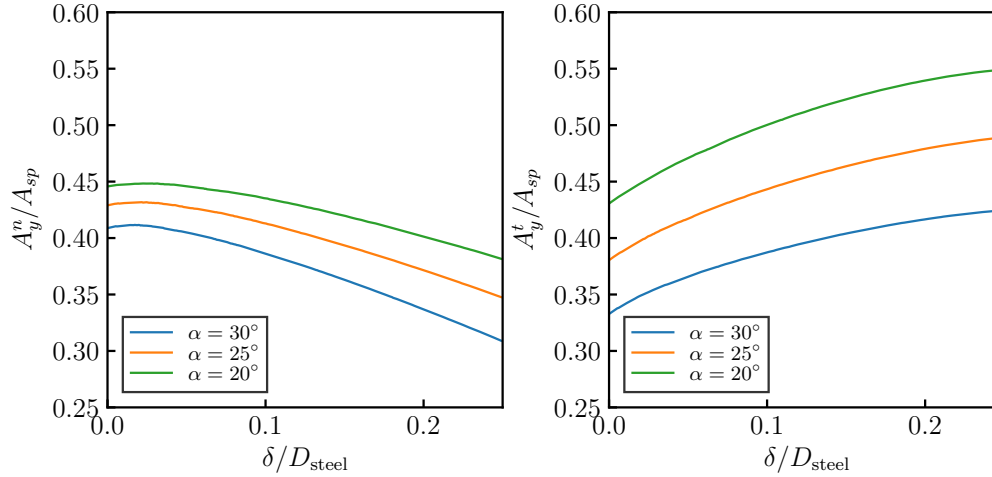


Figure 3.11 – The evolution of projected contact areas  $A_y^n$  and  $A_y^t$  for different loading angles and sphere diameters. The normalised projected contact areas are independent of  $D_{steel}$ .

to Appendix B). This procedure is used for fitting the concrete specimens as reported in this section and will also be used for the mortar specimens.

Fitting  $(\sigma_{pu}, \mu)$  from equation (3.15) onto the displacement path, i.e.  $\delta \in [0 \text{ mm}, 1.0 \text{ mm}]$ , yields regression curves revealing that this model cannot predict the entire shear resistance curve. This was expected because of the rigid perfectly-plastic assumption, whereas the actual onset of the experiment must be elasto-plastic. As a consequence, quite disparate values of both  $\sigma_{pu}$  and  $\mu$  are obtained by regression and even physically impossible negative values can be observed for  $\mu$  (refer Table 3.6). Thus, for analysis of the results, the value of the friction coefficient is set to a physically-consistent value according to Walraven ( $\mu = 0.4$  [6]). Under this constraint, fitting only  $\sigma_{pu}$  yields values that are acceptable both for concrete and mortar. However, Figure 3.12 shows that the global behavior cannot be captured. As a matter of facts, only an average behaviour roughly following the experimental curves can be obtained. Similar conclusions can be observed from fitting against the mortar specimens for the displacement path ( $\delta \in [0 \text{ mm}, 2.0 \text{ mm}]$ ), as seen in Figure 3.13. It is natural to charge this drawback onto the perfectly-plastic nature of the model, and to use it only for the softening parts of experimental results (the post peak-stress regions). Obtained regressions show a much better fit with experimental results. However, in all cases, the best fitted friction coefficients are negative and physically impossible (see Table 3.8, Table 3.9). If  $\mu$  is constrained to a fixed value, again the average behavior may be captured leading to acceptable values for  $\sigma_{pu}$ , but the overall stress-resistance prediction curve remains inaccurate (see Figure 3.14 and Figure 3.15). This works very well for concrete samples, revealing that the presence of aggregates triggers an early onset of plastic flow in the matrix. With mortar samples, on the other end, the absence

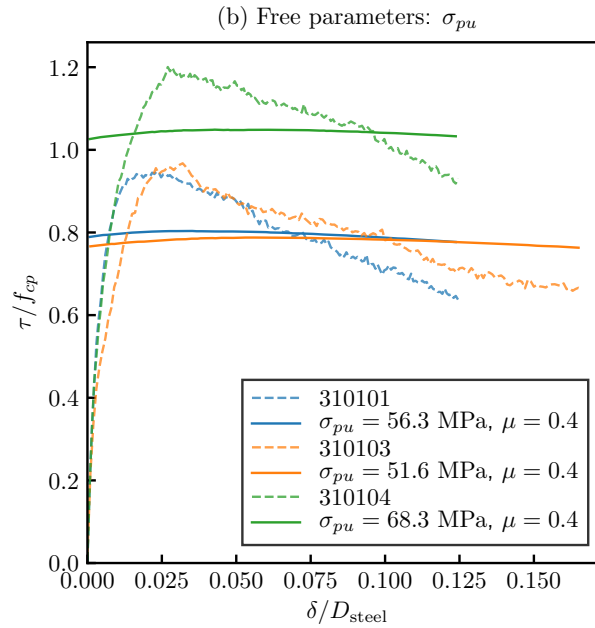


Figure 3.12 – Concrete specimens : Regression of equation (3.15) to experimental results for the entire shear displacement range ( $\delta \in [0 \text{ mm}, 1.0 \text{ mm}]$ ) where only  $\sigma_{pu}$  was fitted with a prescribed  $\mu = 0.4$ .

of confinement favors elasticity (or a delay in onset of plastic flow), which might explain the mis-match with the *Two-Phase model*.

The considerations concerning the obtained values of  $\sigma_{pu}$  and  $\mu$  demonstrate that the geometric model as described by Walraven is incomplete and this for two reasons. First, the hypothesis that the matrix's plastic behavior dominates and the stress-strain relation of the matrix is rigid-perfectly plastic is not applicable for the entire load path: the initial loading phase (before the peak-stress) must be elasto-plastic. Secondly, one has to realize that if the matrix behaves as a perfectly plastic bulk during softening, the contact between matrix and aggregate cannot be deduced from a simple geometric intersection of the pristine geometries. This aspect has already been considered in some previous works [12, 29]. In addition, the potential degradation of the matrix for very large displacements (as subjected to micro-crack development) is neglected in the softening phase. This is at the source of the incoherent predictions of the material parameter  $\sigma_{pu}$ . The ultimate goal of the present work is to introduce a variation of Walraven's method that addresses these issues, therefore allowing a description with physically-sound free parameters. These issues are addressed by *i*) accounting for the surface alterations after contact and *ii*) by introducing free parameters  $\beta_y$  and  $\beta_z$  to account for the elasto-plastic deformation and potential degradation of matrix during the initial loading phase and mimic its effect on perfectly-plastic regime.

**Chapter 3. Review of fundamental assumptions of the Two-Phase Model for aggregate interlocking in cracked concrete using numerical methods and experimental evidence**

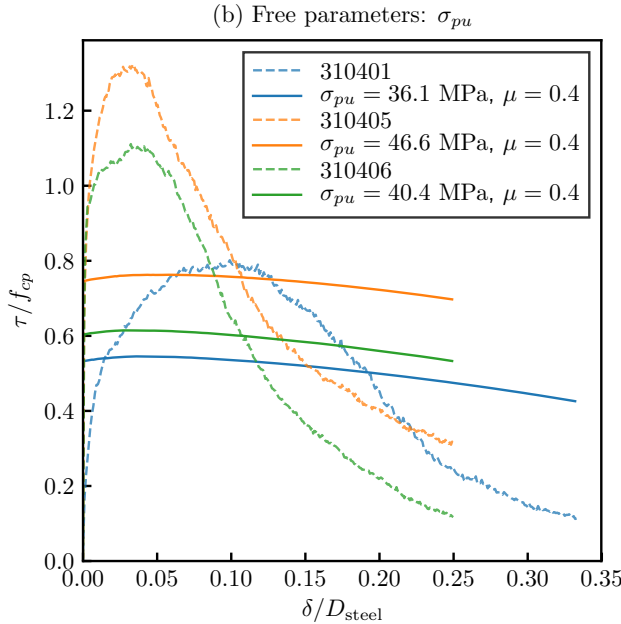


Figure 3.13 – Mortar specimens : Regression of equation (3.15) to experimental results for the entire shear displacement range ( $\delta \in [0 \text{ mm}, 2.0 \text{ mm}]$ ) where only  $\sigma_{pu}$  was fitted with a prescribed  $\mu = 0.4$

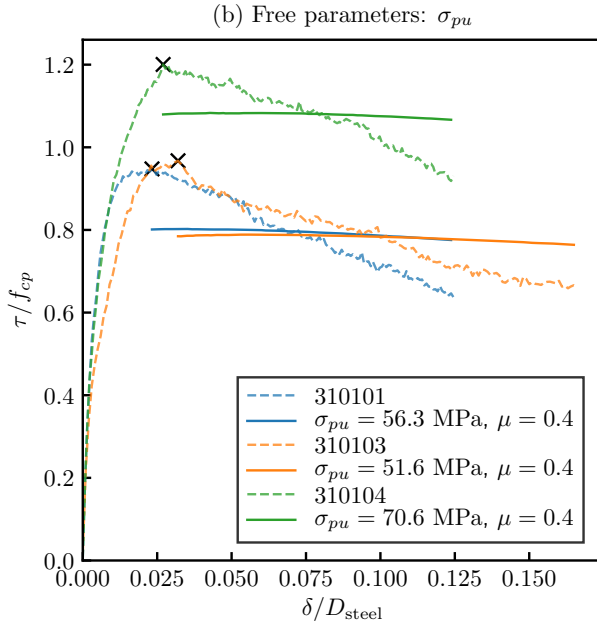


Figure 3.14 – Concrete specimens : Regression of equation (3.15) to experimental results for the post-peak shear displacement range ( $\delta \in [0.2 \text{ mm}, 1.0 \text{ mm}]$ ) where only  $\sigma_{pu}$  was fitted with a prescribed  $\mu = 0.4$ .

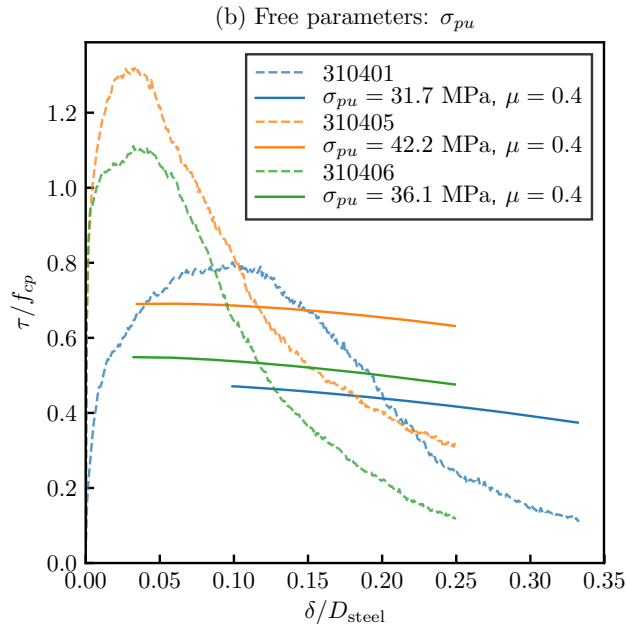


Figure 3.15 – Mortar specimens : Regression of equation (3.15) to experimental results for the post-peak shear displacement range where only  $\sigma_{pu}$  was fitted with a prescribed  $\mu = 0.4$ .

### 3.4.2 Two-Phase model enhancement: surface alterations

A consistent modification of the *Two-Phase model* is proposed in this section to address the described inconsistencies. As previously stated, in such a regime, the mortar/concrete will deform substantially, so that the surface changes have to be taken into account to compute contact surfaces.

To account for this, a possible strategy considers that the deformation of contact area can again be approximated in a purely geometric sense. The idea is to remove any geometric interpenetration between mortar and aggregate bodies created by the imposed homogeneous displacement ( $\delta, w$ ). Such a geometric configuration is illustrated in Figure 3.16a. Because mostly mortar will undergo a plastic flow, only its surface is modified by the vertical projection onto the aggregate surface. Such a projection is done at each incremental step. Figure 3.16b shows the evolution of the contact area with and without considering such a plastic alteration of the surface. Remarkably, the corrected contact area now decreases as a function of  $\delta$ .

The contact patch  $\mathcal{A}$  is deformed as soon as the shear displacement reaches the value corresponding to the peak stress. Figure 3.17 shows the evolution of projected contact areas after taking deformation into consideration. With the corrected projected contact areas ( $A_y^n$  and  $A_y^t$ ), the regression procedure presented in Section 3.4.1 can be employed again.

The regression is done by considering  $\sigma_{pu}$  as free parameter with  $\mu$  fixed to 0.4 (trying to fit both  $\sigma_{pu}$  and  $\mu$  leads potentially to un-physical values similar to the ones presented in the

**Chapter 3. Review of fundamental assumptions of the Two-Phase Model for aggregate interlocking in cracked concrete using numerical methods and experimental evidence**

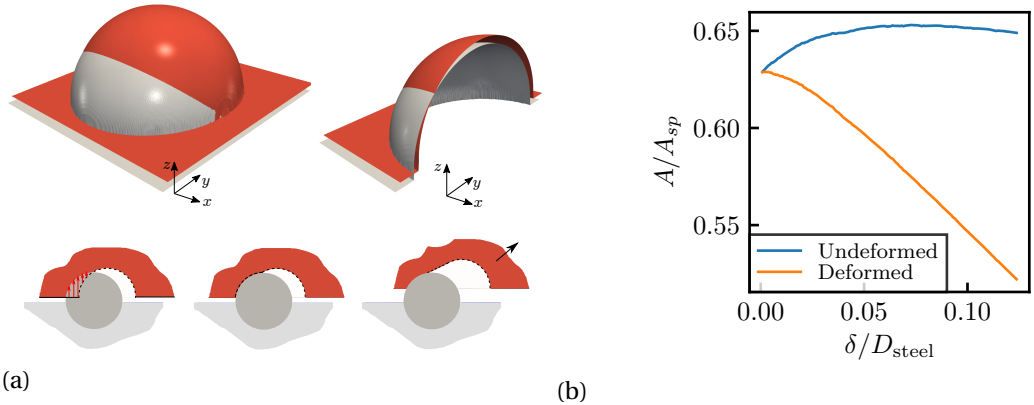


Figure 3.16 – (a) Vertical projection of interlocked mortar surface (red) to the aggregate surface (gray) (b) Evolution of contact area before and after considering deformation of interlocked region for  $\alpha = 30^\circ$

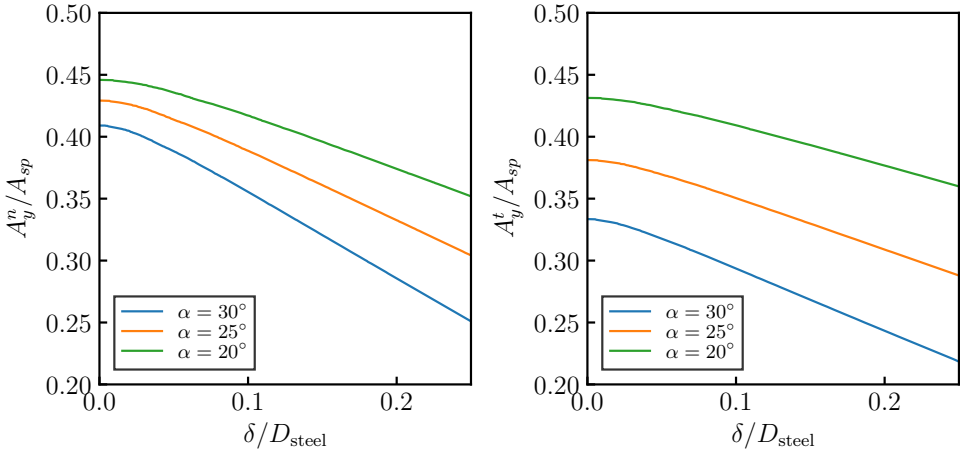


Figure 3.17 – The evolution of projected contact areas  $A_y^n$  and  $A_y^t$  after considering deformation of interlocked region for different loading angles and sphere diameters

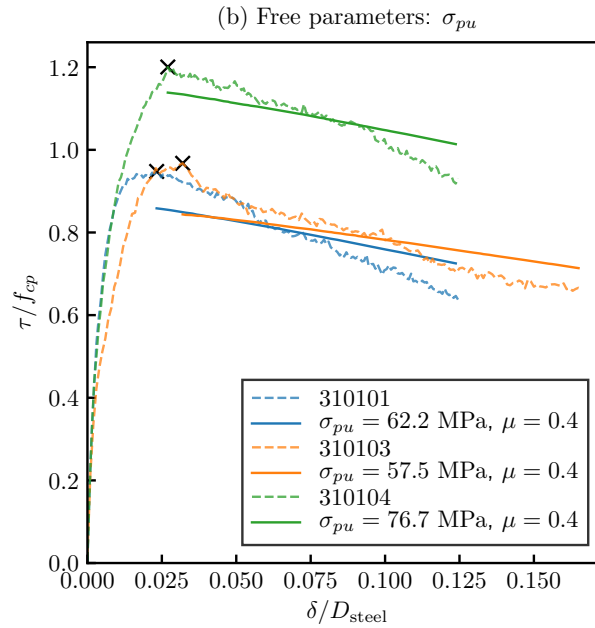


Figure 3.18 – Concrete specimens : Regression of equation (3.15) to experimental results for the post-peak shear displacement range considering deformation of contact area where only  $\sigma_{pu}$  was fitted with a prescribed  $\mu = 0.4$

previous section). Figure 3.18 and Figure 3.19 shows the regression curves for both concrete and mortar specimens.

### 3.4.3 Two-Phase model enhancement: elasto-plastic deformation of matrix

Fitting equation (3.15) with corrected contact area still gives a mismatch with experimental stress-displacement curves. The origin of this discrepancy is the projection strategy employed, which only crudely account for plastic deformations due to contact forces, and therefore leads to inaccurate contact areas. During the pre-peak regime, where elasto-plastic deformation occurs, only some portion of the contact surface will plastify to take the shape of the steel aggregate. To illustrate this point, we take an example of a steel aggregate indenting an elasto-plastic material as shown in Figure 3.20i. Allowing for interpenetration of bodies, the contact area  $\mathcal{A}$  considered, based on our vertical projection strategy, is shown in Figure 3.20i-b in red. However, due to elasto-plastic deformation the actual deformed profile will be different and the actual contact area  $\mathcal{A}^*$  may be much smaller as shown in the Figure 3.20i-c. Figure 3.20ii shows the elasto-plastic deformation of matrix and the correction of the contact area for the geometry considered in our case.

Therefore, the actual contact area will be less than the contact area computed from our projection strategy. At the peak stress, when elasto-plastic regime transitions to perfectly-

**Chapter 3. Review of fundamental assumptions of the Two-Phase Model for aggregate interlocking in cracked concrete using numerical methods and experimental evidence**

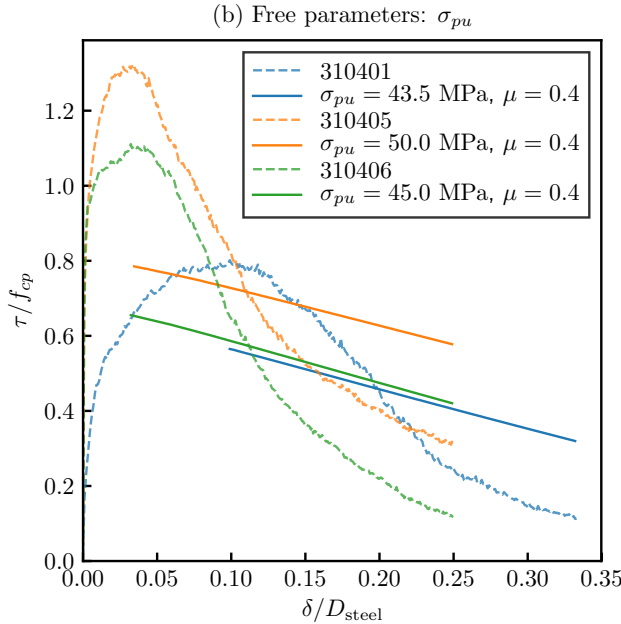


Figure 3.19 – Mortar specimens : Regression of equation (3.15) to experimental results for the post-peak shear displacement range considering deformation of contact area where only  $\sigma_{pu}$  was fitted with a prescribed  $\mu = 0.4$

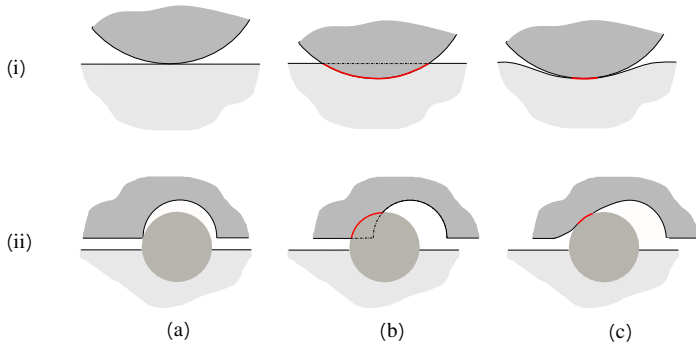


Figure 3.20 – (a) Indentation of an elasto-plastic material by steel aggregate (b) Contact area (A) (in red) computed from vertical projection strategy (c) Actual contact area  $A^*$  (in red) due to elasto-plastic deformation of the material

### 3.4. Review and extension of the Two-Phase model

plastic regime, the actual contact area  $\mathcal{A}^*$  will need a correction factor.

$$\mathcal{A}^* = \mathcal{A} - \mathcal{A}_{ep} \quad (3.17)$$

where  $\mathcal{A}$  is the contact area computed from vertical projection and  $\mathcal{A}_{ep}$  is the correction contact area, to be computed at the transition to perfectly plastic regime *i.e.* at peak stress. The equation (3.15) is then modified to account for the true contact area.

$$\begin{aligned} F(\mathcal{A}^*(w, \delta)) &= F(\mathcal{A}(w, \delta) - \mathcal{A}_{ep}) \\ &= \int_{\mathcal{A}} \boldsymbol{\tau}^P(\mathbf{X}) \cdot \mathbf{e}_y dS - \int_{\mathcal{A}_{ep}} \boldsymbol{\tau}^P(\mathbf{X}) \cdot \mathbf{e}_y dS \\ &= \sigma_{pu} \underbrace{\int_{\mathcal{A}} \mathbf{n}(\mathbf{X}) \cdot \mathbf{e}_y dS}_{A_y^n} + \sigma_{pu}\mu \underbrace{\int_{\mathcal{A}} \mathbf{t}(\mathbf{X}) \cdot \mathbf{e}_y dS}_{A_y^t} - \sigma_{pu}\mathcal{A}_{ep,y} \end{aligned} \quad (3.18)$$

where  $\mathcal{A}_{ep,y}$  is the projection of the correction contact area  $\mathcal{A}_{ep}$  along  $\mathbf{e}_y$  direction. Equation (3.15) can be modified to compute the normal forces by taking the projection along  $\mathbf{e}_z$  direction:

$$\begin{aligned} \langle F_N \rangle &= \int_{\mathcal{A}} \boldsymbol{\tau}^P(\mathbf{X}) \cdot \mathbf{e}_z dS - \int_{\mathcal{A}_{ep}} \boldsymbol{\tau}^P(\mathbf{X}) \cdot \mathbf{e}_z dS \\ &= \sigma_{pu} \underbrace{\int_{\mathcal{A}} \mathbf{n}(\mathbf{X}) \cdot \mathbf{e}_z dS}_{A_z^n} + \sigma_{pu}\mu \underbrace{\int_{\mathcal{A}} \mathbf{t}(\mathbf{X}) \cdot \mathbf{e}_z dS}_{A_z^t} - \sigma_{pu}\mathcal{A}_{ep,z} \end{aligned} \quad (3.19)$$

where  $A_z^n$ ,  $A_z^t$  and  $\mathcal{A}_{ep,z}$  are areas projected along  $\mathbf{e}_z$  direction. We assume that the corrected contact areas  $\mathcal{A}_{ep,y}$  and  $\mathcal{A}_{ep,z}$  are proportional to the  $\mathcal{A}$  projected along  $\mathbf{e}_y$  and  $\mathbf{e}_z$  and can be correlated by introducing parameter  $\beta_y$  and  $\beta_z$ :

$$\begin{aligned} \mathcal{A}_{ep,y} &\propto \mathcal{A}(\mathbf{n}(\mathbf{X}) + \mu\mathbf{t}(\mathbf{X})) \cdot \mathbf{e}_y \\ &= \beta_y \mathcal{A}(\mathbf{n}(\mathbf{X}) + \mu\mathbf{t}(\mathbf{X})) \cdot \mathbf{e}_y \\ &= \beta_y (A_y^n + \mu A_y^t) \end{aligned} \quad (3.20)$$

$$\begin{aligned} \mathcal{A}_{ep,z} &\propto \mathcal{A}(\mathbf{n}(\mathbf{X}) + \mu\mathbf{t}(\mathbf{X})) \cdot \mathbf{e}_z \\ &= \beta_z \mathcal{A}(\mathbf{n}(\mathbf{X}) + \mu\mathbf{t}(\mathbf{X})) \cdot \mathbf{e}_z \\ &= \beta_z (A_z^n + \mu A_z^t) \end{aligned} \quad (3.21)$$

where  $A_y^n$ ,  $A_y^t$  and  $A_z^n$ ,  $A_z^t$  are calculated at  $\{\delta_y = \arg \max_{\delta} \tau(\delta)\}$  and at  $\{\delta_z = \arg \max_{\delta} \sigma(\delta)\}$  respectively. As can be observed from the above equations  $\mathcal{A}_{ep,y}$  and  $\mathcal{A}_{ep,z}$  depend on the loading angle  $\alpha$ , the diameter of the sphere  $D_{\text{steel}}$  and the parameters  $\beta_y$ ,  $\beta_z$ .

### Chapter 3. Review of fundamental assumptions of the Two-Phase Model for aggregate interlocking in cracked concrete using numerical methods and experimental evidence

Fitted : Concrete Specimens							
#	$\alpha$ [°]	$D_{\text{steel}}$ [mm]	$\sigma_{pu}$ [MPa]	$\sigma_{pu}/f_{cp}$ [-]	$\mu$ [-]	$\beta_y$ [-]	$\beta_z$ [-]
310101	30	8	140.91	3.64	0.40	0.52	0.64
310102	25	6	205.29	5.30	0.40	0.73	0.55
310103	25	6	121.43	3.14	0.40	0.49	0.56
310104	25	8	157.62	4.07	0.40	0.49	0.57
310201	25	6	469.05	12.30	0.40	0.85	0.86
310202	20	6	104.66	2.74	0.40	-0.39	2.59
310302	30	8	158.31	3.22	0.40	0.62	0.67
310304	25	6	186.95	3.80	0.40	0.29	0.23

Table 3.4 – Concrete Specimens : Obtained values of  $\sigma_{pu}$ ,  $\beta_y$  and  $\beta_z$  considering contact patch deformation during elasto-plastic regime

This extended numerical model is again fitted to each experimental result separately using the method of least squares. First of all, equation (3.18) is fitted to the experimental tangential forces so that regression values of  $\sigma_{pu}$  and  $\beta_y$  are obtained. The obtained value of  $\sigma_{pu}$  is then used for fitting equation (3.19) to the experimental normal forces with  $\beta_z$  as the only free parameter. Figure 3.21 shows the regression curves for a fixed value of  $\mu = 0.4$  and  $\sigma_{pu}$ ,  $\beta_y$  and  $\beta_z$  as free parameters for concrete specimens. As can be seen, the post-peak behaviour is captured accurately for concrete specimens. The values computed for  $\sigma_{pu}$  of samples 310102 and 310201 (see Table 3.4) are considered as outliers. As discussed in Section 3.3.2, for test 310102 the shear force starts increasing in the softening phase and for test 310201, a large plateau is reached (behaviour attributed to the sphere coming in contact with a large aggregate). The other values obtained for  $\sigma_{pu}/f_{cp}$  are, for the majority of the cases, in the range of values 3 to 4. Also, the values of  $\beta_y$  and  $\beta_z$  obtained from two different fittings are consistent for a given geometry and loading angle, typically between 0.5 and 0.8. A detailed discussion is presented in next section about the values obtained for  $\sigma_{pu}$ ,  $\beta_y$  and  $\beta_z$ . Concerning the mortar specimens, the assumption that the perfectly-plastic regime starts right after the peak stress does not seem to hold (see Figure 3.22) and two post-peak regimes seem to develop. Fitting the equation (3.18) just after the peak stress yields too large values of  $\sigma_{pu}$ . This discrepancy can be explained by the fact that the mortar has a less plastic response than concrete (the plastification allowing to measure the effective  $\sigma_{pu}$  is only reached at a late stage,  $\approx 1.0$  mm). This seems consistent with the experimental results when the fitting starts after 1.0 mm of displacement: the values of  $\sigma_{pu}$  are thus similar to what was obtained for concrete specimens, which were made of mortar with a similar compressive strength (but with larger scatter of the results). It is also interesting to note that the values of  $\beta_y$  and  $\beta_z$  are consistent with each other in all cases.

### 3.4. Review and extension of the Two-Phase model

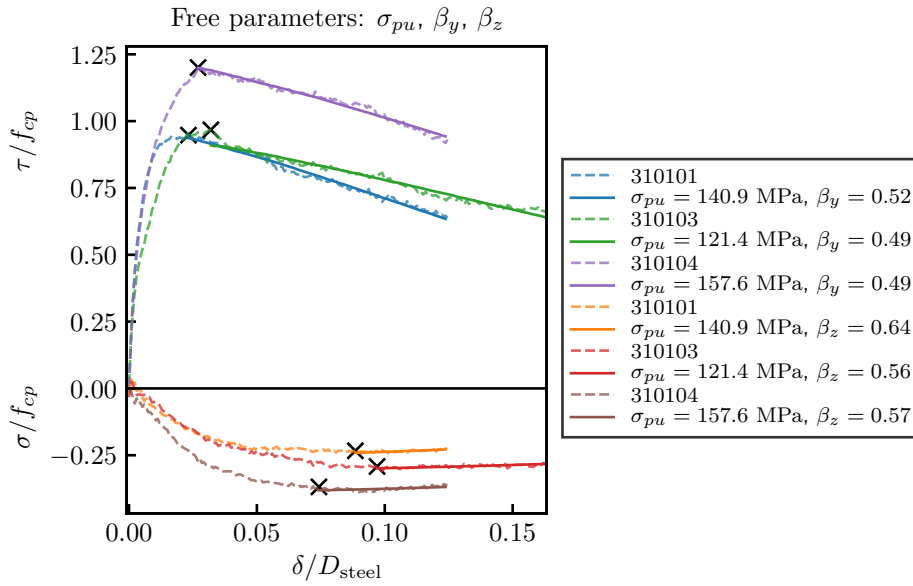


Figure 3.21 – Concrete Specimens : Regression of equation (3.18) and (3.19) to experimental results considering contact patch deformation during elasto-plastic regimes

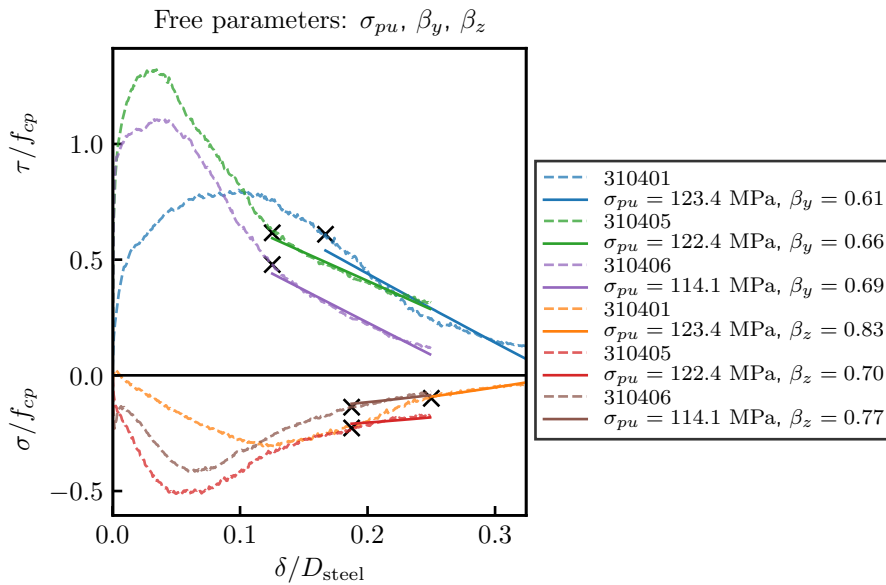


Figure 3.22 – Mortar Specimens : Regression of equation (3.18) and equation (3.19) to experimental results considering contact patch deformation during elasto-plastic regimes

### Chapter 3. Review of fundamental assumptions of the Two-Phase Model for aggregate interlocking in cracked concrete using numerical methods and experimental evidence

Fitted : Concrete Specimens							
#	$\alpha$ [°]	$D_{\text{steel}}$ [mm]	$\sigma_{pu}$ [MPa]	$\sigma_{pu}/f_{cp}$ [-]	$\mu$ [-]	$\beta_y$ [-]	$\beta_z$ [-]
310401	30	6	123.41	3.40	0.40	0.61	0.83
310402	20	6	328.01	9.03	0.40	0.77	0.74
310404	20	8	188.80	5.20	0.40	0.56	0.49
310405	25	8	122.41	3.37	0.40	0.66	0.70
310504	15	8	328.76	7.80	0.40	0.57	0.32
310505	20	8	171.44	4.07	0.40	0.43	0.24
310506	30	8	130.12	3.09	0.40	0.79	0.79
310406	30	8	114.11	3.14	0.40	0.69	0.77

Table 3.5 – Mortar Specimens : Obtained values of  $\sigma_{pu}$ ,  $\beta_y$  and  $\beta_z$  considering contact patch deformation during elasto-plastic regime

### 3.5 Discussion

*The content of this section was developed by Pundir M. under the supervision of Anciaux G.. It does not represent a contribution of Tirassa M..*

The values of  $\sigma_{pu}$  predicted by the previously presented approach yield valuable information allowing to interpret its nature in *Two-Phase models*. As presented in Table 3.4 and Table 3.5,  $\sigma_{pu}/f_{cp}$  is in the same order of magnitude as the ratio observed in various studies. For instance, the analytical works [15] and [13] find  $\sigma_{pu} = 3f_{cp}$  in the rigid-plastic regime during the indentation of an elastic-plastic half-space by a spherical rigid body. Also, for concrete it is observed that a highly confined matrix should produce a higher effective strength, leading to much larger values of  $\sigma_{pu}/f_{cp}$  [22, 25]. Afterall, the *proportionality factor* between  $\sigma_{pu}$  and  $f_{cp}$  depends on the heterogeneity of the bulk and on the shape of the contacting surfaces.

Even if  $\sigma_{pu}$  is taken equal to  $f_{cp}$ , *Two-Phase models* may provide reasonable estimates of the peak tangential resistance in real cases with rough cracked surfaces. This paradox can be explained with the introduction of the statistics, which may compensate for the missing *proportionality factor*. Let us recall the central equation of *Two-Phase models*, as written by Walraven:

$$\langle F_R \rangle = \iint \Psi(D, h) F(D, h) dD dh \quad (3.22)$$

where  $\Psi(D, h)$  is the probability density of circular aggregates of diameter  $D$  being intersected at elevation  $h$ , and  $F(D, h)$  is the force contribution of this particular geometrical situation. The strategy of Walraven was to write  $\Psi(D, h) = \lambda(D)\rho(D, h)$  as a product between the probability density  $\lambda(D)$  of having an aggregate of diameter  $D$  and the probability density  $\rho(D, h)$  of cutting such an aggregate at elevation  $h$ . A first source of inaccuracy comes from the 2D projection the force  $F(D, h)$ , assuming that every slice of matter is not exchanging forces with its the surrounding. Secondly, Walraven assumed that  $\rho(D, h) = 2/D$  which seems to be an adhoc function decaying smoothly with the asperity radius. Both these points may lead to

a hidden modification of the *proportionality factor*  $\sigma_{pu}/f_{cp}$ , explaining how the peak shear resistance could be captured with a wrong  $\sigma_{pu}$  value.

Nevertheless, it was demonstrated that obtaining the correct behaviour along the entire loading path needs an accurate prediction of the contact area. Without a full resolution of the mechanical problem, an area correction had to be introduced,  $\mathcal{A}_{ep}$ , which represents the error in our geometrically-based contact area prediction. This obviously neglected the elasto-plastic onset deformation of the matrix. This error will depend upon  $f_{cp}$  and on the arrangement of aggregates around the steel spheres. Indeed, aggregates close to the interlock contact may create obstacles which would trigger early plastic flows in the matrix, therefore leading to small values of the correction area  $\mathcal{A}_{ep}$ .

All the raised points call for computations resolving explicitly the plastic deformation occurring in the bulk. Only by using large scale finite elements, with fracture, plasticity and contact algorithms, will it be possible to obtain the accurate evolution of contact area and forces, and therefore would enhance *Two-Phase models* predictive capacity. Some more fundamental modeling difficulties are still to be accounted for statistical *Two-Phase models* to describe aggregate interlocking in cracked concrete:

- Aggregates are usually not spherical [16].
- Failures in structures may be triggered by the limited tensile capacity of the matrix, which will therefore develop cracks and thus present a reduced strength [3].
- The range of aggregate sizes to be considered as part of the matrix (and not as aggregate) is not precisely defined.
- Cracks are not straight planes, but have an undulated shape which additionally influences the overall roughness [4].

### 3.6 Conclusions

*Two-Phase models* can predict the shear resistance due to asperity interlock. They encompass a statistical treatment, with a probability density function of interlock situations, and geometrically computed forces as key ingredients. In the past, such theories considered 2D approximations. A 3D extension to the force evaluation has been developed to predict the shear resistance measured during several experiments of well-defined interlock configurations, where statistics can be omitted: concrete and mortar samples have been loaded against three steel spheres in order to stay close to the assumptions of *Two-Phase models*, *i.e.* flat crack plane and spherical aggregates. The main conclusions of this investigation are listed below:

1. For all the presented experiments, both concrete and mortar, the maximum interlock normal/shear stress (*i.e.* the normal/shear strengths) normalized by the equivalent

### Chapter 3. Review of fundamental assumptions of the Two-Phase Model for aggregate interlocking in cracked concrete using numerical methods and experimental evidence

---

plastic resistance ( $f_{cp}$ ) are shown to decrease with increasing loading angle ( $\alpha$ ). However, the load-displacement curves differ strongly. Concrete exhibits a larger scatter, and a generally smaller yield strength. This larger scatter can be explained by the presence of large aggregates within the vicinity of interlocking regions.

2. Walraven's hypothesis of perfectly-plastic deformation of the matrix is not applicable during the initial loading stage for both concrete and mortar. This is justified by the fact that the onset of deformation is necessarily elasto-plastic. A clear plastic behaviour is only completely developed for relatively large penetrations of the aggregates in the matrix (in any case after the shear stress peak).
3. It is demonstrated that strictly adopting Walraven's modelling assumptions leads to un-physical values of the plastic threshold stress ( $\sigma_{pu}$ ) and the friction coefficient ( $\mu$ ). This is obtained by numerical regression of the Two-Phase model onto the experimental results, which yields negative values of the friction coefficient. Upon constraining  $\mu = 0.4$  (as performed by Walraven) and applying the regression only for the post-peak regime, physically-consistent values of  $\sigma_{pu}$  are obtained. This yields however to a significant mismatch with the stress-displacement experimental curves.
4. The novel approach proposed in this paper, allows to obtain a matching post-peak response (dominated by the plastic behaviour of the material), by refining the contact areas employed by the model. First, the contacting area should account for the residual changes in the matrix surface due to plastic deformation during the loading path. This effect globally reduces the contact area for an increasing displacement (which was not accounted in the original Two-Phase model). Secondly, the elastic-plastic deformation of the matrix should be accounted for in order to further improve the measure of the contact area. A scalar correction factor ( $\mathcal{A}_{ep}$ ) has been introduced, yielding to very good agreements with all the experimental results.  
It was also shown that  $\mathcal{A}_{ep}$  is proportional to the geometrically evaluated contact area, with  $\beta$  a proportionality factor, ranging from 0.5 up to 0.8.
5. Contrary to common usage of Walraven's theory, assuming  $\sigma_{pu} = f_{cp}$ , it was shown that the proportionality factor between  $\sigma_{pu}/f_{cp}$  is not constant. In order to predict the entire stress-strain curve (and not only the peak value of the shear resistance), the proportionality factor must be known. This remains difficult as it requires an accurate prediction of the interlocking contact areas, only accessible with the complete resolution of the mechanical problem (for instance with large scale finite elements techniques, involving fracture, plasticity and contact algorithms).

### Acknowledgement

This work has been funded by the Swiss National Science Foundation, research grant 200021\_169649. The authors are very appreciative of the support received.

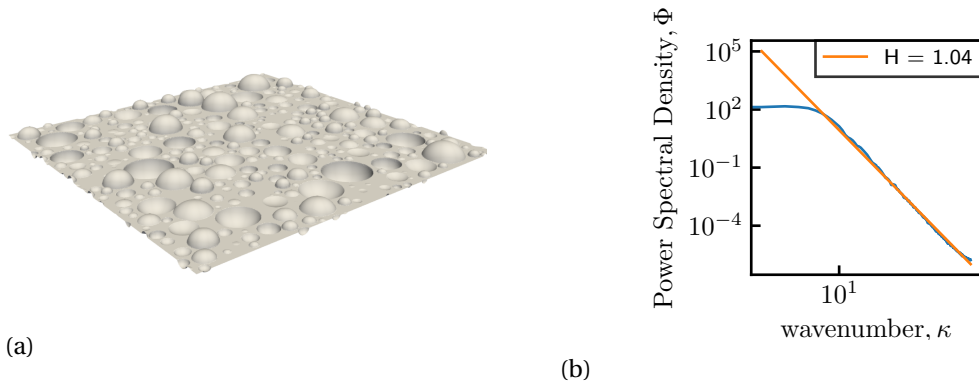


Figure 3.23 – (a) Idealized crack surface for 60% packing density and diameters in range [14 mm, 2 mm] (b) Hurst exponent  $H$  for surface in (a)

## Appendix A. Hurst exponent for Walraven’s surface

*The content of this appendix was developed and implemented by Pundir M. under the supervision of Ancaux G.. It does not represent a contribution of Tirassa M..*

A numerical concrete sample is generated for a given packing density ( $p_k$ ) and an aggregate range ( $[D_{min}, D_{max}]$ ) using placing algorithm proposed in [33]. The aggregates were assumed to be spherical in shape and the fuller distribution curve was used for distribution of aggregates. The numerically fabricated concrete sample is cut at an arbitrarily plane according to the geometrical hypothesis of *Two-Phase model* to generate an idealised crack plane Figure 3.23a. Figure 3.23b shows the Power Spectral Density [21, 34] and corresponding Hurst exponent for such a surface. However, it should be noted that Walraven chose  $D_{min} = 0.25$  mm, while it was set to 2 mm for this study. Similarly, the packing density  $p_k$  used in Walraven’s original model is around 70% while it is 60% for this study.

## Appendix B. Detailed results

*The content of this appendix was developed and implemented by Pundir M. under the supervision of Ancaux G.. It does not represent a contribution of Tirassa M..*

Table 3.6-Table 3.11 present the values of  $\sigma_{pu}$  and  $\mu$  obtained for the various concrete and mortar specimens. Not all tests have been considered, as 310303 and 310305 were subjected to special kinematics and tests 310204, 310301 and 310302 had no clearly identified softening phase. Similarly, the mortar specimens 310403, 310502 and 310503 have been omitted due to their anomalous behaviour during after the peak.

**Chapter 3. Review of fundamental assumptions of the Two-Phase Model for aggregate interlocking in cracked concrete using numerical methods and experimental evidence**

**Review of original formulation according to Walraven**

#	$\alpha$ [°]	$D_{\text{steel}}$ [mm]	Fitted : $\sigma_{pu}, \mu$			Fitted : $\sigma_{pu}$		
			$\sigma_{pu}$ [MPa]	$\sigma_{pu}/f_{cp}$ [-]	$\mu$ [-]	$\sigma_{pu}$ [MPa]	$\sigma_{pu}/f_{cp}$ [-]	$\mu$ [-]
310101	30	8	124.55	3.22	-0.4	56.35	1.46	0.4
310102	25	6	-68.41	-1.77	-2	52.3	1.35	0.4
310103	25	6	96.37	2.49	-0.2	51.56	1.33	0.4
310104	25	8	51.73	1.34	0.8	68.32	1.76	0.4
310201	25	6	-114.42	-3	-1.5	49.45	1.3	0.4
310202	20	6	-88.62	-2.32	-2.7	122.53	3.21	0.4
310302	30	8	263.43	5.35	-0.8	52.55	1.07	0.4
310304	25	6	93.19	1.89	0.7	112.4	2.28	0.4

Table 3.6 – Concrete specimens : Obtained values of  $\sigma_{pu}$  and  $\mu$  for concrete specimens when fitted over the shear displacement range ( $\delta \in [0 \text{ mm}, 1.0 \text{ mm}]$ )

#	$\alpha$ [°]	$D_{\text{steel}}$ [mm]	Fitted : $\sigma_{pu}, \mu$			Fitted : $\sigma_{pu}$		
			$\sigma_{pu}$ [MPa]	$\sigma_{pu}/f_{cp}$ [-]	$\mu$ [-]	$\sigma_{pu}$ [MPa]	$\sigma_{pu}/f_{cp}$ [-]	$\mu$ [-]
310401	30	6	119.83	3.3	-0.5	36.11	0.99	0.4
310402	20	6	282.54	7.77	-0.4	86.37	2.38	0.4
310404	20	8	176.16	4.85	-0.3	74.53	2.05	0.4
310405	25	8	257.54	7.09	-0.7	46.63	1.28	0.4
310505	20	8	221.93	5.26	-0.3	99.03	2.35	0.4
310506	30	8	281.88	6.68	-0.7	48.86	1.16	0.4
310406	30	8	246.59	6.79	-0.7	40.45	1.11	0.4

Table 3.7 – Mortar specimens : Obtained values of  $\sigma_{pu}$  and  $\mu$  when fitted over the shear displacement range ( $\delta \in [0 \text{ mm}, 2.0 \text{ mm}]$ )

#	$\alpha$ [°]	$D_{\text{steel}}$ [mm]	Fitted : $\sigma_{pu}, \mu$			Fitted : $\sigma_{pu}$		
			$\sigma_{pu}$ [MPa]	$\sigma_{pu}/f_{cp}$ [-]	$\mu$ [-]	$\sigma_{pu}$ [MPa]	$\sigma_{pu}/f_{cp}$ [-]	$\mu$ [-]
310101	30	8	187.39	4.84	-0.6	56.26	1.45	0.4
310102	25	6	600.18	15.5	-0.7	68.57	1.77	0.4
310103	25	6	149.67	3.86	-0.5	51.62	1.33	0.4
310104	25	8	193.58	5	-0.5	70.56	1.82	0.4
310201	25	6	547.45	14.35	-0.7	60.57	1.59	0.4
310202	20	6	190.92	5.01	0	131.08	3.44	0.4
310302	30	8	256.1	5.21	-0.8	50.78	1.03	0.4
310304	25	6	258.09	5.25	-0.3	115.35	2.34	0.4

Table 3.8 – Concrete specimens : Obtained values of  $\sigma_{pu}$  and  $\mu$  for concrete specimens when fitted over the post-peak shear displacement range

### 3.6. Conclusions

#	$\alpha$ [°]	$D_{\text{steel}}$ [mm]	Fitted : $\sigma_{pu}, \mu$			Fitted : $\sigma_{pu}$		
			$\sigma_{pu}$ [MPa]	$\sigma_{pu}/f_{cp}$ [-]	$\mu$ [-]	$\sigma_{pu}$ [MPa]	$\sigma_{pu}/f_{cp}$ [-]	$\mu$ [-]
310401	30	6	189.63	5.22	-0.6	31.73	0.87	0.4
310402	20	6	437.14	12.03	-0.5	82.85	2.28	0.4
310404	20	8	288.77	7.95	-0.5	73.23	2.01	0.4
310405	25	8	264.98	7.29	-0.7	42.25	1.16	0.4
310505	20	8	379.15	8.99	-0.5	96.71	2.29	0.4
310506	30	8	307.4	7.29	-0.7	45.22	1.07	0.4
310406	30	8	258.25	7.11	-0.7	36.11	0.99	0.4

Table 3.9 – Mortar specimens : Obtained values of  $\sigma_{pu}$  and  $\mu$  when fitted over the post-peak shear displacement range

#### Two-Phase model enhancement: surface alterations

#	$\alpha$ [°]	$D_{\text{steel}}$ [mm]	Fitted : $\sigma_{pu}, \mu$			Fitted : $\sigma_{pu}$		
			$\sigma_{pu}$ [MPa]	$\sigma_{pu}/f_{cp}$ [-]	$\mu$ [-]	$\sigma_{pu}$ [MPa]	$\sigma_{pu}/f_{cp}$ [-]	$\mu$ [-]
310101	30	8	1,049.86	27.11	-1.1	62.18	1.61	0.4
310102	25	6	2,827.3	73.01	-1	81.76	2.11	0.4
310103	25	6	532.79	13.76	-0.9	57.53	1.49	0.4
310104	25	8	721.59	18.63	-1	76.72	1.98	0.4
310201	25	6	2,597.3	68.1	-1	72.22	1.89	0.4
310202	20	6	-89.85	-2.36	-3.3	146.43	3.84	0.4
310302	30	8	2,046.8	41.6	-1.2	55.89	1.14	0.4
310304	25	6	559.52	11.37	-0.8	129	2.62	0.4

Table 3.10 – Concrete specimens : Obtained values of  $\sigma_{pu}$  and  $\mu$  for concrete specimens when fitted over the post-peak shear displacement range considering surface alterations

#	$\alpha$ [°]	$D_{\text{steel}}$ [mm]	Fitted : $\sigma_{pu}, \mu$			Fitted : $\sigma_{pu}$		
			$\sigma_{pu}$ [MPa]	$\sigma_{pu}/f_{cp}$ [-]	$\mu$ [-]	$\sigma_{pu}$ [MPa]	$\sigma_{pu}/f_{cp}$ [-]	$\mu$ [-]
310401	30	6	832.31	22.9	-1.1	43.54	1.2	0.4
310402	20	6	1,655.6	45.56	-0.9	97.8	2.69	0.4
310404	20	8	1,107.12	30.46	-0.9	83.5	2.3	0.4
310405	25	8	1,357.28	37.35	-1	49.97	1.38	0.4
310505	20	8	1,428.67	33.88	-0.9	110.61	2.62	0.4
310506	30	8	1,881.46	44.61	-1.2	56.15	1.33	0.4
310406	30	8	1,575.41	43.35	-1.2	45.04	1.24	0.4

Table 3.11 – Mortar specimens : Obtained values of  $\sigma_{pu}$  and  $\mu$  for concrete specimens when fitted over the post-peak shear displacement range considering surface alterations

### **Chapter 3. Review of fundamental assumptions of the Two-Phase Model for aggregate interlocking in cracked concrete using numerical methods and experimental evidence**

---

#### **Bibliography**

- [1] Bujadham, B., Mishima, T., and Maekawa, K. (1992). Verification of the universal stress transfer model. *Proc. of JSCE*, 451/V-17:289–300.
- [2] Calvi, P. M., Bentz, E. C., and Collins, M. P. (2017). Pure Mechanics Crack Model for Shear Stress Transfer in Cracked Reinforced Concrete. *Structural Journal*, 114(2):545–554.
- [3] Cavagnis, F., Fernández Ruiz, M., and Muttoni, A. (2015). Shear failures in reinforced concrete members without transverse reinforcement: An analysis of the critical shear crack development on the basis of test results. *Engineering Structures*, 103:157–173.
- [4] Cavagnis, F., Fernández Ruiz, M., and Muttoni, A. (2017). An analysis of the shear-transfer actions in reinforced concrete members without transverse reinforcement based on refined experimental measurements. *Structural Concrete*, 19(1):49–64.
- [5] CEN (European Committee for Standardization) (1994). *EN 196-1. Methods of testing cement – Part 1: Determination of strength*. Brussels, Belgium.
- [6] Dei Poli, S., Gambarova, P., and Karakoç Cengiz (1987). Aggregate Interlock Role in R.C. Thin-Webbed Beams in Shear. *Journal of Structural Engineering*, 113(1):1–19.
- [7] Fenwick, R. C. and Pauley, T. (1968). Mechanism of Shear resistance of Concrete Beams. *Journal of the Structural Division*, 94(10):2325–2350.
- [8] Fernández Ruiz, M. and Muttoni, A. (2007). On Development of Suitable Stress Fields for Structural Concrete. *ACI Structural Journal*, 104(4):495–502.
- [9] fib (International Federation for Structural Concrete) (2013). *fib Model Code for Concrete structures 2010*. Ernst & Sohn, 402 p, Germany.
- [10] Fuller, W. B. and Thompson, S. E. (1907). The laws of proportioning concrete. *Transactions of the American Society of Civil Engineers*, LIX:67–143.
- [11] Gambarova P.G. and Karakoç C. (1983). A new approach to the analysis of the confinement role in regularly cracking concrete elements. *Transactions of the 7. international conference on structural mechanics in reactor technology*, H:251–261.
- [12] Guidotti, R. (2010). *Poinçonnement des planchers-dalles avec colonnes superposées fortement sollicitées*. Ph.D. Thesis, EPFL, Lausanne, Switzerland.
- [13] Hill, R. (1998). *The Mathematical Theory of Plasticity*. Clarendon Press.
- [14] Jacobsen, J. S. (2012). *Constitutive Mixed Mode Behavior of Cracks in Concrete: Experimental Investigations of Material Modeling*. Ph.D. Thesis, Technical University of Denmark, Kongens Lyngby Denmark.
- [15] Johnson, K. L. (1985). *Contact Mechanics*. Cambridge University Press, 451 p.

- 
- [16] Kalliomäki, I., Vehtari, A., and Lampinen, J. (2005). Shape analysis of concrete aggregates for statistical quality modeling. *Machine Vision and Applications*, 16(3):197–201.
- [17] Li, B., Maekawa, K., and Okamura, H. (1989). Contact density model for stress transfer across cracks in concrete. *Journal of the Faculty of Engineering, The University of Tokyo*, 40(1):9–52.
- [18] Muttoni, A. (1989). *Die Anwendbarkeit der Plastizitätstheorie in der Bemessung von Stahlbeton*. PhD thesis, ETH, Zurich, Switzerland.
- [19] Muttoni, A. and Fernández Ruiz, M. (2008). Shear Strength of Members without Transverse Reinforcement as Function of Critical Shear Crack Width. *ACI Structural Journal*, 105(2):163–172.
- [20] Muttoni, A., Fernández Ruiz, M., and Simões, J. T. (2018). The theoretical principles of the critical shear crack theory for punching shear failures and derivation of consistent closed-form design expressions. *Structural Concrete*, 19(1):174–190.
- [21] Nayak, P. R. (1971). Random Process Model of Rough Surfaces. *Journal of Lubrication Technology*, 93(3):398–407.
- [22] Nielsen, M. P. and Hoang, L. C. (2011). *Limit analysis and concrete plasticity*. CRC Press, 788 p., Boca Raton, Florida, 3rd ed edition.
- [23] Persson, B. N. J., Albohr, O., Tartaglino, U., Volokitin, A. I., and Tosatti, E. (2004). On the nature of surface roughness with application to contact mechanics, sealing, rubber friction and adhesion. *Journal of Physics: Condensed Matter*, 17(1):R1–R62. Publisher: IOP Publishing.
- [24] Pundir, M., Tirassa, M., Fernández Ruiz, M., Muttoni, A., and Anciaux, G. (2019). Review of fundamental assumptions of the Two-Phase model for aggregate interlocking in cracked concrete using numerical methods and experimental evidence. *Cement and Concrete Research*, 125:105855.
- [25] Richart, F. E., Brandtæg, A., and Brown, R. L. (1928). A study of the failure of concrete under combined compressive stresses. *University of Illinois. Engineering Experiment Station. Bulletin no. 185*.
- [26] Taylor, H. P. J. (1970). *Investigation of the Forces Carried Across Cracks in Reinforced Concrete Beams in Shear by Interlock of Aggregate*. Number 42.447 in Technical report (Cement and Concrete Association). London, United Kingdom.
- [27] Thomas, T. R. (1998). *Rough Surfaces*. Imperial College Press, 278 p, 2nd edition.
- [28] Tirassa, M., Fernández Ruiz, Miguel, and Muttoni, A. (2018). Modern experimental research techniques for a consistent understanding of aggregate interlocking. In *Proceedings of the 12th fib PhD Symposium in Civil Engineering*, pages 723–730, Prague, Czech Republic.

### **Chapter 3. Review of fundamental assumptions of the Two-Phase Model for aggregate interlocking in cracked concrete using numerical methods and experimental evidence**

---

- [29] Ulaga, T. (2003). *Betonbauteile mit Stab-und Lamellenbewehrung: Verbund-und Zuggliedmodellierung*. Ph.D. Thesis, ETH Zurich, Switzerland.
- [30] Vecchio, F. J. and Collins, M. P. (1986). The modified compression-field theory for reinforced concrete elements subjected to shear. *ACI Journal*, 83(2):219–231.
- [31] VSS Swiss Association of Road and Transportation Experts (2005). *SN670115 - Gesteinskörnungen: Qualitative und quantitative Mineralogie und Petrographie*. Zurich, Switzerland.
- [32] Walraven, J. C. (1981). Fundamental Analysis of Aggregate Interlock. *ASCE Journal of the Structural Division*, 107(11):2245–2270.
- [33] Wriggers, P. (2006). *Computational contact mechanics*. Springer, 518 p, Berlin-New York.
- [34] Yastrebov, V. A., Anciaux, G., and Molinari, J.-F. (2015). From infinitesimal to full contact between rough surfaces: Evolution of the contact area. *International Journal of Solids and Structures*, 52:83–102.

## 4 Influence of cracking and rough surface properties on the transfer of forces in cracked concrete

This chapter consists in a scientific article focusing on the force transfer in concrete cracks subjected to Mixed-Mode kinematics. The evidence of a number of tests is analysed and used as a basis for the development of a mechanically-based model accounting for the crack surface roughness. The article was accepted for publication as follows [37]:

Tirassa M., Fernández Ruiz M., Muttoni A. (2020, in press). Influence of cracking and rough surface properties on the transfer of forces in cracked concrete. *Engineering Structures*.

Max Tirassa planned and carried out the experimental campaign, analysed the obtained data and implemented the presented model under the supervision of the second and third authors.

### **Abstract**

Aggregate interlocking is acknowledged as one of the most significant actions transferring shear forces in cracked concrete structures and has been investigated for several decades. Despite the many experimental programmes and previous efforts to develop models based on mechanical approaches, a number of instrumental issues of the phenomenon are still not fully understood. For example, most researches have focused on the capacity to transfer forces through a given crack surface. However, the development of secondary cracks developing from the initial crack due to stress concentrations has traditionally been disregarded, despite the fact that these secondary cracks are governing in many cases for the overall strength. Also, other important aspects have not been comprehensively investigated, such as the contribution of the residual strength of concrete both in tension and shear during crack development. In

this paper, the results of an experimental programme aimed at the fundamental understanding of the transfer of forces in cracked concrete is presented. This programme comprises detailed measurements of the surface roughness after failure. On that basis, a model considering both the crack surface properties and those of the concrete material is presented, accounting also for the potential development of secondary cracking. The model estimates the transferred forces by considering surface patches in contact and the contribution of the residual strength of the fracture process zone. The results of the model are compared to the test results showing consistent agreement both in terms of failure mode and the capacity to transfer forces as a function of crack opening and sliding.

**Keywords:** concrete cracks; shear transfer; aggregate interlocking; secondary cracking; crack surface roughness; Mixed-Mode fracture; residual tensile strength; mechanical modelling

### 4.1 Introduction

Concrete is a widely used construction material with high compressive strength but associated with a low strength and rather brittle response in tension. Reinforcement is normally arranged to control crack opening and to ensure a suitable transfer of tensile forces in a reliable manner. However, in many design situations, the structural resistance is controlled by the capacity of cracked concrete to transfer stresses without the assistance of any reinforcement. This is for instance the case of beams and slabs without transverse reinforcement subjected to shear. For these members, cracks typically develop in bending and propagate through the web leading to the development of a critical shear crack, potentially disturbing the theoretical compression strut carrying the load to the support (Figure 4.1a) or other alternative load-carrying actions [4–6]. The kinematics of the critical shear crack (governing the local opening and sliding of crack lips) is associated with the location of the centre of rotation (R in Figure 4.1b) near its tip [23]. At every point, the crack opens in the normal direction ( $w$ , see Figure 4.1b, corresponding to Mode I opening, see also Figure 4.2a) and can slide parallel to the crack direction ( $\delta$ , see Figure 4.1b, corresponding to Mode II sliding, Figure 4.2b). In general [4, 5, 7], the crack opens first in Mode I (as the centre of rotation is located near to the investigated point), but later progresses in Mixed-Mode I+II when the crack develops in a curved manner and the centre of rotation shifts its location (even originating a secondary crack from the flexural one, potentially becoming the critical shear crack [4], see Figure 4.1c). Figure 4.2c depicts a typical case following this kinematics, with an initial crack opening  $w_0$  in Mode I followed by a Mixed-Mode opening with constant angle  $\alpha$ .

Due to the possible presence of a Mode II component and accounting for the rough nature of concrete crack surfaces, protruding material (typically aggregates) on one side of the crack can engage contact with the opposite side. This allows for a transfer of interface forces through the crack, a phenomenon commonly named as *aggregate interlocking*. These forces are considered to play a major role in the overall transfer of shear [5, 28, 35], and their calculation can be instrumental for estimating the shear resistance of beams [4–6]. Similarly to beams in shear,

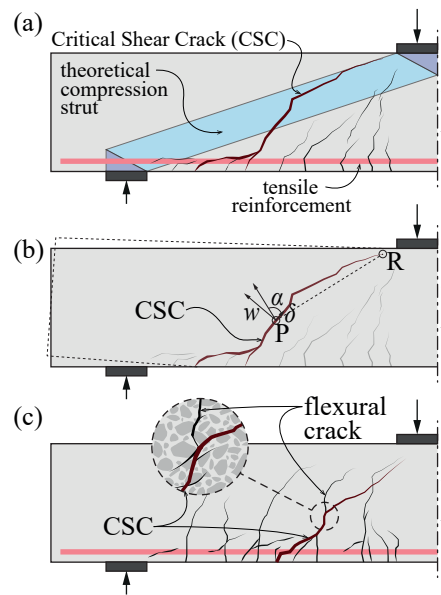


Figure 4.1 – Crack pattern and kinematics for a beam without transverse reinforcement failing in shear: (a) location of critical shear crack and theoretical strut carrying shear; (b) kinematics at a point of the critical shear crack; and (c) beam failing in shear due to development of secondary crack (adapted from [4])

aggregate interlocking is also considered to potentially contribute to the transfer of forces in the case of punching of flat-slabs and footings [24], through rough construction interfaces [32] and has similarities with the shearing of rock surfaces [12].

#### 4.1.1 Scales of roughness

Roughness of crack surfaces plays a major role in the capacity to transfer shear stress across the crack. For the purposes of this article, the following levels of roughness (similar to those introduced in [43]) will be defined:

- *Macro-roughness* is considered to be defined by the global crack geometry, which depends on the behaviour of a full-scale structure, as for example the shear crack shown in Figure 4.1. These cracks are typically not straight, but bi-linear or curved [7], engaging different ratios of opening and sliding along their length.
- *Meso-roughness* is assumed to be related to the material constituents. The typical length to investigate the meso-roughness is comparable to the size of the maximum aggregates ( $D_{\max}$ ). Many testing programmes related to this scale can be found in [13, 19, 21, 27, 28, 35, 41].
- *Micro-roughness* is defined at the scale of the concrete matrix, with an associated length typically between 1/10 and 1/100 of  $D_{\max}$  [19, 21]. It shall be noted that, due to the

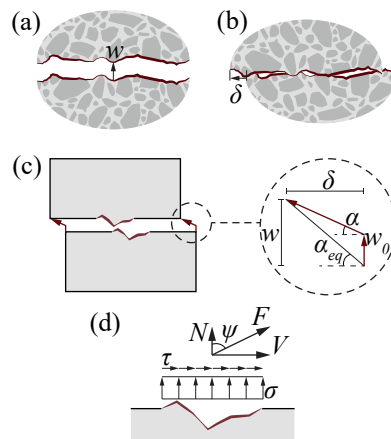


Figure 4.2 – Crack kinematics: (a) Mode I; (b) Mode II; (c) specimen subjected to Mode I followed by Mixed-Mode I+II; and (d) definition of positive stresses and internal forces

fractal nature of concrete surfaces [18], these patches are not planar, but also are rough surfaces.

#### 4.1.2 Experimental investigations

Test programmes on aggregate interlock have traditionally focused on concrete specimens pre-cracked by transverse splitting to induce a single (meso-scale) crack [21, 40]. The transfer of forces associated with this crack is thereafter investigated under combined shear and normal forces [21, 28, 35, 41]. In most cases, the dilatancy occurring when rough surfaces are subjected to Mode II kinematics is restraint by means of confinement normal to the crack plane. In early experiments, this confinement was provided with reinforcement which produced a constant normal force at yielding or by adapting the Mode I opening ( $w$ ) at every load-step.

More recently, testing devices capable of applying loads in two directions and to control the crack kinematics have been developed [13, 27]. These more sophisticated testing equipments also allow pre-cracking the specimens in Mode I as a first load-step (rather than by transverse splitting before testing), and to control the kinematics accurately using multiple jacks in a closed-controlled loop [19]. Typical experimental results have allowed establishing a number of observations showing the influence of several parameters (as crack kinematics, level of crack opening, concrete strength and cracked surface properties) on the capacity to transfer shear forces. With respect to the development of cracking, a number of cases have been observed during experimental programmes reported in the literature. We can classify the different cases in three main categories described in the following.

1. Cracks initiate in Mode I [14] and, for this reason, specimens are often pre-cracked in tension before applying Mixed-Mode kinematics [19, 27, 40]. This first crack will be referred to in the following as the Primary Crack. Once this initial crack is subjected to kinematics with a Mode II component, shear and normal forces develop. When failure

occurs by sliding of this crack, it will be named in the following as an aggregate interlock failure by *Primary Cracking* (PC), see Figure 4.3b.

2. Often, local stress concentrations generate additional *secondary cracks* of varying size, which develop diagonally at an angle of approximately  $45^\circ$  from the primary crack and mostly open in Mode I [13, 19, 27]. Such cracks can remain stable and have limited influence on the overall behaviour, a case which will be named in the following as *Non-Dominant Secondary Cracking* (NDSC), see Figure 4.3b.
3. Under some circumstances, the opening and growth of secondary cracks can progress, and, depending on the specimen geometry and its boundary conditions, this process can lead to a sudden failure [19, 44] due to the uncontrolled development of a secondary crack. This latter case will be named as *Dominant Secondary Cracking* (DSC) in the following (see Figure 4.3b).

It shall be noted that in some tests of the literature, the dominant secondary crack develops not from the primary crack, but from a notch of the specimen. Such results are considered to be influenced by the boundary conditions and potentially not representative of the phenomenon itself. Such tests will be marked in the following as DSC\*.

Different load-displacement curves and strengths are associated with the previously described cracking patterns and failure modes [38], as can be seen in Figure 4.3c for some representative tests of the research programme presented later in this paper (see also Figure 4.8b-e). For PC-tests, the shear forces increase gradually, reach a maximum value and eventually have a softening phase. Tests with NDSC have a similar response, but are typically subjected to higher scatter. Finally, DSC-tests tend to reach higher peak forces and are characterized by a sudden drop in the load when the secondary crack develops in an unstable manner (Figure 4.3c).

In the literature, DSC-tests are often disregarded and considered as non-representative experiments, since most works focus on the response of the PC. However, investigations consistently report the development of secondary cracks at meso-scale [13, 19, 27, 35] as well as at macro-scale in tests on structural members [4–6]. The practical significance of DSC is for instance shown in Figure 4.1c, where a beam without stirrups failing by propagation of a critical shear crack is presented. According to the experimental measurements of Cavagnis et al. [4], such cracks can develop from a flexural one due to the local development of high contact stresses (associated with a large mechanical engagement between crack lips [4]). In addition, the development of DSC is consistent with the generation of secondary cracking in shear for members with transverse reinforcement. The development of such cracks (normally at flatter angles than flexural ones) is instrumental in so-called rotating crack models for the design of members with transverse reinforcement. These practical cases highlight the necessity of adopting general models for aggregate interlocking accounting for potential failures in DSC.

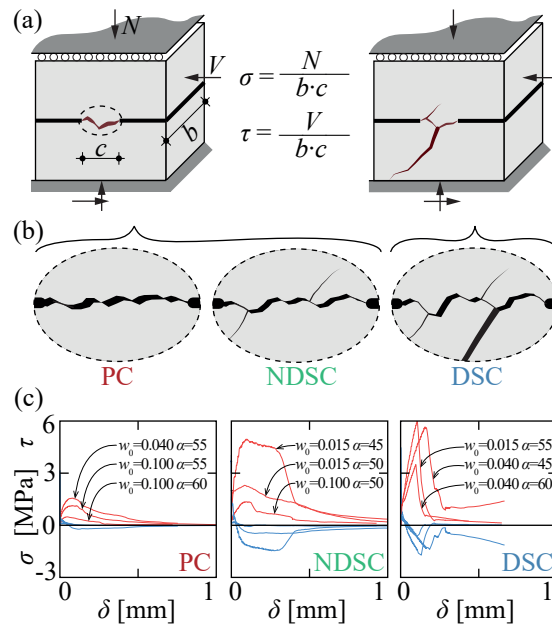


Figure 4.3 – Failure types due to aggregate-interlock engagement (see Section 4.2 for further information on the tests corresponding to the load-displacement curves): (a) meso-scale specimen and applied loads; (b) details of cracking area for various failure modes; and (c) load-sliding curves for tests with different failure modes (for definitions of  $w_0$  and  $\alpha$ , see Figure 4.2)

### 4.1.3 Theoretical approaches

With respect to aggregate interlock considered at the meso-scale, several models based on mechanical approaches can be found in the literature [2, 3, 8, 19]. Two of the most representative ones are the Two-Phase Model by Walraven [40, 41] and the Contact Density Model by Li and Maekawa [21], whose principles will be discussed in this paper, and whose implementation details are summarized in Appendix A and Appendix B.

### 4.1.4 Aims of the present work

Within this frame, this paper is aimed at addressing a number of open questions with respect to the transfer of forces by aggregate interlocking:

- Role of surface roughness on the transfer of forces via aggregate interlock
- Contribution of residual strength in fracture process zones to the transfer of shear and normal forces
- Development of different failure modes (PC, NDSC, DSC) as a function of roughness, material and kinematic parameters

This article presents the results of an experimental programme performed using a test set-up

capable of pre-cracking double-notched concrete specimens in tension and then applying a given Mixed-Mode kinematics. Various types of concrete were investigated as well as different crack kinematics (with varying initial crack openings and opening-to-sliding ratios). Special attention is paid to the final crack surfaces, which were measured using a digital microscope. The results are eventually used to derive a model for the transfer of forces, taking into account the varying surface roughness of the primary crack and the material residual resistance in the fracture process zone.

## 4.2 Experimental programme

### 4.2.1 Test set-up

The test set-up consisted of a high-precision Zwick electromechanical machine (acting in vertical direction) modified by addition of a hydraulic jack in the horizontal direction to apply displacements in two perpendicular directions on double-notched concrete specimens (Figure 4.4). The specimens were glued on steel plates as shown in Figure 4.4b. Following this procedure, it was possible to pre-crack the specimens up to an initial crack opening  $w_0$  by performing a Mode I tension test in the vertical direction. Once the selected crack opening was reached, the initial Mode I phase ended and the specimens were subjected to Mixed-Mode with an imposed angle  $\alpha = \arctan(\Delta w / \Delta \delta)$ . To that aim, the horizontal jack applied shear displacements which resulted in sliding  $\delta$  at the crack interface, while the vertical jack allowed additional increases of  $w$  to follow the desired kinematics. During testing, the lower specimen half was fixed, while the upper part could move thanks to low-friction linear roller guides. The crack opening and sliding were measured using a custom-made arrangement consisting of strain gauges calibrated using LVDTs for that purpose. Such device allowed for independent measurements of vertical and horizontal displacements. The displacement-control device is further described in [38].

The initial displacement rate of 0.1  $\mu\text{m/s}$  was selected so that for a typical test resulting in PC, the initial Mode I part lasted 5-15 minutes depending on the value of  $w_0$  (tensile strength was reached after about five minutes), while the Mixed-Mode phase lasted about an hour to reach the maximum shear force. After the peak was reached, the displacement rate was progressively increased until the test finished when the forces were very low or the maximum stroke was reached (approximately 3 mm). Apart from the recordings from the load cells and the displacement-measuring devices, most tests were additionally monitored using Digital Image Correlation.

### 4.2.2 Specimens

The test specimens were produced from several concrete prismatic specimens that were cast and cured under sealed conditions for at least 28 days. They were then demoulded and cut into slices of thickness  $b$  (nominal thickness equal to 50 mm) using a circular saw

## Chapter 4. Influence of cracking and rough surface properties on the transfer of forces in cracked concrete

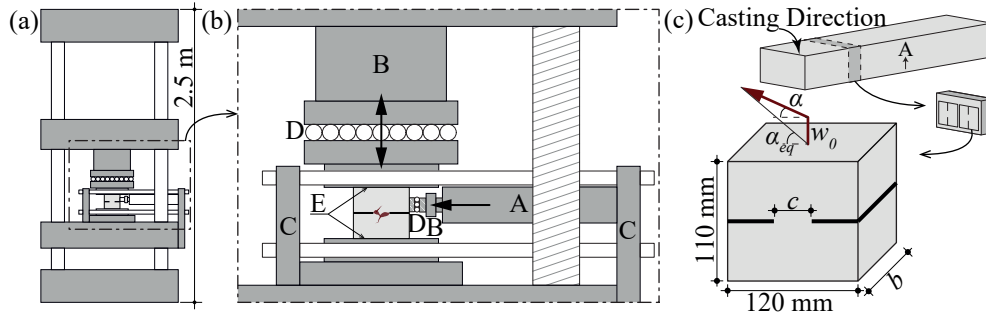


Figure 4.4 – Test set-up: (a) front view; (b) detail of front-view: A-horizontal jack; B-load cells; C-steel holding plates; D-sliding roller guides; E-glueing planes; and (c) production process, typical specimen and applied kinematics

Table 4.1 – Mix designs for the concrete castings

	Casting #		
	02 & 03	04 & 05	07
$D_{\max}$ [mm]	16	8	8
Water [ $\text{kg}/\text{m}^3$ ]	172	204	177
Cement [ $\text{kg}/\text{m}^3$ ]	310	316	321
Cement Type	CEMII	CEMII	CEMII
Aggregates [ $\text{kg}/\text{m}^3$ ]	A-LL42.5R	A-LL42.5N (white)	A-LL 42.5N
	1955	1809	1853
Petrography of aggregates	Hard gravel, Rhone valley, Riddes (CH), limestone, granitoids, sandstone, quartzite	Medium-Hard gravel, Quarry in Villeneuve (CH), ~95% limestone	Medium-Hard gravel, Pit in Savigny (CH), ~85% limestone
$f_{c,28}$ [MPa]	32.8 30.6	29.8 25.7 24.7	30.1 37.1 28.9

(see process in Figure 4.4c). Two specimens with notches of varying length were obtained from each slice with a water-jet cutting machine. The orientation of the specimens was selected in order to minimize the influence of the casting direction (Mode I pre-cracking direction was perpendicular to the casting direction, thus reducing the influence on the tensile strength of weak interfacial transition zones between aggregates and cement matrix due to bleeding [10, 16]). The final shape of the specimens is shown in Figure 4.4c, where the width of the crack plane between the notches is indicated as parameter  $c$ . Three different concrete castings were prepared with the mix designs reported in Table 4.1. The granulometric curves for the different mixes are additionally presented in Figure 4.5. The exact geometry of the specimens and compressive strength of concrete at the day of testing ( $f_c$ ) is reported in Table 4.2, where the first two digits of the specimen numbers indicate the corresponding casting batch.

## 4.2. Experimental programme

Table 4.2 – Dimensions of tested specimens, crack kinematics, compressive concrete strength and failure mode (the first two digits of the specimen number indicate the casting, the middle digits the slice number, see Table 4.1 for  $D_{\max}$  and other information; PC: failure by primary cracking; NDSC: failure with non-dominant secondary cracking; DSC: failure by dominant secondary cracking starting at primary crack; DSC\*: failure by secondary cracking originating at notches)

#	$b$ [mm]	$c$ [mm]	$w_0$ [mm]	$\alpha$ [°]	$f_c$ [MPa]	Failure
021501	51	18.0	0.040	40	38	DSC*
021601	51	19.0	0.025	45	38	NDSC
022002	51	19.0	0.015	45	38	NDSC
022101	51	19.0	0.100	40	39	DSC
022102	51	24.0	0.040	45	39	NDSC
030101	52	26.5	0.100	60	39	DSC
030201	51	20.5	0.040	45	39	DSC
030802	51	23.5	0.100	55	39	PC
030901	50	25.0	0.100	60	39	PC
040501	50	24.0	0.015	50	29	NDSC
040601	51	33.5	0.020	50	29	NDSC
050101	50	23.5	0.100	45	32	DSC
050102	50	18.5	0.025	50	32	NDSC
050202	50	18.5	0.015	45	32	DSC*
050301	51	23.5	0.040	55	32	PC
050302	51	19.0	0.025	45	32	NDSC
050401	50	22.5	0.040	50	32	NDSC
050801	51	23.5	0.100	50	32	NDSC
050802	51	18.5	0.015	55	32	DSC
050902	51	18.5	0.015	50	32	NDSC
070101	52	18.5	0.040	60	47	PC
070302	50	19.0	0.015	55	47	DSC
070501	51	26.5	0.040	60	47	DSC
070601	50	24.0	0.100	50	47	NDSC
070902	50	17.0	0.015	55	48	PC
071401	51	19.5	0.015	50	48	PC

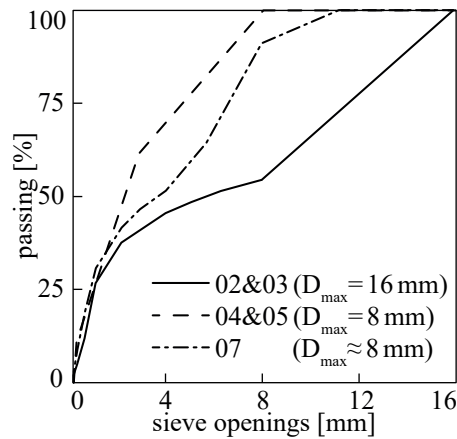


Figure 4.5 – Granulometric curves for the concrete castings

### 4.2.3 Test results

Figure 4.6 presents a summary of the maximum measured strengths as a function of the angle at failure accounting for the initial crack opening ( $\alpha_{eq}$ , see Figure 4.4c). This figure also includes tests from the literature for comparison purposes [19]. Further details of the specimens are given in Table 4.2 and the complete shear and normal curves recorded for all specimens are reported in Appendix C.

As shown in Figure 4.6, tests develop higher forces for kinematics with a larger Mode II component (corresponding to values of  $\alpha_{eq} < 60^\circ$ ). The tests of current research tend to fail in DSC or NDSC while for higher values ( $\alpha_{eq} > 65^\circ$ ), PC was dominating. Although the applied kinematics influence the failure mode, they are insufficient to entirely explain it. As discussed in the following section, the surface roughness of the initial crack and its distribution represent additional instrumental parameters governing the crack development. Nevertheless, the use of  $\alpha_{eq}$  as a parameter results in a clear trend even though the initial crack opening  $w_0$  can vary significantly. Moreover, it can be seen that tests with PC and NDSC behave similarly, while specimens with DSC diverge significantly from them and are associated with higher interlocking forces.

An aspect extensively discussed by previous researchers is the relationship between the tangential and the normal force developing under given kinematics [21, 40], expressed using the angle  $\psi$  hereafter ( $\tan \psi = \tau/|\sigma|$ , see Figure 4.2d). Figure 4.7a illustrates a typical response for this parameter. The plot shows the measured values of  $\tau$  and  $\sigma$  and the corresponding values of  $\psi$  as a function of the recorded sliding  $\delta$ . It can be noted that after the initial Mode I phase ( $\delta = 0$ , Figure 4.7b), some residual tensile strength is still present between the notches, resulting in values  $\sigma > 0$ . At this moment, shear displacements are applied ( $\delta > 0$ ), leading to an active engagement of the cracked surfaces. This results in a rapid increase in the shear stress  $\tau$  but also in the development of additional compressive normal stresses ( $\sigma$ ) related to aggregate interlocking to avoid crack dilatation above the limits set by the kinematics (angle

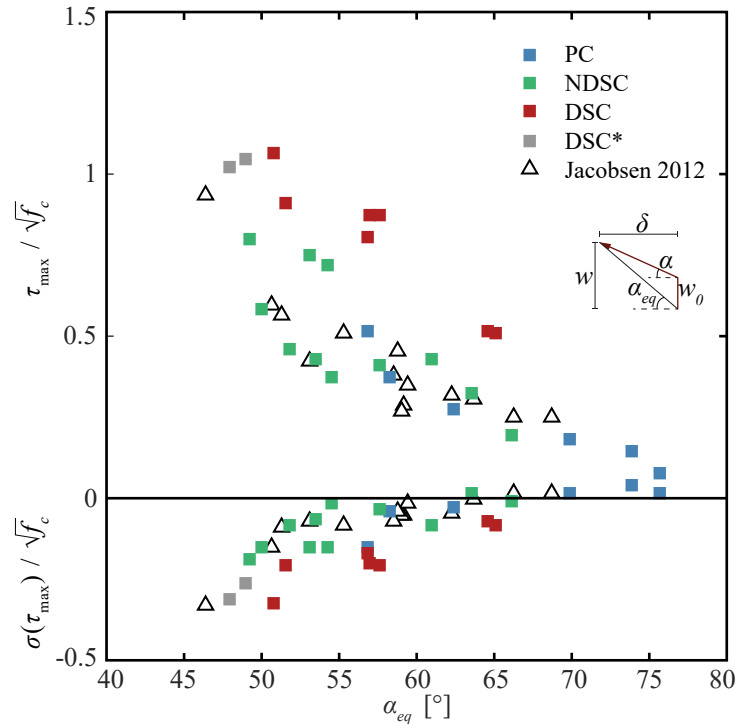


Figure 4.6 – Peak values at instant  $\tau = \tau_{\max}$  as a function of  $\alpha_{eq}(= \arctan(w(\tau_{\max})/\delta(\tau_{\max})))$  (including tests from [19, 42])

$\alpha$ ). The value  $\psi_{\max}$  is reached consequently when  $\sigma$  becomes zero (Figure 4.7c). Thereafter, both  $\tau$  and  $|\sigma|$  continue to increase (Figure 4.7d), but the normal forces tend to become more significant as the sliding increases (resulting into progressively decreasing values of  $\psi$ ). This behaviour occurred for all tests, showing the significance of crack dilatation and of the associated normal forces. As a result, the rate of decrease in  $\psi$  after its peak value depends on the externally applied kinematics, with lower values of  $\alpha_{eq}$  (associated with higher values of  $\sigma$ ) leading to lower values of  $\psi$ . This trend can be observed in Figure 4.8, where the values of  $\psi$  are reported at the instant  $\tau_{\max}$  for all tests as a function of the applied kinematics. This response is in addition confirmed by the results of pure Mode II tests (performed by Li et al. [21]) corresponding to low values of  $\alpha_{eq}$  and resulting in values  $\tau \approx \sigma$  ( $\psi$  close to  $45^\circ$ ).

#### 4.2.4 Surface roughness

As previously highlighted by a number of studies [19, 21], the crack geometry and the crack surface are important parameters governing the forces transferred through aggregate interlocking. For the present investigation, the specimen surfaces were scanned after failure using a Keyence VHX 5000 digital microscope with VH-Z100R lens at 100X magnification. This allowed for the detailed recording of the surface geometry, with a data-point approximately every  $2 \mu\text{m}$  (Figure 4.9b). The surface was approximated as a series of profiles defined as parallel to the shearing direction (Figure 4.9c, thus assuming the direction perpendicular to loading can be

**Chapter 4. Influence of cracking and rough surface properties on the transfer of forces in cracked concrete**

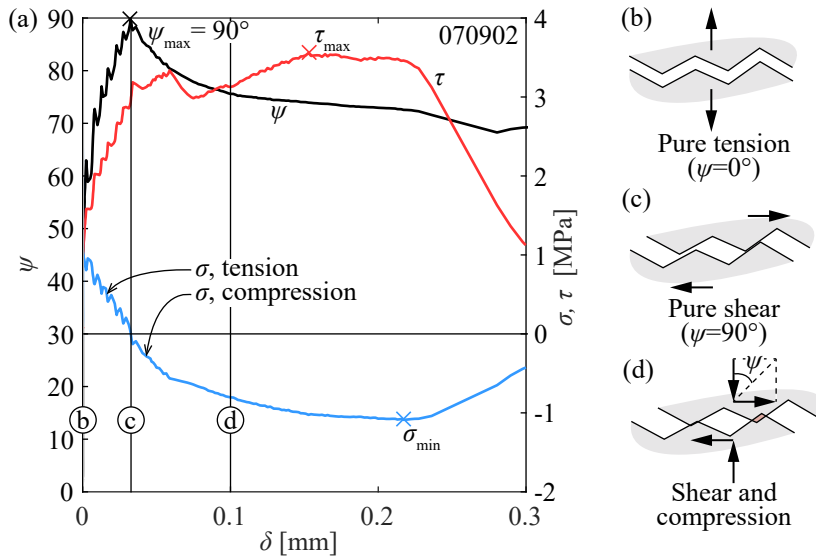


Figure 4.7 – Activation of interlocking forces for test 070902: (a) evolution of  $\psi$ ; (b) forces acting on crack after Mode I phase; (c) progressive activation of  $\tau$ , while  $\sigma$  goes to zero; and (d) increasing normal forces to control crack dilatation

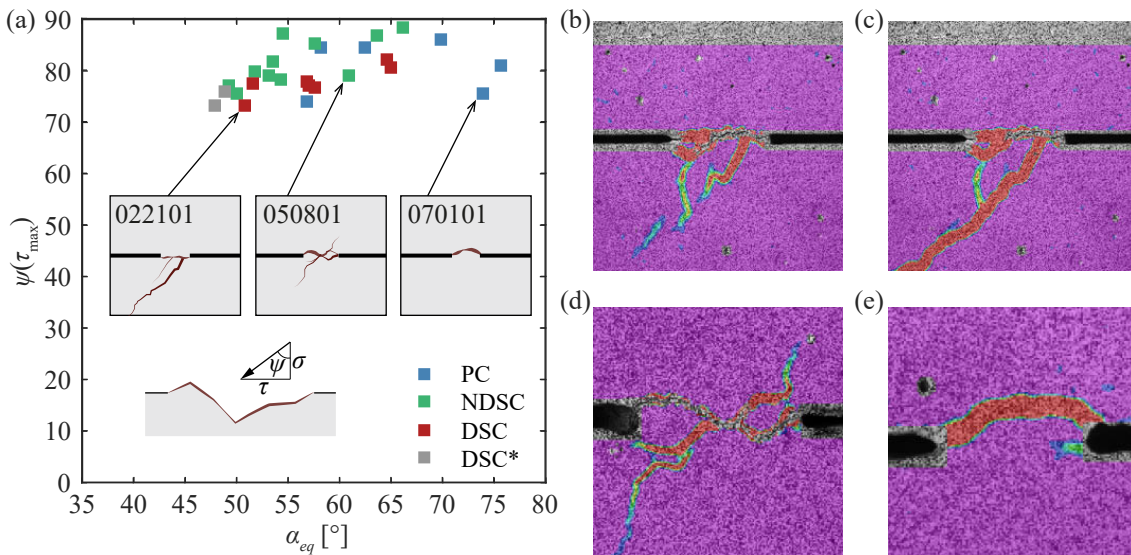


Figure 4.8 – (a) Value of  $\psi$  at  $\tau = \tau_{max}$  for all tests; (b) DIC-image for test 022101 (DSC) shortly prior to peak shear stress; (c) DIC-image for test 022101 after peak and propagation of secondary crack; (d) DIC-image for test 050801 (NDSC) at peak shear stress; and (e) DIC-image for test 070101 (PC) at peak shear stress (for tests with NDSC and PC the cracking pattern did not change significantly after the peak)

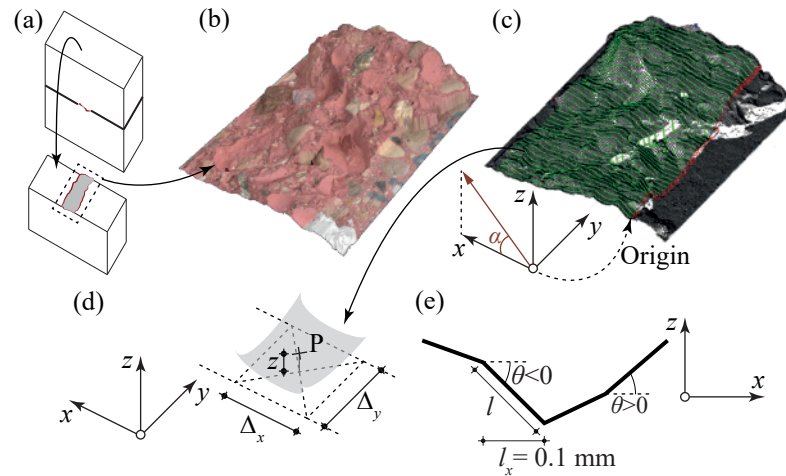


Figure 4.9 – Example of crack surface (specimen 070501): (a) Scan of upper half of tested specimen; (b) Scanned surface; (c) Extraction of profiles (green); (d) For every profile-point P,  $z$ -coordinates are averaged in the surrounding area  $\Delta_x\Delta_y$ ; and (e) profile and parameters for calculation of roughness index

neglected). These sections were spaced 1 mm from each other in the  $y$ -direction, while the  $x$ -coordinate was assigned every 0.1 mm. For each point, the corresponding  $z$ -coordinate was calculated as the average value in a zone of size  $\Delta_x$  and  $\Delta_y$ , both equal to 0.1 mm (Figure 4.9d-e). The inclination  $\theta$  of each micro-segment with respect to the horizontal was calculated on this basis.

The roughness of the crack surfaces at the considered scale can be characterized in several manners:

1. The relative distribution of profile-segments as a function of their steepness  $\sum_{\Delta\theta} l / \sum l_x$ , where  $\Delta\theta$  specifies the considered interval of angles. The average relative occurrence of segments inclined within intervals of  $\Delta\theta = 10^\circ$  is reported in Figure 4.10. It can be noted that surfaces corresponding to DSC have a higher percentage of steep segments in the range  $50^\circ < \theta < 90^\circ$ . As shown in Figure 4.10b, such segments are the most likely to engage contact for the kinematic ranges investigated in this research ( $40^\circ < \alpha < 60^\circ$ ). Differently, segments with negative or rather small values of  $\theta$  (Figure 4.10c-d) are less likely to engage in contact with the opposite crack side. With respect to surfaces of tests resulting in NDSC and PC, they are observed to have relatively few steep segments, which explains why they result in weaker forces and limited secondary crack propagation.
2. The profile roughness index  $R_p$  (called  $A_t$  in [21]), defined as:

$$R_p = \frac{\sum l}{\sum l_x} \quad (4.1)$$

where  $l$  is the length of a segment and  $l_x$  its projection with respect to the horizontal (Figure 4.9e). Values  $R_p$  close to 1.00 indicate rather flat cracks while higher values of  $R_p$

## Chapter 4. Influence of cracking and rough surface properties on the transfer of forces in cracked concrete

---

(recorded up to approximately 1.30) indicate rougher surfaces. The calculated values are reported in Table 4.3.

3. Similarly to  $R_p$ , the surface roughness index  $R_s$  compares the horizontal projection of the crack surface  $\Sigma A_0$  with the crack surface  $\Sigma A_i$  (Figure 4.12b):

$$R_s = \frac{\Sigma A_i}{\Sigma A_0} \quad (4.2)$$

The term  $\Sigma A_i$  is calculated by considering the surface as a grid of data points identifying a series of triangles whose areas are summed. The roughness area index depends on the selected grid spacing and increases for smaller spacings [20]. To allow for a reliable comparison of the measured values, several authors set the distance between two data-points as equal to 0.25 mm [17, 29]. In [17], the following relation between compressive strength and  $R_s$  was proposed:

$$R_s = \frac{2}{f_c^{1/8}} \quad (4.3)$$

where  $f_c$  is expressed in [MPa]. Figure 4.11 compares Equation (4.3) with the  $R_s$  values for surfaces from the literature and the scans from the present experimental programme, classified according to the failure mode. Considering the variability of concrete, this comparison shows a relatively good match between Equation 4.3 and the test results presented in this paper, which are, however, subjected to some level of scatter. This can be explained by the fact that the tested surfaces were relatively small and thus subjected to greater variability compared to the more average estimate of Equation 4.3. The figure confirms in any case that simplified approaches for estimating the concrete roughness only based on the maximum aggregate size  $D_{\max}$  [6, 9, 23] should be improved by also accounting for the influence of the concrete strength.

4. The absolute value  $\Delta_{z,\max} = z_{\max} - z_{\min}$  (top and bottom points of the surface, see Figure 4.9).

The calculated values for the investigated surfaces of the various indexes are reported in Table 4.3 and summarized in Figure 4.12. From the various indexes and values (see Figure 4.12), the following observations can be made:

- Consistent agreement is found between  $R_p$ ,  $R_s$  and  $\Delta_{z,\max}$ . PC corresponds to the lowest values of these indexes, that increase consistently for NDSC and DSC.
- Larger aggregate sizes correspond to higher roughness indexes.
- A limited percentage of steep segments (related to higher values of  $R_p$  and  $R_s$ ) seems sufficient to develop high contact forces and usually leads to DSC failures (particularly for values of  $R_p$  above 1.15)

Table 4.3 – Measured values of various roughness indicators

#	Failure	$R_p$ [-]	$R_s$ [-]	$\Delta_{z,max}$ [mm]
021501	DSC*	1.21	1.35	9.65
021601	NDSC	1.20	1.25	7.50
022002	NDSC	1.21	1.34	7.60
022101	DSC	1.25	1.43	10.61
022102	NDSC	1.18	1.30	9.19
030101	DSC	1.29	1.43	9.35
030201	DSC	1.18	1.25	8.06
030802	PC	1.16	1.25	8.74
030901	PC	1.14	1.21	7.00
040501	NDSC	1.13	1.27	5.88
040601	NDSC	1.16	1.26	7.79
050101	DSC	1.25	1.39	10.37
050102	NDSC	1.16	1.27	8.43
050202	DSC*	1.16	1.24	7.74
050301	PC	1.15	1.22	7.37
050302	NDSC	1.15	1.22	6.61
050401	NDSC	1.15	1.23	8.77
050801	NDSC	1.14	1.21	7.52
050802	DSC	1.32	1.40	8.30
050902	NDSC	1.18	1.31	6.80
070101	PC	1.11	1.18	8.67
070302	DSC	1.22	1.32	9.16
070501	DSC	1.16	1.26	8.98
070601	NDSC	1.12	1.19	6.62
070902	PC	1.15	1.21	5.27
071401	PC	1.10	1.15	6.54

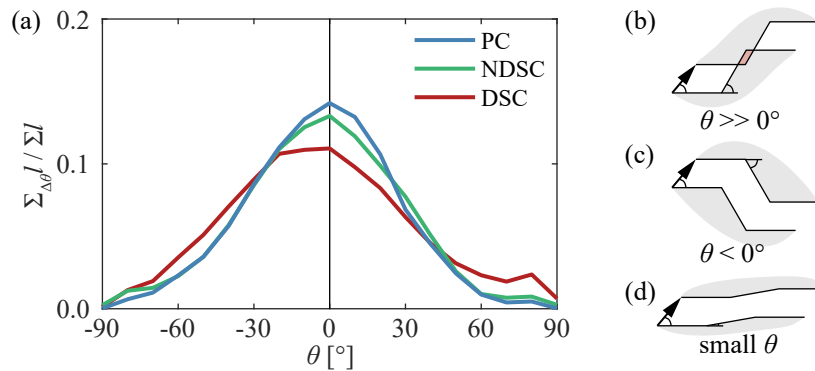


Figure 4.10 – Influence of angles  $\theta$  (a) Average distributions, classified by failure mode; (b) segment with large  $\theta$  (in contact); (c) segment with  $\theta < 0^\circ$  (no contact); and (d) segment with small  $\theta$  (no contact)

**Chapter 4. Influence of cracking and rough surface properties on the transfer of forces in cracked concrete**

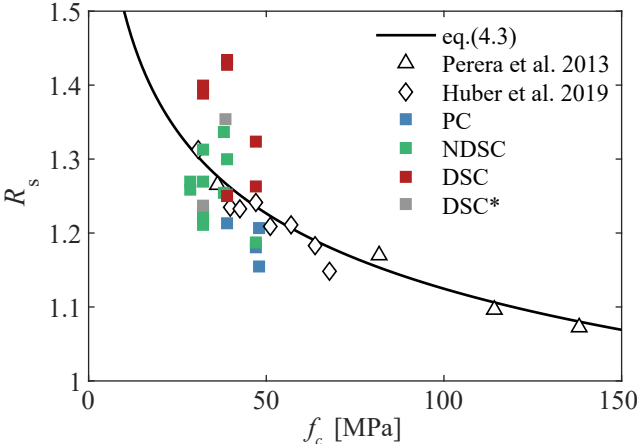


Figure 4.11 – Comparison of measured  $R_s$  values with equation (4.3) and tests from the literature [17, 29]

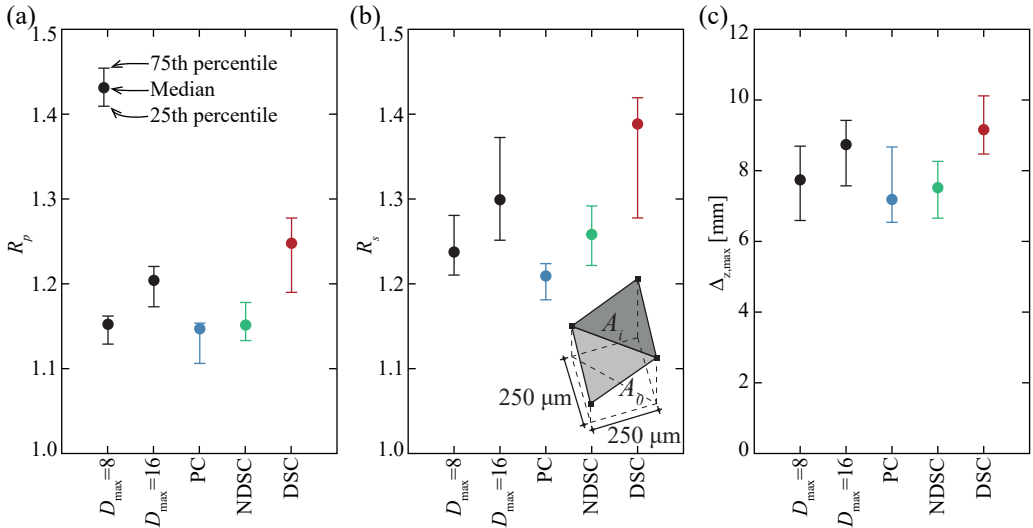


Figure 4.12 – Distribution of various roughness indicators: (a)  $R_p$ ; (b)  $R_s$ ; and (c)  $\Delta_{z,max}$

## 4.3 Consistent modelling of transfer of forces through cracked concrete

The modelling approaches for aggregate interlock proposed by Walraven [40] (see Appendix A) and Li et al. [21] (see Appendix B) focus on the transfer of forces due to interface contacts and provide good estimates for tests resulting in PC and NDSC. However, they are not addressed at cases governed by DSC, which are observed in some full scale structures like concrete beams without transversal reinforcement failing in shear [4]. Moreover, since they were mostly calibrated on specimens pre-cracked by splitting, and with limited control over the initial crack opening, these models do not account for the potential of cracked concrete to transfer tensile and shear stresses due to residual material tensile resistance and soundness. This residual tensile strength of concrete cracks is observed in Mode I tests [36], and the phenomenon is also considered in models for shear transfer in beams [6] and punching of slabs [34]. Hillerborg [14] explained the residual tensile strength of concrete for small deformations by introducing the concept of the *fracture process zone*. Such zones are characterized by localized, but not fully developed, cracking, and possess the capacity to transfer forces due to the material bridging the discontinuity. This effect is actually not negligible in the local transfer of forces at a crack and shall also be accounted for to formulate a more comprehensive approach to the phenomenon.

The model presented hereafter is grounded on the approach of Li et al. [21] with respect to the consideration of contacts between crack lips, but accounts also for the residual material strength of cracks which are not fully developed. Such an approach is applicable to cases with monotonic loading resulting in PC, NDSC and DSC, as will be shown through a comparison with the experiments, and suitably reproduces the complete load-displacement response of the specimens, including their softening branch.

### 4.3.1 Model outline

The surface roughness is used as an input parameter using the parallel profiles obtained from the final failure surface as described in Section 4.2.4 (or any analytical function for it). The contact state is calculated at each point as a function of the profile-geometry and the externally applied kinematics. In particular, the local effective penetration  $p$  is determined for each segment and load-step (see Section 4.3.2). Two cases can result:

1. The segment is penetrating material on the opposite crack-side. The procedure outlined in Section 4.3.3 is applied to determine the contact forces.
2. The segment is separated from the opposite crack-side, but can still transfer forces due to the residual soundness of the fracture process zone. The procedure outlined in Section 4.3.4 is thus applied.

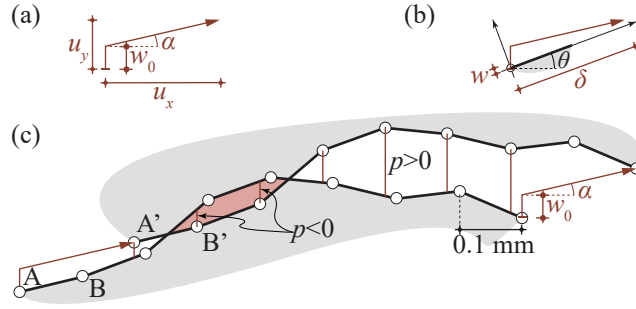


Figure 4.13 – Calculation of contact properties: (a) projection of kinematics on global coordinate system; (b) projection of kinematics on local coordinate system corresponding to a segment; and (c) procedure to calculate  $p$

### 4.3.2 Contact events

In order to determine the occurrence of a contact, the model considers that the segments at each side of a crack behave as solid (undeformable) bodies. A 2D analysis will be performed, considering  $x$  as the horizontal axis and  $y$  as the vertical one (previously referred to as  $z$ -axis in the 3D roughness analysis of Section 4.2.4). By imposing the displacements resulting from the crack kinematics ( $u_x, u_y$ ) (see Figure 4.13a) at each point, the location of the displaced segment can be derived (Figure 4.13c). On that basis, an auxiliary geometric parameter  $p$  can be calculated, related to the local material penetration. When this parameter is positive ( $p > 0$  in Figure 4.13c), the two sides of the crack are not in contact. When it turns negative ( $p < 0$ , red areas in Figure 4.13c), the two areas overlap and contact forces develop. This procedure is simple and efficient to apply (alternative approaches based on the local opening could be used [31]). It allows in addition the calculation of local opening and sliding of a segment  $i$  ( $\delta_i$  and  $w_i$  calculated according to the segment direction, refer to Figure 4.13b) as:

$$\begin{bmatrix} \delta_i \\ w_i \end{bmatrix} = \begin{bmatrix} \cos(\theta_i) & \sin(\theta_i) \\ -\sin(\theta_i) & \cos(\theta_i) \end{bmatrix} \begin{bmatrix} u_x \\ u_y \end{bmatrix} \quad (4.4)$$

It can be noted that in fact, the sides of the crack are not rigid but also deform during the loading process. Consideration of this issue will not be included for simplicity reasons, but can be consulted in [31].

### 4.3.3 Penetrating segments

When  $p_{ij} \leq 0$ , the segment  $i$  is penetrating the opposite side of the crack during load-step  $j$  (see Figure 4.14a) and the procedure described in this section is followed. The contact compressive stress  $\sigma_{c,ij}$  acting on the crack interface is calculated using an elastic-plastic

### 4.3. Consistent modelling of transfer of forces through cracked concrete

constitutive law expressed by:

$$\sigma_{c,ij} = 343 f_c^{1/3} |w_{ij}| \leq \eta_c f_c \quad [\text{MPa}] \quad (4.5)$$

where  $f_c$  is the compressive strength of concrete in [MPa] and  $w$  is the crack opening in [mm]. The elastic part was originally introduced in [21], while limiting the contact stresses to a maximum of  $\eta_c f_c$  is necessary to account for the material crushing strength. The parameter  $\eta_c$  accounts for the effective concrete resistance and depends upon two phenomena: the brittleness of concrete in compression and the enhancement of the resistance (and toughness) under confined conditions. The general formulation of the factor  $\eta_c$  thus results:

$$\eta_c = \eta_{f_c} + \eta_{\text{conf}} \quad (4.6)$$

The brittleness of concrete in compression can be considered by means of a brittleness coefficient  $\eta_{f_c}$  accounting for potential stress redistributions. This expression considers that an enhanced material brittleness (characterized in a global manner by the material compressive strength) leads to higher decreases of overall strength when some regions soften while others attain their peak strength. According to [22], this coefficient can be evaluated as  $\eta_{f_c} = \left( \frac{30 [\text{MPa}]}{f_c} \right)^{1/3} \leq 1$  (see also [9]).

The second parameter ( $\eta_{\text{conf}}$ ) accounts for the enhanced strength and material toughness under confined conditions [26]. Such enhancement of the strength is proposed to be approximated by the following expression:

$$\eta_{\text{conf}} = 3 - 11 (R_p - 1) \geq 0 \quad (4.7)$$

where  $R_p \geq 1$  is calculated using Equation 4.1. The confinement effect in contact regions is considered to be higher for low values of  $R_p$  because in this case fewer contacts occur [30], leading to relatively isolated zones of concrete crushing (high confinement stresses can develop due to the undamaged material surrounding the contact area). For rougher surfaces, on the contrary, the contacts increase in number, resulting in more damaged areas and lower levels of confinement around them. On this basis, the expression for  $\eta_{\text{conf}}$  was fitted in accordance to the experimental results. Further work in this field should however lead to a more refined approach for this expression.

With respect to the inclination of the contact forces, they might not develop perpendicular to the surface, refer to angle  $\gamma$  in Figure 4.14b. This angle is taken as  $0^\circ$  in [21], implying that no friction acts on the surface. However, as pointed out in previous studies [41], some friction is likely to be present. It can be noted that the local value  $\gamma$  has influence on the overall relationship between  $\tau$  and  $\sigma$ , as discussed in Section 4.2.3. For example, Mode II tests tend to result in similar values of  $\tau$  and  $\sigma$ , while in Mixed-Mode tests with large values of  $\alpha$ ,  $\tau$  is generally larger than  $\sigma$ . In the absence of more specific data, and in accordance to the test

## Chapter 4. Influence of cracking and rough surface properties on the transfer of forces in cracked concrete

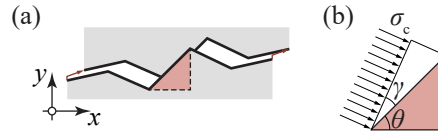


Figure 4.14 – Modelling of penetrating segments; (a) Crack profile in contact under the applied kinematics; and (b) contact stress acting on interface

results later presented, a constant value of  $\gamma = 10^\circ$  will be adopted in the following. However, it should be considered that  $\gamma$  can need some future research and adjustment for different kinematics (potentially varying as a function of parameter  $\psi$  discussed with Figure 4.8). On this basis, for a unitary length, it results (Figure 4.14b):

$$(\sigma, \tau)_{P,ij} = (-\sigma_{c,ij} \cos^2(\gamma), \sigma_{c,ij} \sin(\gamma) \cos(\gamma)) \quad (4.8)$$

Once the stresses acting on the crack interface are determined, they are eventually rotated to the global coordinate system, deriving the contribution of each segment in contact to the total transferred force.

### 4.3.4 Contribution of residual strength

In cases of positive crack opening ( $p_{ij} > 0$ , crack separation) and for small openings, there is a potential for some residual resistance due to material bridging and thus a capability to transfer forces. The total transferred force can be directly related to the residual tensile strength of concrete and thus to the level of crack opening. This contribution is estimated using the following equation in accordance to the experimental evidence presented in this paper:

$$(\sigma, \tau)_{S,ij} = (-v_{\sigma,ij} f_{ct}, v_{\tau,ij} \sqrt{f_c}) S_{ij} \quad (4.9)$$

where  $f_c$ ,  $f_{ct}$ ,  $\sigma$  and  $\tau$  are expressed in [MPa]. The dimensionless parameter  $S$  accounts for the material soundness, with  $S = 1$  referring to undamaged material conditions and  $S = 0$  for a fully damaged material. This soundness parameter can be estimated using a similar expression as for the Mode I residual tensile strength of concrete but with generalized parameters. Various expressions can be found in the literature for this purpose, as for example those proposed by Reinhardt [33] or Ng et al. [25]. In this investigation, the equation proposed by Hordijk [15] for Mode I residual tensile strength will be generalized as follows:

$$S_{ij} = \left(1 + (c_1 u_{M,ij} / w_c)^3\right) e^{-c_2 (u_{M,ij} / w_c)} - u_{M,ij} / w_c (1 + c_1^3) e^{-c_2}, \quad S_{ij} \geq 0 \quad (4.10)$$

According to its original formulation [15], the values  $c_1 = 3$ ,  $c_2 = 6.93$  and  $w_c = 5.14 \frac{G_F}{f_{ct}} = 5.14 \frac{0.073 f_c^{0.18}}{0.3 f_c^{2/3}}$  [mm] can be adopted ( $w_c$ ,  $G_F$  and  $f_{ct}$  are determined in accordance to [6, 9, 15]).

### 4.3. Consistent modelling of transfer of forces through cracked concrete

With respect to parameter  $u_M$ , it accounts for the considered kinematics. Since the original formulation was developed for Mode I, the kinematics is characterized only by the opening of the crack ( $u_M = w$ ). In the present case, it is assumed that a similar approach is also valid for a Mixed-Mode case, by using a generalized displacement parameter whose value is calculated as:

$$u_{M,ij} = \sqrt{w_{ij}^2 + (0.3\delta_{ij})^2} \quad [\text{mm}] \quad (4.11)$$

where  $w$  is the opening normal to the crack and  $\delta$  its relative sliding. This assumption allows accounting for the additional damage due to crack sliding in the fracture process zone although to a lesser degree compared to the crack opening (the value of coefficient 0.3 was selected as a reasonable average estimate finely fitting test results, but could be tailored in specific cases related to the local shear strength of material). As can be noted, the material strength (correlated to  $f_{ct}$  in pure tension and to  $\sqrt{f_c}$  in pure shear [9]) is reduced for larger openings and for sliding of the FPZ.

The dimensionless parameters  $\nu$  of Equation (4.9) are functions of  $\delta$ , as they consider the increasing potential for force transfer due to material bridging as crack-sliding increases (enhanced number of contacts). For the parameter  $\nu_\sigma$ , accounting for the activation of normal forces, the following equation is proposed:

$$\nu_{\sigma,ij} = 1 - \left( 100 \frac{\delta_{ij}}{D_{\max}} \right) \geq -2 \quad [-] \quad (4.12)$$

This equation is justified by the fact that when  $\delta$  increases, the normal stresses turn from tension values ( $\nu_\sigma > 0$ ) to compressive ones ( $\nu_\sigma < 0$ , refer to experimental results later discussed in Figure 4.15).

With respect to parameter  $\nu_\tau$ , it accounts for the activation of the friction forces in rough surfaces of the fracture process zone. It varies between 0 and 2, to consider that the local stresses increase for larger sliding (enhanced activation of bridging material), and is proposed to be evaluated as:

$$\nu_{\tau,ij} = 200 \frac{|\delta_{ij}|}{D_{\max}} \leq 2 \quad [-] \quad (4.13)$$

The expressions proposed (Equations 4.10-4.13) show overall good agreement when compared to test results. They have been selected to provide a consistent transition to pure Mode I and to fit reasonably the experimental results presented in this article. Nevertheless, further work is needed to consolidate them and to better clarify their limits of applicability.

### 4.3.5 Model results

By summing both contributions (regions under penetration or separation), the total transferred force can be calculated. Figure 4.15 reports the model estimates for three representative tests with different failure modes and compares them to the experimental results (marked with a dotted line when the development of a DSC did not allow to respect the imposed kinematics). Further details are given in Table 4.4, where the maximum shear stresses of several models are also compared with the experimental values (2PM, referring to the Two-Phase Model by Walraven [40] according to the fitted expressions given in [6] and *fib* referring to *fib*'s Model Code 2010, equations 5.1-48 and 5.1-49 [9]). As it can be noted, the proposed approach yields a reasonable agreement for almost all specimens. Such consistency is found both in terms of maximum strength and deformation at peak load, and is better than for the other investigated models (Table 4.4). The post-peak response is also reasonably reproduced, particularly for PC and NDSC, but the residual strength is normally overestimated for DSC. A significant amount of scatter can still be observed, which can be explained by the very limited crack surface of the tests (measuring approximately 1000 mm<sup>2</sup>). In actual cases, the contributions are averaged over a significantly larger surface, thus leading to a reduction of the scatter.

With respect to the contributions due to penetration (P) and the residual tensile strength of the fracture process zone (separation S) to the overall strength, Figure 4.16 presents the results of two specimens failing by DSC. It can be noted that in one case (Figure 4.16a, associated with a large initial crack opening), the forces almost exclusively derive from penetrating segments, while in the other (Figure 4.16b, associated with a lower initial crack opening), the governing contribution is that of the residual tensile strength. This shows that both contributions are necessary to consistently reproduce the phenomenon in a general manner and that the fracture process zone can govern for low crack widths. The plots for all experiments are reported in Appendix C. It can be noted from these results that long post-peak softening phases are mainly governed by penetrating material parts engaging contacts. Also, it can be noted that the contribution of the fracture process zone has a significant influence on the failure mode and transferred forces, particularly at low displacement levels.

More details on the role of the different contributions are presented in Figure 4.17 for all tests. Although subjected to a significant scatter, it can be observed that rougher surfaces (associated with higher values of  $R_p$  and to DSC failure mode) yield to higher resistances and tend to be dominated by contacts due to material penetration. On the contrary, smoother surfaces (associated with lower values of  $R_p$  and PC failure modes) yield to lower resistances and tend to be highly dependant on the contribution of the residual tensile strength.

The relevance of the development of dominant secondary cracking shown in the experiments can be related to the fact that the protruding material has relatively large protuberances compared to the tested region. In particular cases, as for beams without transverse reinforcement failing in shear, this can be associated with the engagement of meso-roughness (large zones with steeper inclination, Figure 4.1c, see [4]). Otherwise, a small region of protruding material

### 4.3. Consistent modelling of transfer of forces through cracked concrete

Table 4.4 – Summary of results: ratios of values obtained experimentally and by modelling; “exp” refers to test values, “mod” to the proposed model, “2PM” to the equations in Appendix A for a Two-Phase Model [6] (fitted on the basis of the formulation by Walraven [41]) and “*fib*” to the equations (5.1-48, 5.1-49) in *fib*’s Model Code 2010 [9]

#	failure	exp/mod			exp/2PM			exp/ <i>fib</i>		
		$\tau_{\max}$	$\sigma_{\min}$	$\delta(\tau_{\max})$	$\tau_{\max}$	$\sigma_{\min}$	$\delta(\tau_{\max})$	$\tau_{\max}$	$\sigma_{\min}$	$\delta(\tau_{\max})$
30802	PC	0.69	0.00	0.35	1.01	0.00	0.39	0.54	0.00	0.29
30901	PC	0.97	0.00	0.33	0.59	0.00	0.28	0.35	0.00	0.21
50301	PC	1.26	1.15	0.91	1.14	0.82	0.83	0.61	0.41	0.35
70101	PC	0.71	-0.21	-	0.82	-0.15	0.29	0.45	0.12	0.13
70902	PC	0.74	1.15	3.82	1.42	2.04	3.92	0.95	1.77	0.76
71401	PC	1.72	2.21	0.55	0.80	0.58	0.72	0.53	0.35	0.15
AVG	PC	1.02	0.72	1.19	0.96	0.55	1.07	0.57	0.44	0.32
COV	PC	0.40	1.32	1.25	0.31	1.50	1.32	0.36	1.52	0.75
21601	NDSC	0.50	0.35	0.47	0.81	0.50	0.85	0.55	0.29	0.30
22002	NDSC	1.13	1.33	0.95	1.18	1.08	1.50	0.93	0.69	0.32
22102	NDSC	0.97	0.50	0.73	0.85	0.44	0.42	0.52	0.21	0.21
40501	NDSC	0.46	0.42	1.90	0.91	0.80	1.71	0.66	0.38	0.33
40601	NDSC	0.90	0.71	3.03	1.78	1.50	2.01	1.18	0.68	0.51
50102	NDSC	0.90	0.91	2.83	1.84	1.81	1.52	1.13	0.83	0.48
50302	NDSC	0.91	1.48	1.65	1.14	1.15	1.23	0.73	0.54	0.41
50401	NDSC	1.06	0.57	0.61	1.01	0.44	0.40	0.55	0.17	0.17
50801	NDSC	1.28	2.29	3.28	2.14	2.41	0.80	0.93	0.71	0.50
50902	NDSC	0.43	0.28	1.41	0.79	0.59	1.41	0.56	0.30	0.28
70601	NDSC	1.65	0.25	3.15	0.98	0.28	0.46	0.41	0.12	0.31
AVG	NDSC	0.93	0.83	1.82	1.22	1.00	1.12	0.74	0.45	0.35
COV	NDSC	0.40	0.77	0.60	0.39	0.67	0.50	0.35	0.56	0.33
21501	DSC*	1.12	0.80	0.93	1.63	1.15	0.62	1.06	0.59	0.33
22101	DSC	1.10	1.04	1.00	2.54	2.62	0.77	1.34	0.92	0.58
30101	DSC	0.66	0.42	1.33	3.80	3.69	1.62	2.24	-1.11	1.22
30201	DSC	1.36	1.38	1.63	1.90	1.41	0.94	1.16	0.67	0.47
50101	DSC	1.41	0.87	1.32	3.31	3.30	0.76	1.44	0.85	0.48
50202	DSC*	1.25	1.26	1.56	1.65	1.73	2.28	1.21	0.90	0.49
50802	DSC	0.81	1.0	2.92	2.22	2.42	3.74	1.58	1.41	0.69
70302	DSC	1.00	0.94	2.61	2.43	2.69	2.68	1.63	2.28	0.52
70501	DSC	0.77	0.53	3.89	2.82	2.90	1.23	1.55	-2.30	0.53
AVG	DSC	1.05	0.91	1.91	2.48	2.43	1.63	1.47	0.47	0.59
COV	DSC	0.25	0.34	0.53	0.30	0.35	0.66	0.24	2.92	0.43
AVG	all	0.99	0.83	1.73	1.60	1.39	1.28	0.95	0.45	0.42
COV	all	0.34	0.74	0.65	0.53	0.78	0.76	0.50	1.87	0.54

**Chapter 4. Influence of cracking and rough surface properties on the transfer of forces in cracked concrete**

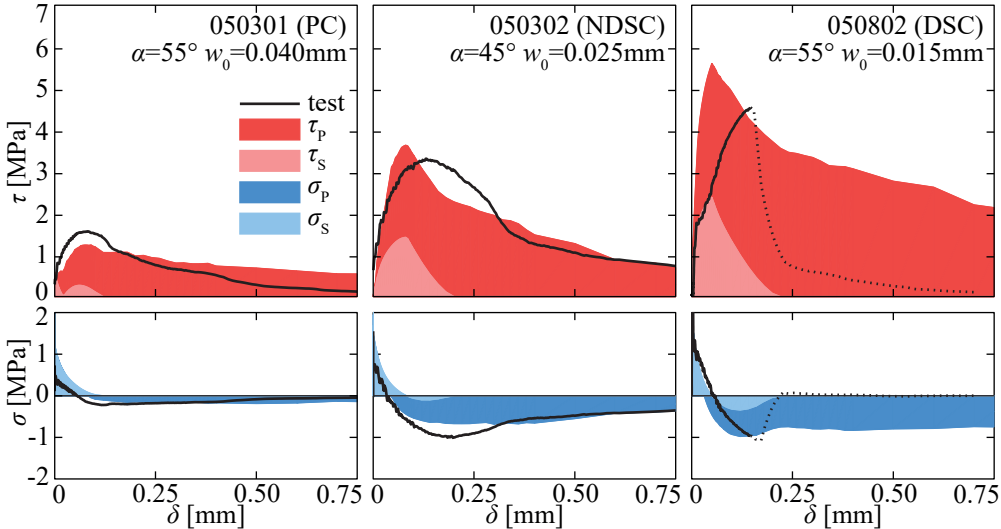


Figure 4.15 – Comparison of model estimates with experimental results for three tests with varying failure mode (subscript P indicates contributions due to penetrating segments, while subscript S indicates the contribution of the residual tensile strength)

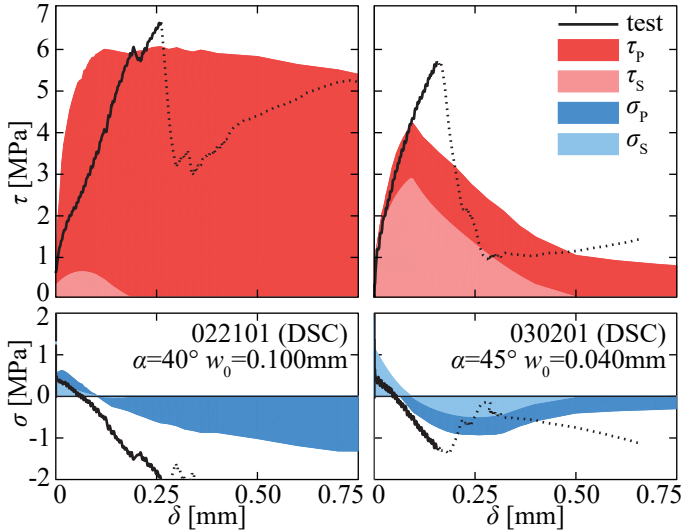


Figure 4.16 – Two tests with DSC and different relative contributions from contacts in penetration (subscript P) and separation (subscript S)

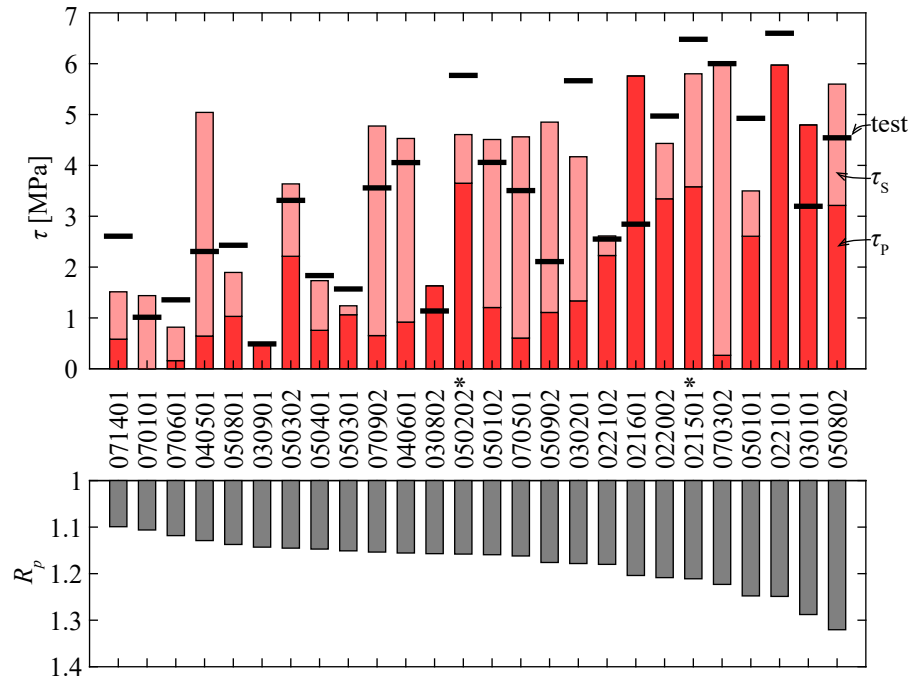


Figure 4.17 – Model contributions, ordered by surface roughness  $R_p$

engages secondary cracks which develop in a potentially stable manner, as a redistribution of stresses to other regions is possible. In these cases, the global behaviour can be observed to be less governed by secondary cracking considering the average response of the phenomenon. Finally, Figure 4.18a shows that the peak values  $\tau_{\max}$  calculated with the proposed model suitably account for the influence of surface roughness (characterized by the parameter  $R_p$ ) with no marked trend in the results. As it can be noted, the material roughness is the most reliable indicator for the type of failure observed (with low roughness associated with PC and higher roughness associated with DSC). Neglecting the role of this parameter, as for instance performed in the equations for aggregate interlocking proposed by Cavagnis et al. [6] (fitted on the basis of the Two-Phase Model of Walraven [41]) yields however to a clear trend (see Figure 4.18b), with a consistent underestimation of the transferred load for increasing values of the surface roughness. Such approaches are thus in principle suitable for the range of  $R_p$  corresponding to PC or NDSC failure modes (see Figure 4.18b). A correction of the equations by Cavagnis et al. [6] to account for this effect is presented in Appendix D. It shall also be highlighted that all expressions provided in this manuscript have been verified for the range of experiments available and presented, but future work is required to consolidate its application to other cases (high-strength concrete, cyclic response...).

## 4.4 Conclusions

This paper investigates the transfer of forces through cracked concrete by means of a review of the phenomenon at micro-structural level. The results of a specific testing programme

## Chapter 4. Influence of cracking and rough surface properties on the transfer of forces in cracked concrete

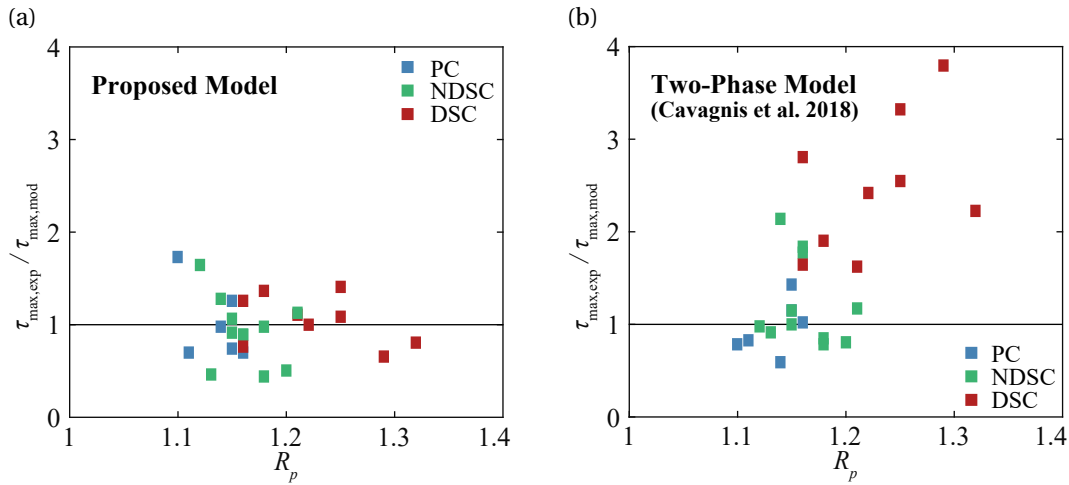


Figure 4.18 – Peak values  $\tau_{\max}$  as a function of the roughness index  $R_p$ : (a) Proposed model; and (b) Two-Phase-Model

are presented as well as a comprehensive modelling frame for the phenomenon. The main conclusions of this investigation are summarized below:

1. The actual roughness of the crack surface plays a major role in the failure mode and capacity to transfer shear forces. Notably, the presence of steep segments engaging large contact forces can govern the response and observed failure mode.
2. For the considered surfaces, the crack surface roughness is related to the concrete strength and the maximum aggregate size.
3. In some tests, the development of secondary cracks at an angle of approximately  $45^\circ$  to the primary crack has been observed.
4. The development of secondary cracks is usually associated with rough surfaces characterized by an increased amount of steep segments or by flat kinematics resulting in significant amounts of material engagement.
5. Other than forces developed due to direct contacts, a significant amount of force can potentially be transferred by the residual tensile strength of concrete both in tension and shear.
6. Consistent modelling of the phenomenon of transfer of forces through cracked concrete can be performed on the basis of these ideas. A model for this purpose is presented in this paper, showing better performance than classical approaches and allowing to determine the amount of force transferred by penetration and separation and applicable for all potential failure modes.

---

Notation	Description
2PM	Two-Phase Model [41]
CSC	Critical Shear Crack
DIC	Digital Image Correlation
DSC	Dominant Secondary Crack/Cracking
DSC*	DSC starting from specimen's notch
NDSC	Non-Dominant Secondary Crack/Cracking
PC	Primary Crack/Cracking

---

Table 4.5 – Notations

## **Acknowledgements**

This work has been funded by the Swiss National Science Foundation, research grant 200021\_169649. The authors are very appreciative of the support received.

The authors also thank Professor Frank J. Vecchio from the University of Toronto, for his review and comments in drafting the manuscript.

**Chapter 4. Influence of cracking and rough surface properties on the transfer of forces in cracked concrete**

Symbol	Description	Physical Dimension
$A_0$	horiz. proj. of surface element	area
$A_i$	area of surface element	area
$D_{\max}$	maximum aggregate size	length
$G_F$	fracture energy	force/area
$N$	force normal to crack plane	force
$R_p$	roughness number (profile)	-
$R_s$	roughness number (surface)	-
$S$	soundness index	-
$V$	force tangential to crack plane	force
$b$	specimen thickness, depth of crack plane	length
$c$	width of crack plane	length
$c_i$	constant value	-
$f_c$	concrete compressive resistance	force/area
$f_{ct}$	concrete tensile resistance	force/area
$l$	length of segment	length
$l_x$	length of horiz. proj. of segment	length
$p$	segment penetration	length
$u_M$	generalized Mixed-Mode opening	length
$u_x$	displacement along horiz. $x$ -axis	length
$u_y$	displacement along vert. $y$ -axis	length
$w$	crack opening normal to crack plane	length
$w_0$	initial Mode I crack opening	length
$w_c$	crack opening without tensile strength	length
$\alpha$	Mixed-Mode opening angle (to crack plane)	angle
$\alpha_{eq}$	Overall opening angle (to crack plane)	angle
$\gamma$	contact force angle to crack plane	angle
$\delta$	crack sliding parallel to crack plane	length
$\eta_c$	concrete strength factor	-
$\eta_{f_c}$	brittleness factor	-
$\eta_{\text{conf}}$	confinement factor	-
$\theta$	inclination of crack-profile segment	angle
$\lambda_R$	factor for surface roughness	-
$\nu_\sigma$	$\sigma$ -activation due to FPZ interlocking	-
$\nu_\tau$	$\tau$ -activation due to FPZ interlocking	-
$\sigma$	stress normal to crack plane	force/area
$\sigma_c$	contact stress	force/area
$\tau$	stress parallel to crack plane	force/area
$\psi$	angle to $x$ -axis in $\sigma$ - $\tau$ plot	angle

Table 4.6 – Symbols

## Appendix A: Two-Phase Model and simplified expressions based on it

The Two-Phase Model [40, 41] idealizes concrete at the meso-scale as a material consisting of rigid, spherical aggregates surrounded by a perfectly plastic cement matrix. Cracks are considered as planar with protruding aggregates. If the system is subjected to sliding, the aggregates can engage the opposite side and transfer forces through aggregate-matrix contact. Under these assumptions, the Two-Phase Model considers the surface as consisting of 2D-profiles parallel to the loading direction, similar to the ones of Section 4.2.4. Using stochastic considerations for the granulometric distribution of aggregates it is possible to calculate the overall contact area. Finally, the model considers a rigid-plastic constitutive material law and a constant friction coefficient to account for the inclination of the force resulting at each contact. The Two-Phase Model has constituted one of the most comprehensive and consistent approaches for dealing with aggregate interlock issues. Despite its limitations [31] its principles have been successfully adopted to shear [4, 39] and punching shear [11] cases. The original formulation of the Two-Phase Model has further been adapted to various kinematics and recently analytical expressions have been proposed by Cavagnis et al. [6] fitting the predictions of the Two-Phase Model but simple enough to be integrated analytically:

$$\tau = \sqrt{f_c} \frac{c_3 \bar{\delta}^{-4/3}}{(c_2 \bar{w})^{1.8+c_2 \bar{\delta}}} \quad (4.14a)$$

$$\sigma = \sigma_{res} - \sqrt{f_c} \frac{c_4 \bar{\delta}^{-4/3}}{(c_2 \bar{w})^{3+c_2 \bar{\delta}}} \quad (4.14b)$$

where  $\sigma_{res} = f_{ct}(1 - (w/w_c)^{c_1}) \geq 0$  is the residual tensile strength of concrete measured in [MPa],  $c_1 = 0.31$ ,  $c_2 = 40$ ,  $c_3 = 35$  and  $c_4 = 400$  are constants,  $w_c = \frac{G_F}{f_{ct}} \frac{1+c_1}{c_1}$  is the value of crack opening in [mm] for which the residual tensile resistance vanishes [33],  $G_F = 0.073 f_c^{0.18}$  is the fracture energy in [MPa],  $f_{ct}$  is the tensile resistance of concrete calculated as  $f_{ct} = 0.3 f_c^{2/3}$  [MPa],  $f_c < 50$  MPa and  $f_{ct} = 0.3(50 f_c)^{1/3}$  [MPa] for  $f_c \geq 50$  MPa,  $\bar{\delta} = \delta/d_{ag}$  and  $\bar{w} = w/d_{ag}$  are the normalized crack openings using an average roughness value depending on the maximum aggregate size as  $d_{ag} = \min(40, 16+D_{\max})$  for  $f_c \leq 60$  MPa and  $d_{ag} = \min(40, 16+D_{\max}(60/f_c)^2)$  for  $f_c > 60$  MPa.

## **Appendix B: Contact Density Model**

The Contact Density Model [1, 21] idealizes the roughness of a concrete surface as a collection of segments (called *contact units*) each with a given inclination with respect to a horizontal crack plane. The geometry of these contact units can be obtained by scanning of the concrete surface as shown in Figure 4.9. A contact density function is then adopted to represent the overall distribution of inclinations.

For every direction  $\theta$ , the model considers all the corresponding segments and calculates the local kinematics, determining the crack opening. If a contact is detected, an elastic-plastic material law is applied, and the resulting contact stress is considered to be normal to the segment. For monotonic loading paths, the following equations are obtained [21]:

$$\tau = g \left( \frac{\delta \sin^3 \beta + w \cos^3 \beta}{3} - \frac{\delta w}{3\sqrt{\delta^2 + w^2}} + 0.5w_{lim} \cos^2 \beta \right) \quad (4.15a)$$

$$\sigma = g \left( \frac{-\delta \cos^3 \beta + w \sin^3 \beta}{3} - w \sin \beta + \frac{\delta^2 + 2w^2}{3\sqrt{\delta^2 + w^2}} + w_{lim} \left( \frac{\pi}{4} - \frac{\beta}{2} - \frac{\sin(2\beta)}{4} \right) \right) \quad (4.15b)$$

where  $g = 0.5A_t R_s K(w)$ ,  $A_t = 4/\pi$  [mm<sup>2</sup>],  $R_s = \frac{436}{A_t} f_c^{1/3}$  [MPa/mm<sup>3</sup>],  $w_{lim} = 0.04$  [mm],  $\beta = \arcsin \left( \frac{w_{lim}\delta + w\sqrt{w^2 + \delta^2 - w_{lim}^2}}{w^2 + \delta^2} \right)$  if  $\delta \geq w_{lim}$  and  $\beta = \frac{\pi}{2}$  if  $\delta \leq w_{lim}$ .

Appendix C: Model results

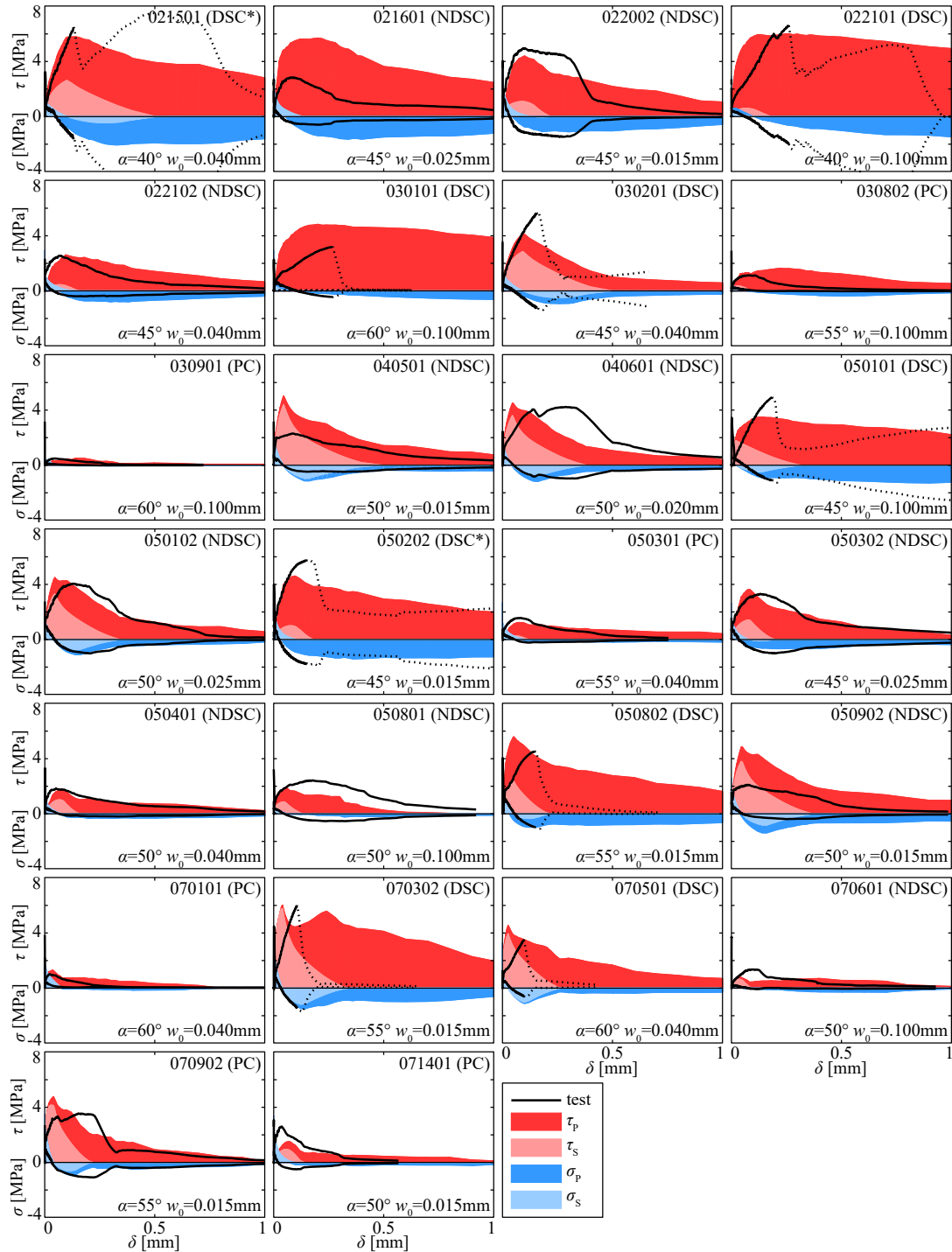


Figure 4.19 – Comparison of model estimates with experimental results for all tests; dotted lines indicate that the global kinematics are not respected due to DSC.

**Appendix D: Parameter accounting for surface roughness**

As shown in Figure 4.18b, the results obtained with the approximated equations based on the Two-Phase Model from [6] and reported in Appendix A show a clear trend when plotted against the profile roughness index  $R_p$ . These equations can be modified to account for the surface roughness by introducing the following parameter:

$$\lambda_R = \left( \frac{R_p}{R_{p,ref}} \right)^4 \leq 3, \quad R_{p,ref} = 1.10 \quad (4.16)$$

The equations thus become:

$$\tau = \lambda_R \sqrt{f_c} \frac{c_3 \bar{\delta}^{-4/3}}{(c_2 \bar{w})^{1.8+c_2 \bar{\delta}}} \quad (4.17a)$$

$$\sigma = \sigma_{res} - \lambda_R \sqrt{f_c} \frac{c_4 \bar{\delta}^{-4/3}}{(c_2 \bar{w})^{3+c_2 \bar{\delta}}} \quad (4.17b)$$

with  $\lambda_R$  increasing the estimates for surfaces which are significantly rougher than those of typical tests resulting in primary cracking, as can be seen in Figure 4.20 and Table 4.7.

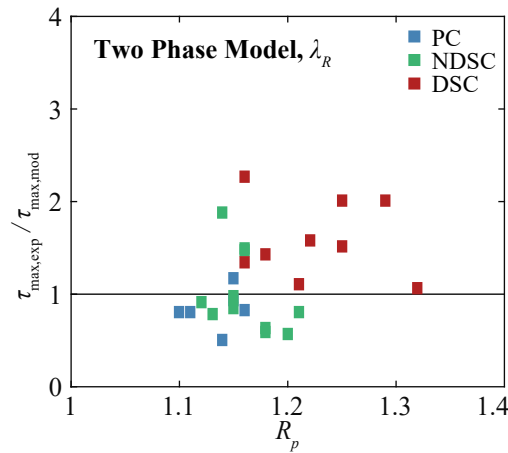


Figure 4.20 – Peak values  $\tau_{max}$  of Two-Phase-Model with parameter  $\lambda_R$  as a function of the roughness index  $R_p$

	exp/ (2PM, $\lambda_R$ )		
	$\tau_{max}$	$\sigma_{min}$	$\delta(\tau_{max})$
AVG	1.17	0.99	1.28
COV	0.42	0.72	0.76

Table 4.7 – Summary of model results; “2PM,  $\lambda_R$ ” refers to results obtained with Equation 4.17

---

## Bibliography

- [1] Bujadham, B., Mishima, T., and Maekawa, K. (1992). Verification of the universal stress transfer model. *Proc. of JSCE*, 451/V-17:289–300.
- [2] Calvi, P. M., Bentz, E. C., and Collins, M. P. (2017). Pure Mechanics Crack Model for Shear Stress Transfer in Cracked Reinforced Concrete. *Structural Journal*, 114(2):545–554.
- [3] Carol, I., Prat, P. C., and López, C. M. (1997). Normal/Shear Cracking Model: Application to Discrete Crack Analysis. *Journal of Engineering Mechanics*, 123(8):765–773.
- [4] Cavagnis, F, Fernández Ruiz, M., and Muttoni, A. (2015). Shear failures in reinforced concrete members without transverse reinforcement: An analysis of the critical shear crack development on the basis of test results. *Engineering Structures*, 103:157–173.
- [5] Cavagnis, F, Fernández Ruiz, M., and Muttoni, A. (2017). An analysis of the shear-transfer actions in reinforced concrete members without transverse reinforcement based on refined experimental measurements. *Structural Concrete*, 19(1):49–64.
- [6] Cavagnis, F, Fernández Ruiz, M., and Muttoni, A. (2018). A mechanical model for failures in shear of members without transverse reinforcement based on development of a critical shear crack. *Engineering Structures*, 157:300–315.
- [7] Cavagnis, F, Simões, J. T., Ruiz, M. F., and Muttoni, A. (2020). Shear Strength of Members without Transverse Reinforcement Based on Development of Critical Shear Crack. *Structural Journal*, 117(1):103–118.
- [8] Divakar, M. P., Fafitis, A., and Shah, S. P. (1987). Constitutive Model for Shear Transfer in Cracked Concrete. *Journal of Structural Engineering*, 113(5):1046–1062.
- [9] fib (International Federation for Structural Concrete) (2013). *fib Model Code for Concrete structures 2010*. Ernst & Sohn, 402 p, Germany.
- [10] Giaccio, G. and Giovambattista, A. (1986). Bleeding - Evaluation of its effects on concrete behaviour. *Materials and Structures*, 19(4):265–271.
- [11] Guidotti, R. (2010). *Poinçonnement des planchers-dalles avec colonnes superposées fortement sollicitées*. Ph.D. Thesis, EPFL, Lausanne, Switzerland.
- [12] Haeri, H., Sarfarazi, V., and Lazemi, H. A. (2016). Experimental study of shear behavior of planar nonpersistent joint. *Computers and Concrete*, 17(5):639–653.
- [13] Hassanzadeh, M. (1992). *Behavior of Fracture Process Zones in Concrete Influenced by Simultaneously Applied Normal and Shear Displacements*. Ph.D. Thesis, Lund University, Sweden.
- [14] Hillerborg, A. (1983). Analysis of one single crack. In *Fracture Mechanics of Concrete (Developments in civil engineering)*, pages 223 – 249, Amsterdam, Netherlands. Wittmann, Folker H.

#### Chapter 4. Influence of cracking and rough surface properties on the transfer of forces in cracked concrete

---

- [15] Hordijk, D. A. (1992). Tensile and tensile fatigue behaviour of concrete; experiments, modelling and analyses. *Heron*, 37(1).
- [16] Hsu, T. T. C. and Slate, F. O. (1963). Tensile Bond Strength Between Aggregate and Cement Paste or Mortar. *ACI Journal Proceedings*, 60(4):465–486.
- [17] Huber, T., Huber, P., and Kollegger, J. (2019). Influence of aggregate interlock on the shear resistance of reinforced concrete beams without stirrups. *Engineering Structures*, 186:26–42.
- [18] Issa, M. A., Issa, M. A., Islam, M. S., and Chudnovsky, A. (2003). Fractal dimension—a measure of fracture roughness and toughness of concrete. *Engineering Fracture Mechanics*, 70(1):125–137.
- [19] Jacobsen, J. S. (2012). *Constitutive Mixed Mode Behavior of Cracks in Concrete: Experimental Investigations of Material Modeling*. Ph.D. Thesis, Technical University of Denmark, Kongens Lyngby, Denmark.
- [20] Lange, D. A., Jennings, H. M., and Shah, S. P. (1993). Relationship between Fracture Surface Roughness and Fracture Behavior of Cement Paste and Mortar. *Journal of the American Ceramic Society*, 76(3):589–597.
- [21] Li, B., Maekawa, K., and Okamura, H. (1989). Contact density model for stress transfer across cracks in concrete. *Journal of the Faculty of Engineering, The University of Tokyo*, 40(1):9–52.
- [22] Muttoni, A. (1989). *Die Anwendbarkeit der Plastizitätstheorie in der Bemessung von Stahlbeton*. PhD thesis, ETH, Zurich, Switzerland.
- [23] Muttoni, A. and Fernández Ruiz, M. (2008). Shear Strength of Members without Transverse Reinforcement as Function of Critical Shear Crack Width. *ACI Structural Journal*, 105(2):163–172.
- [24] Muttoni, A., Fernández Ruiz, M., and Simões, J. T. (2018). The theoretical principles of the critical shear crack theory for punching shear failures and derivation of consistent closed-form design expressions. *Structural Concrete*, 19(1):174–190.
- [25] Ng, T. S., Htut, T. N. S., and Foster, S. J. (2012). Fracture of steel fibre reinforced concrete—The unified variable engagement model. Technical Report R-460, School of Civil and Environmental Engineering, The University of New South Wales, Sydney.
- [26] Nielsen, M. P. and Hoang, L. C. (2011). *Limit analysis and concrete plasticity*. CRC Press, 788 p., Boca Raton, Florida, 3rd ed edition.
- [27] Nooru-Mohamed, M. B. (1992). *Mixed-Mode Fracture of Concrete: An Experimental Approach*. Ph.D. Thesis, Delft University of Technology, Sweden.
- [28] Paulay, T. and Loeber, P. J. (1974). Shear Transfer By Aggregate Interlock. *ACI Special Publication*, 42:1–16.

- [29] Perera, S. V. T. J. and Mutsuyoshi, H. (2013). Shear Behavior of Reinforced High-Strength Concrete Beams. *ACI Structural Journal; Farmington Hills*, 110(1):43–52.
- [30] Pundir, M. and Anciaux, G. (2020). Numerical generation and contact analysis of rough surfaces in concrete. Submitted for review, available on HAL: <https://hal.archives-ouvertes.fr/hal-02573481>.
- [31] Pundir, M., Tirassa, M., Fernández Ruiz, M., Muttoni, A., and Anciaux, G. (2019). Review of fundamental assumptions of the Two-Phase model for aggregate interlocking in cracked concrete using numerical methods and experimental evidence. *Cement and Concrete Research*, 125:105855.
- [32] Randl, N. (2013). Design recommendations for interface shear transfer in fib Model Code 2010. *Structural Concrete*, 14(3):230–241.
- [33] Reinhardt, H. W. (1984). Fracture Mechanics of an Elastic Softening Material like Concrete. *Heron*, 29(2).
- [34] Simões, J. T., Ruiz, M. E., and Muttoni, A. (2018). Validation of the Critical Shear Crack Theory for punching of slabs without transverse reinforcement by means of a refined mechanical model. *Structural Concrete*, 19(1):191–216.
- [35] Taylor, H. P. J. (1970). *Investigation of the Forces Carried Across Cracks in Reinforced Concrete Beams in Shear by Interlock of Aggregate*. Number 42.447 in Technical report (Cement and Concrete Association). London, United Kingdom.
- [36] Tirassa, M., Fernández Ruiz, M., Anciaux, G., and Muttoni, A. (2017). Interface Stresses in Cracked Concrete: Testing for Review of Its Fundamentals. In *2017 fib Symposium High Tech Concrete: Where Technology and Engineering Meet*, pages 740–748. Maastricht, Netherlands.
- [37] Tirassa, M., Fernández Ruiz, M., and Muttoni, A. (2020, in press). Influence of cracking and rough surface properties on the transfer of forces in cracked concrete. *Engineering Structures*.
- [38] Tirassa, M., Fernández Ruiz, Miguel, and Muttoni, A. (2018). Modern experimental research techniques for a consistent understanding of aggregate interlocking. In *Proceedings of the 12th fib PhD Symposium in Civil Engineering*, pages 723–730, Prague, Czech Republic.
- [39] Ulaga, T. (2003). *Betonbauteile mit Stab- und Lamellenbewehrung: Verbund- und Zuggliedmodellierung*. Ph.D. Thesis, ETH Zurich, Switzerland.
- [40] Walraven, J. C. (1980). *Aggregate Interlock: a Theoretical and Experimental Analysis*. Ph.D. Thesis, Delft University of Technology, Sweden.
- [41] Walraven, J. C. (1981). Fundamental Analysis of Aggregate Interlock. *ASCE Journal of the Structural Division*, 107(11):2245–2270.

#### **Chapter 4. Influence of cracking and rough surface properties on the transfer of forces in cracked concrete**

---

- [42] Walraven, J. C., Vos, E., and Reinhardt, H. W. (1979). Experiments on shear transfer in cracks in concrete. Part I. Technical report, Delft University of Technology, Sweden.
- [43] Wittmann, F. H. (1983). Structure of concrete with respect to crack formation. *Fracture mechanics of concrete*, 43(5):6.
- [44] Østergaard, Olesen, and Poulsen (2007). Biaxial Testing Machine for Mixed Mode Cracking of Concrete. In *Fracture mechanics of concrete and concrete structures*, volume 1, page 8, Catania, Italy. CRC Press.

## 5 An interlocking approach for the rebar-to-concrete contact in bond

This chapter discusses the similarities between aggregate interlocking and bond between rebars and concrete. It presents a new experimental approach and extends the model described in Chapter 4 to the case of bond. The content was submitted for review as the following scientific article [28]:

Tirassa M., Fernández Ruiz M., Muttoni A. (2020). An interlocking approach for the rebar-to-concrete contact in bond.

Max Tirassa planned and carried out the experimental campaign, analysed the obtained data and implemented the presented model under the supervision of the second and third authors.

### **Abstract**

The bond response of deformed bars in structural concrete is a phenomenon governed to a large extent by the rib-to-concrete contact and interaction, with contact forces depending both on material properties and on the kinematics between the contact surfaces (slip and potential separation between the bar and concrete). This phenomenon, presenting similarities with aggregate interlocking in cracked concrete, is however difficult to investigate in an experimental manner by means of conventional test arrangements. In this paper, an experimental and theoretical investigation on the phenomenon is presented by means of an innovative experimental test set-up performed with bar off-cuts and allowing to track the development of bond and confinement stresses for given contact kinematics. The surface of the rebars was scanned to analyse the contact and roughness properties for various cases. The experimental results are eventually analysed by using a mechanical model accounting for the surface properties and rib-to-concrete mechanical engagement. Good agreement in terms of maximum stresses and load-displacement curves is found. On that basis, the practical implications to calculate bond stresses on cracked concrete are discussed.

**Keywords:** bond between reinforcement and concrete; bond modelling; experimental results;

rib geometry; rib interlocking; cracks & cracking

### 5.1 Introduction

Bond between concrete and reinforcement allows for transfer of forces and their composite response. Bond forces have been identified to depend upon three main physical phenomena, namely adhesion, friction and mechanical interlocking between the ribs of the reinforcement bars and the surrounding concrete (see [2, 5, 7]). The latter action is generally dominant for ribbed bars whenever a relative slip occurs. In this case, Figure 5.1a-b, the mechanical engagement of the rib and the concrete allows for development of compression struts in the concrete equilibrated by means of transverse tensile stresses (see Figure 5.1b, [27]). It can be observed that the transfer of forces in this case is potentially sensitive to the presence of cracks and to the contact interface between the concrete and the rebar, see Figure 5.1c-d. This is justified by the fact that these cracks reduce the surface where the mechanical engagement can develop [1] and lead consequently to a reduction of the bond strength.

A phenomenon presenting several similarities with bond, and thus useful for its understanding, is aggregate interlocking, which accounts for the transfer of forces between concrete surfaces separated by cracks. This transfer is known to efficiently occur when two sides of a concrete crack enter in contact due to their relative sliding. As a consequence of the rough nature of concrete cracks, material protruding from one side engages with the opposite and contact forces develop. Such contact forces depend on the kinematics of the crack (Figure 5.1e presenting pure Mode I and Figure 5.1f Mixed-Mode I+II), on the surface of the crack (roughness) and on the concrete properties (matrix and aggregates). Aggregate interlocking plays a significant role in carrying shear in reinforced concrete beams without shear reinforcement (see [3, 26]) and has been a topic of research for several decades [16, 17, 29]. Despite the similarities between both phenomena, some differences persist. They are mostly due to the nature of the material, to the geometry of the interface surface and to the confinement conditions developing at localized contacts.

Within this context, this paper investigates the bond response as a function of the relative displacement between a rebar and its surrounding concrete. This is performed on the basis of an experimental programme developed on different bar surfaces subjected to Mixed-Mode kinematics. Based on these results, the principles of a model for aggregate interlocking in concrete previously developed by the authors is extended to the investigated cases. This model is shown to consistently reproduce the new experimental results as well as pull-out tests in cracked concrete from the literature, where the bond reduction as a function of the crack width can be efficiently predicted.

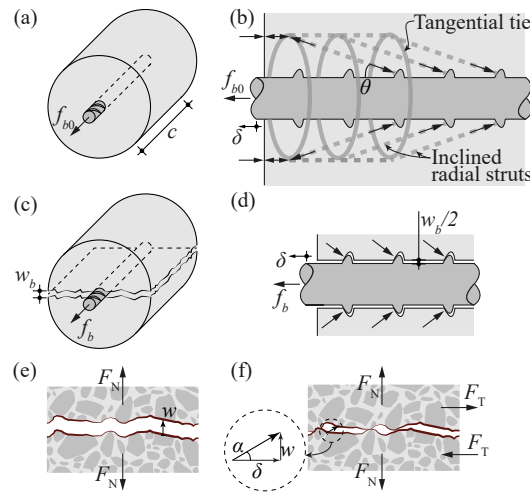


Figure 5.1 – (a) Pull-out of reinforcement; (b) struts carrying bond forces and tangential ties according to [27]; (c) pull-out of reinforcement in cracked conditions; (d) corresponding cross-section at the bar; (e) concrete crack subjected to Mode I kinematics; and (f) concrete crack subjected to Mixed-Mode kinematics

## 5.2 Experimental programme

The experimental programme consists of Mixed-Mode tests where the interaction between a rebar's steel surface and a cementitious material is investigated. Figure 5.2 shows the geometry of the specimens used to analyse the interface forces between rebar and concrete. They were produced by welding reinforcement bars to steel supports. The rebar had a nominal diameter  $d_b = 25$  mm, with ribs spaced  $s_R = 14.6$  mm and a maximum radial height of 1.8 mm. The bond index of the rebar was  $f_R = \frac{A_R}{u_c s_R} = 0.074$  (where  $A_R = 85 \text{ mm}^2$  refers to the rib area on a transversal section as described in [5] and  $u_c = \pi d_b$  is the contact perimeter) and the reinforcing steel was grade B500B according to EN10080 [4]. The specimens had a width  $b = 20$  mm and the sides of the rebars were cut accordingly (Figure 5.2c-d). The steel bars were placed in a formwork which allowed casting of concrete or mortar on top of the ribbed surface (Figure 5.2a-b). In some cases, sheets of expanded polystyrene were installed at the ends prior to casting in order to reduce the length  $c$  of the test-interface and thus the contact forces (Figure 5.2b).

Most rebars were welded so that the highest point of the ribs remained vertical ( $\beta = 0^\circ$  as shown in Figure 5.2c). However, for some specimens, the rebars were rotated by  $90^\circ$  ( $\beta = 90^\circ$  as shown in Figure 5.2d) or upside-down ( $\beta = 180^\circ$ ), to investigate sides with a different rib pattern. After casting and curing under sealed conditions for at least 28 days, the specimens were demoulded and prepared for testing. The specimens were placed into the test set-up with the steel part on top of the concrete part, as shown in Figure 5.3. The steel part was typically fixed with screws to the testing equipment, using the arrangement depicted in Figure 5.3b. The bottom concrete surface was then glued to a steel plate fixed on the testing equipment using a two-component glue. To avoid detachment of concrete parts due to the development

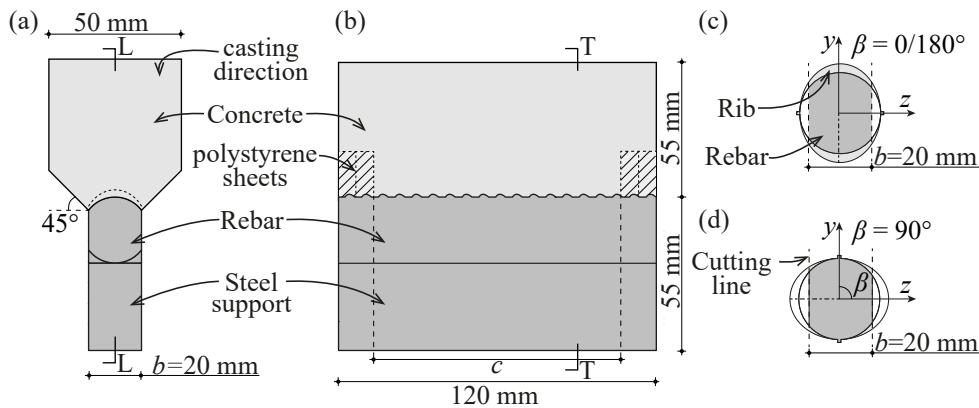


Figure 5.2 – Investigated specimens: (a) cross section T-T; (b) longitudinal section L-L; (c) cross section of rebar with  $\beta = 0^\circ$ ; and (d) cross section of rebar with  $\beta = 90^\circ$

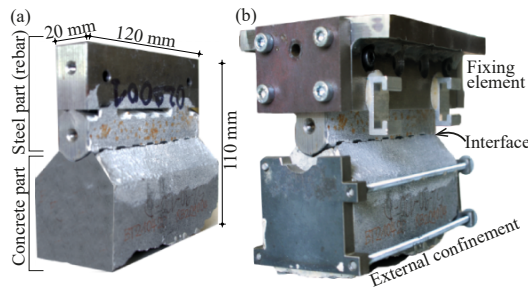


Figure 5.3 – Test specimens: (a) specimen after demoulding and turned upside down; and (b) specimen prepared for testing

of macroscopic secondary cracks during testing (propagation of conical cracks as described by Goto [15]), the material was confined longitudinally using externally applied threaded bars (Figure 5.3b).

Initially, tests were performed using the test set-up described in Pundir et al. [24], where the maximum horizontal force was limited to approximately 19 kN. In order to attain higher forces (thus widening the range of applied kinematics), a larger machine was also used (based on the same principle but consisting of two perpendicular hydraulic jacks connected to a stiff steel frame, see Figure 5.4). In both cases, the specimens were fixed to the machine and the horizontal jack pushed sideways on the specimen (with low-friction slides allowing for horizontal movement), while the vertical jack ensured the predefined kinematics (according to a given angle  $\alpha$ , see Figure 5.4c). Table 5.1 lists the performed tests indicating the effective contact length  $c$ , the applied kinematics (angle  $\alpha$  between the relative displacement vector and the bar axis), the concrete cylinder compressive strength  $f_c$  and the rebar orientation  $\beta$ . While most specimens were tested in Mixed-Mode with constant opening angle  $\alpha$ , tests 210409 and 210410 have been conducted under special kinematics consisting in a Mode I phase until an initial crack opening  $w_0$  was reached (Figure 5.4d), followed by pure Mode II ( $\alpha = 0^\circ$ ). For the specimen notation, the first two digits indicate the casting batch: castings 04, 07 and 09 were made out of concrete, while casting 15 consisted of mortar, as detailed in

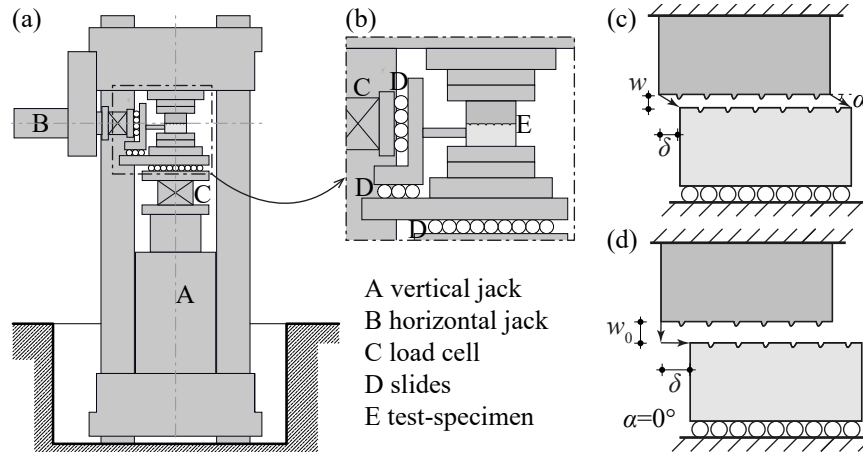


Figure 5.4 – Second test set-up: (a) global view; (b) detail around the specimen; (c) specimen subjected to Mixed-Mode I+II kinematics; and (d) specimen subjected to Mode I followed by Mode II kinematics

Table 5.2, where the mix design and the maximum aggregate size  $D_{\max}$  are also reported.

### 5.2.1 Interface surfaces of rebars

The interface surface between steel and cementitious material has a major influence on the forces developed during testing. To investigate this aspect, two areas from the rebars used for testing were scanned using a Keyence VHX 5000 digital microscope with VH-Z100R lens at 100X magnification. This device can scan an area with a length of about 40 mm, so that two full ribs are recorded for each scan (see Figure 5.5). The obtained data were used to extract longitudinal profiles spaced 1 mm from each other with a data-point every 0.1 mm as shown in Figure 5.5c-d. The profiles show significant flat portions (refer to values  $\zeta \sim 0^\circ$  in Figure 5.5e-f) and are relatively different compared to those of the cracked concrete surfaces presented in [28]. Although the ribs are not symmetric with respect to the centre axis, for  $\beta = 0^\circ$  all profiles are relatively similar, while for  $\beta = 90^\circ$  their shape changes significantly depending on the position (higher profiles at the sides of the surface). This can also be seen in Figure 5.6, where the cumulative distribution of the maximum profile heights is presented for each of the considered cases, showing that the heights are more evenly distributed for  $\beta = 0^\circ$  than for  $\beta = 90^\circ$  (heights measured vertically in the direction of the imposed displacement of the tests and with the radial component). For some rib-profiles, the maximum vertical height is larger than the nominal rib height of 1.80 mm which is measured radially (see Figure 5.6b).

The surface data can be used to determine the rib area on a transversal section and the contact area between rebar and concrete for the various cases considered in this paper. The obtained values are reported in Table 5.3, together with other parameters characterizing the various geometries. Figure 5.5e-f reports the relative occurrence of segments within groups of similar steepness ( $\Delta\zeta = 10^\circ$ ). These distributions show that the rib-profiles are not symmetrical,

## Chapter 5. An interlocking approach for the rebar-to-concrete contact in bond

Table 5.1 – Tests on rebar interfaces, including results at maximum bond stress  $\tau_{\max}$ . For test 1509,  $w_0$  is marked with an asterisk (\*) because the crack opening increased up to  $\approx 0.15$  mm in later stages of the test (see Figure 5.16). The column “contact” reports the rib orientation with respect to the loading direction: “F” indicates contact occurring on the flat side of the rib, “S” on the steep side (see Figure 5.7)

#	$c$ [mm]	$\alpha$ [°]	$w_0$ [mm]	$f_c$ [MPa]	$\beta$ [°]	contact [-]	$\tau_{\max}$ [MPa]	$\sigma(\tau_{\max})$ [MPa]	$\delta(\tau_{\max})$ [mm]	$w(\tau_{\max})$ [mm]
0401	120	25	0.00	34	0	S	3.29	-1.81	0.80	0.37
0402	120	25	0.00	34	0	S	3.71	-1.98	0.70	0.32
0702	120	25	0.00	45	0	F	3.82	-1.65	0.40	0.19
0703	100	20	0.00	45	0	F	7.29	-4.03	0.40	0.15
0704	80	20	0.00	45	0	F	4.43	-3.36	0.90	0.33
0705	80	15	0.00	45	0	F	4.78	-3.40	1.50	0.40
0706	120	30	0.00	45	0	S	1.21	-0.57	1.00	0.58
0708	120	25	0.00	45	0	S	4.10	-2.08	0.90	0.42
0709	120	20	0.00	45	0	F	4.12	-2.38	0.90	0.33
0710	120	20	0.00	45	0	F	3.23	-2.44	0.80	0.29
0902	120	30	0.00	61	0	S	1.68	-0.79	0.40	0.23
1503	120	25	0.00	40	0	S	5.34	-2.00	0.60	0.28
1505	100	20	0.00	40	0	S	5.97	-3.64	1.00	0.36
1506	100	10	0.00	41	0	S	9.45	-7.16	0.80	0.14
1507	100	15	0.00	41	0	S	8.42	-5.18	0.70	0.19
1509	80	0	0.10*	41	0	F	12.20	-8.94	0.50	0.11
1510	80	0	0.15	41	0	F	8.19	-8.86	1.10	0.14
1521	120	5	0.00	41	90	S	6.74	-4.95	0.40	0.03
1522	100	10	0.00	41	90	S	5.37	-3.12	0.40	0.07
1523	100	5	0.00	41	90	F	5.80	-6.31	0.70	0.06
1524	80	5	0.00	41	90	S	4.13	-3.43	0.50	0.04
1525	100	20	0.00	40	180	F	5.37	-3.15	0.70	0.25

Table 5.2 – Mix designs; additional information on series 15 can be found in [24] where it corresponds to series 3104)

Series #	04	07	09	15
$D_{\max}$ [mm]	8	8	16	2
Water [kg/m <sup>3</sup> ]	204	177	165	250
Cement [kg/m <sup>3</sup> ]	316	321	330	500
Aggregates [kg/m <sup>3</sup> ]	1809	1853	1880	1500
$f_{c,28}$ [MPa]	28.0	40.2	61.1	38.3

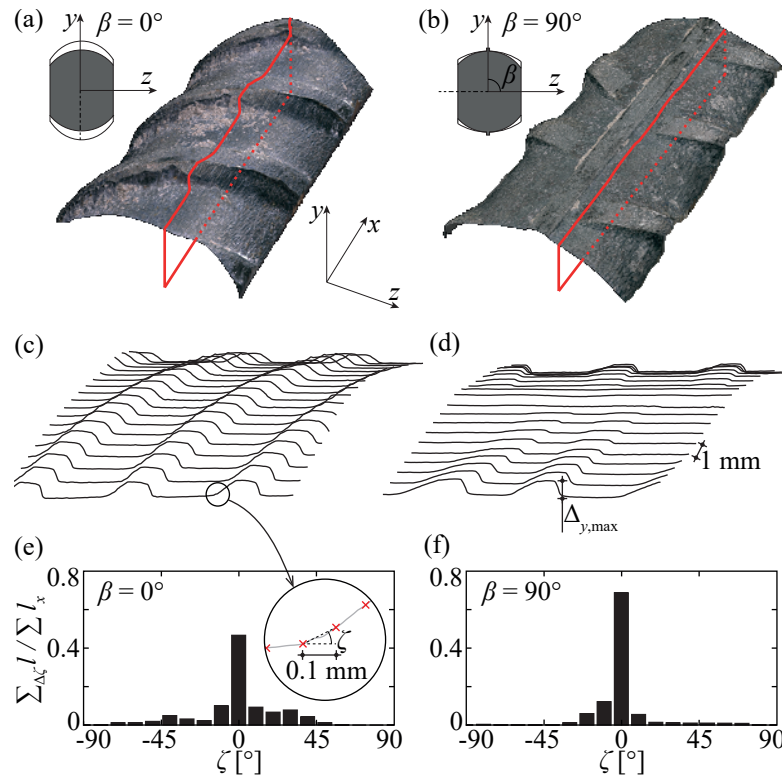


Figure 5.5 – Rebar surface scans (a) rebar with  $\beta = 0^\circ$ ; (b) rebar with  $\beta = 90^\circ$ ; (c)-(d) extracted longitudinal profiles; and (e)-(f) Distribution of surface angles  $\zeta$  for the two cases

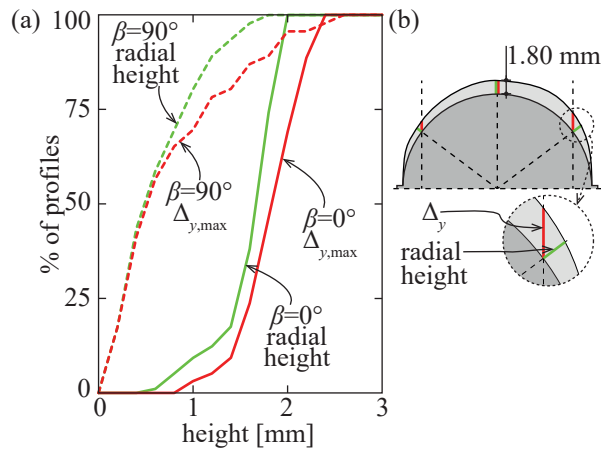


Figure 5.6 – Profile heights (a) relative distributions; and (b) detail describing differences between vertical (red) and radial (green) heights

Table 5.3 – Geometric characteristics for the considered cases

	Full rebar	$\beta = 0/180^\circ$	$\beta = 90^\circ$	Unit
$d_b$	25.0	-	-	[mm]
$b$	-	20.0	20.0	[mm]
$u_c$	78.5	23.1	23.1	[mm]
$s_R$	14.6	14.6	14.6	[mm]
$A_R$	85.0	36.2	15.0	[mm <sup>2</sup> ]
$f_R$	0.074	0.107	0.044	[-]

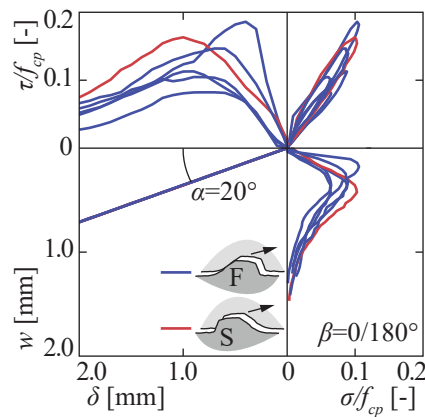


Figure 5.7 – Load-displacement curves for tests with the same kinematics and different orientation of the rib profiles

but are instead characterized by a flatter and a steeper side (respectively left and right in Figure 5.5c-d). Depending on the orientation of the rib profiles with respect to the loading direction, the contact between steel and concrete can differ. The orientation is thus specified in the column “contact” of Table 5.1. For tests marked with “F”, the contact is located on the flatter sides of the ribs, while for tests marked with “S”, the contact is located on the steep side (see Figure 5.7). Despite these differences in geometry, it was observed that the loading direction had no significant influence on the response for the tested specimens (compared to the orientation of the bar, and the variations in concrete properties), as shown in Figure 5.7 for six nominally-identical specimens (one tested against the steep side of the ribs (“S”) and five against the flat side (“F”)). The plots show that the behaviour for tests with same applied kinematics and different loading directions remains within the experimental scatter.

### 5.2.2 Main experimental results

The complete load-displacement curves obtained during testing are reported in Section 5.3. In this section, some detailed considerations are performed, focusing in particular on the maximum value of the contact stresses. Figure 5.8a shows the test results for a typical Mixed-Mode test performed on a rebar interface, which consists in curves relating the two main kinematic test parameters ( $w$ ,  $\delta$ ) and the two applied stresses ( $\sigma$ ,  $\tau$ ). For low levels of load, the

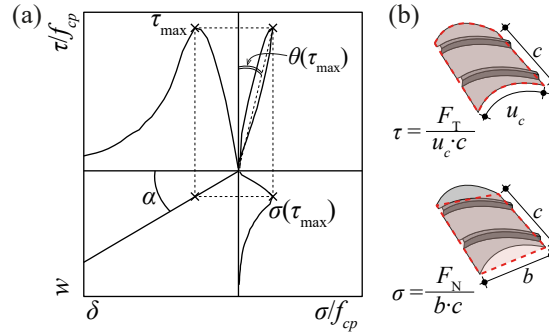


Figure 5.8 – (a) Typical test result; and (b) geometrical normalization of measured forces

normalized confinement and bond stresses increase almost linearly. The stiffness in this phase shows a significant level of variability, suggesting that first stages are not merely governed by the macroscopic elastic material response, but also by the variation of surface adhesion and the potential presence of voids (discussed in [14]) or aggregates [24] next to the contact surface. As the load increases, a non-linear phase follows, leading to the peak bond value  $\tau_{\max}$ . Thereafter, the bond stresses  $\tau$  gradually decrease, while the highest normal stress  $|\sigma|_{\max}$  is reached shortly thereafter and eventually also decreases.

Different normalizations are used to derive  $\tau$  and  $\sigma$  from the normal and tangential forces ( $F_N$  and  $F_T$  respectively). As shown in Figure 5.8b,  $\sigma$  is the normal force divided by the horizontal projection of the rebar surface ( $\sigma = \frac{F_N}{b \cdot c}$ ), while  $\tau$  is the tangential force divided by the curved surface of the bar ( $\tau = \frac{F_T}{u_c \cdot c}$ , with  $u_c = 23.1$  mm for the investigated geometry). This difference accounts for the fact that the bond stress is an average of stresses which are all oriented longitudinally, whereas the nominal confinement stress  $\sigma$  results from the vectorial sum of radially oriented stresses normal to the bar surface. Figure 5.9 shows the peak bond stresses  $\tau_{\max}$  and the associated confinement stress,  $\sigma(\tau_{\max})$  as a function of the opening angle  $\alpha_{eq} = \arctan\left(\frac{w(\tau_{\max})}{\delta(\tau_{\max})}\right)$ . To account for the various strengths of the concrete and mortar mixes, in figures and tables the stresses are normalized with respect to  $f_{cp} = \eta_{f_c} f_c$ , where  $f_c$  is the cylinder concrete strength at the day of testing and  $\eta_{f_c}$  is a coefficient accounting for the brittleness of concrete:

$$\eta_{f_c} = \left(\frac{f_{c,\text{ref}}}{f_c}\right)^{1/3} \leq 1 \quad (5.1)$$

with  $f_{c,\text{ref}} = 30$  MPa (see [6, 22]). In general, test results are subjected to some scatter, particularly those performed on concrete specimens, where the possible contact and interaction between ribs and large aggregates led to higher variations than for the mortar specimens of series 15 (see also [24]). Some trends can however be clearly identified. For instance, the peak bond stresses are strongly dependent on the value of the opening angle  $\alpha_{eq}$ , with flatter kinematics resulting in higher peak stresses. Bars oriented at  $\beta = 0^\circ$  and  $\beta = 180^\circ$  behaved similarly, and will be grouped as  $\beta = 0/180^\circ$ . For  $\beta = 90^\circ$ , the lower ribs (see Figure 5.5e-f and Figure 5.6) resulted in smaller stresses, as shown in Figure 5.9.

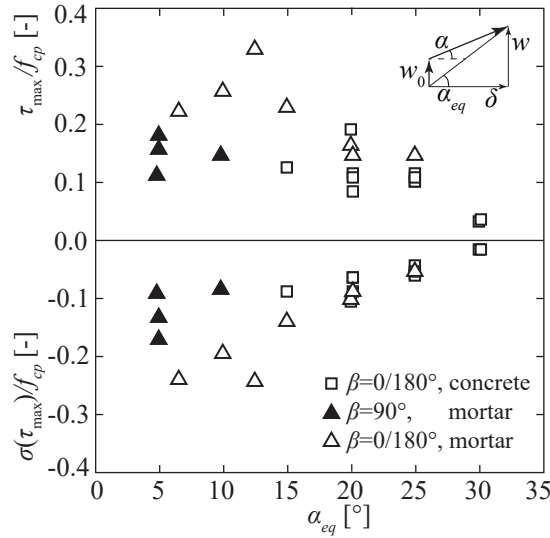


Figure 5.9 – Peak stresses as a function of  $\alpha_{eq}$

With respect to the interface opening and sliding at maximum bond stress (Figure 5.10), no clear trend is visible for the sliding  $\delta$ , and the opening  $w$  increases for increasing values of  $\alpha_{eq}$  (Figure 5.10). It can be noted that the displacements could be normalized by means of an equivalent rib height, defined as the rib area on a transversal section  $A_R$  divided by the specimen width  $b$ . Although this normalization would result in a reduction of the experimental scatter, it was not used for simplicity and due to the limited amount of different cases which are considered in the present investigation.

An important parameter characterizing the interlock phenomenon and deserving to be commented is the ratio between bond and confinement stresses, which can be expressed by means of the value  $\theta = \arctan(|\sigma|/\tau)$  (corresponding to the angle in the  $\sigma - \tau$  plot shown in Figure 5.8a). This parameter is relevant since it is one of the most important parameters in the model by Tepfers [27] (see angle  $\theta$  in Figure 5.1b) and is also used elsewhere [9, 14]. Figure 5.11a shows that the value of  $\theta$  evolves during the tests (refer also to Figure 5.8a) and reveals a dependence on the applied kinematic angle  $\alpha$ . For a typical case,  $\tau$  increases initially (increase also related to the activation of adhesion) while the values of  $\sigma$  remain low, resulting into values  $\theta < 20^\circ$ . As the displacements increase, larger areas engage contact, increasing the bond stress. Also, due to the larger amount of vertical dilatation, the confinement stress  $\sigma$  increases to ensure the imposed kinematics. This results in increasing values of  $\theta$ , up to  $\theta \approx 45^\circ$  ( $|\sigma| \approx \tau$ ). For lower values of  $\alpha$ , the relative increase in  $\sigma$  becomes more significant resulting into higher values of  $\theta$ . This is particularly noticeable in tests with Mode I kinematics followed by Mode II ( $\alpha = 0^\circ$ ). In these cases, no additional opening is allowed after the initial phase, and the large confinement stress  $\sigma$  results in particularly high values of  $\theta$  (refer to Figure 5.11a). The increased values of  $\theta$  for smaller angles  $\alpha_{eq}$  is also visible in Figure 5.11b, where the confinement stress  $\sigma$  is represented as a function of the bond stress  $\tau$ . It can be seen that the development of  $\theta$  is associated to the non-linear relationship between  $\tau$  and  $\sigma$  (the angle  $\theta$  being directly visible in a  $\tau - \sigma$  plot, see Figure 5.8a).

### 5.3. Modelling of bond by consideration of surface interlocking

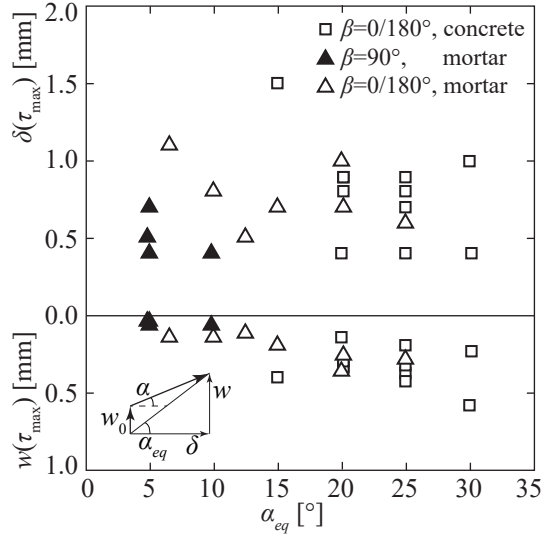


Figure 5.10 – Displacements at  $\tau_{max}$  as a function of  $\alpha_{eq}$

### 5.3 Modelling of bond by consideration of surface interlocking

#### 5.3.1 Model description

In this section, the model for aggregate interlocking presented in [28], based on the consideration of rough surface contact and whose basic assumptions will be briefly recalled, is adapted to estimate the contact forces in the rib-interlocking tests described in Section 5.2. This approach requires tailoring the surface roughness properties to those of the rebar ribs as well as suitably considering the particularities in terms of materials, interfaces and confinement conditions of localized contacts.

To that aim, the contact forces by mechanical engagement will be estimated as presented in Figure 5.12a. The geometry of the ribs is considered according to the surface measurements performed (see Figure 5.5). Such geometry will be used together with the applied kinematics to define the area that requires to be deformed ( $a_p$  in Figure 5.12b) according to [24]. When contact occurs, stresses develop at the contact interface (refer to Figure 5.12a), whose activation is calculated based on the assumption of Li et al. [17] with an elastic-plastic behaviour:

$$\sigma_c = 343 f_c^{1/3} \lambda_c \leq \eta_c f_c \quad [\text{MPa, mm}] \quad (5.2)$$

where  $f_c$  is the concrete compressive strength in [MPa] and  $\lambda_c$  refers to the relative displacement describing the activation of the contact in [mm]. For the analysis of aggregate interlocking presented in [28], the value  $\lambda_c$  was assumed to be dependent on the surface penetration and calculated for each segment of a given section, thus neglecting the progressive accumula-

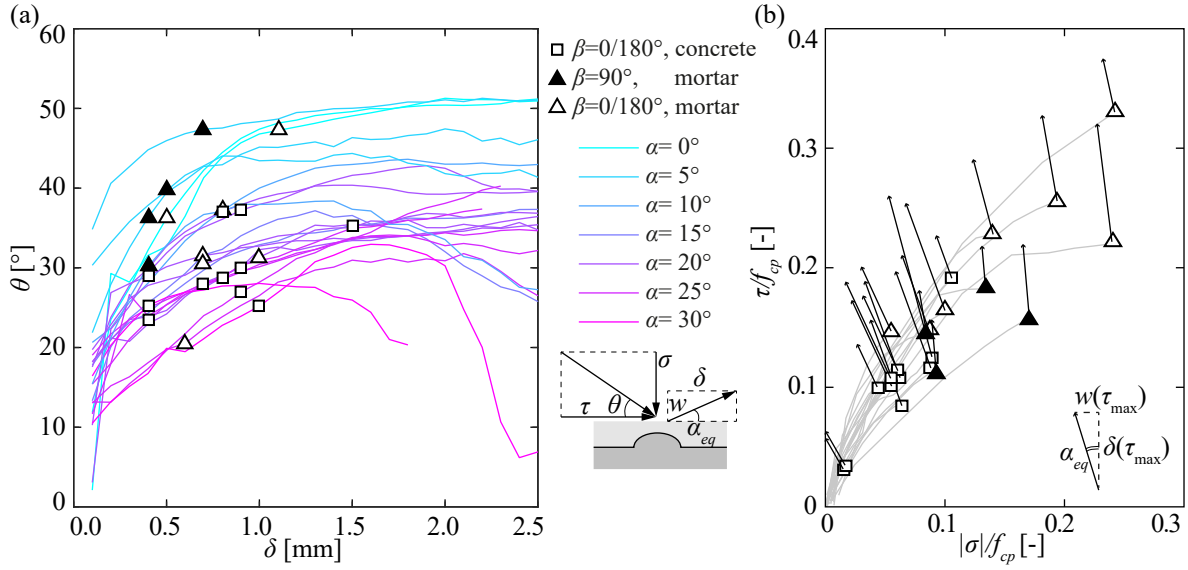


Figure 5.11 – Relationship between  $\sigma$  and  $\tau$ : (a) Value of  $\theta = \arctan(|\sigma|/\tau)$  as a function of  $\delta$  (the markers indicate the values associated to the peak bond stress  $\tau_{\max}$ ); and (b) Relation between  $|\sigma|$  and  $\tau$  up to the peak bond stress  $\tau_{\max}$  (the vectors show the displacement at peak stress  $\tau_{\max}$ , with  $w$  and  $\delta$  associated to  $\sigma$  and  $\tau$ , respectively)

tion of damage. This approach is adapted for the present case on the basis of a calculation of the area of the concrete deformed near the ribs (see Figure 5.12b). The contact activation is thus determined with an adjusted average penetration depth (penetration area divided by contact length) with the following expression:

$$\lambda_c = \frac{0.2 a_{pc}}{\sqrt{l_x^2 + l_y^2}} \quad [\text{mm}] \quad (5.3)$$

where  $l_x$  and  $l_y$  refer to the projections of the contact length (Figure 5.12a) and  $a_{pc}$  is the cumulative penetration, defined as the sum of the previously deformed areas at each load-step ( $a_{p,i}$ ):

$$a_{pc} = \sum_{i=1}^{i=n} a_{p,i} \quad [\text{mm}^2] \quad (5.4)$$

The maximum stress that can be transferred by contact in Equation 5.2 is limited by the compressive strength of the concrete matrix estimated as  $\eta_c f_c$ . In this expression, the term  $\eta_c$  accounts both for the limited deformation capacity of concrete and its confined response [28]. The general formulation of the factor  $\eta_c$  can be expressed as:

$$\eta_c = \eta_{f_c} + \eta_{\text{conf}} \quad [-] \quad (5.5)$$

### 5.3. Modelling of bond by consideration of surface interlocking

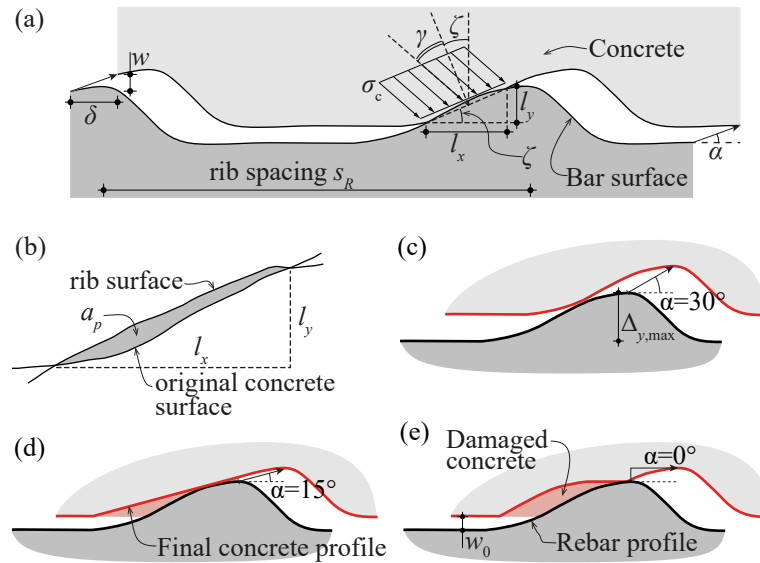


Figure 5.12 – (a) Engagement of contact stresses between bar ribs and concrete; (b) detail of damaged area (c) rebar-rib subjected to  $\alpha = 30^\circ$  (barely scratched concrete surface); (d) rebar-rib subjected to  $\alpha = 15^\circ$  (deeper penetration into the material); and (e) rebar-rib subjected to Mode I followed by Mode II

where  $\eta_{fc}$  accounts for the brittleness of high strength concrete in compression (as previously defined in Equation 5.1), accounting for the fact that some regions of concrete might be in softening while others attain their peak strength. The parameter  $\eta_{conf}$  accounts for the enhanced compressive resistance of confined concrete [23]. As suggested in Figure 5.12c-e, the amount of engaged material in the contact (and thus potentially confined) changes as a function of the applied kinematics (angle  $\alpha$  and initial opening  $w_0$ ) and the shape of the surface profile. Higher ribs engage more concrete which is thus better confined, resulting in larger contact forces. The confinement also depends on the kinematics, and in particular on the crack opening  $w$ . The role of the angle  $\alpha$  is also shown in Figure 5.12c-e, where the amount of the penetration area is shown to highly depend on this parameter, with better confinement conditions for lower values of  $\alpha$ . Compared to contacts in concrete cracks (where  $\eta_{conf}$  varies as a function of the roughness, see [28]), the cases investigated in this article are characterized by a level of confinement which is relatively uniform for each surface type. The parameter  $\eta_{conf}$  is thus adopted as follows:

$$\eta_{conf} = \frac{\Delta_{y,max}}{20 w} \leq 3 \quad [-] \quad (5.6)$$

The expression accounts for the fact that confinement increases when more material is engaged in the contact, corresponding to higher roughness and larger values of  $\Delta_{y,max}$ . The crack opening  $w$  (related also to the applied kinematics  $\alpha$ ) has the opposite effect and therefore tends to reduce  $\eta_{conf}$  (Figure 5.12c-d).

As for aggregate interlock [17], the average contact stress  $\sigma_c$  calculated according to previ-

ously introduced equations is assumed to develop at an angle  $\gamma$  with respect to the contact surface, thus accounting for local friction (Figure 5.12a). For concrete surfaces, characterized by large number of contacts with varying properties, good estimates are obtained using a constant value of  $\gamma$  (for instance,  $\gamma = 10^\circ$  according to [28]), which represents an average for the whole surface. In the present case, with more uniform contact properties and profiles,  $\gamma$  can be estimated more accurately by using the experimental evidence shown in Figure 5.11a. According to the experimental measurements, the bond response is characterized at first contact stages by low values of the angle  $\theta$  between the compression struts and the bar, and this value increases thereafter. As shown in Figure 5.11a, this observation is consistent for all considered bar orientations and kinematics. Following this evidence, the value of the friction angle  $\gamma$  is assumed for modelling purposes to depend upon the relative sliding of the bar (as the parameter characterizing the activation of bond). For low levels of sliding, the value of the angle  $\gamma$  is considered to be higher (corresponding to lower values of  $\theta$ ), and decreases thereafter (corresponding to higher values of  $\theta$ ). In absence of a more precise formulation, a linear relationship according to the experimental evidence will be assumed:

$$\gamma = 30^\circ \left(1 - \frac{\delta}{\delta_{ref}}\right) \geq 0 \quad (5.7)$$

with  $\delta_{ref} = 10$  mm. Having determined the intensity and orientation of the stresses acting upon the contact plane, they can be transferred to the global reference system with the following equations:

$$\tau = \frac{1}{u_c c} \sum_{\text{sections}} \sigma_c l_x (\cos^2 \gamma \tan \zeta + \sin \gamma \cos \gamma) \quad (5.8a)$$

$$\sigma = \frac{1}{b c} \sum_{\text{sections}} \sigma_c l_x (\cos^2 \gamma - \sin \gamma \cos \gamma \tan \zeta) \quad (5.8b)$$

where  $\zeta$  is the inclination of the contact surface, defined as shown in Figure 5.12a:

$$\zeta = \arctan \left( \frac{l_y}{l_x} \right) \quad (5.9)$$

As it will be shown, such approach provides reasonable estimates for  $\tau$  and  $\sigma$  near the maximum tangential stress. For low amounts of sliding, the measured values of  $\theta$  are however significantly lower as shown in Figure 5.11a. This is mostly due to the role of the adhesion between concrete and rebar, which allows for development of bond stresses without significant confinement stresses. This contribution will be accounted for in the following by considering the bond strength of plain bars (bars without ribs) as a lower bound of the adhesion stresses, but decreasing this contribution as a function of the opening of the interface. As a first estimate of this contribution, the bond strength of plain bars is adopted from Model Code 2010 [6] with a progressive activation of this contribution for increasing levels of bar sliding and a linear

### 5.3. Modelling of bond by consideration of surface interlocking

decay for increasing openings of the interface crack:

$$\tau_{ad} = 0.3 \sqrt{f_c} \sqrt{\frac{\delta}{\delta_1}} \left(1 - \frac{w}{w_1}\right) \geq 0 \quad \text{if } \delta \leq \delta_1 \text{ [MPa]} \quad (5.10a)$$

$$\tau_{ad} = 0.3 \sqrt{f_c} \left(1 - \frac{w}{w_1}\right) \geq 0 \quad \text{if } \delta > \delta_1 \text{ [MPa]} \quad (5.10b)$$

where  $w_1 = 0.1$  mm is assumed as the limit crack opening at which adhesion stresses vanish and  $\delta_1$  corresponds to the relative slip for their full activation (assumed to be 0.1 mm according to [6]).

#### 5.3.2 Model results

With the addition of the initial adhesion stresses, the model results provide estimates of  $\theta$  which are consistent with the experimentally observed trend at all levels of sliding, as shown in Figure 5.13a (whose results can be directly compared to the experimental measurements of Figure 5.11a). The good agreement can also be seen in Figure 5.13b, where the calculated angle  $\theta$  at peak bond stress  $\tau_{\max}$  is compared to the experimental results (see Figure 5.11b). Moreover, the model is capable to capture the difference between the confinement stresses (and thus the angle  $\theta$ ) activated for  $\beta = 0/180^\circ$  and for  $\beta = 90^\circ$ , respectively. In addition, the calculated values of  $\theta$  are similar to those obtained for pull-out tests under constant confinement stress performed by Modena [21] and Gambarova and Rosati [12] and reported in [5], where  $\theta$  varies from approximately  $22^\circ$  for cases with low bond stresses up to  $33^\circ$  for high bond stresses. The same behaviour is also observed in tests of Gambarova and Karakoc [9] shown in [14], where  $\theta$  varies between  $35^\circ$  and  $50^\circ$ .

Figure 5.14 shows the full behaviour obtained applying the mechanical model to tests on rebars with  $\beta = 0/180^\circ$ , while the case  $\beta = 90^\circ$  is presented in Figure 5.15. Figure 5.16 shows two Mode II tests, one with constant crack opening and one where  $w$  increased from  $w_0 = 0.10$  to  $\approx 0.15$  mm. The tests are normalized by  $f_{cp}$ , thus considering the concrete strength and brittleness. For each value of  $\alpha$ , the model calculations were performed using an average of the  $f_c$  values of the corresponding tests. Moreover, with respect to the asymmetric shape of the ribs discussed in Section 5.2.1, the model results represent the average of two calculations, one for each rib orientation.

When taking into account the amount of experimental scatter (see coefficients of variation of experimental values shown in the left-hand side part of Table 5.4), reasonable agreement is obtained in terms of maximum bond stress  $\tau_{\max}$  for most cases (see Table 5.4). The overall load-displacement curves and estimates for  $\theta$  show good agreement as well. This indicates that the proposed expressions for evaluation of the various contact and strength parameters provide a reasonable estimate for them. Nevertheless, to generalize the presented approach, further experimental evidence is necessary in order to investigate different rebar geometries and sizes, various materials and to consider a wider range of kinematics.

**Chapter 5. An interlocking approach for the rebar-to-concrete contact in bond**

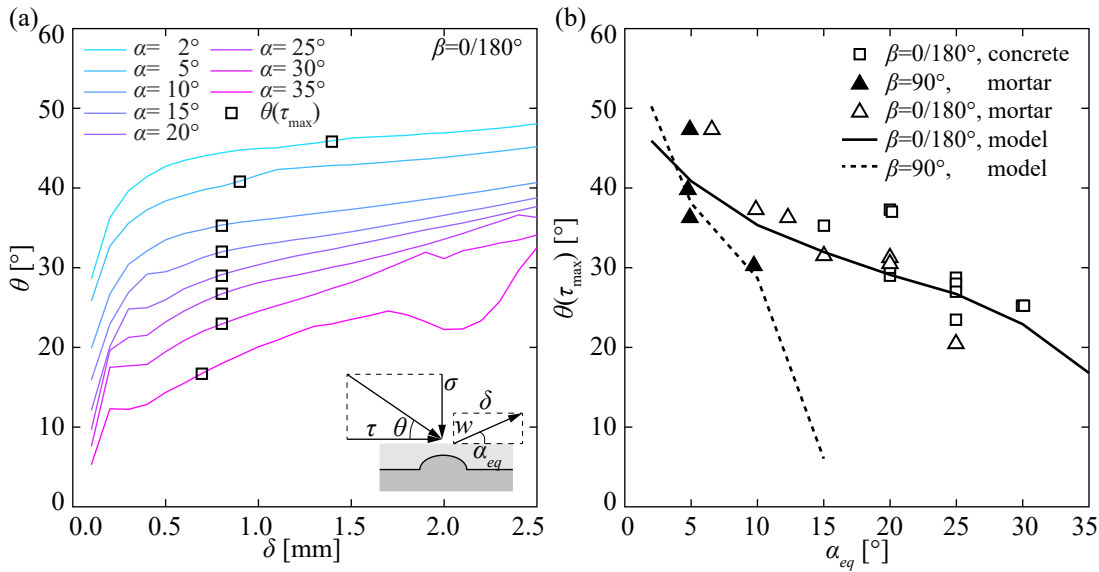


Figure 5.13 – Model estimates for  $\theta = \arctan(|\sigma|/\tau)$  as a function of  $\delta$  (surfaces with  $\beta = 0/180^\circ$ ; the marker indicates the value at  $\tau_{max}$ ); and (b) comparison of the angle  $\theta$  at peak bond stress  $\theta(\tau_{max})$  between experimental and calculated values (see also Figure 5.11b)

Table 5.4 – Experimental and model results at  $\tau_{max}$ ; the COV (in percent) for averaged values is reported in brackets

			Experimental results (averages)					Model results [exp/mod]			
$\alpha$	$w_0$	$\beta$	# of tests	$\frac{\tau_{max}}{f_{cp}}$	$\frac{\sigma(\tau_{max})}{f_{cp}}$	$\delta(\tau_{max})$	$w(\tau_{max})$	$\tau_{max}$	$\sigma(\tau_{max})$	$\delta(\tau_{max})$	$w(\tau_{max})$
[°]	[mm]	[°]	[-]	[-]	[-]	[-]	[-]	[-]	[-]	[-]	[-]
<i>Mixed-Mode tests with <math>\beta = 0/180^\circ</math></i>											
10	0.00	0	1	0.26 (-)	-0.19 (-)	0.80 (-)	0.14 (-)	0.97	1.03	1.00	1.00
15	0.00	0	2	0.18 (45)	-0.12 (36)	1.10 (51)	0.29 (52)	0.88	0.92	1.38	1.37
20	0.00	0/180	6	0.13 (30)	-0.08 (23)	0.78 (27)	0.28 (27)	0.88	0.99	0.98	0.98
25	0.00	0	5	0.12 (18)	-0.06 (16)	0.68 (28)	0.32 (28)	1.00	0.93	0.85	0.85
30	0.00	0	2	0.03 (1)	-0.02 (1)	0.70 (61)	0.40 (61)	0.44	0.49	0.87	0.87
AVG			-	-	-	-	-	0.84	0.87	1.02	1.01
COV			-	-	-	-	-	(27)	(25)	(21)	(21)
<i>Mixed-Mode tests with <math>\beta = 90^\circ</math></i>											
5	0.00	90	3	0.15 (24)	-0.13 (30)	0.53 (29)	0.05 (29)	1.20	1.35	0.76	0.74
10	0.00	90	1	0.15 (-)	-0.08 (-)	0.40 (-)	0.07 (-)	2.22	2.36	0.80	0.78
<i>Mode II tests with <math>\beta = 0^\circ</math></i>											
0	0.10*	0	1	0.33 (-)	-0.24 (-)	0.50 (-)	0.11 (-)	1.02	0.92	0.63	1.10
0	0.15	0	1	0.22 (-)	-0.24 (-)	1.10 (-)	0.14 (-)	0.70	0.75	0.61	0.92

### 5.3. Modelling of bond by consideration of surface interlocking

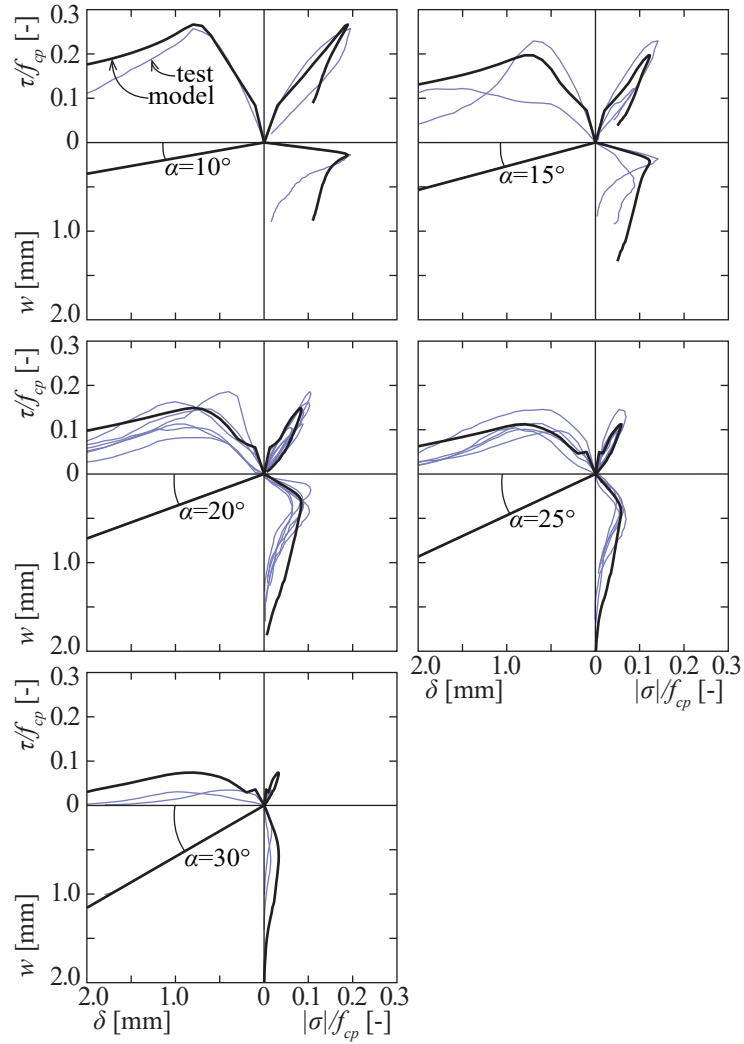


Figure 5.14 – Model results for surface with  $\beta = 0/180^\circ$

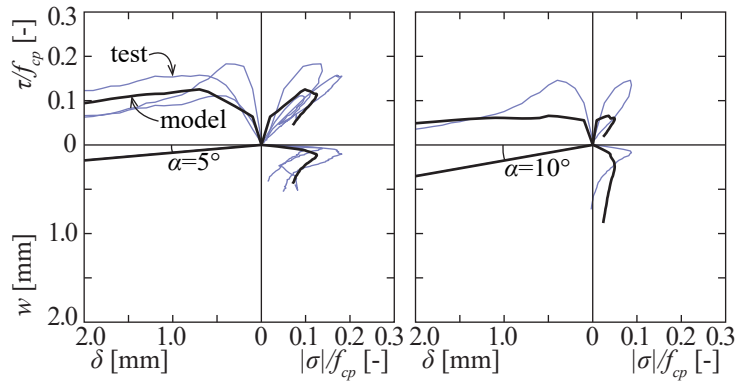


Figure 5.15 – Model results for surface with  $\beta = 90^\circ$

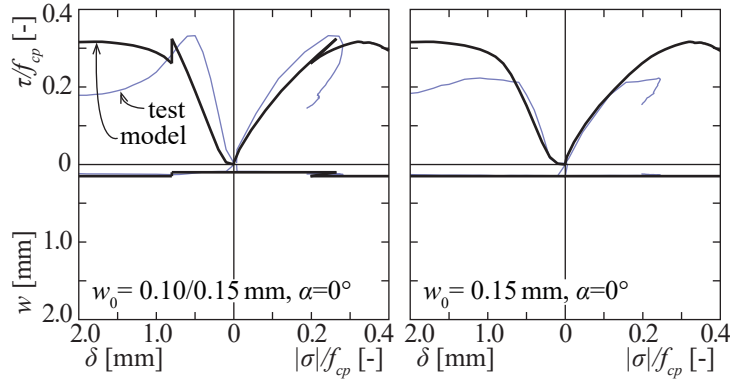


Figure 5.16 – Model results for Mode II tests,  $\beta = 0^\circ$  (the discontinuity in the model estimates in the left plot correspond to an increase in crack opening from 0.10 mm to 0.15 mm)

## 5.4 Application to bond under cracked conditions

In this section, the model is further applied to a particular aspect concerning bond, namely the reduction in bond strength occurring when cracks develop in a plane parallel to the rebars and failure occurs due to pull-out, as discussed in Brantschen et al. [1] (Figure 5.1c-d).

This aspect relates to a practical situation, as regions where bond stresses develop are in many cases subjected to cracking (as for two-way slabs for instance). In a previous work by Brantschen et al. [1], this phenomenon was investigated in detail showing that the ratio  $f_b/f_{b0}$  (where  $f_b$  refers to the bond strength related to pull-out failures in cracked conditions and  $f_{b0}$  to the bond strength in uncracked conditions, refer to Figure 5.1b,d) can be described as a function of the crack opening and the rib geometry. Similar to the current work, the model of Brantschen et al. [1] is based on the analysis of the decrease of rib contact area for increasing crack opening, and its results were confirmed by several pull-out tests performed on cracked concrete specimens with various crack openings. Such tests are similar to the Mode I-Mode II tests presented in this paper, as the concrete surrounding the rebars is cracked before the bars are pulled out of the concrete in Mode II (Figure 5.17a-c). The results presented in [1] can thus be reproduced on the basis of the model presented in this paper. Equation (5.8a) allows for the calculation of the bond forces, and their relative decay can be compared with the experimental results for various crack openings. To that aim, the average bond stress can be calculated based on the longitudinal contact forces for a given crack width ( $F_b(w_b)$ ):

$$f_b = \frac{F_b(w_b)}{d_b \pi c} \quad (5.11)$$

The calculation of  $F_b$  can be performed assuming that the contribution of the sides of the rebar (where the presence of the crack decreases the interlocking potential) is negligible. The maximum force  $F_b(w_b)$  developed during a pull-out test with an initial crack of  $w_b$  corresponds thus to twice (one per side) the maximum force  $F_{H,\max}(w_b/2)$  developed by

Mode II kinematics with an initial opening  $w_0 = w_b/2$ . (see Figure 5.17a-c):

$$F_b(w_b) = 2 F_{H,\max}(w_b/2) \quad (5.12)$$

By introducing Equation 5.12 into Equation 5.11, the maximum bond stress results:

$$f_b = \frac{2 F_{H,\max}(w_b/2)}{d_b \pi c} \quad (5.13)$$

On this basis, the ratio  $f_b/f_{b0}$  can be directly calculated. With respect to the value  $f_{b0}$ , the approximation  $f_{b0} \approx 2.5 f_{ct} \approx 0.75 f_c^{2/3}$  (similar value to [20]) will be adopted as an average value for pull-out conditions.

Figure 5.17d reports experimental results of pull-out tests in cracked conditions from the literature [1, 8, 10, 11, 13, 18, 19, 25] as collected by Brantschen et al. [1] and with the addition of the two Mode I-Mode II tests from the present experimental programme (1509 and 1510 marked in grey). It can be observed that these two interlocking tests are in agreement with the rest of the experimental data. Crack openings are normalized with  $\frac{\kappa_f w_b}{f_R(u_c/\pi)}$ , where  $u_c$  is the contact perimeter,  $\kappa_f$  a geometric factor usually taken as  $0.75 n_l$  [1] and  $n_l$  the number of ribs on any transversal rebar-section (refer to Table 5.3 for information on  $f_R$ ; for the off-cut specimens used in the present research it was considered  $n_l = 4$ , corresponding to the geometry of a bar with four lugs were the ones on the sides were removed). The plot shows also the estimates from the model described in [1] as well as the results obtained with the model of Section 5.3. The results of this model are shown for different levels of initial crack opening and for two potential rib orientations ( $\beta = 0^\circ$  and  $\beta = 90^\circ$ ). The results of the proposed model correctly describe the decay on the bond stresses for increasing crack openings (Figure 5.17d). The strength is somewhat overestimated for very low crack openings where other failure modes (as rip-off of the concrete between ribs) can be governing.

## 5.5 Conclusions

The present paper deals with the bond and confinement stresses between reinforcement bars and the surrounding concrete as a function of the material and contact surface properties and accounting for the contact kinematics. An experimental programme consisting in rebar-to-concrete interfaces subjected to various Mixed-Mode kinematics is presented, as well as mechanical and modelling considerations. The main conclusions of the paper are given below.

1. There is a clear analogy between aggregate interlock forces and rebar-to-concrete bond forces. Both depend on the mechanical engagement of surfaces and are influenced by similar parameters.
2. Tests on bar-to-concrete interfaces rapidly develop high tangential forces, while confinement forces increase only for larger amounts of sliding (corresponding to an increased necessity to arrest dilatancy).

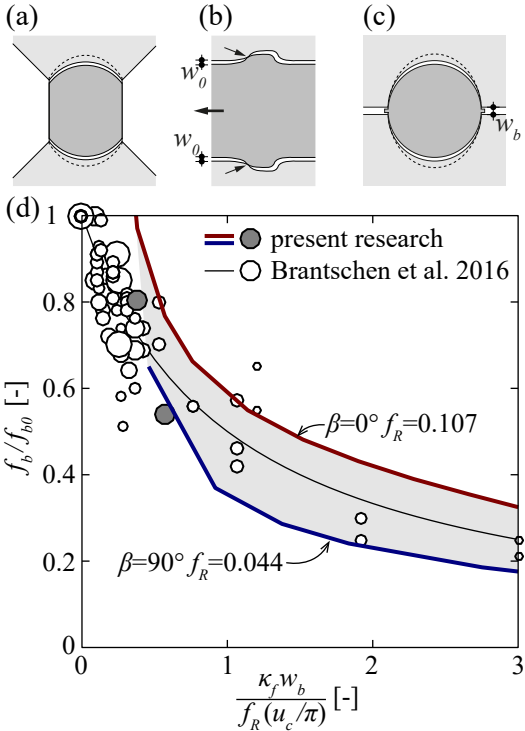


Figure 5.17 – Analogy between interlocking of rebar surfaces and pull-out tests (a) transversal section of a double interlocking test; (b) longitudinal section; (c) transversal section of pre-cracked pull-out test; and (d) bond strength reduction as a function of crack opening

3. The rib geometry can be taken into account to consistently investigate the phenomenon of bond for a given kinematics. Variations in rib geometries influence the calculated contact properties, and might thus be one of the sources of experimental scatter.
4. Since the rib's geometry and height are not constant over the bar perimeter, the experiments and the model show a clear influence of the bar orientation on the activated bond and confinement stresses.
5. The model is also shown to be suitable for estimating the maximum bond pull-out force under cracked conditions. The results are compared to pull-out tests and a model from the literature [1], showing sound agreement. The mechanical analogies between aggregate interlocking and bond in cracked conditions are thus shown to be sufficient for a similar treatment of the two phenomena.

## Bibliography

- [1] Brantschen, F., Faria, D., Fernández Ruiz, M., and Muttoni, A. (2016). Bond behaviour of straight, hooked, U-shaped and headed bars in cracked concrete. *Structural Concrete*, 17(5):799–810.
- [2] Cairns, J. (2015). Bond and anchorage of embedded steel reinforcement in fib Model Code 2010. *Structural Concrete*, 16(1):45–55.
- [3] Cavagnis, F., Fernández Ruiz, M., and Muttoni, A. (2017). An analysis of the shear-transfer actions in reinforced concrete members without transverse reinforcement based on refined experimental measurements. *Structural Concrete*, 19(1):49–64.
- [4] CEN (European Committee for Standardization) (2005). *CEN 10080:2005 “Steel for the reinforcement of concrete: Weldable reinforcing steel-General”*. Brussels, Belgium.
- [5] fib (2000). *fib Bulletin 10: Bond of reinforcement in concrete*. fib, 434 p.
- [6] fib (2013). *fib Model Code for Concrete structures 2010*. Ernst & Sohn, 402 p, Germany.
- [7] fib (2014). *fib Bulletin 72. Bond and anchorage of embedded reinforcement: Background to the fib Model Code for Concrete Structures 2010*. fib, 170 p.
- [8] Gambarova, P. G. (1981). On aggregate interlock mechanism in reinforced concrete plates with extensive cracking. *IABSE reports of the working commissions*, 34:99–120.
- [9] Gambarova, P. G. and Karakoc, C. (1982). Shear-confinement interaction at the bar-to-concrete interface. *Bond in concrete*, pages 82–98.
- [10] Gambarova, P. G. and Rosati, G. (1990). Aderenza armatura-calcestruzzo e fessurazione longitudinale, per barre di grosso diametro. *Studi e Ricerche*, 12:45–79.

## Chapter 5. An interlocking approach for the rebar-to-concrete contact in bond

Table 5.5 – Symbols and notations: Latin letters

Symbol	Description	Dimension
$A_R$	rib area on transversal section	area
F	rib contact occurs on flat side	-
$F_N$	normal force	force
$F_T$	tangential force	force
$F_b$	pull-out force	force
S	rib contact occurs on steep side	-
$a_p$	area of penetration	area
$a_{pc}$	cumulative penetration	area
$b$	specimen width	length
$c$	specimen length	length
$d_b$	rebar diameter	length
$f_R$	bond index	-
$f_b$	bond resistance in cracked concrete	stress
$f_{b0}$	bond res. in un-cracked concrete	stress
$f_c$	concrete compressive resistance	stress
$f_{c,28}$	compressive resistance at 28 days	stress
$f_{c,ref}$	reference compressive resistance	stress
$f_{cp}$	concrete plastic resistance	stress
$f_{ct}$	concrete tensile resistance	stress
$i$	generic load step	-
$l_x$	horizontal contact length	length
$l_y$	vertical contact length	length
$n_l$	number of ribs	-
$s_1$	limit sliding value for adherence	length
$s_R$	rib spacing	length
$u_c$	contact perimeter	length
$w$	crack or interface opening	length
$w_0$	initial Mode I opening	length
$w_1$	limit opening value for adherence	length
$w_b$	crack opening in pull-out test	length

Table 5.6 – Symbols and notations: Greek letters

Symbol	Description	Dimension
$\Delta_{y,max}$	max. height of surface profile	length
$\alpha$	Mixed-Mode opening angle	angle
$\alpha_{eq}$	overall Mixed-Mode opening angle	angle
$\beta$	rib rotation with respect to its axis	angle
$\gamma$	angle of stress to contact plane	angle
$\delta$	crack or interface sliding	length
$\delta_{ref}$	reference sliding to calculate $\gamma$	length
$\zeta$	inclination of segment or contact	angle
$\eta_c$	concrete resistance factor (total)	-
$\eta_{conf}$	confinement factor	-
$\eta_{fc}$	brittleness factor	-
$\theta$	inclination of contact stress	angle
$\kappa_f$	factor for rib geometry	-
$\lambda_c$	activation of contact	length
$\sigma$	confinement stress	stress
$\sigma_c$	contact stress	stress
$\tau$	bond stress	stress
$\tau_{ad}$	tangential stress due to adherence	stress

- [11] Gambarova, P. G. and Rosati, G. (1993). Aderenza armatura-calcestruzzo e fessurazione longitudinale per barre di piccolo diametro. *Studi e Ricerche*, 14:1–27.
- [12] Gambarova, P. G. and Rosati, G. (1996). Bond and splitting in reinforced concrete: test results on bar pull-out. *Materials and Structures*, 29:267–276.
- [13] Gambarova, P. G. and Zasso, B. (1985). Aderenza armatura-calcestruzzo e fessurazione longitudinale da spacco: una sintesi di alcuni recenti risultati sperimentali. *Studi e ricerche*, (7):7–54.
- [14] Giuriani, E., Plizzari, G., and Schumm, C. (1991). Role of Stirrups and Residual Tensile Strength of Cracked Concrete on Bond. *Journal of Structural Engineering*, 117(1):1–18.
- [15] Goto, Y. (1971). Cracks Formed in Concrete Around Deformed Tension Bars. *Journal Proceedings*, 68(4):244–251.
- [16] Jacobsen, J. S. (2012). *Constitutive Mixed Mode Behavior of Cracks in Concrete: Experimental Investigations of Material Modeling*. Ph.D. Thesis, Technical University of Denmark, Kongens Lyngby, Denmark.
- [17] Li, B., Maekawa, K., and Okamura, H. (1989). Contact density model for stress transfer across cracks in concrete. *Journal of the Faculty of Engineering, The University of Tokyo*, 40(1):9–52.

## Chapter 5. An interlocking approach for the rebar-to-concrete contact in bond

---

- [18] Lindorf, C. (2011). *Bond fatigue in reinforced concrete under transverse tension*. PhD Thesis, Dresden University, Germany.
- [19] Mahrenholtz, C. (2012). *Seismic bond model for concrete reinforcement and the application to column-to-foundation connections*. PhD Thesis, Stuttgart University, Stuttgart, Germany.
- [20] Marti, P., Alvarez, M., Kaufmann, W., and Sigrist, V. (1998). Tension Chord Model for Structural Concrete. *Structural Engineering International*, 8(4):287–298.
- [21] Modena, C. (1992). Bond behaviour with longitudinal cracks of normal and epoxy coated deformed bars. In *Proc. int. conf. "Bond in Concrete: from research to practice"*, Comité Euro-International du Béton, pages 5.31–5.40, Riga, Latvia. CEB-RTU.
- [22] Muttoni, A. (1989). *Die Anwendbarkeit der Plastizitätstheorie in der Bemessung von Stahlbeton*. PhD thesis, ETH, Zurich, Switzerland.
- [23] Nielsen, M. P. and Hoang, L. C. (2011). *Limit analysis and concrete plasticity*. CRC Press, 788 p., Boca Raton, Florida, 3rd ed edition.
- [24] Pundir, M., Tirassa, M., Fernández Ruiz, M., Muttoni, A., and Ancaix, G. (2019). Review of fundamental assumptions of the Two-Phase model for aggregate interlocking in cracked concrete using numerical methods and experimental evidence. *Cement and Concrete Research*, 125:105855.
- [25] Simons, I. N. (2007). *Verbundverhalten von eingemörtelten Bewehrungsstäben unter zyklischer Beanspruchung*. PhD Thesis, Stuttgart University, Germany.
- [26] Taylor, H. P. J. (1970). *Investigation of the Forces Carried Across Cracks in Reinforced Concrete Beams in Shear by Interlock of Aggregate*. Number 42.447 in Technical report (Cement and Concrete Association). London, United Kingdom.
- [27] Tepfers, R. (1973). *A theory of bond applied to overlapped tensile reinforcement splices for deformed bars*. PhD thesis, Chalmers University of Technology, Göteborg, Sweden.
- [28] Tirassa, M., Fernández Ruiz, M., and Muttoni, A. (2020, in press). Influence of cracking and rough surface properties on the transfer of forces in cracked concrete. *Engineering Structures*.
- [29] Walraven, J. C. (1981). Fundamental Analysis of Aggregate Interlock. *ASCE Journal of the Structural Division*, 107(11):2245–2270.

# 6 Conclusions and Outlook

This thesis presents the results of a research programme focused on aggregate interlocking and the transfer of forces across rough interfaces subjected to sliding. It comprises several scientific articles [3–7], each focusing on different aspects of the topic. This chapter summarizes the overall conclusions and discusses some aspects concerning the interlocking of surfaces in concrete structures which could be addressed in future research projects.

## 6.1 Main conclusions

The experimental campaign comprises concrete specimens made with various concrete mixes, as well as specimens where the interlocking of steel-to-concrete interfaces is investigated. Testing occurred with set-ups capable of acting in two perpendicular directions, allowing to pre-crack the specimens and applying precise Mixed-Mode kinematics upon the resulting cracks or interfaces. DIC measurements were performed for most of the tests and in some cases, the shape of the final crack surface was recorded.

The experimental data are used as a basis for a theoretical investigation and to develop a mechanically based model capable of describing the recorded load-displacement curves under consideration of the applied kinematics, the material properties and the surface roughness. The model, introduced in Chapter 4, is capable to determine the contact properties in a simplified manner and to estimate the forces exchanged at the crack level using an elastic-plastic material law. In Chapter 5 it is extended to the case of bond, where the interlocking between rebar-ribs and concrete material is modelled.

The main conclusions are the following:

- A simple set-up arrangement is presented, capable of pre-cracking double-notched specimens and subjecting the resulting crack plane (or interface) to precise Mixed-Mode kinematics. The arrangement is shown to be suitable for investigating the topic of aggregate interlocking, providing results which are consistent with each other and with tests from the literature, although subjected to a significant amount of experimental scatter.

- The test results confirm that cracks subjected to small initial openings and flat opening angles develop higher forces compared to cracks subjected to large initial openings and steeper opening angles.
- Digital Image Correlation is a suitable tool for tracking the development of cracks. The DIC-data can be used to classify tests as a function of the crack dominating the experimental behaviour (Primary Crack, Non-Dominant Secondary Cracking, Dominant Secondary Crack). This classification is also reflected in the different shape of the recorded load-displacement curves.
- Dominant Secondary Cracking corresponds to the development of a new crack, which (in absence of sufficient transverse confinement) can propagate in a brittle manner from the initial interlocking interface with an inclination of approximately  $45^\circ$ . Specimens characterized by this phenomenon are sometimes neglected in the literature, although it can also be observed in full-scale structures. In this research, tests failing by secondary cracking are reported and analysed. They generally have particularly rough surfaces, often characterized by large protuberances triggering secondary cracking.
- The interlocking for interfaces with simple geometries can be tested with specimens where mortar is cast against steel surfaces of varying shape (spheres, rebar-ribs). These specimens behave consistently with each other and allow investigating the force transfer in conditions where the local contact properties can be precisely assessed. The use of concrete instead of mortar generally results in a larger degree of experimental scatter, due to the potential interaction between large aggregates and the steel protuberances.
- The tests show that the normal/confinement stress tends to increase after the shear/bond stress, as it is activated to oppose crack dilatancy for fixed kinematics. The relation between normal and shear stress can thus vary over the course of a test and is dependent on the external kinematics.
- A review of the Two-Phase Model [8] is presented in Chapter 3, based on experimental results corresponding to its geometric hypotheses (flat crack with spherical protuberances). A descriptive model using a refined analysis of the contact properties is introduced as well. This enables the discussion of several theoretical limitations, like the hypotheses regarding the contact stress or the changes in surface roughness due to accumulating damage.
- Despite its theoretical limitations, the Two-Phase Model is shown to be consistent with the experimental results for concrete cracks with Primary Cracking or Non-Dominant Secondary Cracking in terms of maximum shear forces [1, 8]. For tests with the development of a Dominant Secondary Crack, the model can be improved using a parameter accounting for the particularly high surface roughness associated with these cases.
- Several concrete mixes were employed, and the resulting crack surfaces were recorded using digital microscopy. The amount of data can be suitably reduced by approximating

the surface as a series of longitudinal crack-profiles, spaced 1 mm from each other and with a data point every 0.1 mm.

- The crack-roughness can be approximated with simple parameters calculated using data from surface scans. These parameters are indicative of the ultimate failure mode, with rougher cracks increasing the likelihood of failure by the propagation of a secondary crack. The concrete strength and the maximum aggregate size are found to influence the measured crack surface roughness.
- A mechanically based model is presented in Chapter 4, providing reasonable estimates of the load-displacement curves for tests on concrete cracks. The model can be used both for tests with interlocking occurring at the primary crack and tests failing by propagation of a secondary crack. It accounts for the local contact properties, their variation over the course of a test (e.g. initial activation phase, additional material strength due to confinement) and the potential for residual soundness in cracks with small opening.
- The model is extended to the case of bond between rebar ribs and concrete material, as both phenomena depend on the mechanical engagement of surface protuberances. It is shown to suitably reproduce the decreasing pull-out force in cracked conditions observed in tests from the literature. Moreover, the model is useful for estimating the relative intensity of bond and confinement stresses, associated with the inclination of the contact force.

## 6.2 Outlook and future works

The interlocking of concrete interfaces is a complex, multi-scale problem. Although several research projects investigated the matter and enabled a better understanding of the phenomenon, some aspects remain unclear. This section presents a selection of notable points which could be addressed by future researchers:

- To estimate the aggregate interlocking forces, the model presented in Chapter 4 uses data obtained by scanning concrete surfaces as an input. However, such detailed information is usually not available for practical applications. A possible solution is outlined in Appendix D of Chapter 4, where simple roughness parameters (rather than the entire surface scan) are shown to be suitable for improving the performance of the analytical equations proposed in [1]. Nevertheless, it remains unclear how to correctly estimate such parameters knowing only basic material properties, and thus without the need for processing actual crack surfaces. More research could establish a link between concrete mix properties (e.g. concrete strength, type and shape of aggregates) and such roughness indicators. An interesting starting point is presented by Huber et al. [2], where a simple empirical equation allows relating the concrete strength with the surface roughness. This expression could likely be improved by also accounting for the aggregate sizes and the relative strength between cement matrix and aggregates.

- To estimate the local contact stresses, developing when material on opposite crack-sides starts engaging, the model in Chapter 4 considers an elastic-plastic constitutive law, in accordance with the experimental evidence. These contact stresses are shown to be significantly influenced by the degree of material confinement, which can cause increases well above the cylinder compressive resistance. The model thus applies an approximate approach, which is shown to provide suitable results for the analysed cases. Nevertheless, experimental evidence showing how the concrete properties, the contact size, and the penetration depth influence the developing stresses could help supporting the proposed expressions and extending them to a wider range of cases. Such evidence could also improve the understanding of how the initial activation/elastic phase is influenced by various material and contact parameters.
- Similar to the previous point, the mechanism of friction acting at each contact remain unclear. The present research shows that the relation between confinement and shear stresses changes over the course of each test. These changes cannot be entirely attributed to the inclination of the contact plane, thus suggesting that the friction coefficient may vary. Clarifying the parameters influencing the contact stress inclination for various kinematics would represent a step forward in the understanding of both aggregate interlocking and bond.
- The present research focuses on aggregate interlocking at small scales, with specimens characterized by a relatively small fracture plane. The roughness measurements are thus subjected to significant scatter, while larger crack planes would result in a more average roughness. Further research could thus be aimed at studying the propagation of secondary cracks in full-scale structures as a function of the local roughness and varying degrees of material confinement.
- With respect to the study of bond between rebars and concrete, this research project reports the results obtained by interlocking single rebar surfaces with concrete material. This novel approach has some advantages compared to standard pull-out tests, as it enables a precise control of the confinement forces acting upon the interlocking surface. However, a limited amount of cases were analysed, and only one type of rebar was utilised. To further verify and extend the presented approach, additional testing is required, considering a wider range of rebar geometries and applied kinematics (in particular for Mode-II tests in cracked conditions).

## Bibliography

- [1] Cavagnis, F, Fernández Ruiz, M., and Muttoni, A. (2018). A mechanical model for failures in shear of members without transverse reinforcement based on development of a critical shear crack. *Engineering Structures*, 157:300–315.
- [2] Huber, T., Huber, P., and Kollegger, J. (2019). Influence of aggregate interlock on the shear resistance of reinforced concrete beams without stirrups. *Engineering Structures*, 186:26–42.

- [3] Pundir, M., Tirassa, M., Fernández Ruiz, M., Muttoni, A., and Anciaux, G. (2019). Review of fundamental assumptions of the Two-Phase model for aggregate interlocking in cracked concrete using numerical methods and experimental evidence. *Cement and Concrete Research*, 125:105855.
- [4] Tirassa, M., Fernández Ruiz, M., Anciaux, G., and Muttoni, A. (2017). Interface Stresses in Cracked Concrete: Testing for Review of Its Fundamentals. In *2017 fib Symposium High Tech Concrete: Where Technology and Engineering Meet*, pages 740–748. Maastricht, Netherlands.
- [5] Tirassa, M., Fernández Ruiz, M., and Muttoni, A. (2020). An interlocking approach for the rebar-to-concrete contact in bond. *[Submitted for review]*.
- [6] Tirassa, M., Fernández Ruiz, M., and Muttoni, A. (2020, in press). Influence of cracking and rough surface properties on the transfer of forces in cracked concrete. *Engineering Structures*.
- [7] Tirassa, M., Fernández Ruiz, Miguel, and Muttoni, A. (2018). Modern experimental research techniques for a consistent understanding of aggregate interlocking. In *Proceedings of the 12th fib PhD Symposium in Civil Engineering*, pages 723–730, Prague, Czech Republic.
- [8] Walraven, J. C. (1981). Fundamental Analysis of Aggregate Interlock. *ASCE Journal of the Structural Division*, 107(11):2245–2270.



# Appendix 1: Results at maximum shear stress for concrete cracks

This appendix summarizes the parameters measured at the maximum shear stress  $\tau_{\max}$  for interlocking tests on concrete cracks. Table A1.1 reports these values in addition to the observed failure mode, the concrete strength, the applied kinematics and the specimen dimensions. The geometric parameters are defined in Figure A1.1a. Additional information on specimens with special geometries can be found in the next section. The data is available for download on Zenodo, doi: 10.5281/zenodo.3894515.

Table A1.1 – Properties of concrete specimens and experimental results at  $\tau_{\max}$  (the first two digits of the test-number indicate the casting, see Table 2.1 for additional information including the maximum aggregate size; the geometric parameters are defined in Figure A1.1; specimens with particular geometries, like those where  $c$  is marked with “\*”, are detailed in the next section)

#	fail.	$l$ [mm]	$h$ [mm]	$b$ [mm]	$c$ [mm]	$f_c$ [Mpa]	$w_0$ [mm]	$\alpha$ [°]	$\tau_{\max}$ [MPa]	$\sigma(\tau_{\max})$ [MPa]	$\delta(\tau_{\max})$ [mm]	$w(\tau_{\max})$ [mm]
010401	DSC	120	110	29.7	24.6	38.6	0.040	50	4.80	-0.76	0.10	0.16
020804	NDSC	120	110	20.1	34.6	38.4	0.025	50	2.62	-0.43	0.09	0.13

Continued on next page

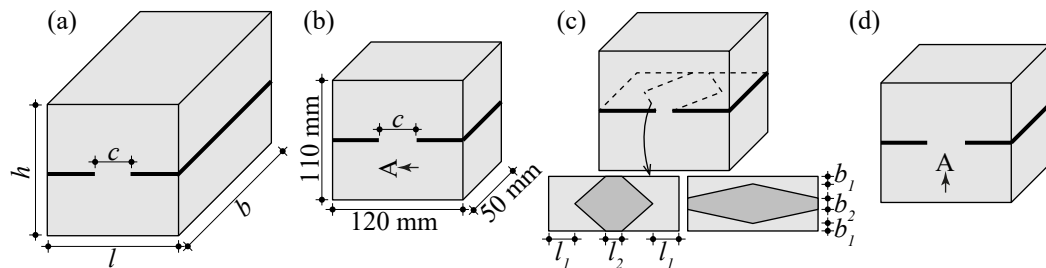


Figure A1.1 – Specimen geometries; (a) parameters defining overall dimensions; (b) dimensions and casting direction for typical specimens; (c) parameters defining the fracture plane for specimens with special notches; and (d) special specimens with casting direction parallel to Mode I direction

**Appendix 1**

Table A1.1 – continued from previous page

#	fail.	$l$ [mm]	$h$ [mm]	$b$ [mm]	$c$ [mm]	$f_c$ [Mpa]	$w_0$ [mm]	$\alpha$ [°]	$\tau_{max}$ [MPa]	$\sigma(\tau_{max})$ [MPa]	$\delta(\tau_{max})$ [mm]	$w(\tau_{max})$ [mm]
021402	NDSC	120	110	50.3	34.3	38.4	0.025	55	2.35	-0.05	0.06	0.11
021501	DSC	120	110	50.5	18.2	38.6	0.040	40	6.48	-1.64	0.13	0.15
021502	DSC	120	110	50.2	23.4	38.6	0.500	0	9.03	-5.81	0.52	0.50
021601	NDSC	120	110	51.0	18.9	38.5	0.025	45	2.84	-0.52	0.09	0.12
021602	PC	120	110	51.0	24.7	38.5	0.025	60	1.46	0.21	0.03	0.08
021701	DSC	120	110	50.2	22.0	38.5	0.015	40	6.18	-1.82	0.08	0.09
021702	NDSC	120	110	50.0	28.1	38.5	0.100	45	2.58	-0.76	0.27	0.37
022001	PC	120	110	51.3	24.8	38.5	0.015	60	1.93	0.35	0.01	0.04
022002	NDSC	120	110	51.0	19.1	38.5	0.015	45	4.97	-1.16	0.09	0.11
022101	DSC	120	110	50.6	19.2	38.6	0.100	40	6.60	-2.00	0.26	0.32
022102	NDSC	120	110	50.8	24.0	38.6	0.040	45	2.55	-0.22	0.07	0.11
030101	DSC	120	110	51.8	26.6	38.5	0.100	60	3.20	-0.44	0.27	0.56
030102	NDSC	120	110	51.5	23.9	38.5	0.040	60	1.58	0.20	0.11	0.22
030201	DSC	120	110	50.6	20.5	38.6	0.040	45	5.67	-1.27	0.15	0.19
030202	DSC	120	110	50.6	24.8	38.6	0.100	40	3.45	-0.41	0.10	0.19
030301	DSC	120	110	50.6	18.1	38.6	0.015	55	4.81	-0.87	0.13	0.20
030302	DSC	120	110	50.7	23.3	38.6	0.500	0	8.56	-7.05	0.69	0.53
030401	DSC	120	110	50.5	19.5	38.6	0.040	40	7.99	-2.46	0.12	0.14
030402	DSC	120	110	50.6	21.1	38.6	0.040	50	4.43	-0.72	0.13	0.19
030801	DSC	120	110	50.2	17.8	38.6	0.025	40	6.51	-1.72	0.08	0.09
030802	PC	120	110	50.5	23.3	38.6	0.100	55	1.14	0.08	0.08	0.21
030901	PC	120	110	49.5	25.0	38.6	0.100	60	0.49	0.08	0.05	0.18
030902	DSC	120	110	49.5	17.0	38.6	0.040	40	6.93	-2.12	0.11	0.13
031001	DSC	120	110	49.9	21.0	38.6	0.040	50	4.95	-1.01	0.11	0.17
031002	NDSC	120	110	49.8	19.1	38.6	0.040	55	1.68	0.16	0.05	0.11
031101	DSC	120	110	50.3	25.0	38.6	0.100	50	4.11	-1.10	0.29	0.45
031102	PC	120	110	50.3	17.0	38.6	0.015	50	4.16	-1.53	0.40	0.49
031601	DSC	120	110	51.5	54.8	38.7	0.040	50	2.32	0.22	0.06	0.11
031602	DSC	120	110	51.7	53.8	38.7	0.100	50	2.05	-0.40	0.19	0.32
031702	DSC	120	110	51.0	56.0	38.6	0.040	45	3.14	-0.12	0.07	0.11
031902	NDSC	120	110	51.1	56.0	38.7	0.100	55	1.43	-0.15	0.27	0.49
040301	PC	120	110	50.2	29.0	28.8	0.025	50	3.17	-0.56	0.19	0.25
040302	DSC	120	110	50.3	23.5	28.9	0.015	40	5.55	-1.49	0.10	0.09
040401	PC	120	110	50.7	34.0	29.0	0.100	40	3.03	-0.79	0.24	0.30
040501	NDSC	120	110	50.2	24.1	28.9	0.015	50	2.31	-0.34	0.09	0.12
040502	NDSC	120	110	50.2	29.6	28.8	0.025	55	3.32	-0.76	0.30	0.46
040601	NDSC	120	110	50.8	33.7	29.0	0.020	50	4.06	-0.80	0.14	0.18
040602	DSC	120	110	50.7	39.0	29.1	0.040	40	3.76	-0.82	0.11	0.13
040701	PC	120	110	50.7	34.1	29.1	0.100	50	0.77	0.02	0.12	0.25
040702	DSC	120	110	50.7	39.1	29.2	0.040	60	1.89	-0.05	0.09	0.19
040801	PC	120	110	50.9	33.8	29.2	0.015	55	1.83	-0.05	0.06	0.10
040802	DSC	120	110	50.8	25.0	29.3	0.020	45	4.32	-0.98	0.09	0.11
040901	NDSC	120	110	51.4	34.7	29.3	0.020	55	2.78	-0.40	0.15	0.23
040902	NDSC	120	110	51.2	25.7	29.3	0.040	45	2.14	-0.25	0.12	0.16

Continued on next page

**Results at maximum shear stress for concrete cracks**

Table A1.1 – continued from previous page

#	fail.	$l$ [mm]	$h$ [mm]	$b$ [mm]	$c$ [mm]	$f_c$ [Mpa]	$w_0$ [mm]	$\alpha$ [°]	$\tau_{\max}$ [MPa]	$\sigma(\tau_{\max})$ [MPa]	$\delta(\tau_{\max})$ [mm]	$w(\tau_{\max})$ [mm]
041001	DSC	120	110	50.3	35.0	29.4	0.040	55	2.99	-0.12	0.10	0.18
041101	DSC	120	110	51.2	19.4	29.8	0.025	45	7.57	-2.41	0.24	0.26
041201	DSC	120	110	51.1	34.6	29.4	0.100	45	2.62	-0.32	0.11	0.21
041202	DSC	120	110	51.2	25.1	29.4	0.015	60	2.89	-0.36	0.12	0.23
041301	PC	120	110	50.1	34.0	29.5	0.020	60	1.24	0.07	0.07	0.14
041401	NDSC	120	110	50.9	34.0	29.6	0.100	60	2.56	-0.45	0.07	0.21
041402	NDSC	120	110	50.9	24.8	29.6	0.100	55	0.98	0.18	0.08	0.21
041501	PC	120	110	50.9	34.3	29.6	0.100	60	0.74	0.24	0.05	0.19
050101	DSC	120	110	49.9	23.7	32.0	0.100	45	4.93	-1.13	0.19	0.29
050102	NDSC	120	110	50.0	18.7	32.0	0.025	50	4.06	-0.86	0.13	0.18
050201	DSC	120	110	50.0	23.6	32.0	0.040	45	4.55	-1.08	0.09	0.13
050202	DSC	120	110	50.0	18.7	32.0	0.015	45	5.77	-1.77	0.15	0.16
050301	PC	120	110	50.9	23.7	32.0	0.040	55	1.57	-0.16	0.08	0.16
050302	NDSC	120	110	51.0	18.8	32.0	0.025	45	3.31	-0.86	0.13	0.16
050401	NDSC	120	110	50.4	22.7	32.0	0.040	50	1.83	0.10	0.05	0.10
050801	NDSC	120	110	50.7	23.6	32.0	0.100	50	2.43	-0.48	0.16	0.30
050802	DSC	120	110	50.7	18.6	32.0	0.015	55	4.54	-0.97	0.15	0.22
050901	DSC	120	110	50.5	23.8	32.0	0.025	50	4.45	-1.23	0.14	0.19
050902	NDSC	120	110	50.6	18.6	32.0	0.015	50	2.11	-0.10	0.07	0.10
060101	DSC	120	110	48.7	28.9	44.2	0.040	40	6.07	-1.67	0.09	0.12
060102	DSC	120	110	49.0	28.6	44.6	0.015	50	5.46	-1.26	0.12	0.16
060201	PC	120	110	50.5	28.9	44.7	0.040	60	0.95	-0.13	0.18	0.35
060301	NDSC	120	110	50.0	29.6	44.7	0.040	45	2.57	-0.31	0.12	0.16
060402	NDSC	120	110	50.3	29.5	44.1	0.100	45	1.50	-0.22	0.15	0.25
060502	PC	120	110	50.1	29.5	44.0	0.025	50	3.61	-0.87	0.14	0.19
060902	PC	120	110	49.9	17.1	46.4	0.025	45	4.14	-1.00	0.51	0.12
061101	PC	120	110	50.2	31.8	46.4	0.040	50	2.21	-0.47	0.13	0.20
061102	DSC	150	110	50.2	31.9	46.3	0.040	50	6.18	-1.51	0.16	0.24
061302	NDSC	150	110	50.4	31.9	46.5	0.025	45	5.44	-1.39	0.15	0.18
061401	PC	120	110	49.9	19.5	46.8	0.025	45	3.04	-0.56	0.09	0.11
061402	NDSC	120	110	49.9	24.8	46.8	0.025	55	2.63	-0.61	0.12	0.20
061501	NDSC	120	110	50.5	18.9	46.8	0.025	40	5.14	-1.39	0.10	0.10
061502	PC	120	110	50.6	25.0	46.8	0.100	40	2.22	-0.60	0.23	0.29
061601	NDSC	120	110	49.8	28.1	46.8	0.100	55	0.55	0.07	0.09	0.23
061602	PC	120	110	49.8	21.8	46.8	0.040	40	3.71	-0.79	0.11	0.14
061701	NDSC	120	110	50.7	19.1	46.9	0.040	45	2.45	-0.68	0.18	0.22
061801	PC	120	110	49.5	25.0	46.9	0.040	55	0.81	0.06	0.04	0.10
061802	NDSC	120	110	50.5	19.1	46.9	0.015	40	5.78	-1.64	0.10	0.10
070101	PC	120	110	51.8	18.6	47.3	0.040	60	1.01	0.26	0.02	0.08
070102	PC	120	110	51.8	18.8	47.3	0.015	60	2.72	-0.56	0.23	0.41
070201	DSC	120	110	50.6	18.8	47.2	0.015	45	6.41	-1.57	0.10	0.11
070202	DSC	120	110	50.6	18.8	47.2	0.015	50	6.57	-1.57	0.16	0.20
070301	PC	120	110	50.7	19.0	47.2	0.025	50	4.09	-1.05	0.13	0.18
070302	DSC	120	110	50.5	18.9	47.2	0.015	55	6.00	-1.42	0.10	0.16

Continued on next page

## Appendix 1

Table A1.1 – continued from previous page

#	fail.	$l$ [mm]	$h$ [mm]	$b$ [mm]	$c$ [mm]	$f_c$ [Mpa]	$w_0$ [mm]	$\alpha$ [°]	$\tau_{\max}$ [MPa]	$\sigma(\tau_{\max})$ [MPa]	$\delta(\tau_{\max})$ [mm]	$w(\tau_{\max})$ [mm]
070401	PC	120	110	50.7	19.4	47.2	0.040	50	2.34	-0.12	0.07	0.12
070501	DSC	120	110	51.4	26.7	47.3	0.040	60	3.50	-0.58	0.10	0.21
070502	NDSC	120	110	51.6	23.1	47.7	0.025	60	1.54	-0.12	0.08	0.16
070601	NDSC	120	110	50.1	23.9	47.3	0.100	50	1.36	-0.04	0.09	0.21
070602	PC	120	110	50.1	26.5	47.3	0.100	60	0.43	0.09	0.06	0.20
070701	PC	120	110	50.4	23.6	47.5	0.020	60	1.35	0.48	0.00	0.02
070702	PC	120	110	50.4	17.7	47.5	0.020	40	5.72	-1.96	0.13	0.13
070802	NDSC	120	110	49.5	17.1	47.6	0.020	45	5.29	-1.42	0.19	0.21
070901	PC	120	110	49.5	25.3	47.6	0.500	0	10.64	-9.13	1.44	0.57
070902	PC	120	110	49.5	17.1	47.6	0.015	55	3.56	-1.03	0.15	0.23
071002	PC	120	110	49.8	19.1	47.5	0.020	50	2.65	-0.28	0.06	0.09
071101	PC	120	110	50.4	21.0	47.5	0.020	55	1.94	0.12	0.03	0.06
071102	DSC	120	110	50.3	19.1	47.5	0.020	45	6.02	-1.32	0.09	0.12
071201	DSC	120	110	51.8	24.6	47.8	0.040	50	5.09	-0.84	0.08	0.14
071202	PC	120	110	51.9	62.9	47.8	0.040	45	2.20	-0.19	0.08	0.12
071301	NDSC	120	110	51.2	32.2	47.8	0.040	45	3.19	-0.59	0.17	0.22
071302	PC	120	110	51.3	19.6	47.8	0.040	50	2.63	-0.51	0.10	0.16
071401	PC	120	110	50.8	19.5	48.1	0.015	50	2.61	-0.26	0.04	0.06
071402	NDSC	120	110	50.8	19.8	47.8	0.040	45	5.05	-1.35	0.14	0.18
071501	PC	120	110	51.1	36.0	47.8	0.040	50	1.00	-0.02	0.04	0.09
071502	PC	120	110	51.1	27.2	47.8	0.040	50	1.61	-0.23	0.10	0.16
080101	PC	120	110	50.0	23.2	10.3	0.015	45	0.84	0.10	0.02	0.03
097001	DSC	200	200	200.0	65.0	74.4	0.040	55	5.39	-1.46	0.05	0.07
097002	DSC	200	200	200.0	83.0	74.6	0.100	55	4.71	-1.31	0.06	0.10
097003	DSC	200	200	200.0	51.2	74.7	0.040	55	6.62	-2.68	0.04	0.06

### A1.1 Special specimens

The measurements of typical specimens are  $l = 120$  mm,  $h = 110$  mm and  $b \approx 50$  mm (Figure A1.1b). However, Table A1.1 also contains information regarding some special specimens which were tested as well. These exceptions are the following:

- The “Triroc” set-up described in Section 2.2 (see Figure 2.3) allowed testing larger probes. This is the case for specimens 097001, 097002 and 097003, where  $l = h = b = 200$  mm. They were cast as individual cubes, and the notches were cut using a circular saw. For standard tests the horizontal force was applied to the upper specimen half, while on the Triroc it acted on the lower half. Consequently, the secondary crack depicted in the DIC images propagate upwards rather than downwards.
- For typical specimens, secondary cracks sometimes developed starting from the notches, suggesting a potential influence of the chosen geometry. To investigate this aspect, specimens with special notches were produced, which limited stress concentrations

## A1.1. Special specimens

Table A1.2 – Dimensions of specimens with diagonal cuts (refer to Figure A1.1c for the definitions of the various parameters)

#	$b$ [mm]	$l_1$ [mm]	$l_2$ [mm]	$b_1$ [mm]	$b_2$ [mm]	Area [mm <sup>2</sup> ]
031601	51.5	12	14	0	0	2820
031602	51.7	13	14	0	0	2779
031702	51.0	12	16	0	0	2856
031902	51.1	12	16	0	0	2862
071202	51.9	0	0	0	3	3264
071301	51.2	31	7	0	0	1651
071501	51.1	13	0	6	0	1838
071502	51.1	33	0	0	0	1391

and allowed for a larger fracture plane. These notches consisted in diagonal cuts in the specimen corners and were introduced using a circular saw. The resulting crack plane had approximately the shape of a rhombus, with the concrete progressively increasing in thickness as shown in Figure A1.1c. That way, there were no sudden changes in the geometry of the crack plane, thus reducing potential stress concentrations. Nevertheless, no significantly different behaviour of these specimens could be observed. The tests are marked with “\*” in column  $c$  of Table A1.1, because the reported value is calculated so that  $b \cdot c$  corresponds to the actual crack area. The exact geometric parameters of these special specimens are detailed in Table A1.2.

- As described in Section 2.1, to avoid a potential influence of the casting direction, the typical specimens were cut so that the crack plane was parallel to the casting direction. Tests 040902, 071201, 071302 and 071402 are an exception to this procedure. They were cut with the crack plane perpendicular to the casting direction (see Figure A1.1d). No significant change in behaviour was recorded with respect to the standard tests.



## Appendix 2: Detailed results for concrete cracks

In this appendix, detailed experimental results for concrete specimens are reported (the data is also available for download on Zenodo, doi: 10.5281/zenodo.3894515). For each test, a single plot is used to present the four main parameters  $w$ ,  $\delta$ ,  $\tau$  and  $\sigma$ . This allows showing their mutual relationships while maintaining a compact representation by using four different axes, each with zero at the origin. Starting from the top and proceeding counter-clockwise:

- The upper part of the vertical axis corresponds to  $\tau$ , expressed in [MPa].
- The left part of the horizontal axis reports  $\delta$  in [mm].
- The lower part of the vertical axis shows the crack opening  $w$  in [mm].
- The right part of the horizontal axis shows  $\sigma$  in [MPa]. While all other axes have increasing positive values, this axis shows increasing negative values, corresponding to compression. Although the axis is cut at zero, when  $\sigma > 0$  (corresponding to tensile stresses) the curve is plotted on the left side of the origin.

The values corresponding to  $\tau_{\max}$  are marked with a symbol. For tests failing by DSC, the curves are dotted after the instant of secondary crack propagation, because this part of the curves is not representative of the interface behaviour. As described in Section 2.2, the applied kinematics were monitored using two pairs of 2D-displacement measurement devices placed across the primary crack. As soon as the crack kinematics concentrated in a secondary crack, the crack opening and sliding across the initial primary crack become meaningless. Moreover, secondary cracks separated part of the specimen, which often started rotating and leaned against parts of the set-up (an early variant of the set-up even included a reaction element which only carried forces for tests with dominant secondary cracking). This allowed carrying significant shear forces, often resulting in a second peak, which is not representative of the behaviour of the initial crack.

## Appendix 2

For some tests, a picture of the final crack surface is shown (upper half of the specimen). Finally, the crack patterns at significant instants are reported, as recorded with DIC:

- The first image (left) shows the initial crack pattern, after Mode I cracking.
- For tests with DSC, the second image shows the cracks shortly before reaching the maximum load and thus the propagation of the secondary crack. The third image is taken shortly after, and typically corresponds to the final crack pattern.
- For tests with PC and NDSC, the second image corresponds to  $\tau_{\max}$ . For these tests, the crack pattern usually did not develop significantly thereafter. Nevertheless, in some cases a third image is shown, corresponding to the final crack pattern.

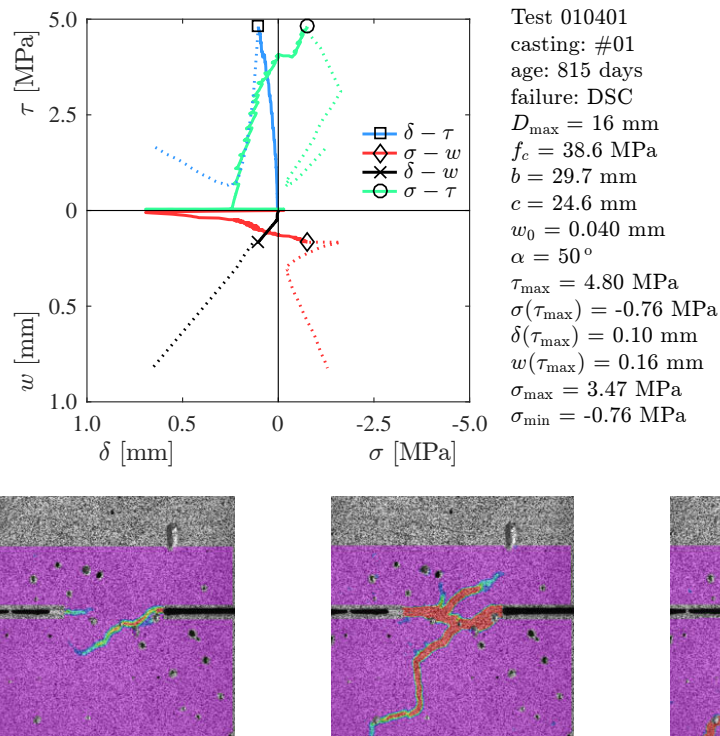


Figure A2.1 – Results for test 010401

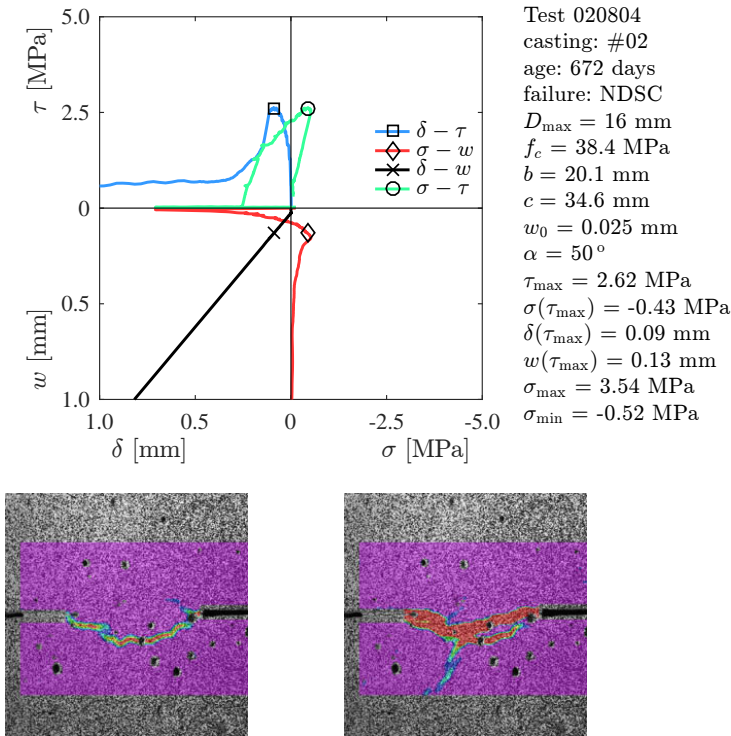


Figure A2.2 – Results for test 020804

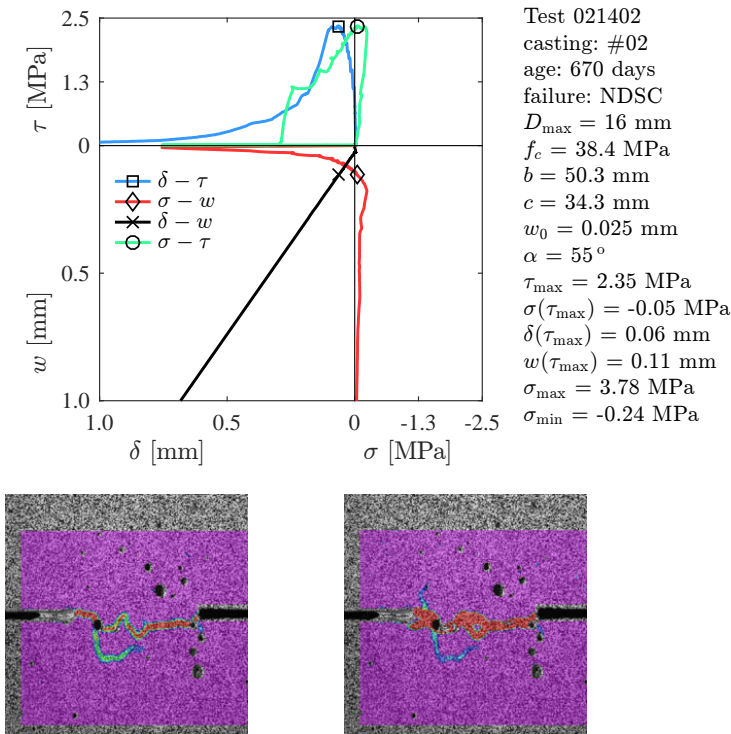


Figure A2.3 – Results for test 021402

Appendix 2

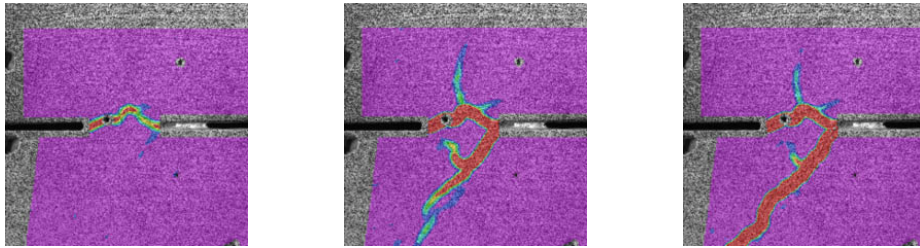
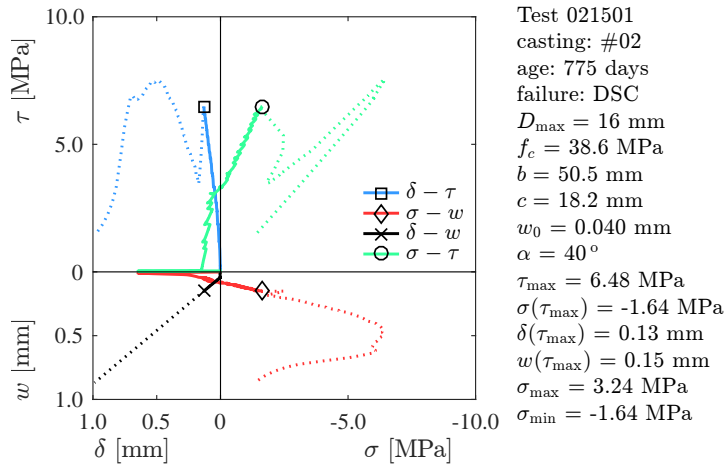


Figure A2.4 – Results for test 021501

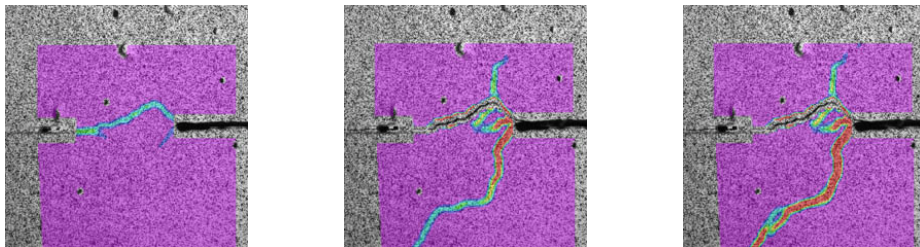
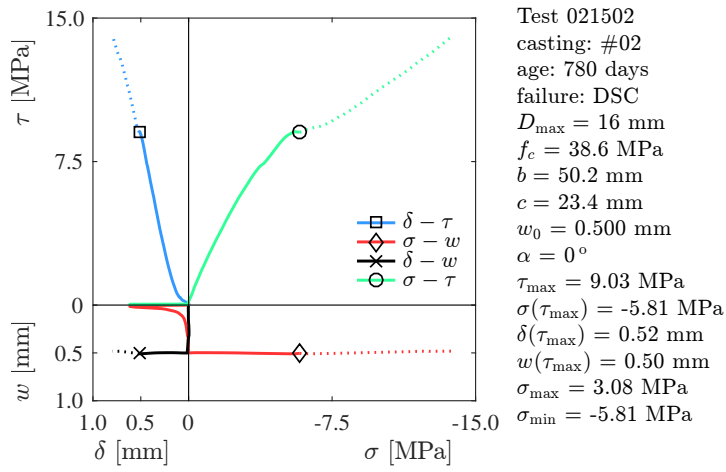


Figure A2.5 – Results for test 021502

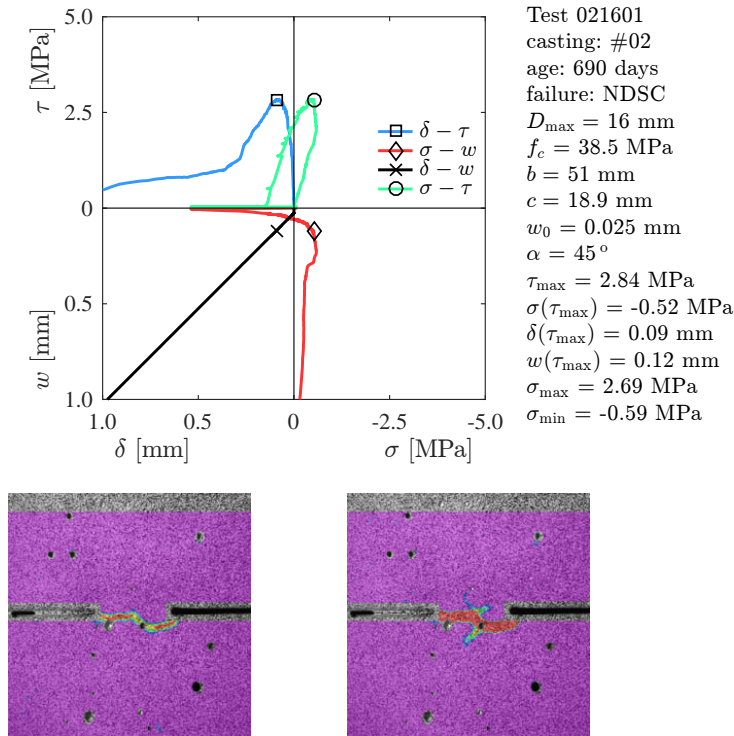


Figure A2.6 – Results for test 021601

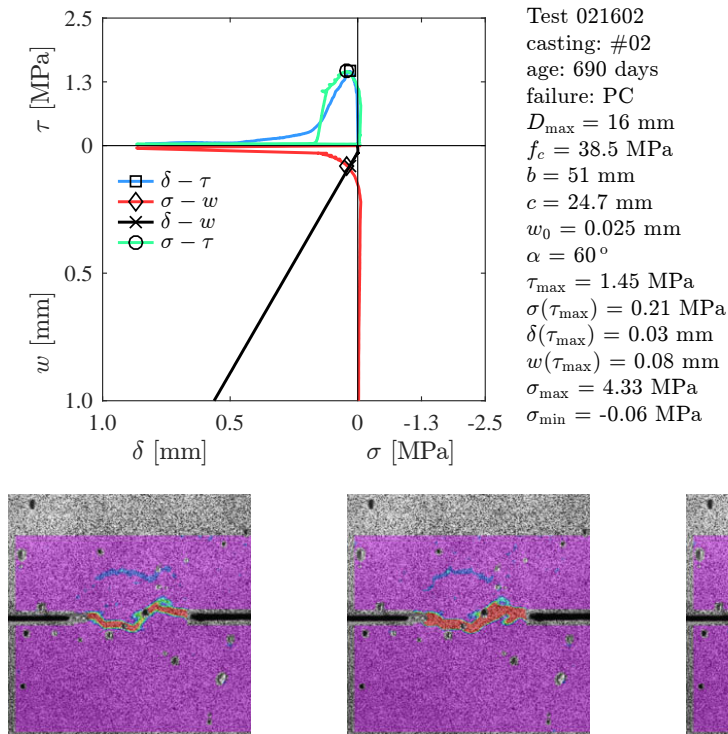


Figure A2.7 – Results for test 021602

Appendix 2

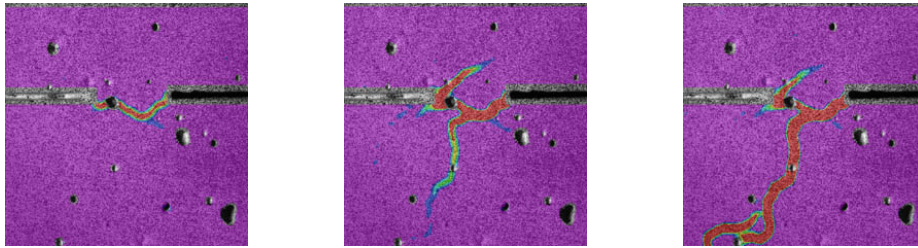
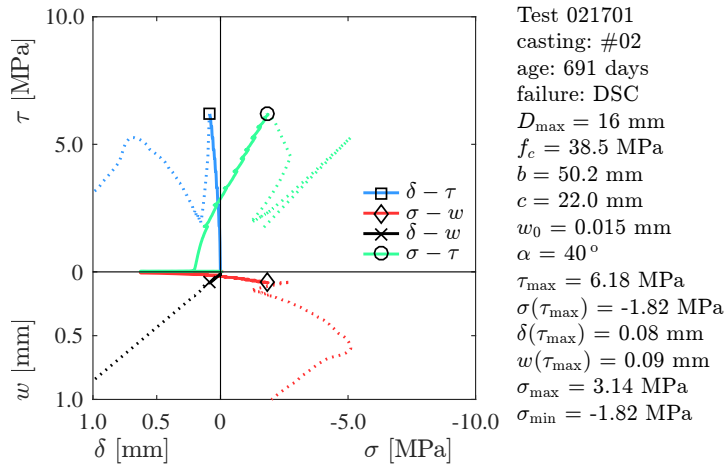


Figure A2.8 – Results for test 021701

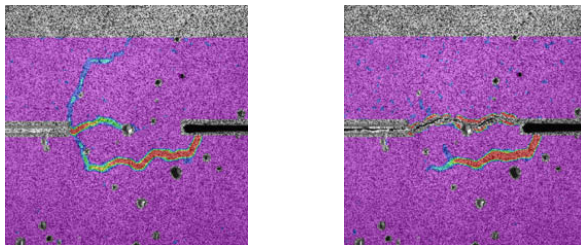
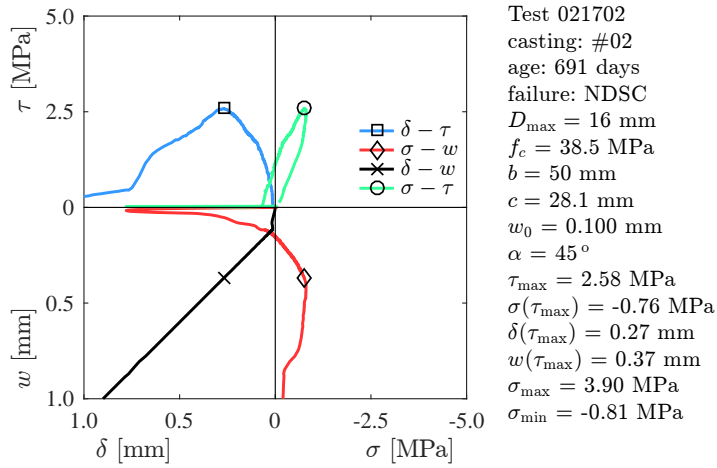


Figure A2.9 – Results for test 021702

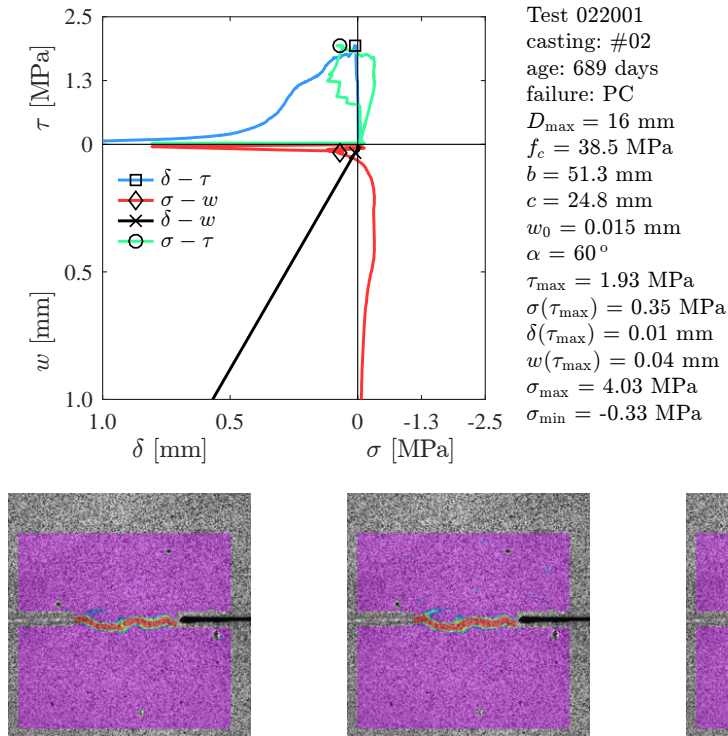


Figure A2.10 – Results for test 022001

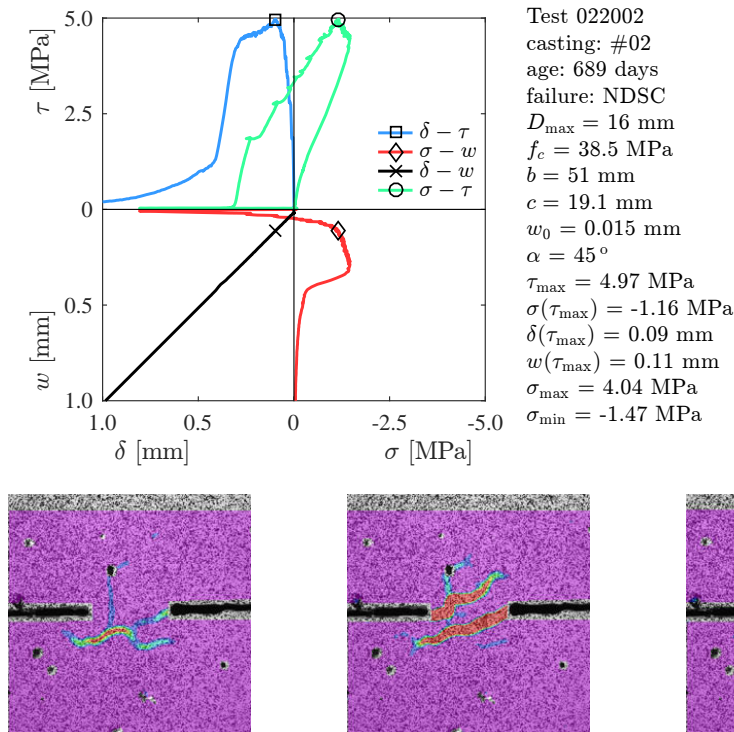


Figure A2.11 – Results for test 022002

Appendix 2

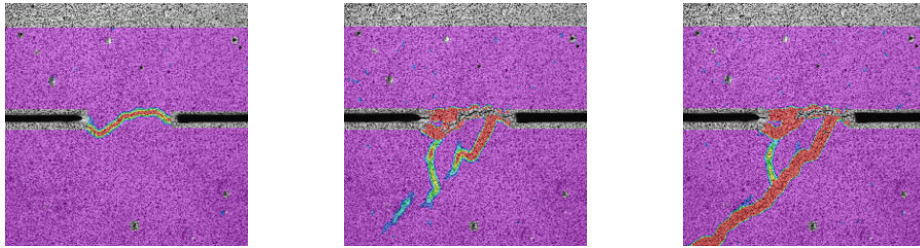
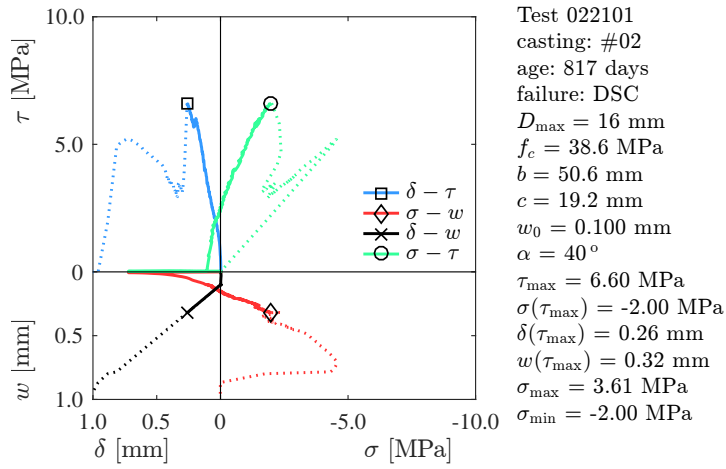


Figure A2.12 – Results for test 022101

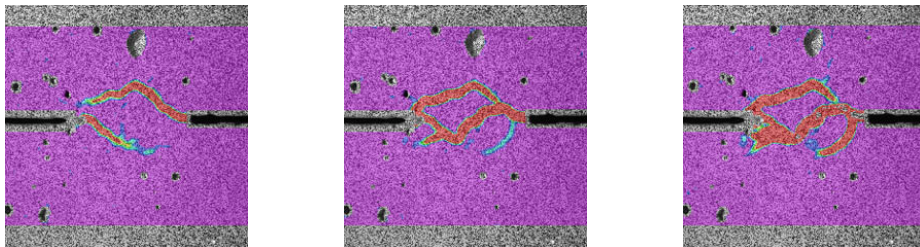
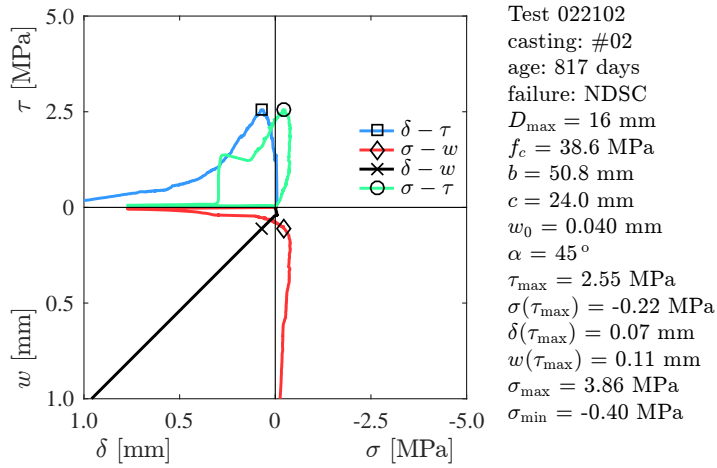


Figure A2.13 – Results for test 022102

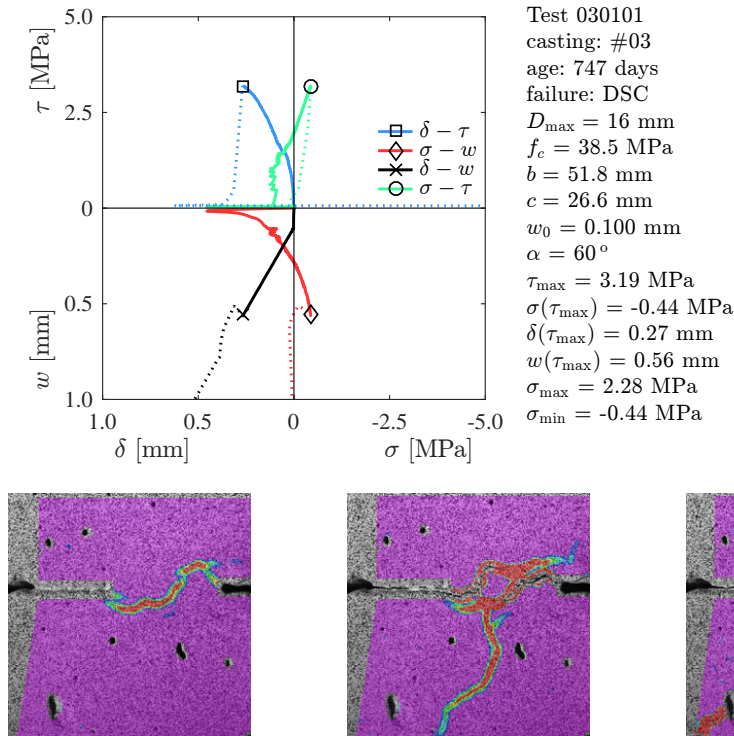


Figure A2.14 – Results for test 030101

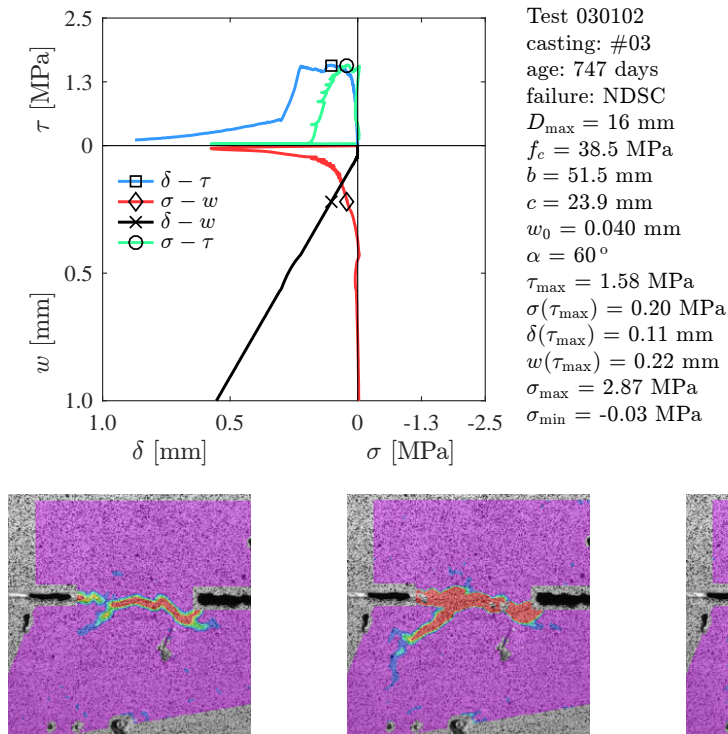


Figure A2.15 – Results for test 030102

Appendix 2

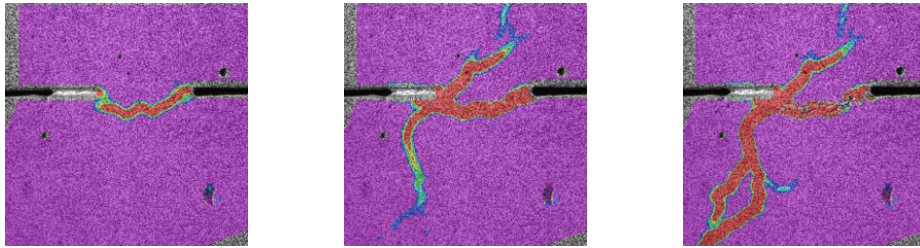
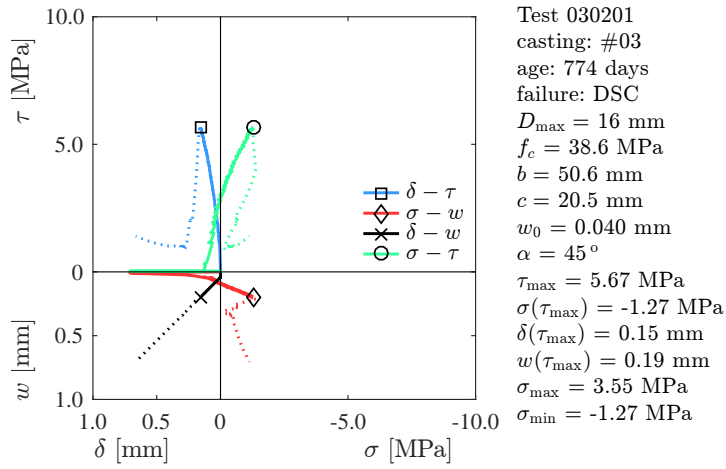


Figure A2.16 – Results for test 030201

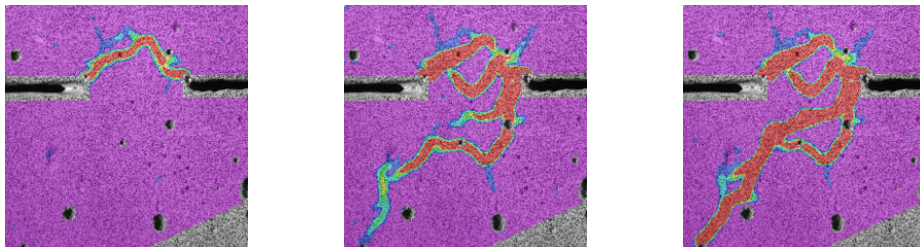
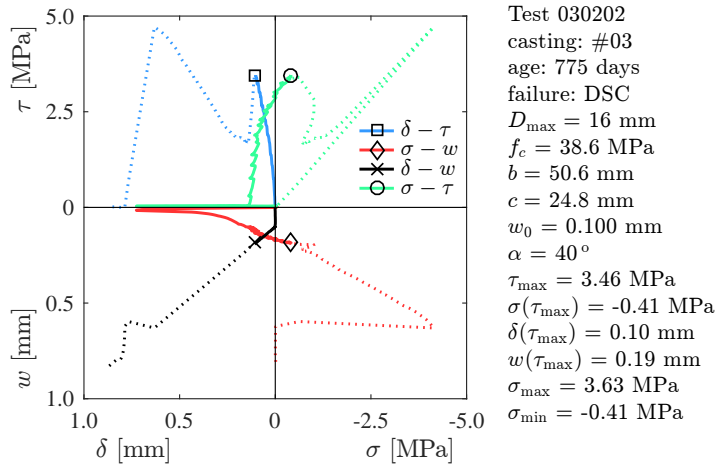


Figure A2.17 – Results for test 030202

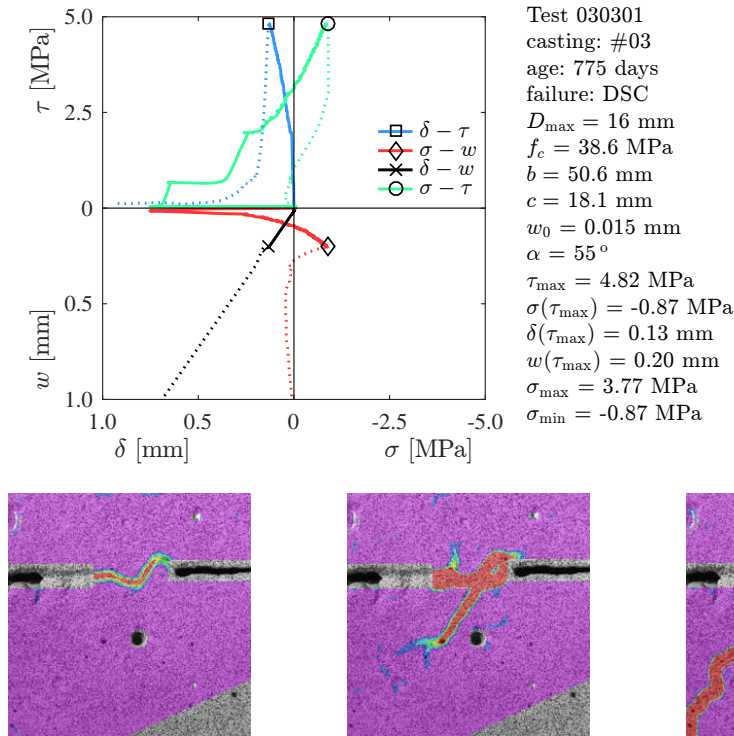


Figure A2.18 – Results for test 030301

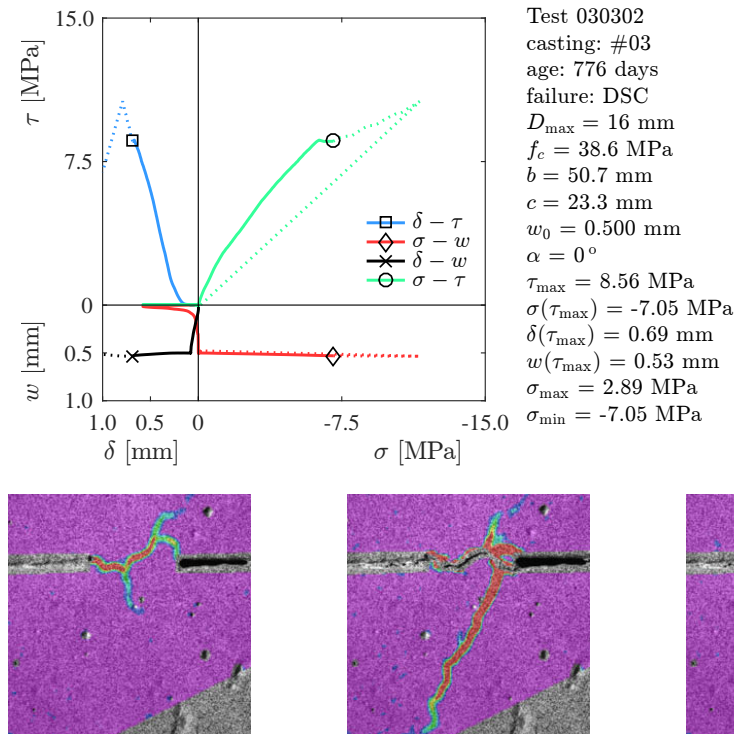


Figure A2.19 – Results for test 030302

Appendix 2

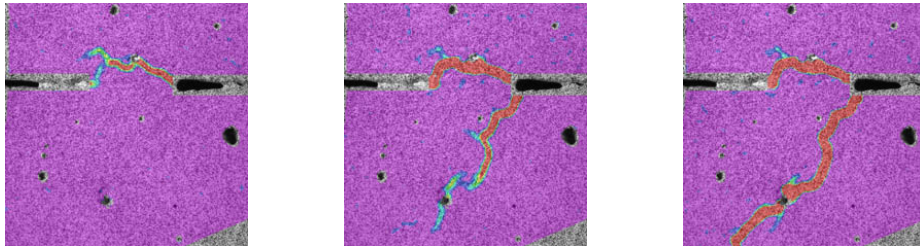
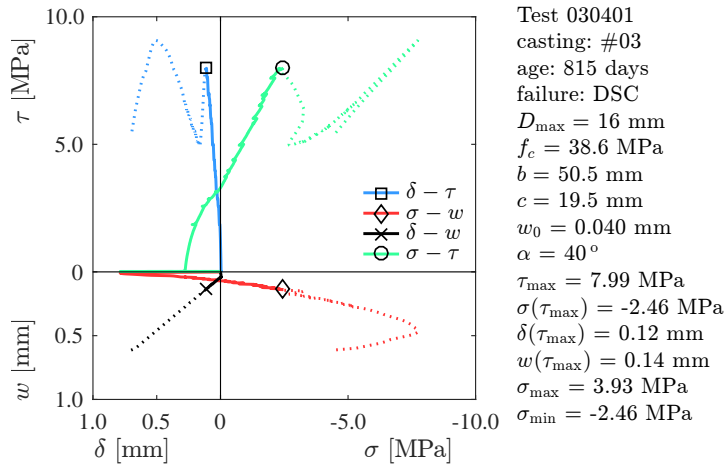


Figure A2.20 – Results for test 030401

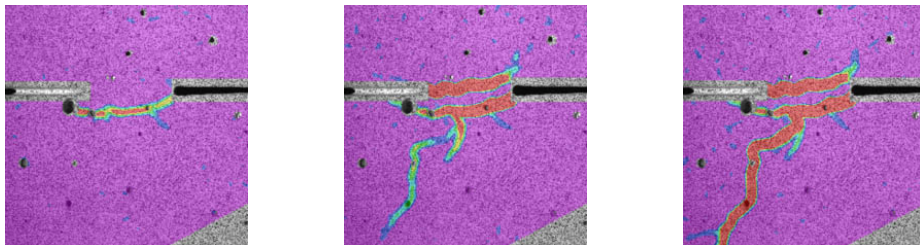
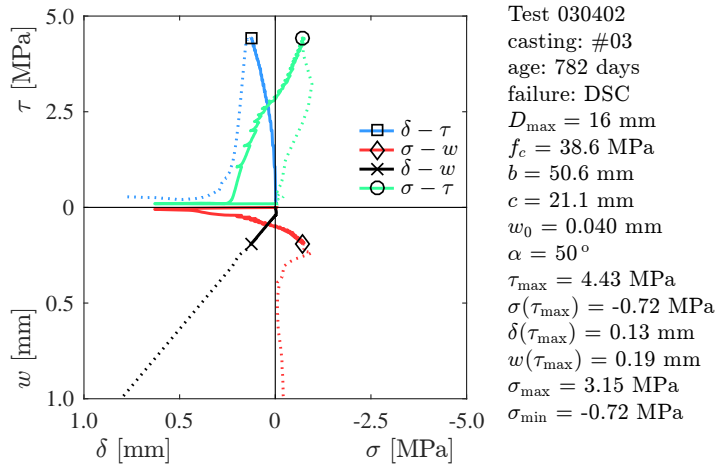


Figure A2.21 – Results for test 030402

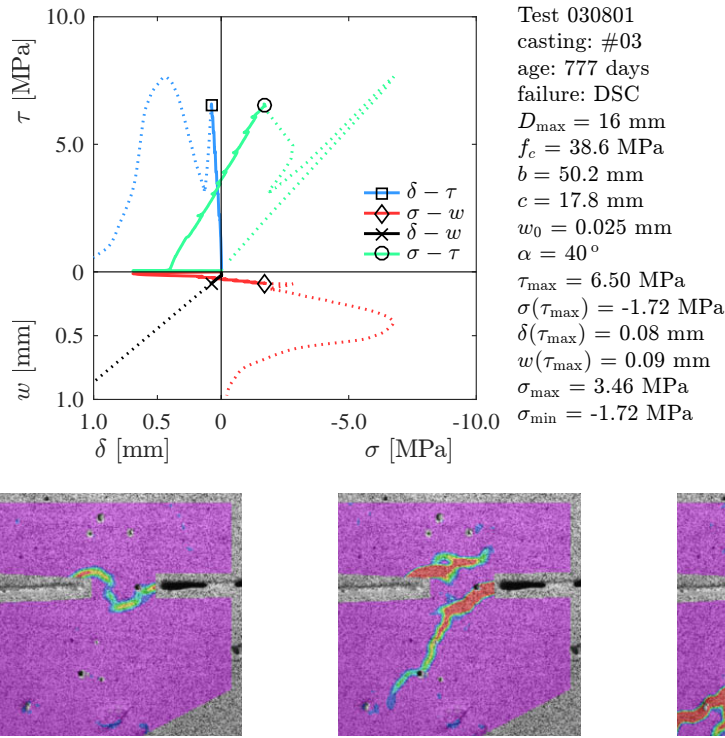


Figure A2.22 – Results for test 030801

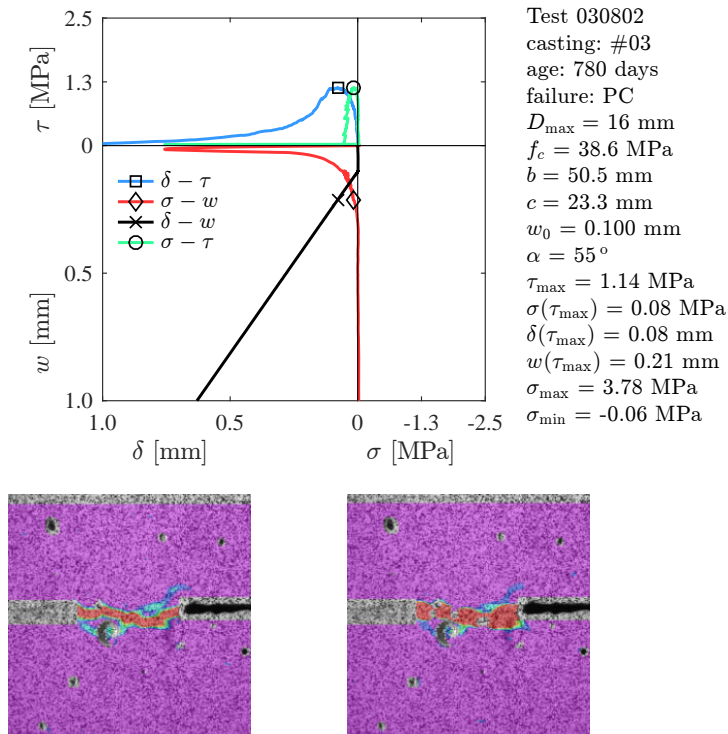


Figure A2.23 – Results for test 030802

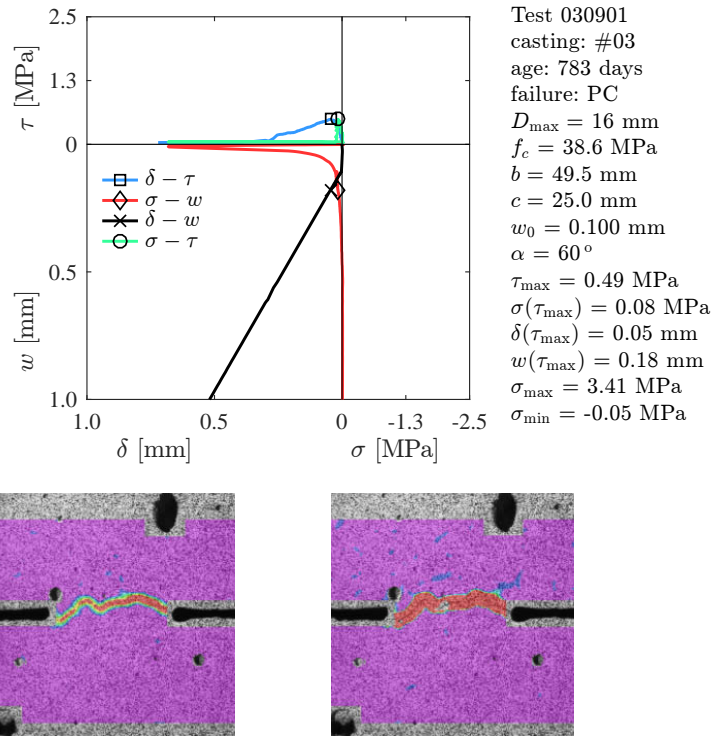


Figure A2.24 – Results for test 030901

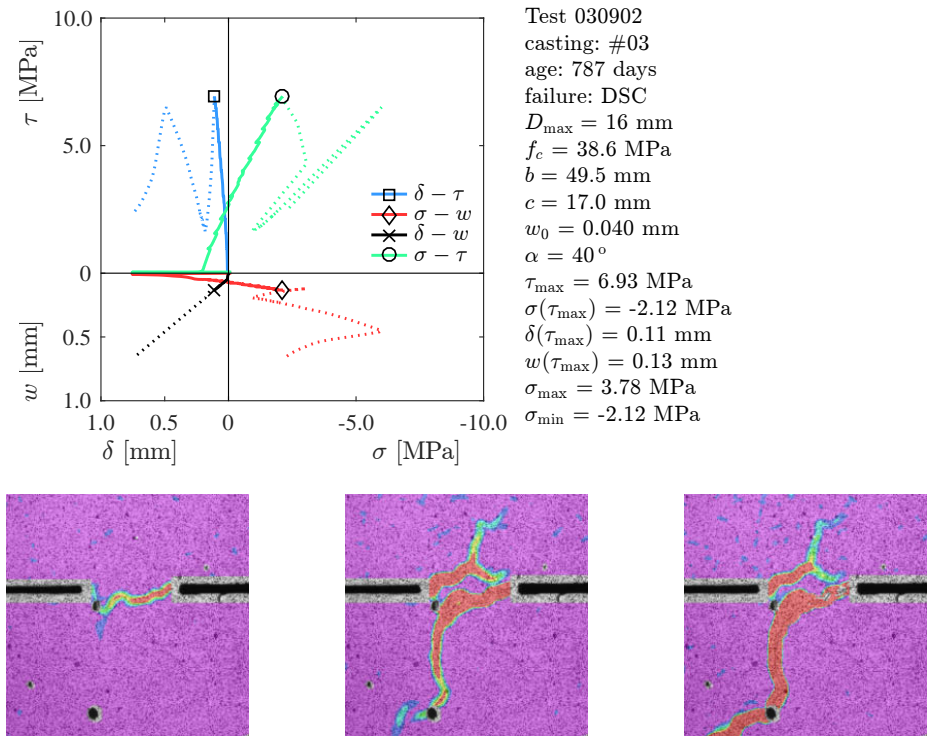


Figure A2.25 – Results for test 030902

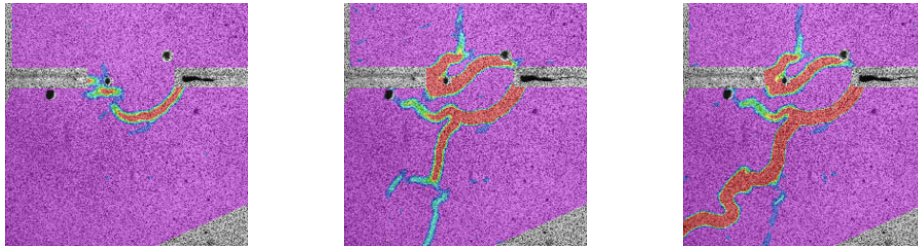
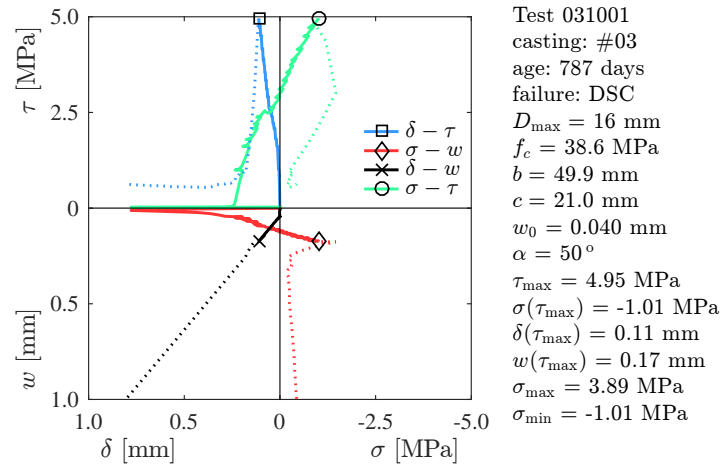


Figure A2.26 – Results for test 031001

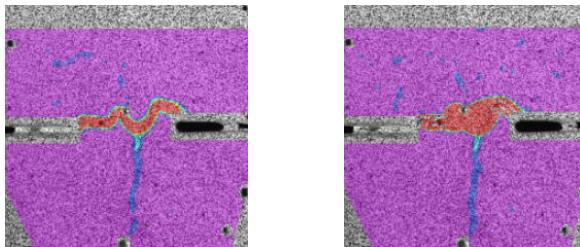
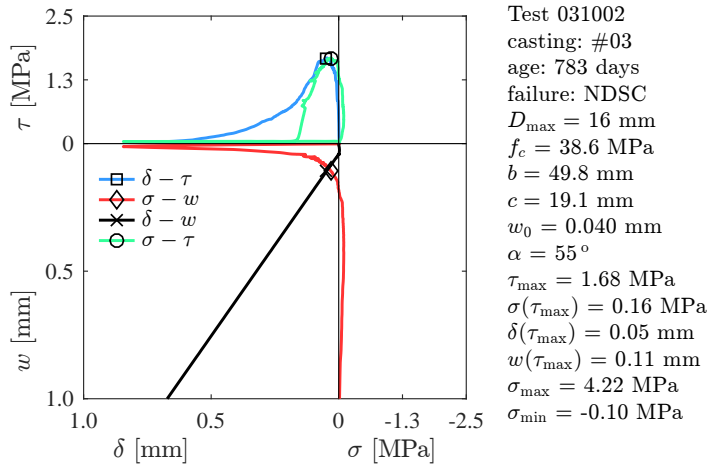


Figure A2.27 – Results for test 031002

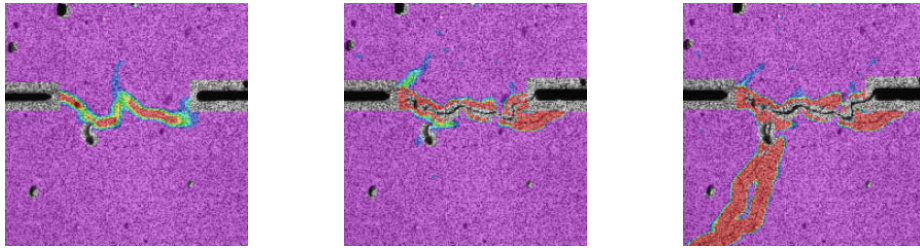
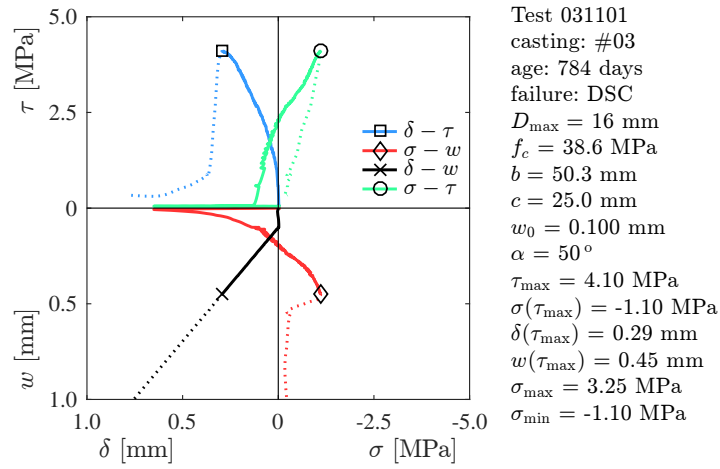


Figure A2.28 – Results for test 031101

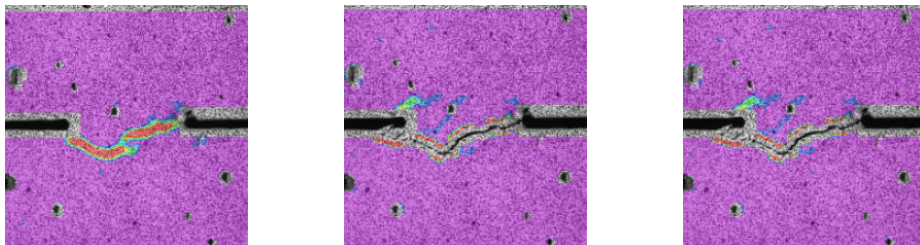
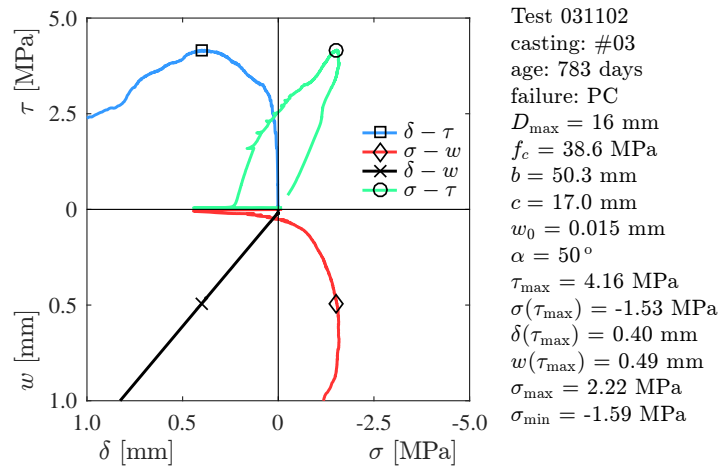


Figure A2.29 – Results for test 031102

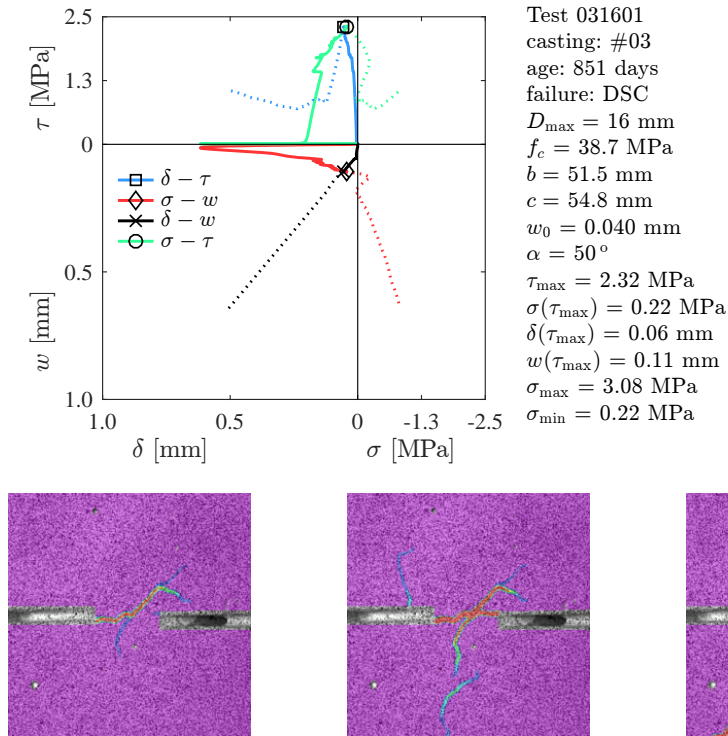


Figure A2.30 – Results for test 031601

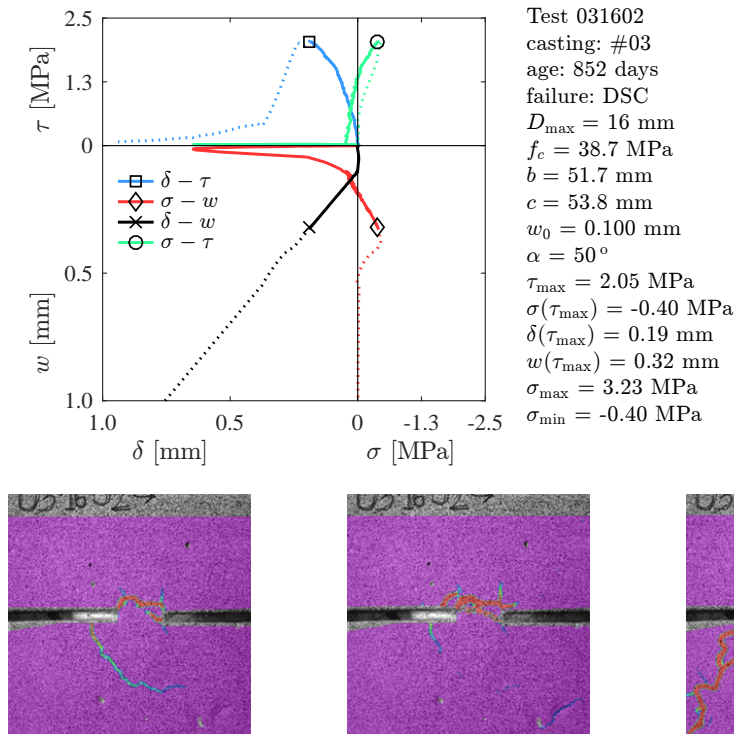


Figure A2.31 – Results for test 031602

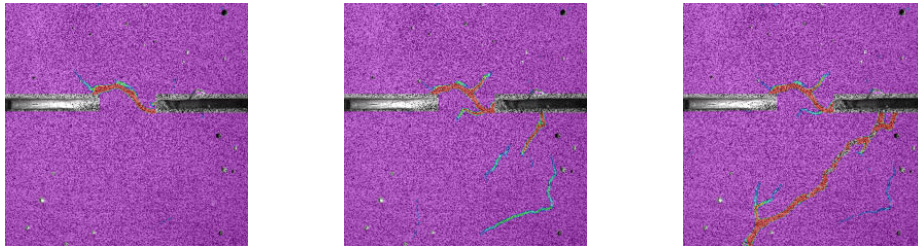
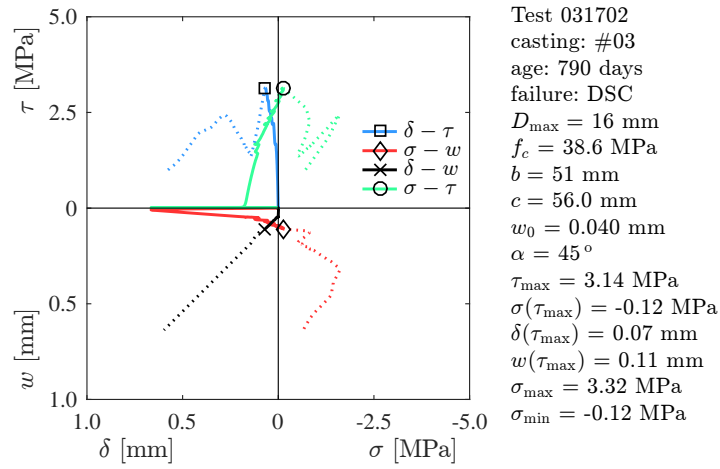


Figure A2.32 – Results for test 031702

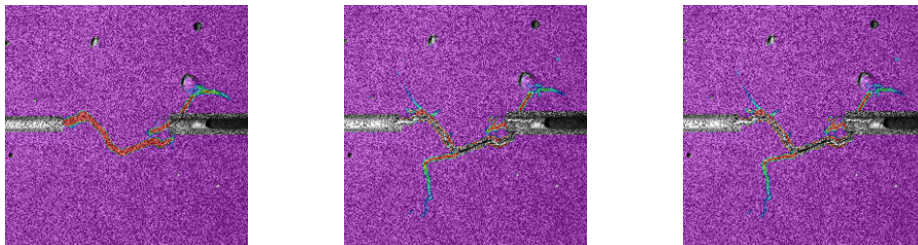
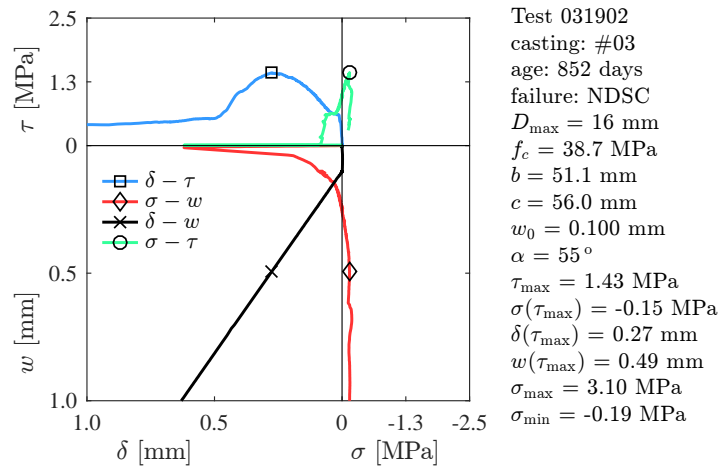


Figure A2.33 – Results for test 031902

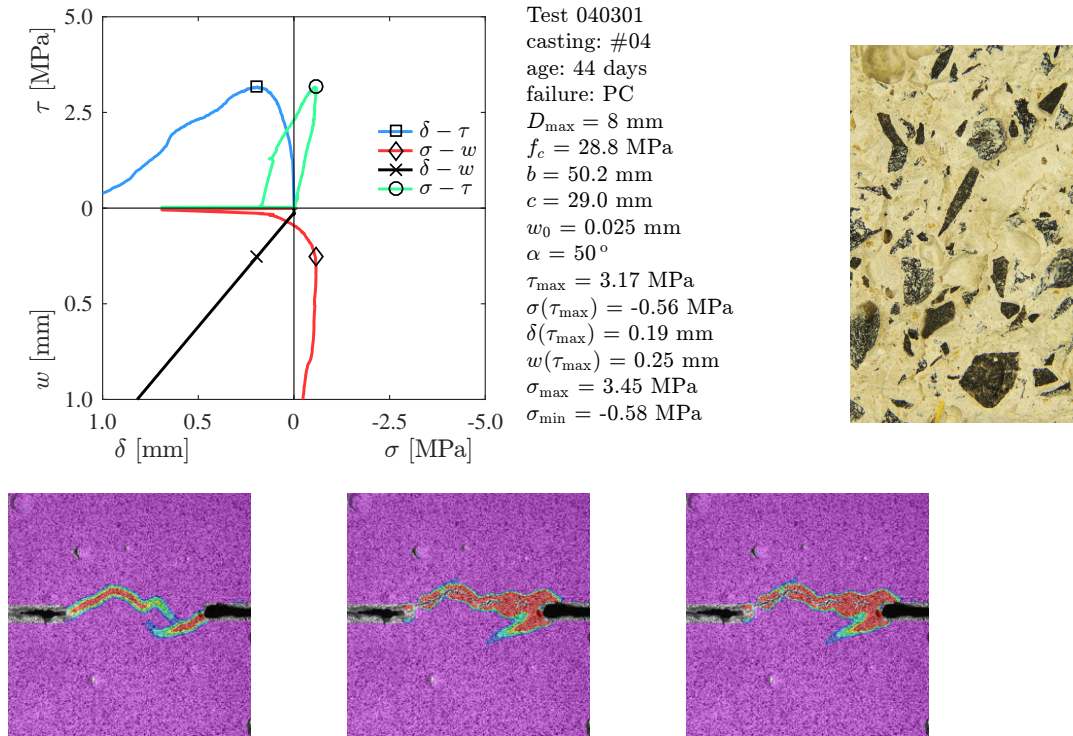


Figure A2.34 – Results for test 040301

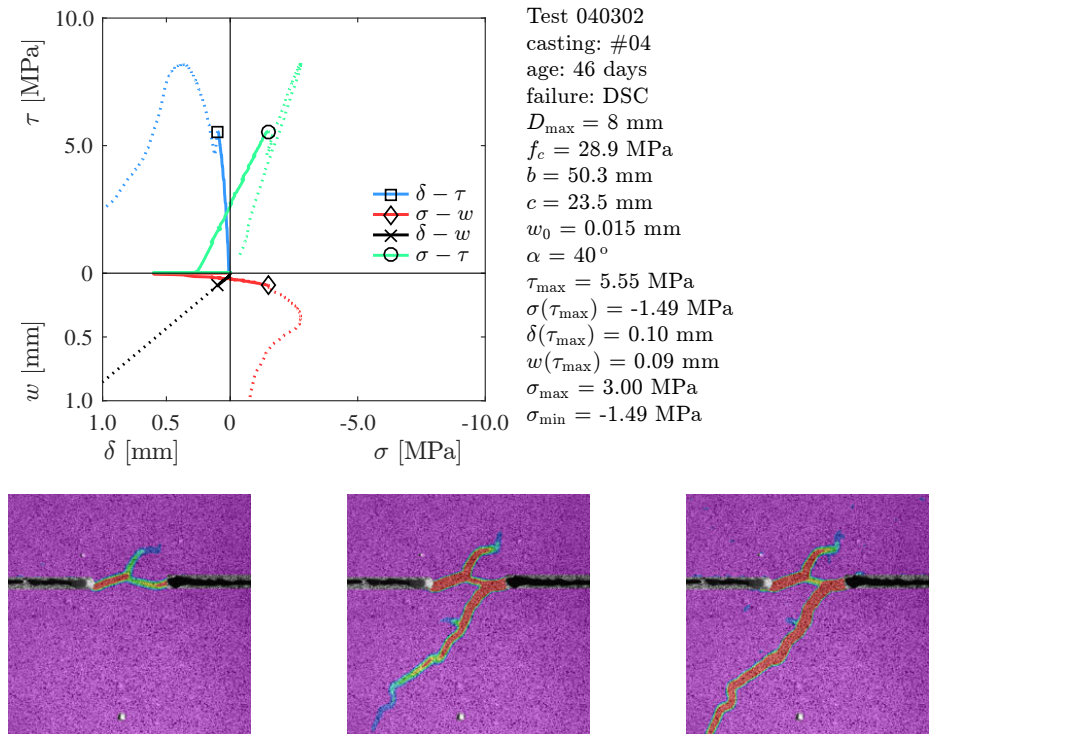


Figure A2.35 – Results for test 040302

Appendix 2

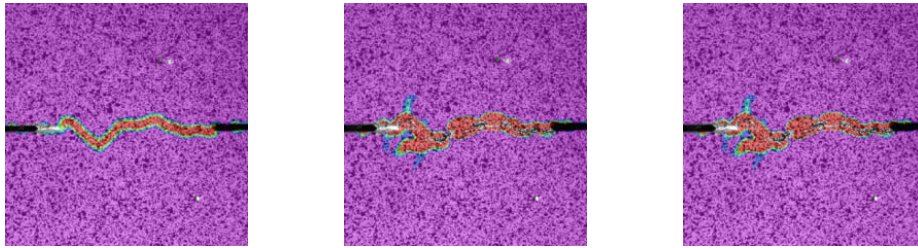
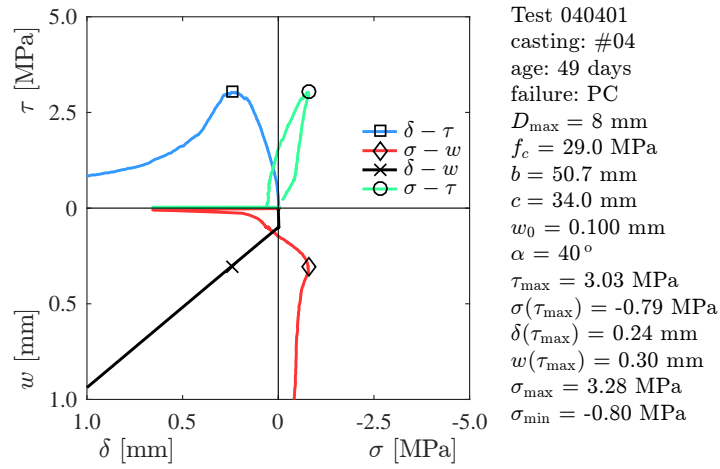


Figure A2.36 – Results for test 040401

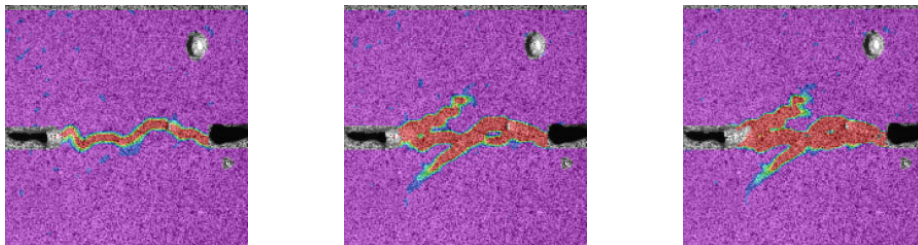
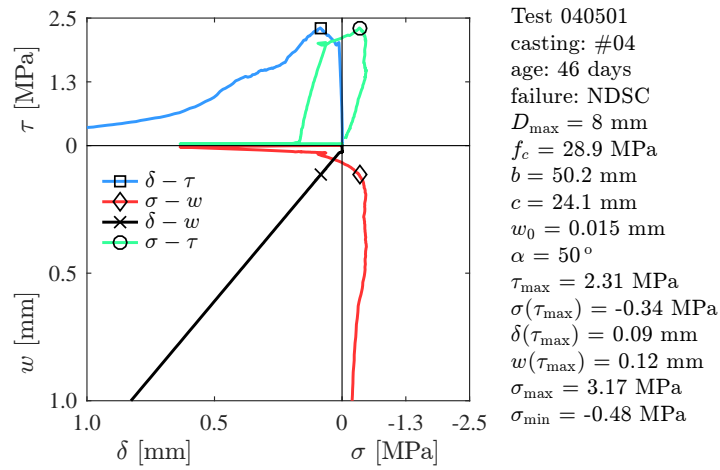


Figure A2.37 – Results for test 040501

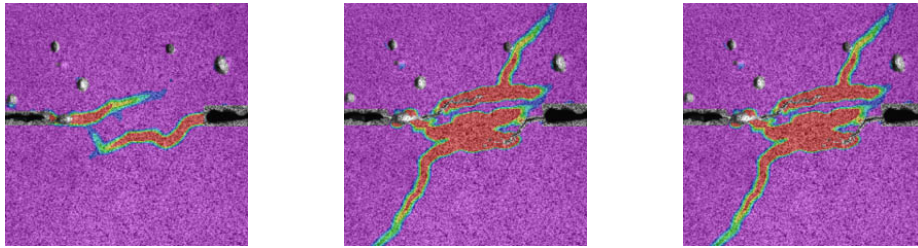
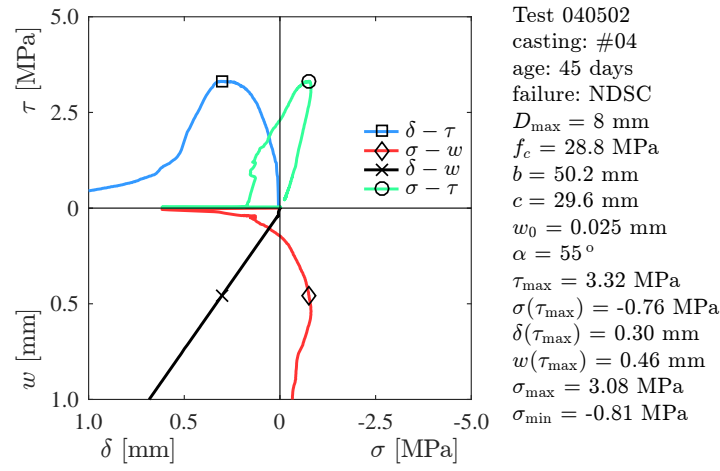


Figure A2.38 – Results for test 040502

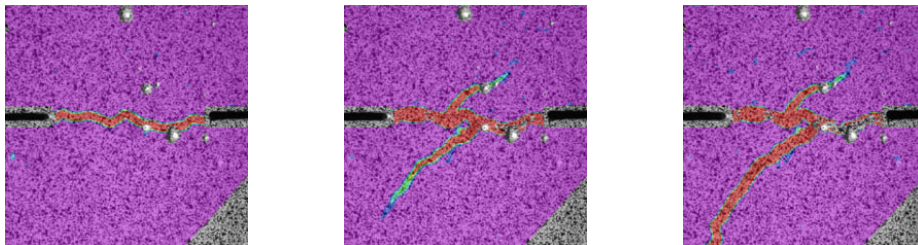
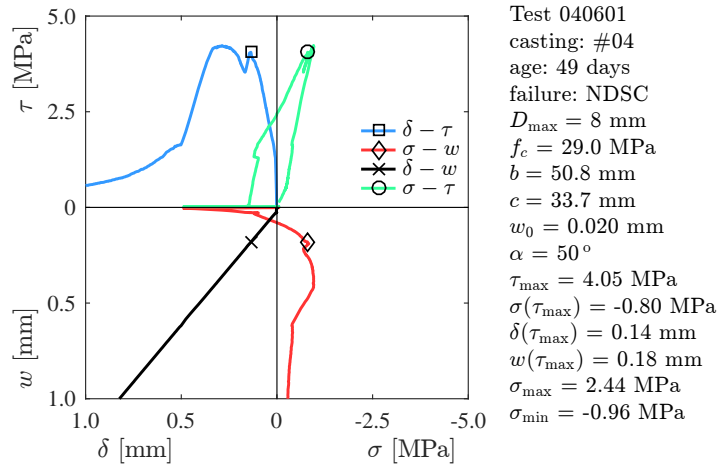


Figure A2.39 – Results for test 040601

Appendix 2

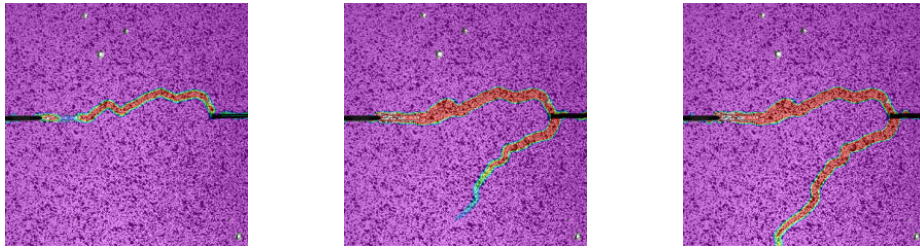
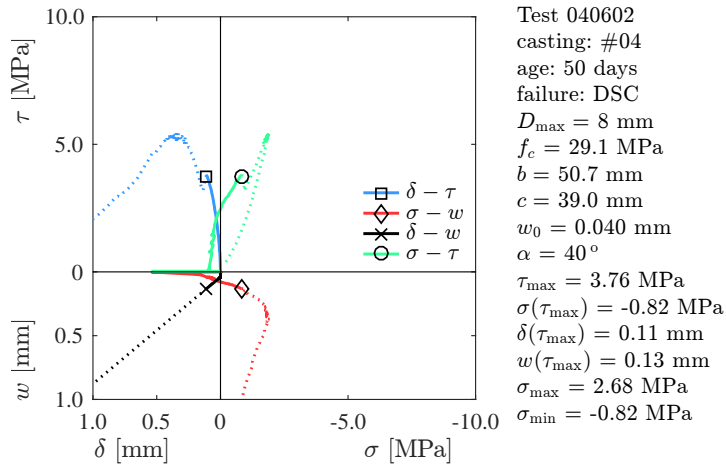


Figure A2.40 – Results for test 040602

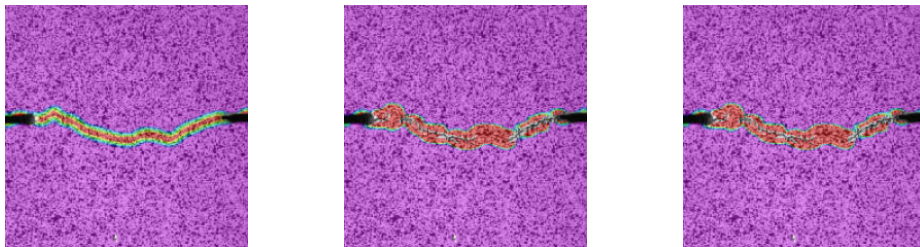
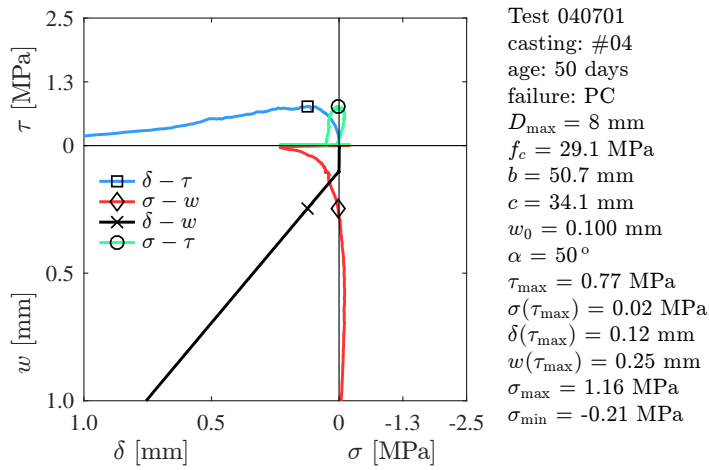


Figure A2.41 – Results for test 040701

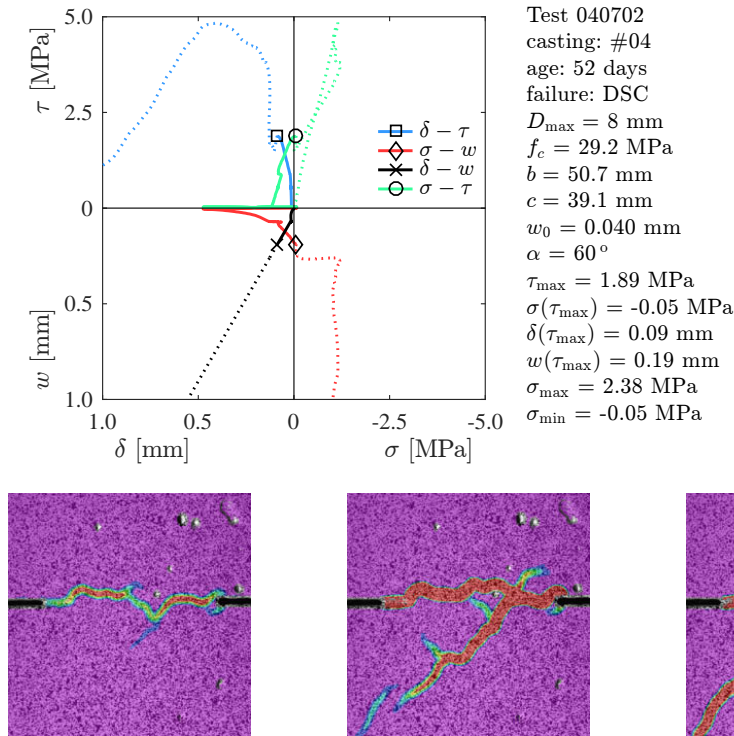


Figure A2.42 – Results for test 040702

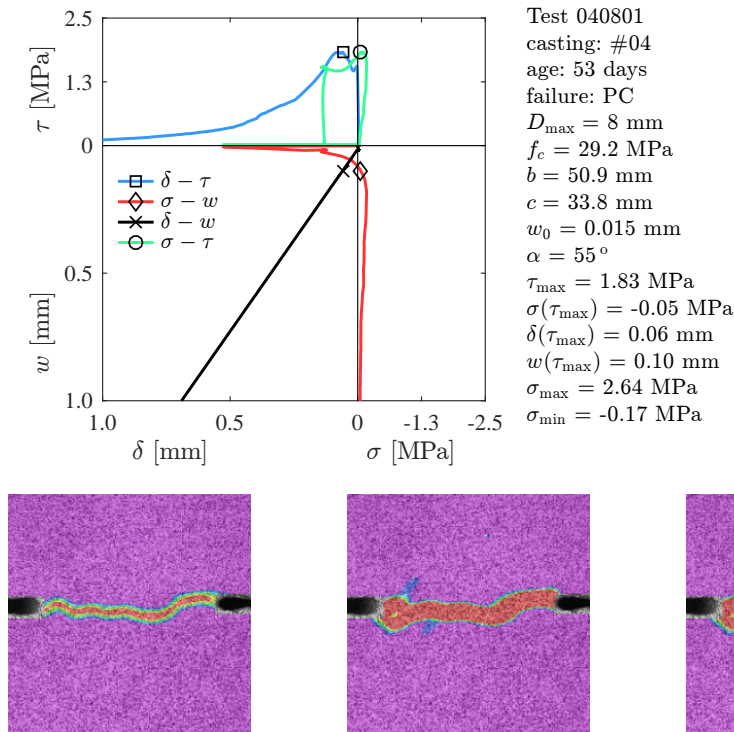


Figure A2.43 – Results for test 040801

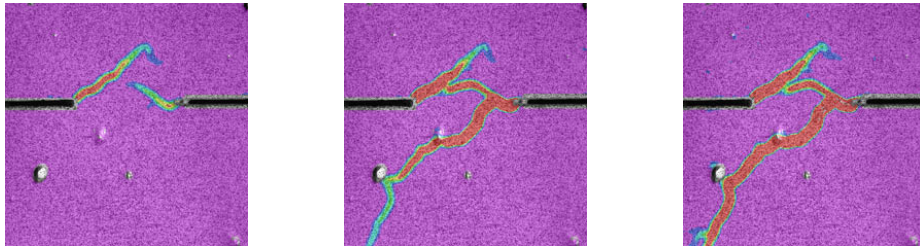
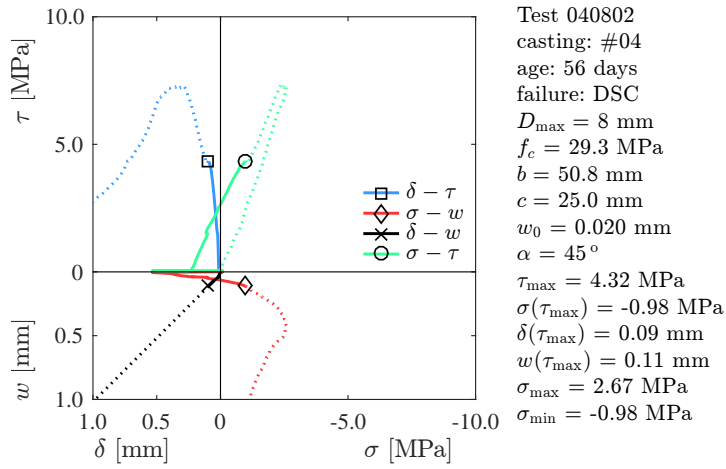


Figure A2.44 – Results for test 040802

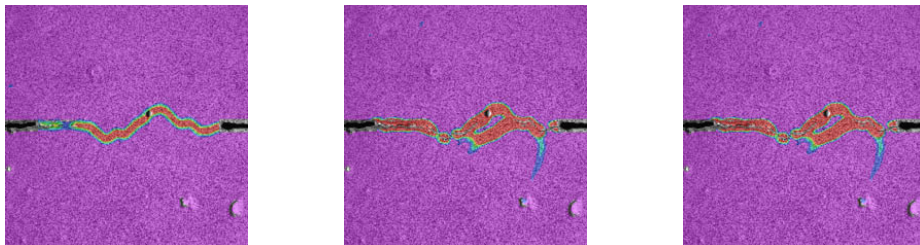
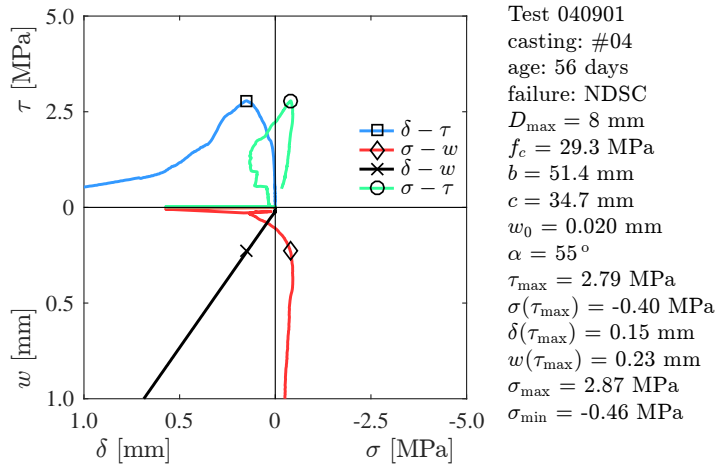


Figure A2.45 – Results for test 040901

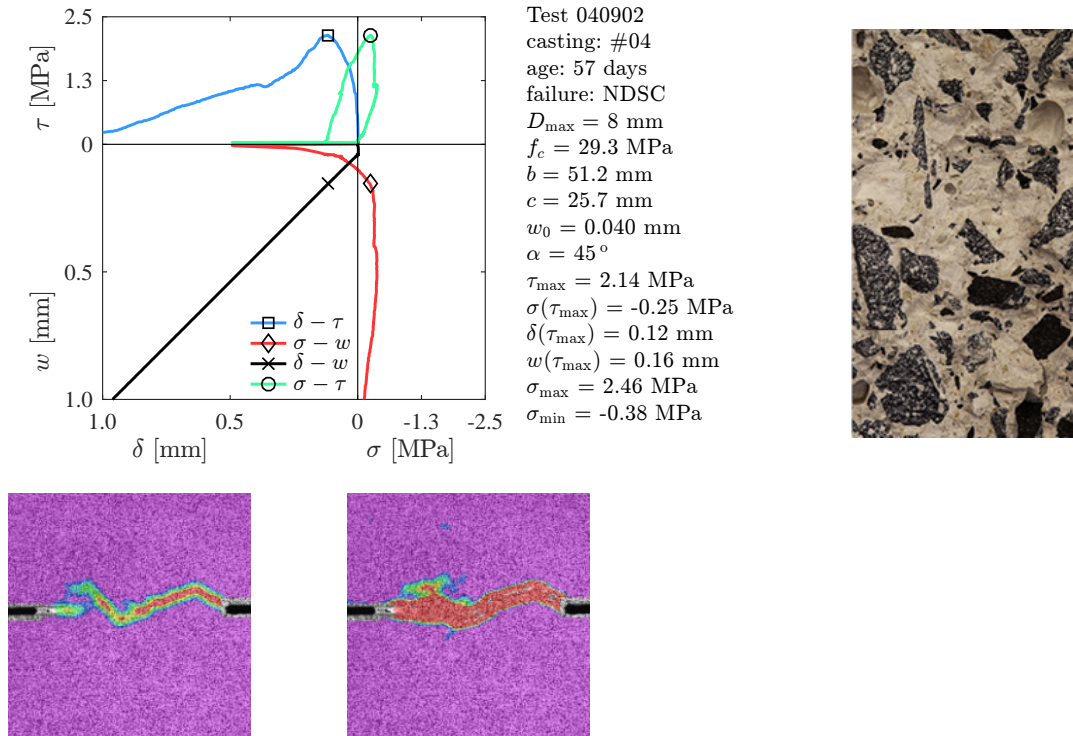


Figure A2.46 – Results for test 040902

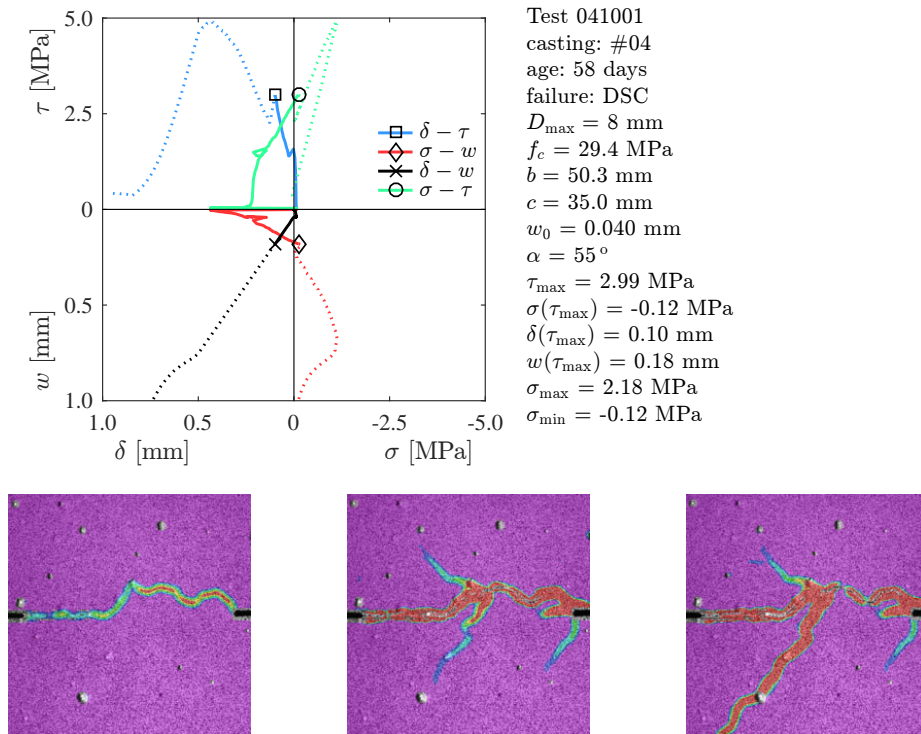


Figure A2.47 – Results for test 041001

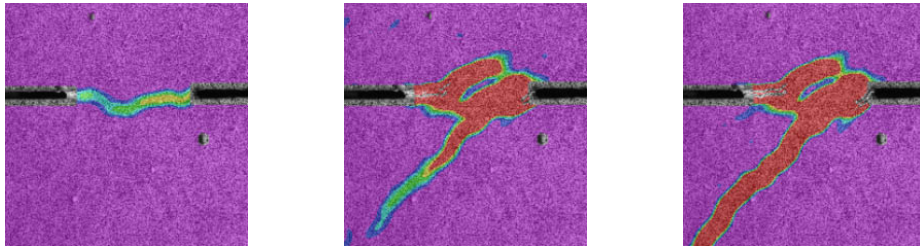
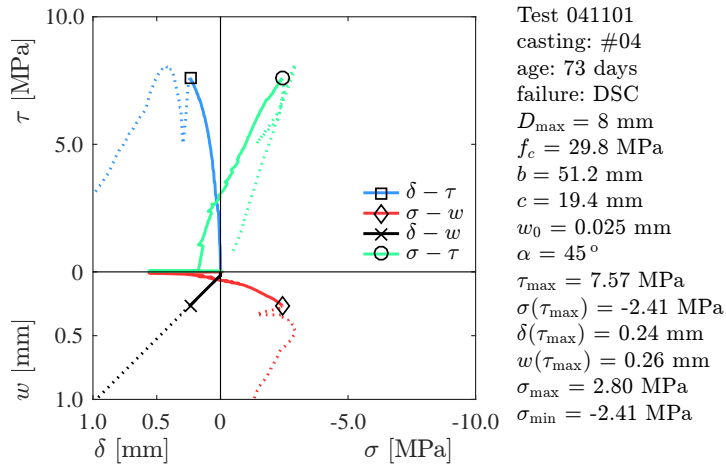


Figure A2.48 – Results for test 041101

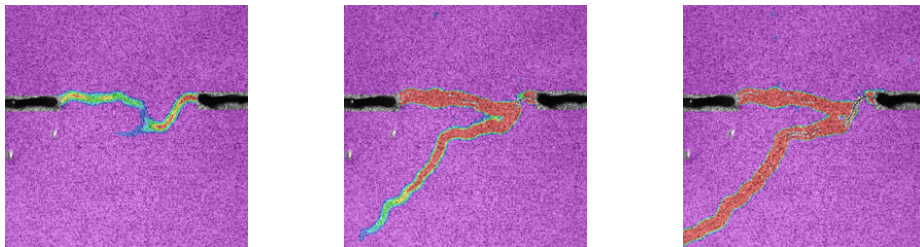
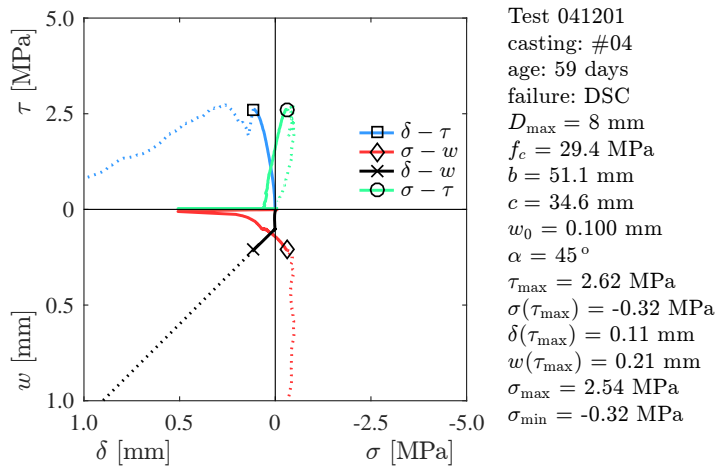


Figure A2.49 – Results for test 041201

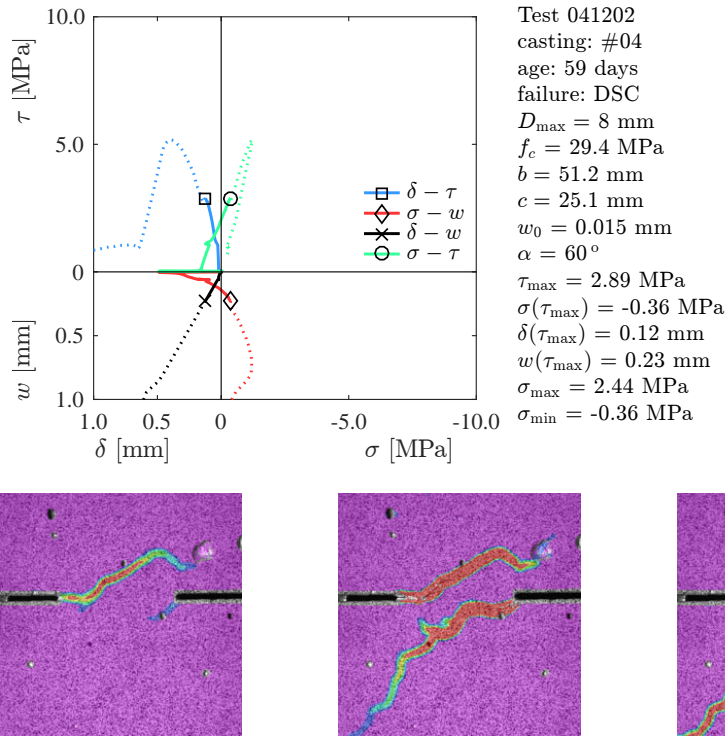


Figure A2.50 – Results for test 041202

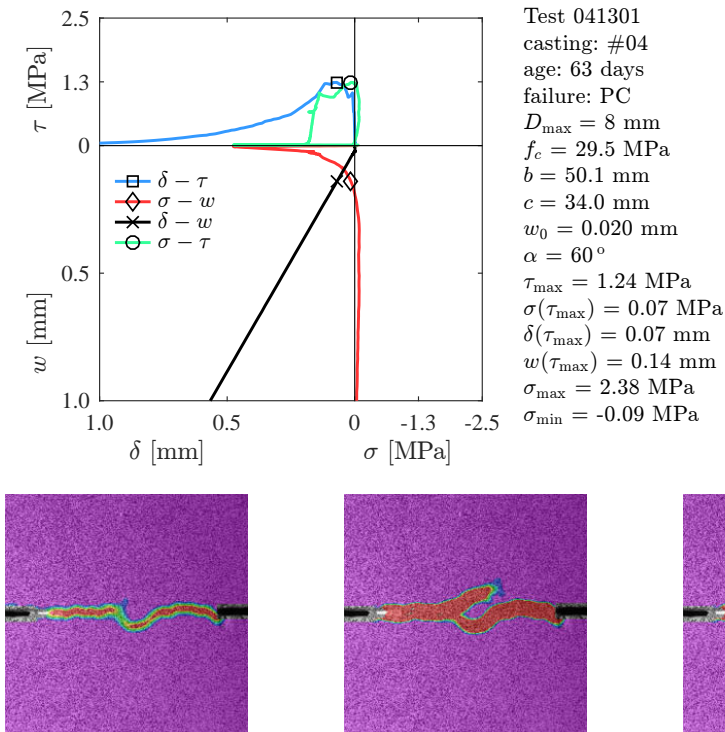


Figure A2.51 – Results for test 041301

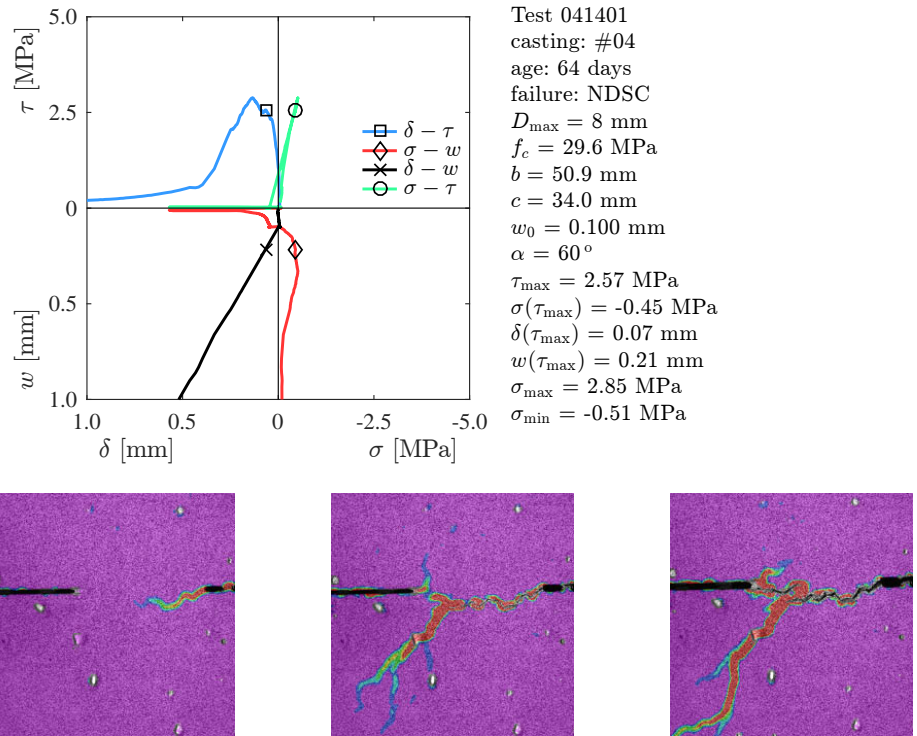


Figure A2.52 – Results for test 041401

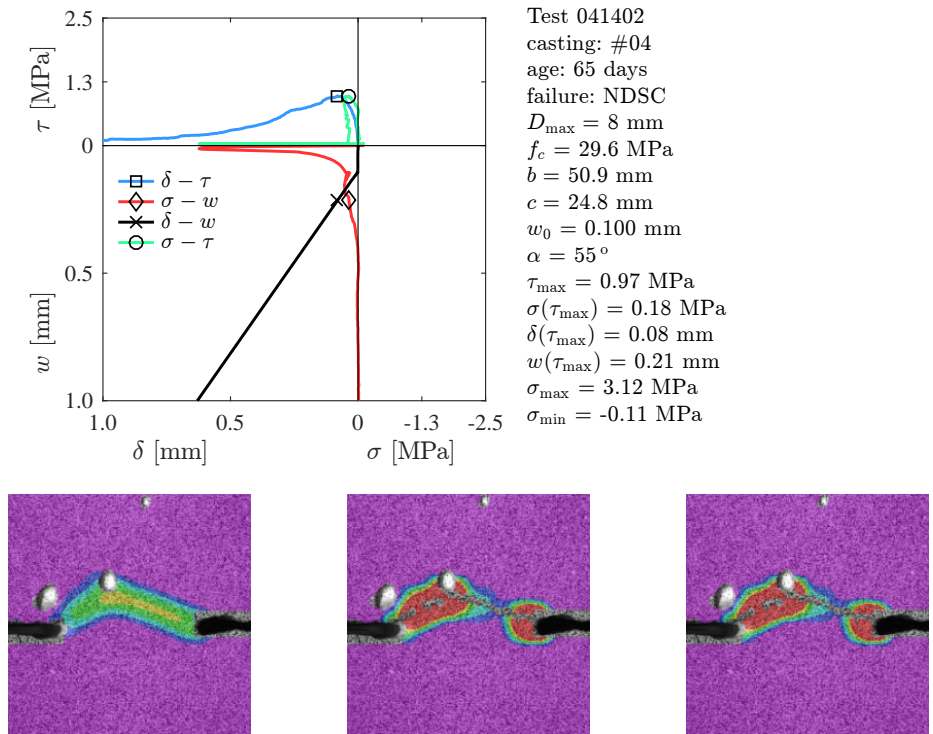


Figure A2.53 – Results for test 041402

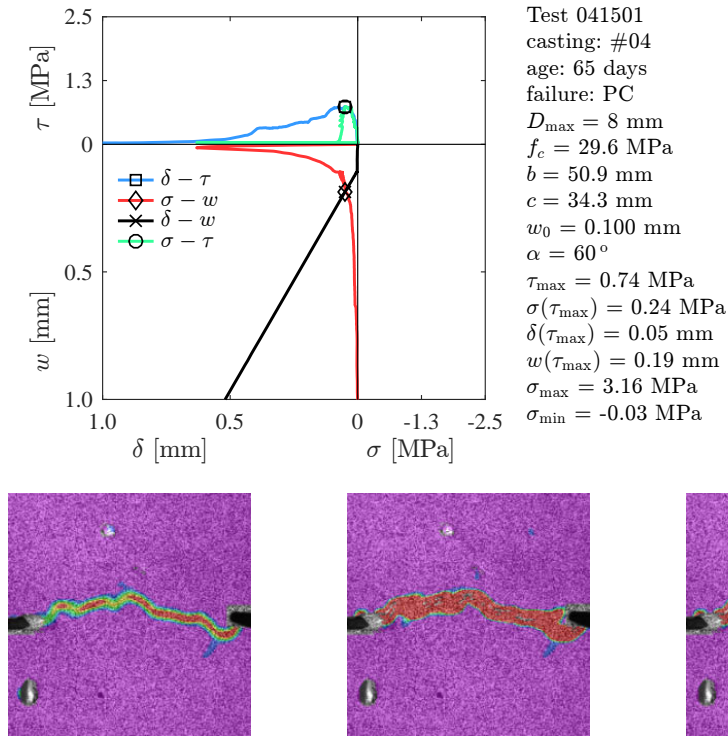


Figure A2.54 – Results for test 041501

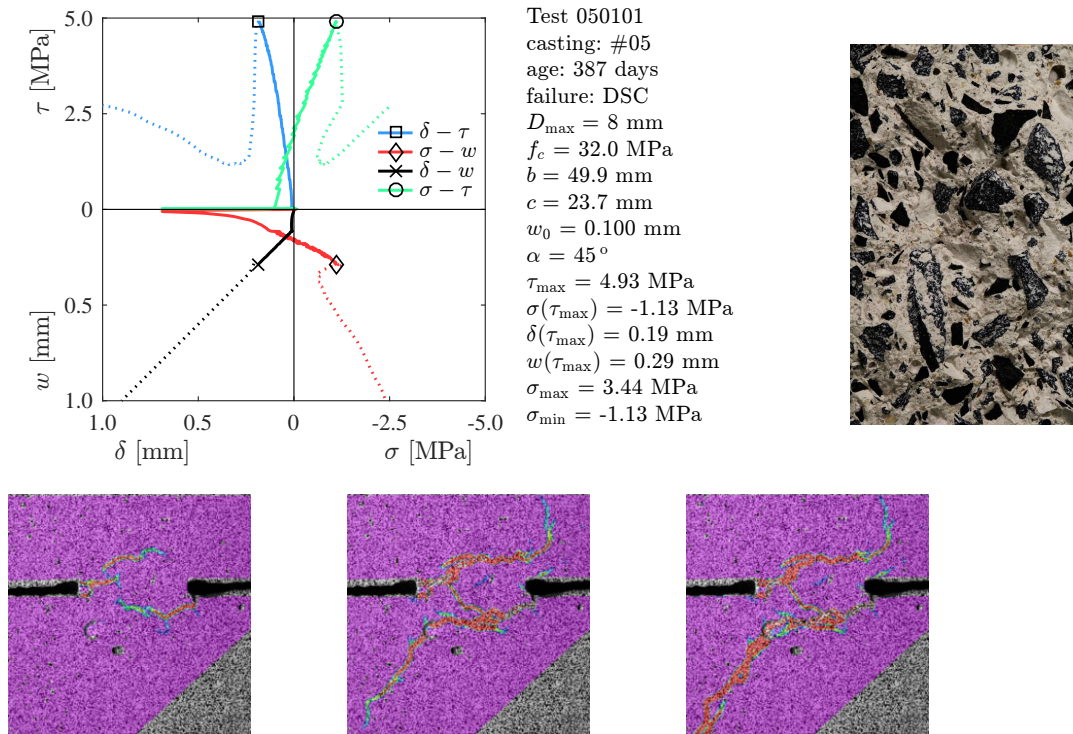


Figure A2.55 – Results for test 050101

Appendix 2

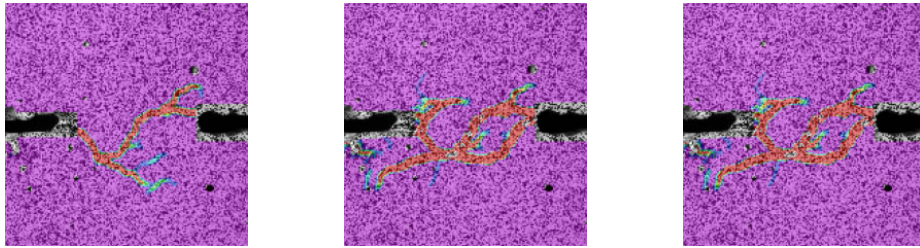
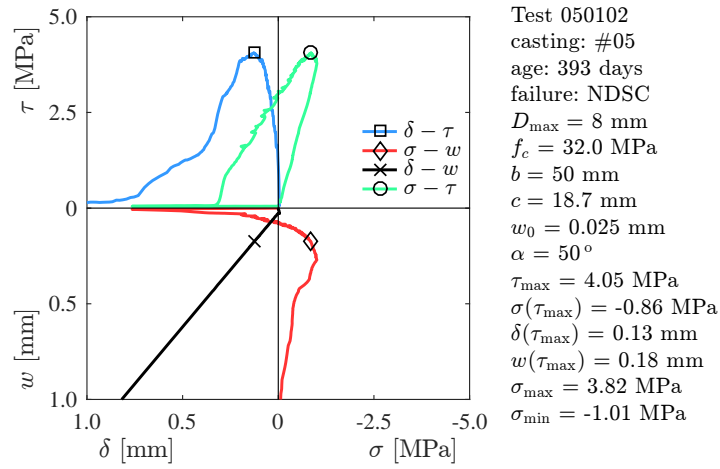


Figure A2.56 – Results for test 050102

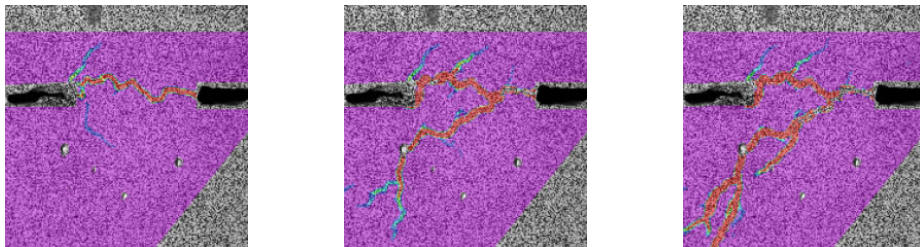
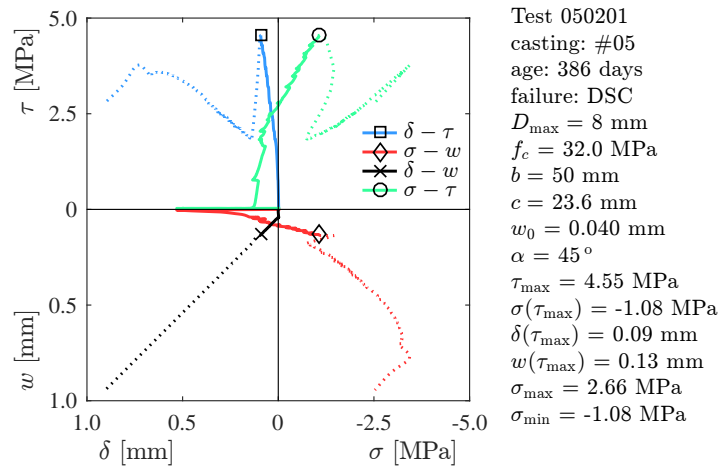


Figure A2.57 – Results for test 050201

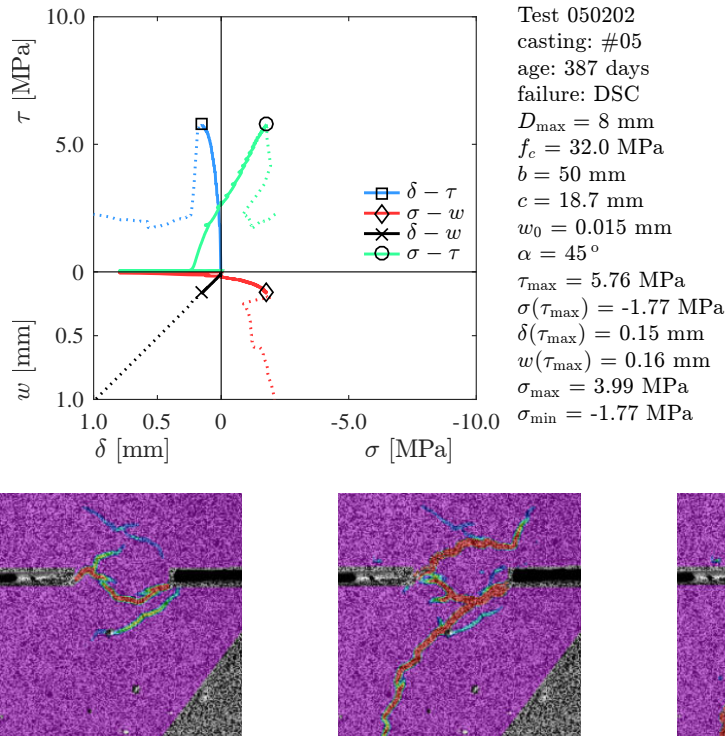


Figure A2.58 – Results for test 050202

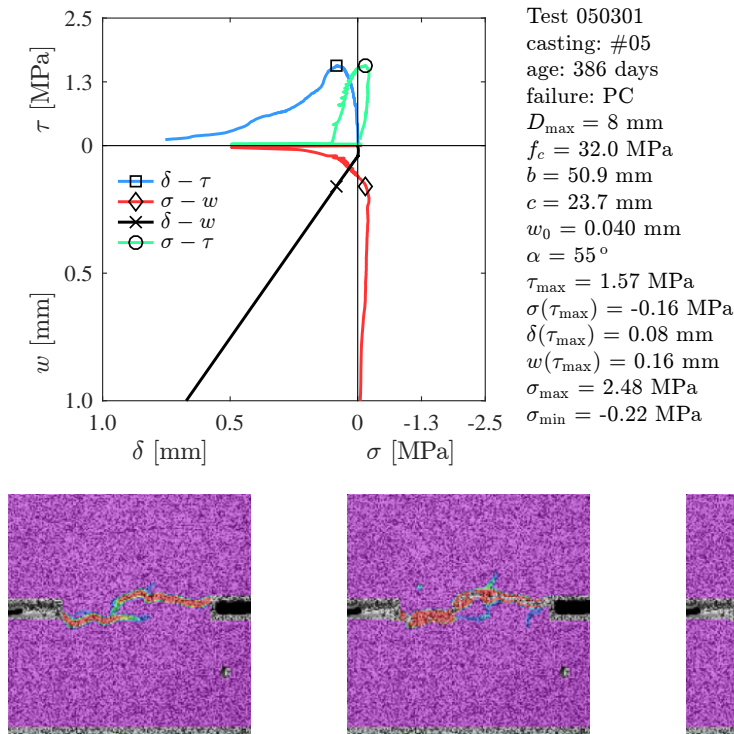


Figure A2.59 – Results for test 050301

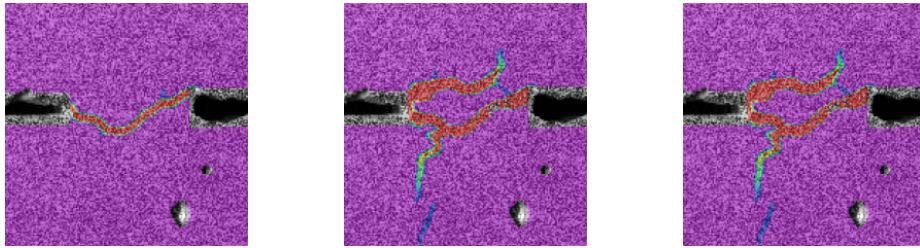
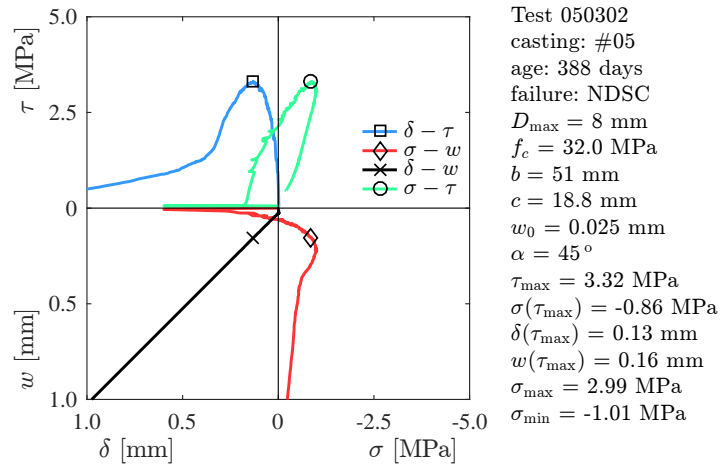


Figure A2.60 – Results for test 050302

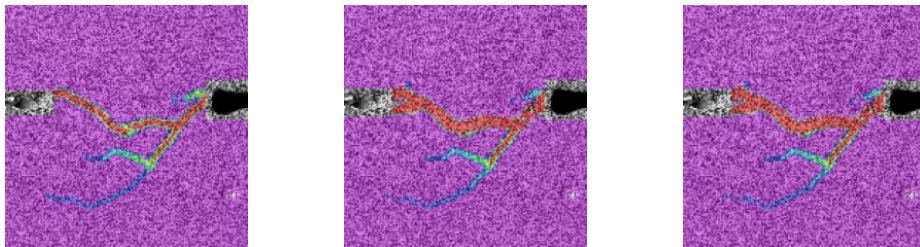
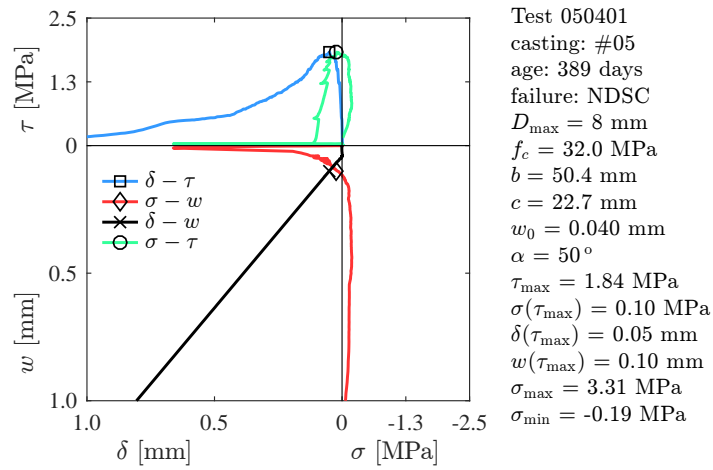


Figure A2.61 – Results for test 050401

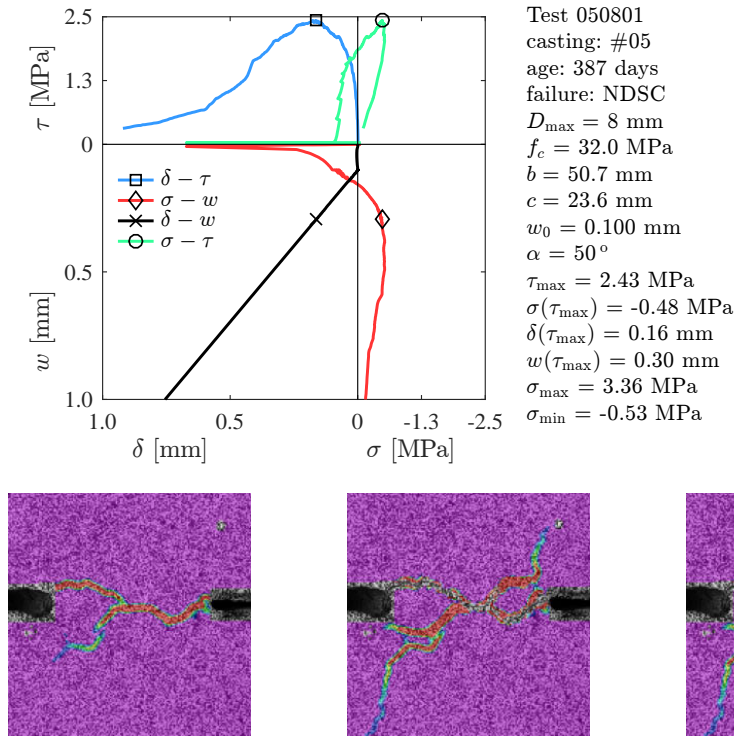


Figure A2.62 – Results for test 050801

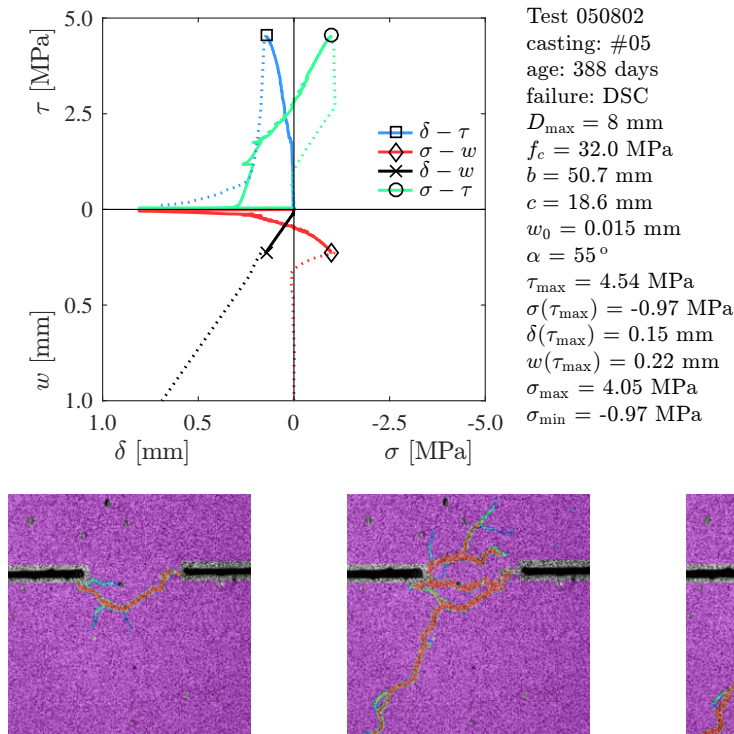


Figure A2.63 – Results for test 050802

Appendix 2

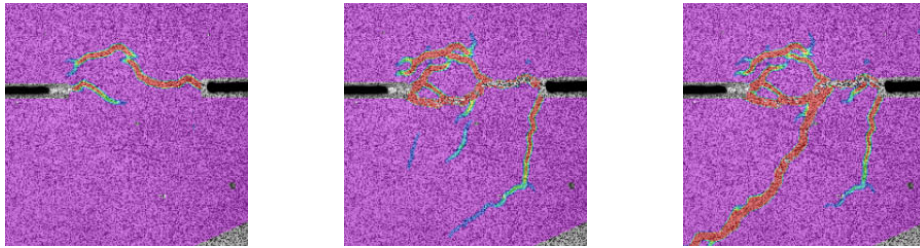
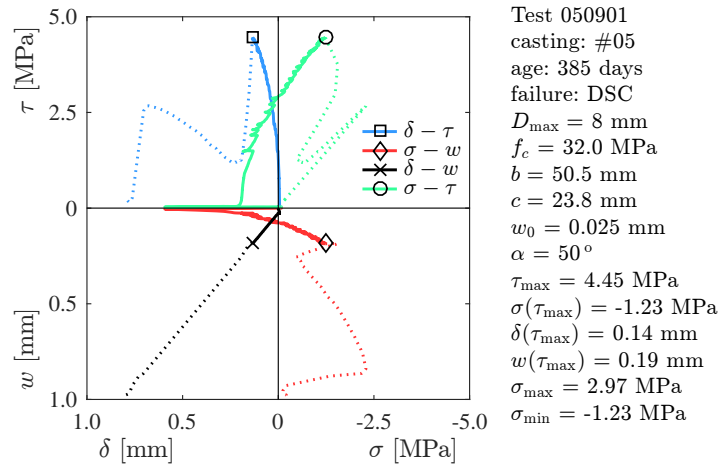


Figure A2.64 – Results for test 050901

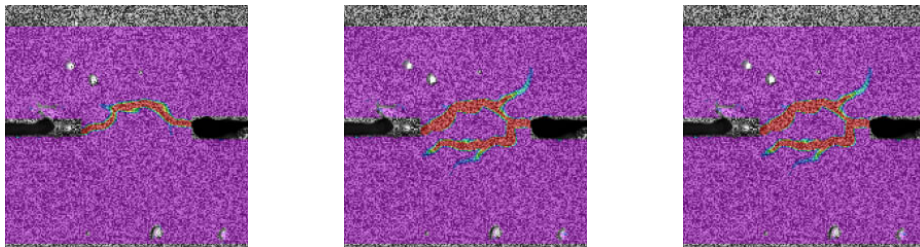
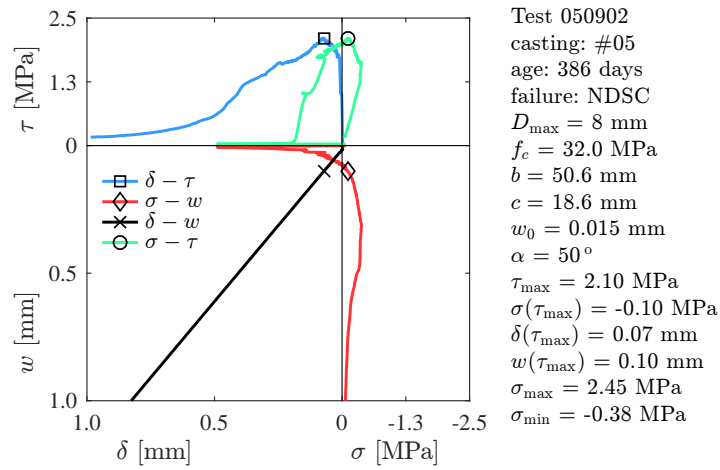


Figure A2.65 – Results for test 050902

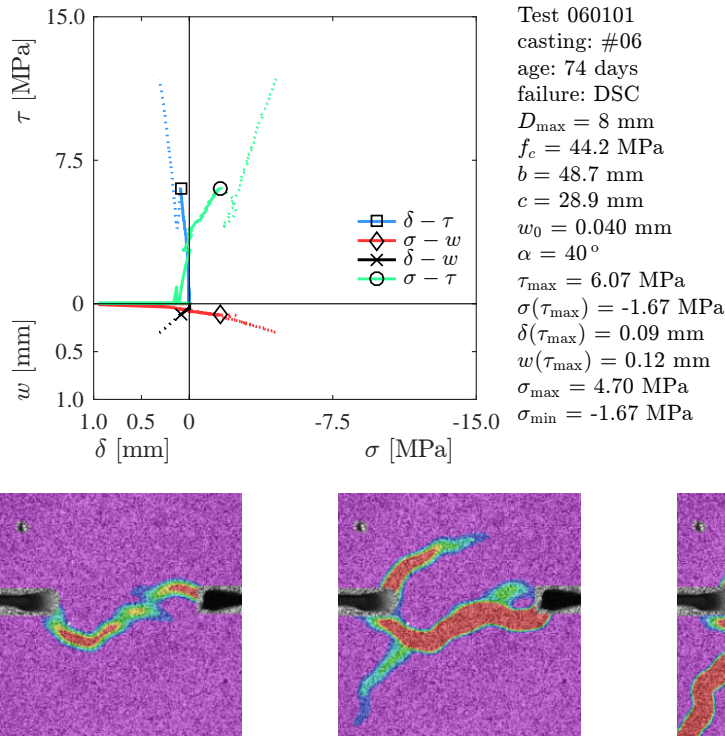


Figure A2.66 – Results for test 060101

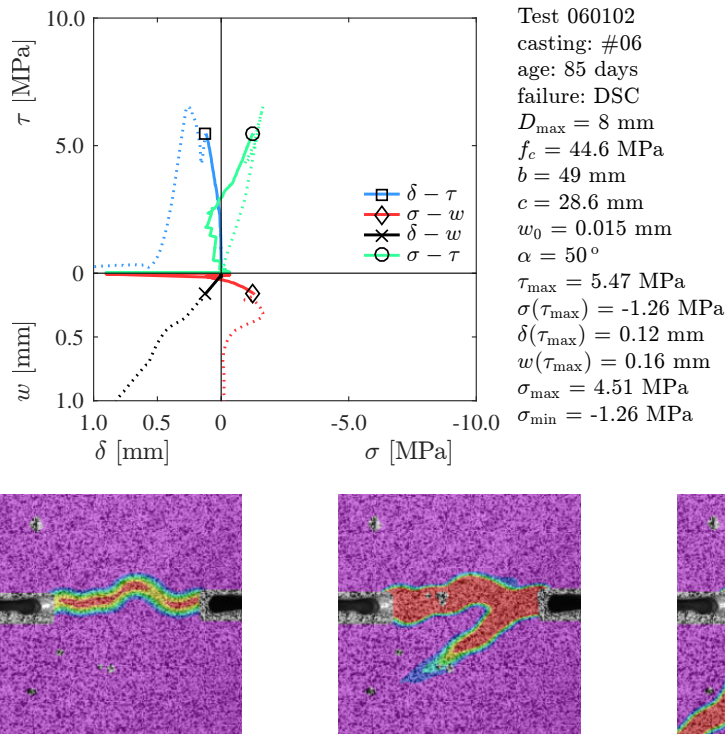


Figure A2.67 – Results for test 060102

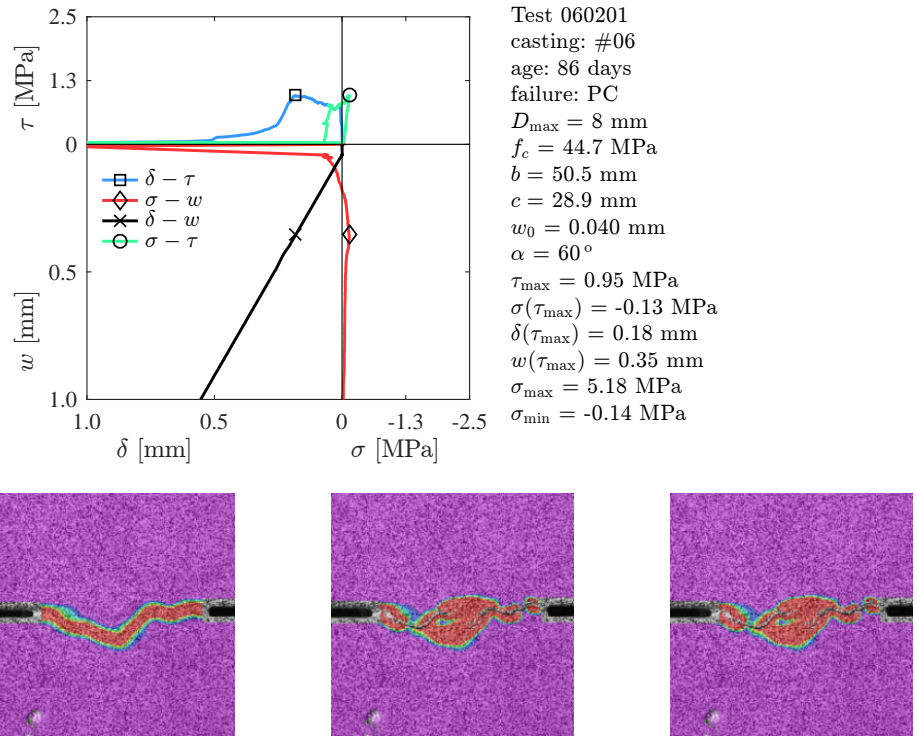


Figure A2.68 – Results for test 060201

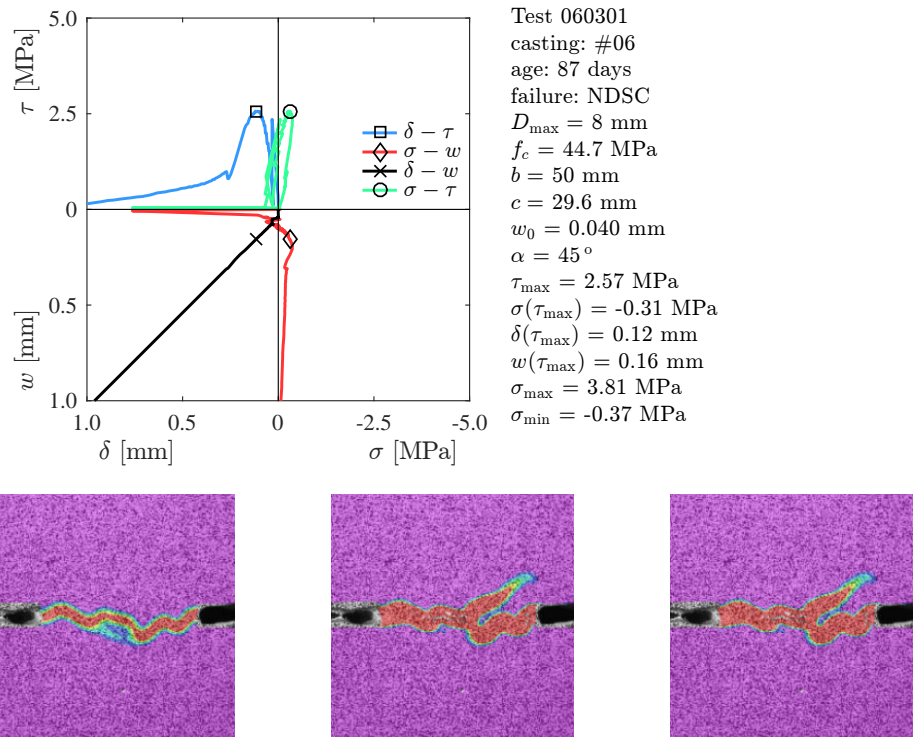


Figure A2.69 – Results for test 060301

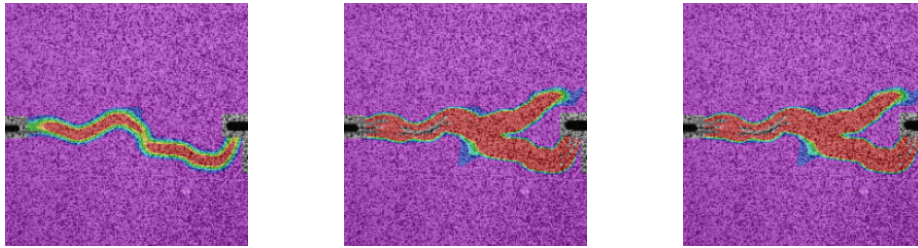
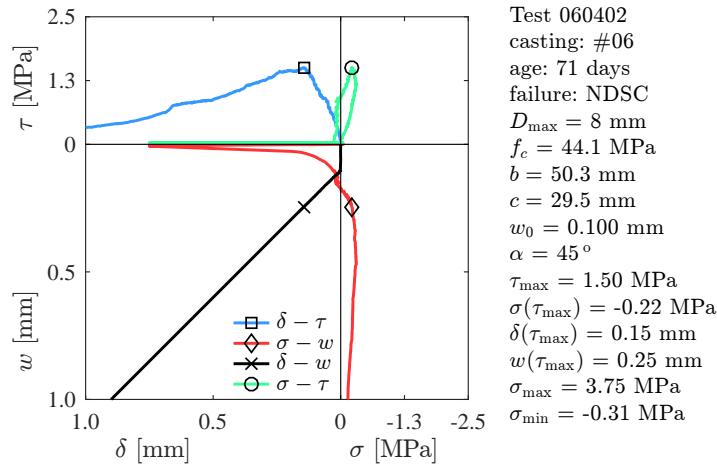


Figure A2.70 – Results for test 060402

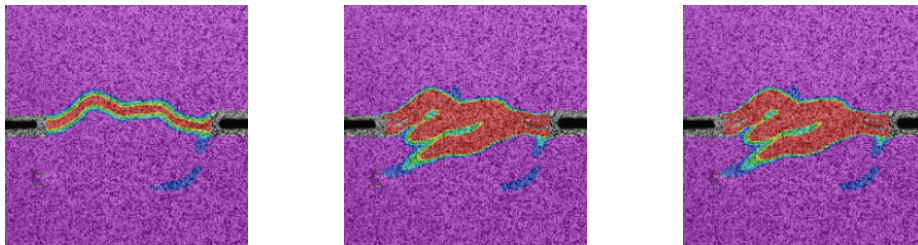
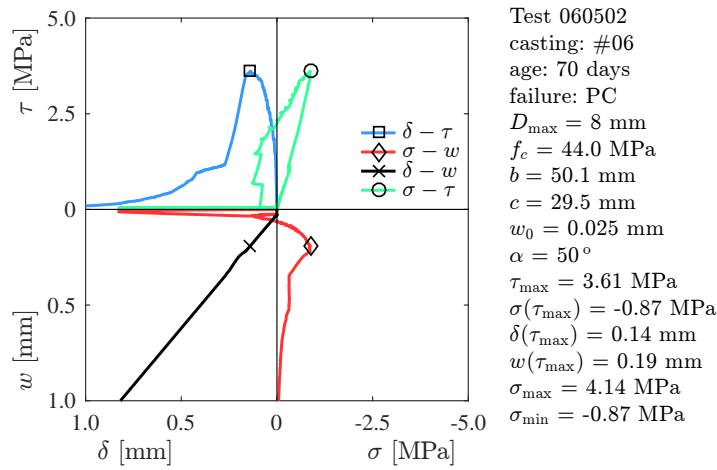


Figure A2.71 – Results for test 060502

Appendix 2

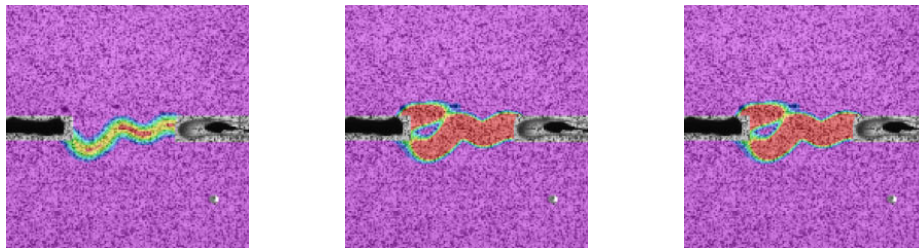
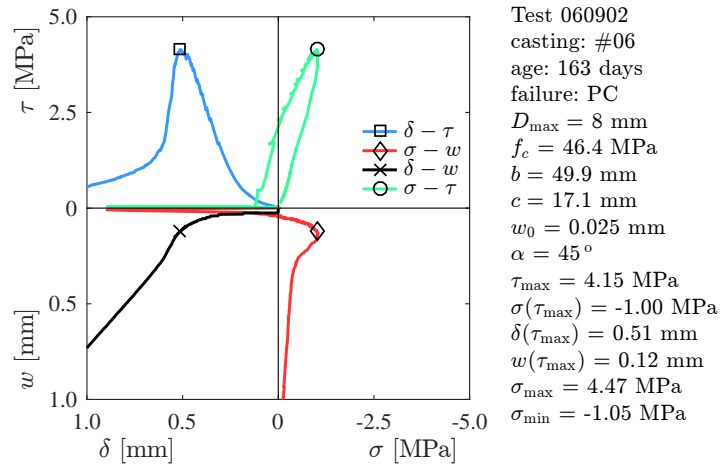


Figure A2.72 – Results for test 060902

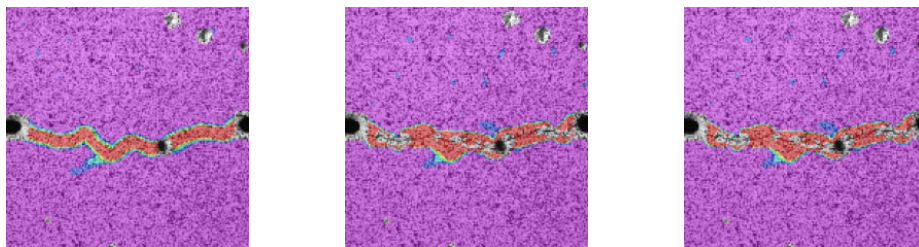
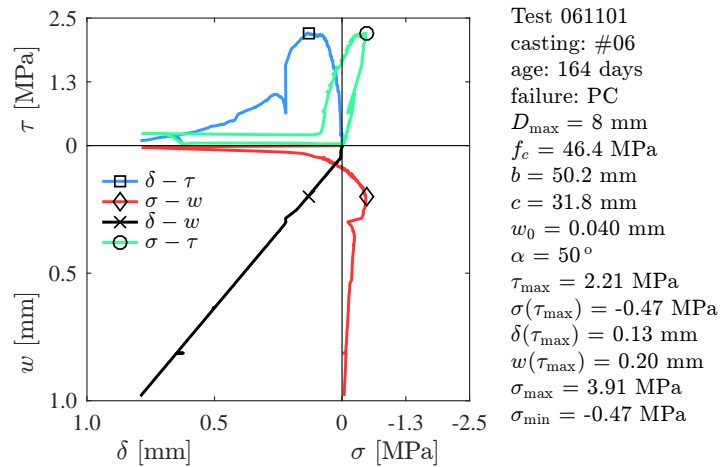


Figure A2.73 – Results for test 061101

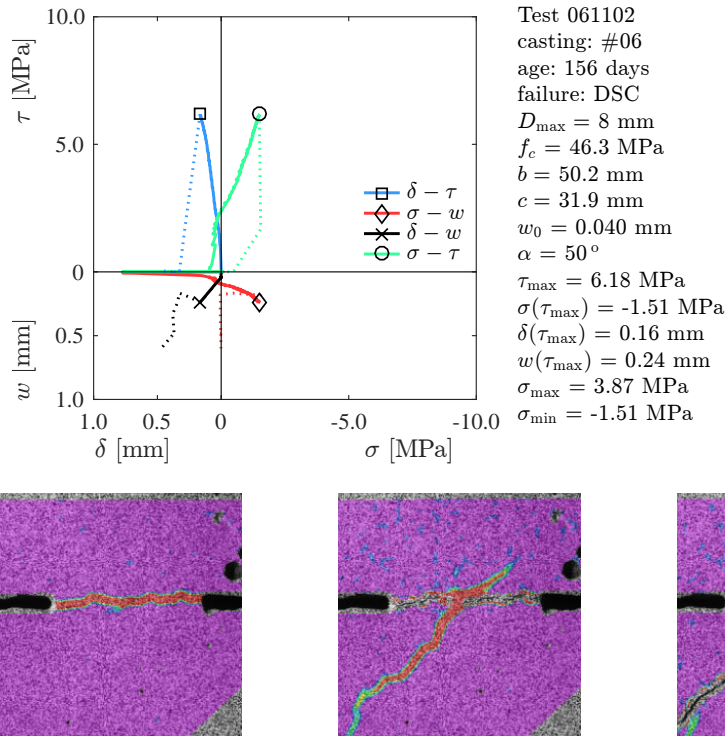


Figure A2.74 – Results for test 061102

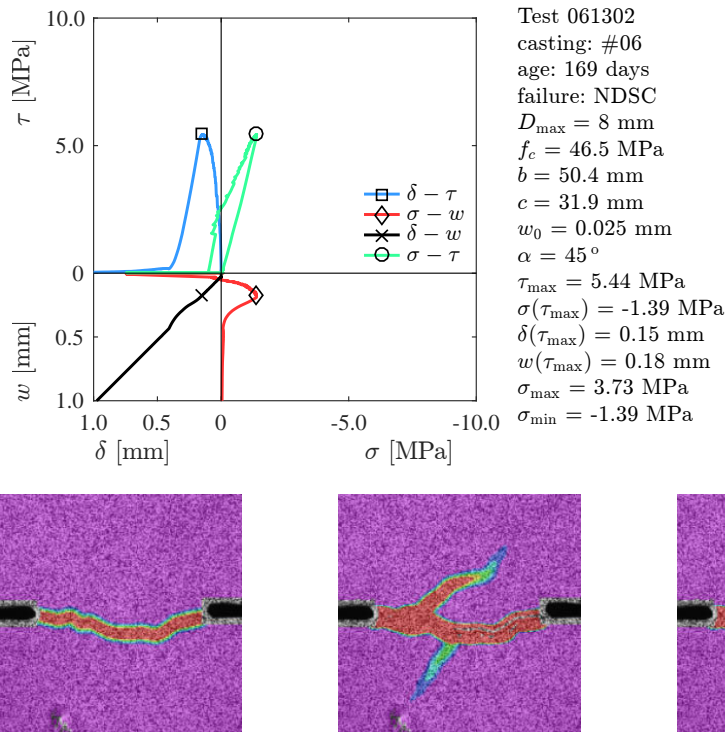


Figure A2.75 – Results for test 061302

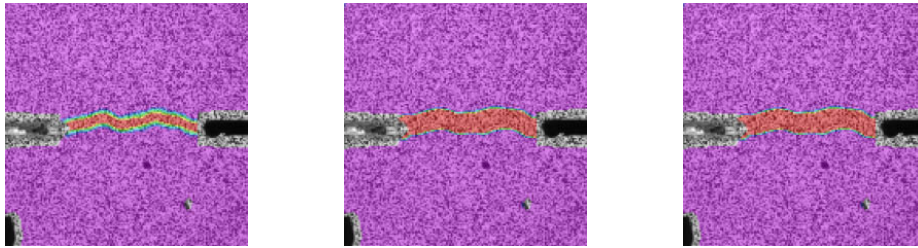
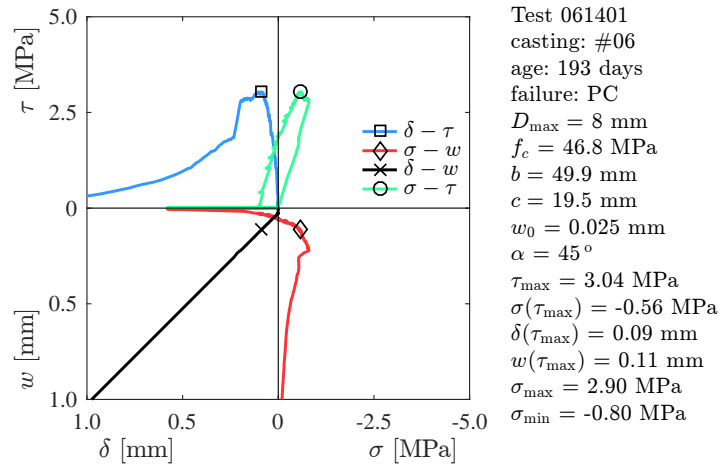


Figure A2.76 – Results for test 061401

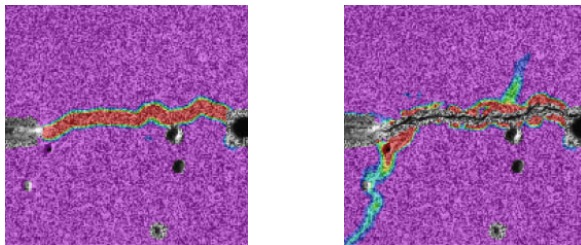
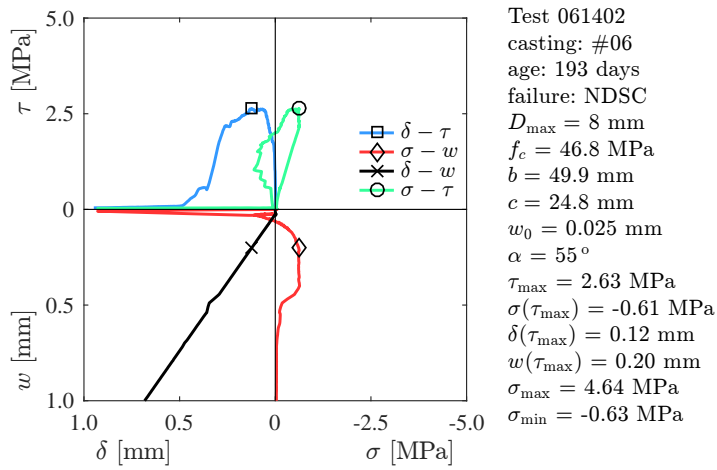


Figure A2.77 – Results for test 061402

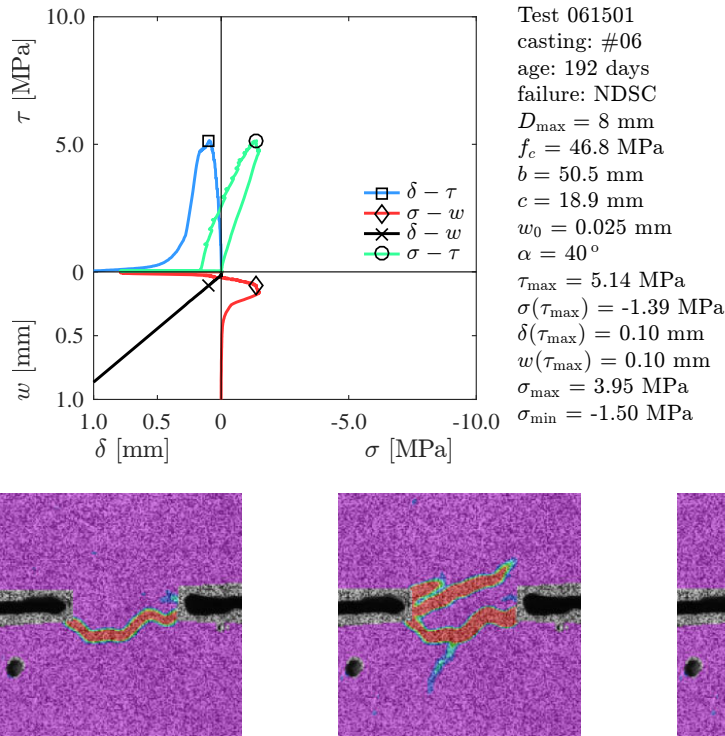


Figure A2.78 – Results for test 061501

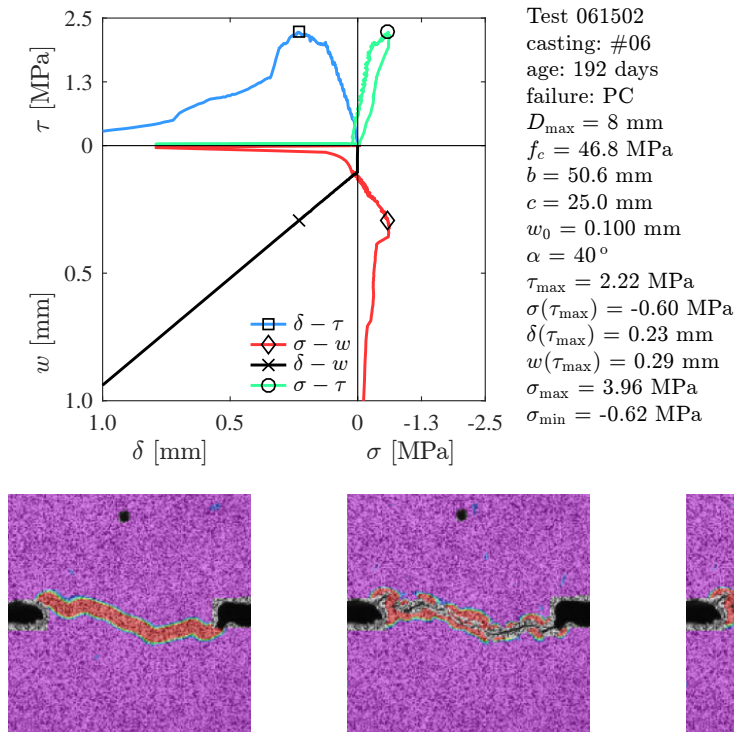


Figure A2.79 – Results for test 061502

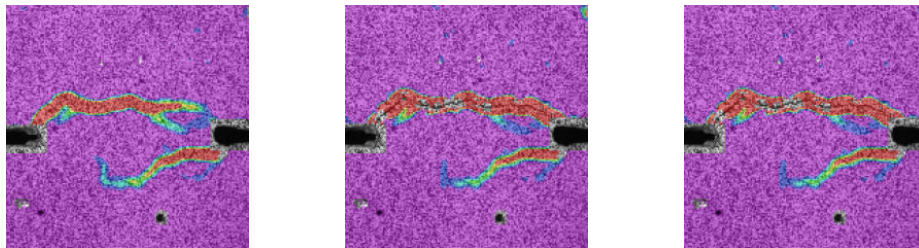
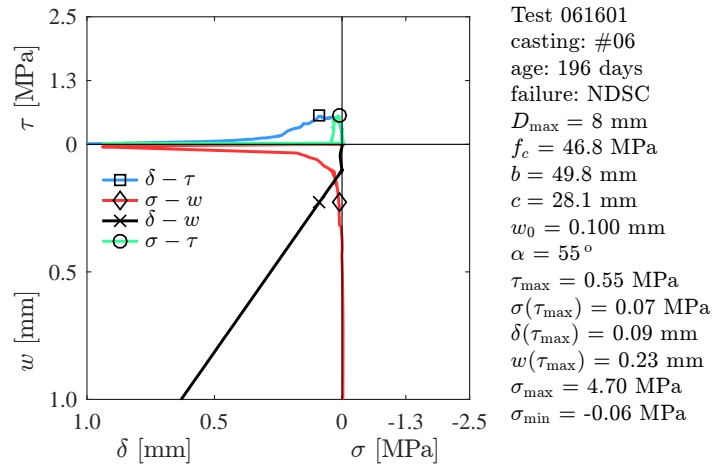


Figure A2.80 – Results for test 061601

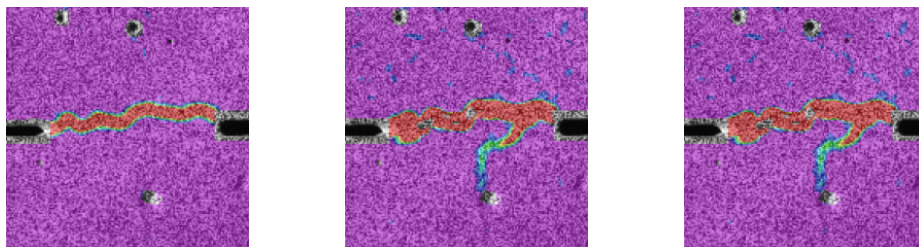
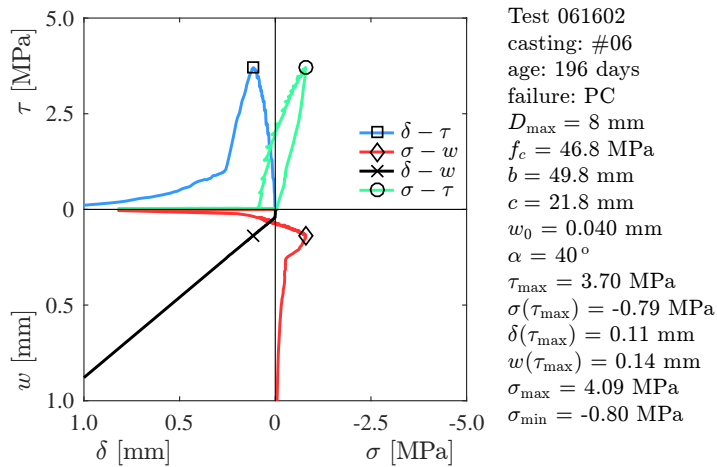


Figure A2.81 – Results for test 061602

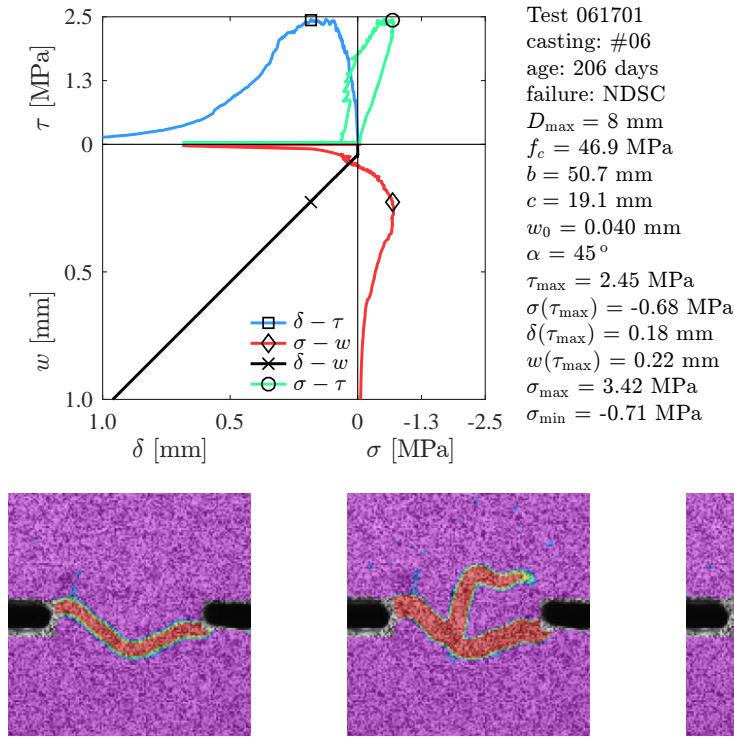


Figure A2.82 – Results for test 061701

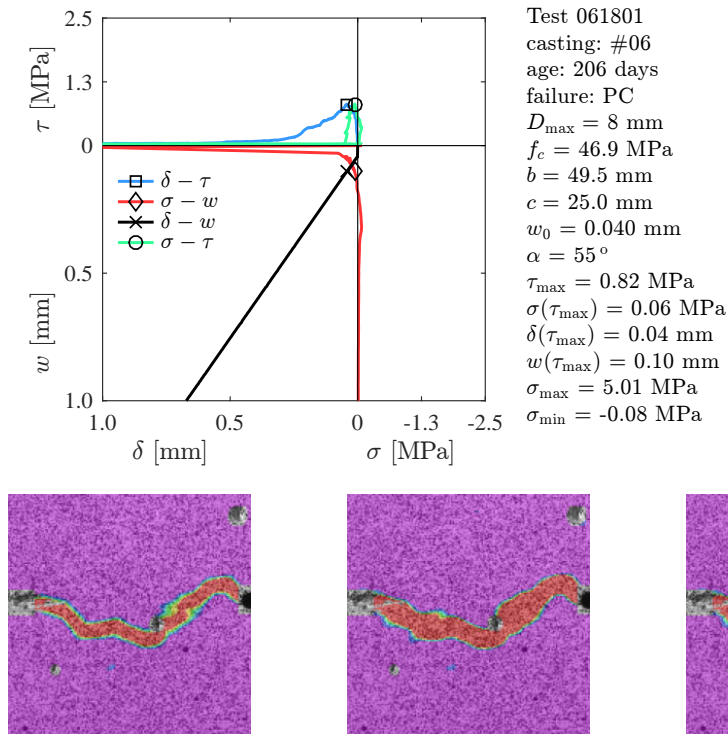


Figure A2.83 – Results for test 061801

Appendix 2

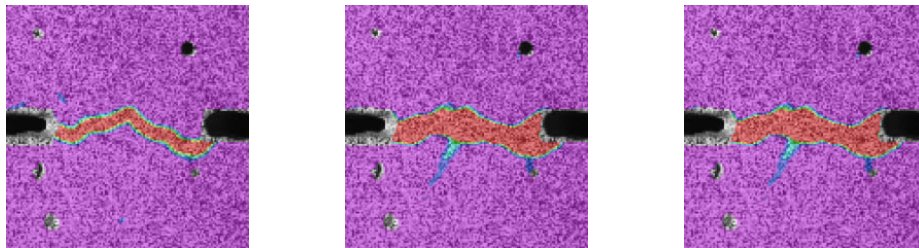
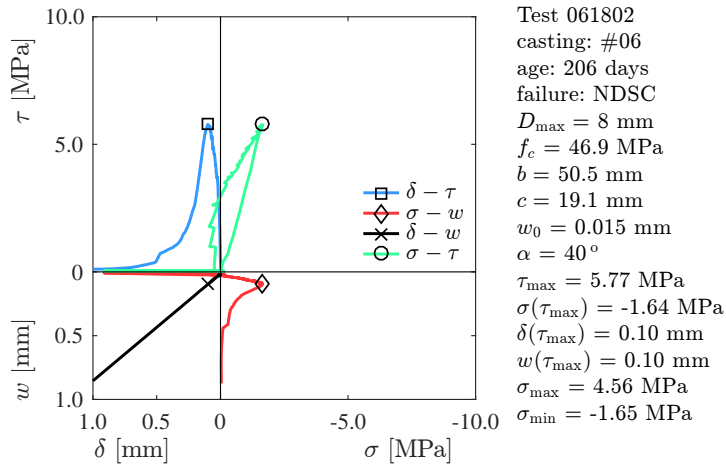


Figure A2.84 – Results for test 061802

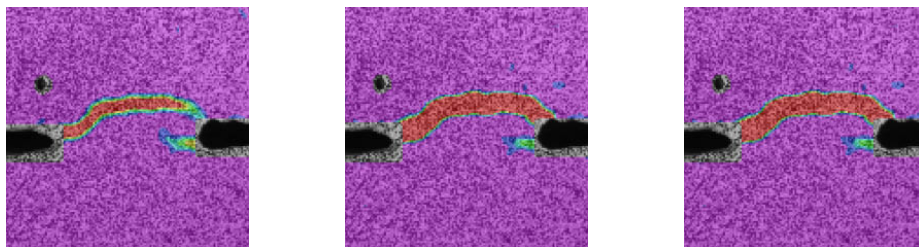
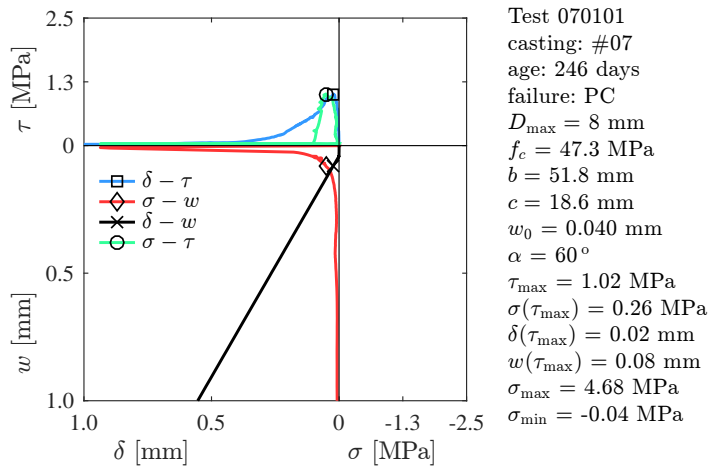


Figure A2.85 – Results for test 070101

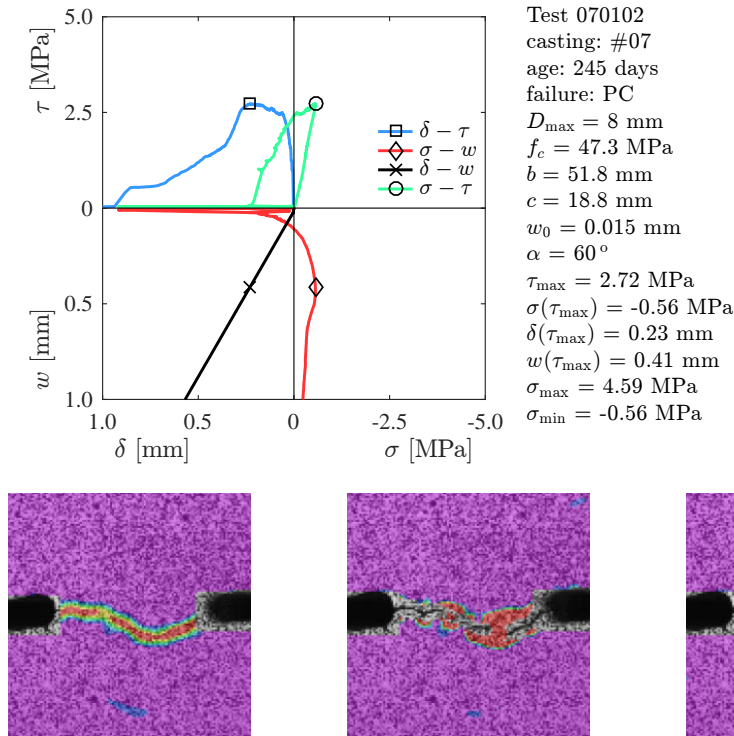


Figure A2.86 – Results for test 070102

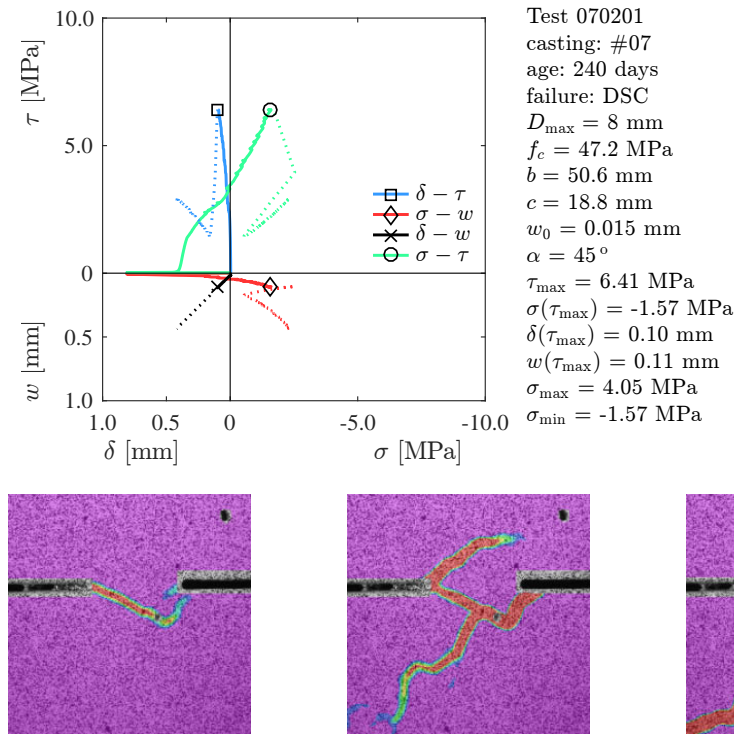


Figure A2.87 – Results for test 070201

Appendix 2

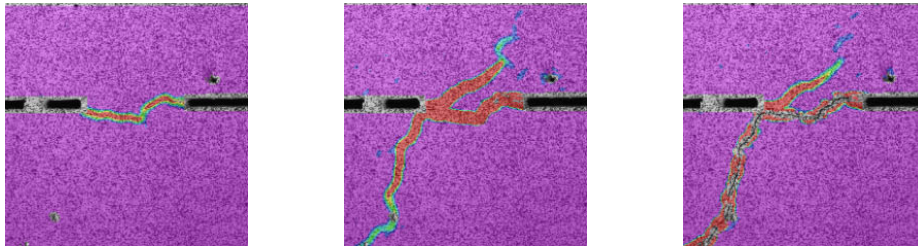
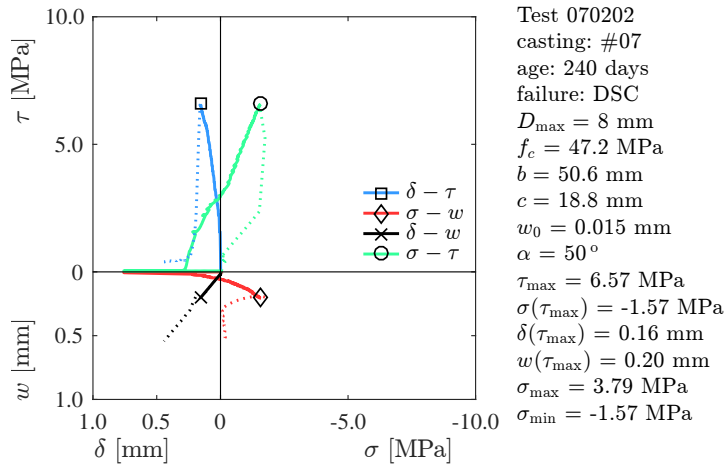


Figure A2.88 – Results for test 070202

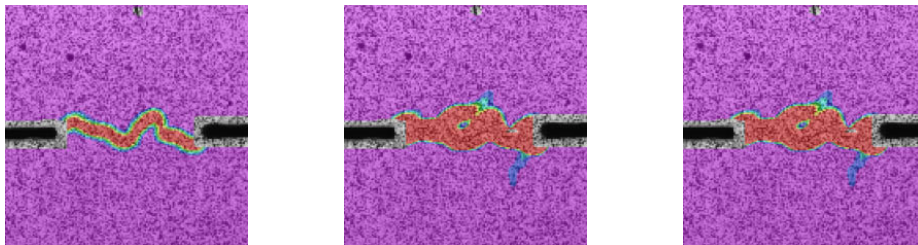
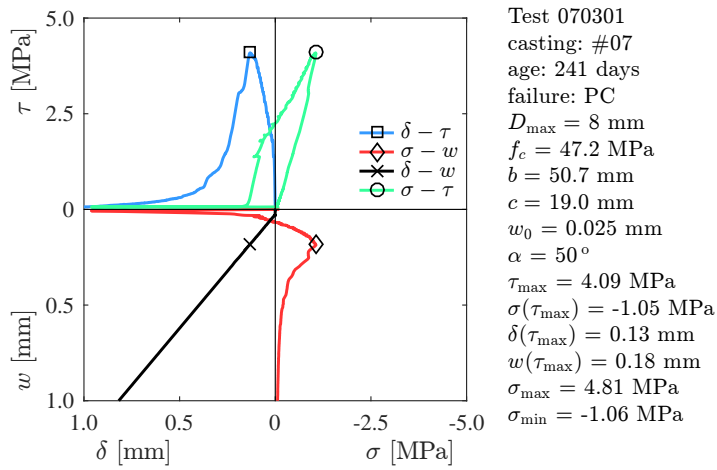


Figure A2.89 – Results for test 070301

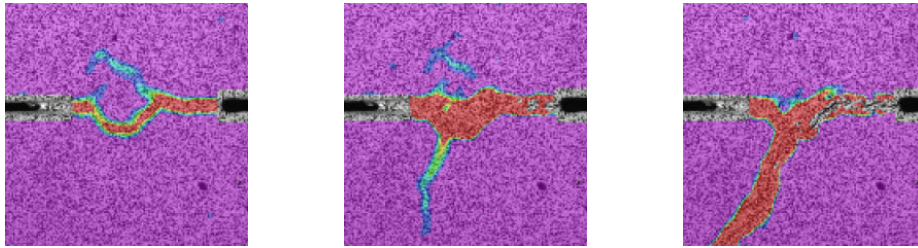
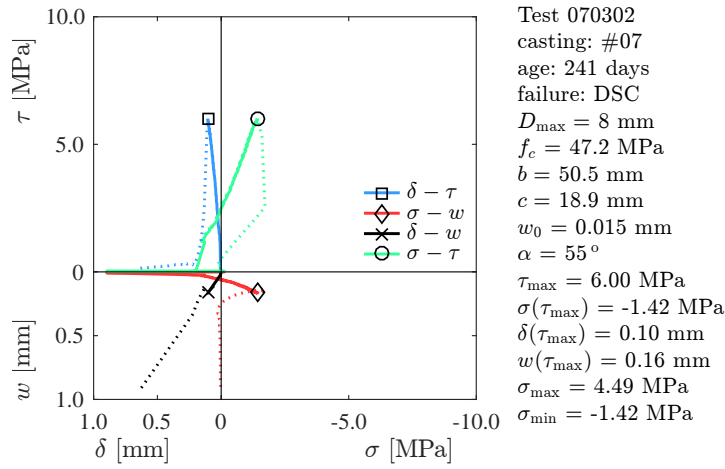


Figure A2.90 – Results for test 070302

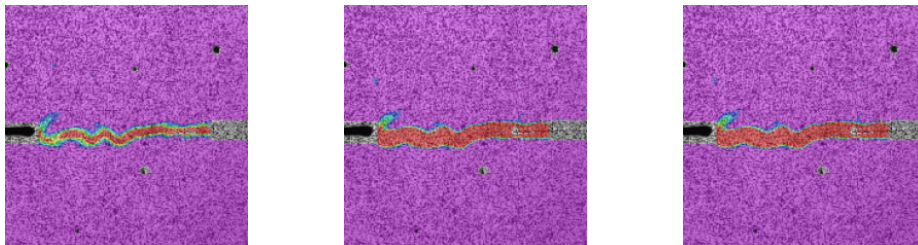
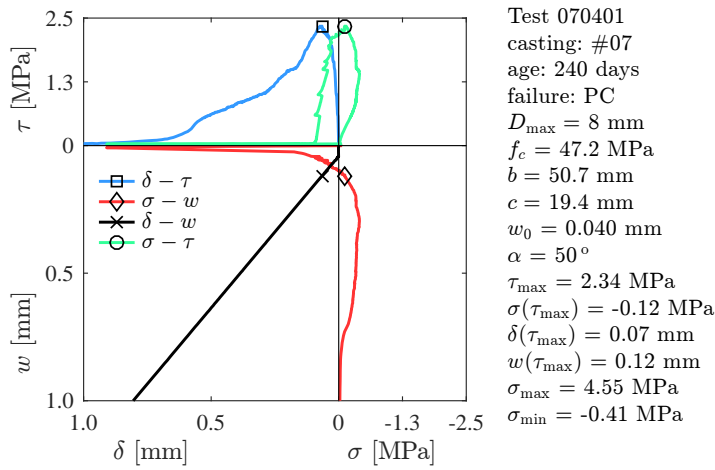


Figure A2.91 – Results for test 070401

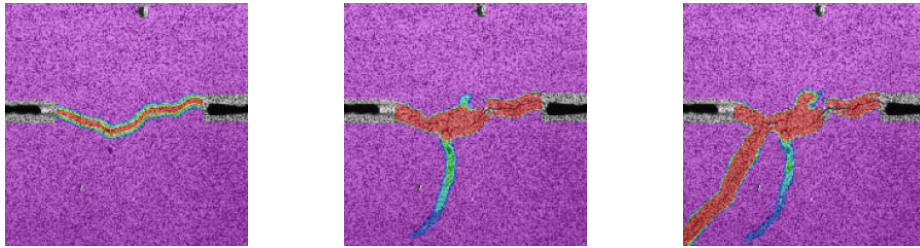
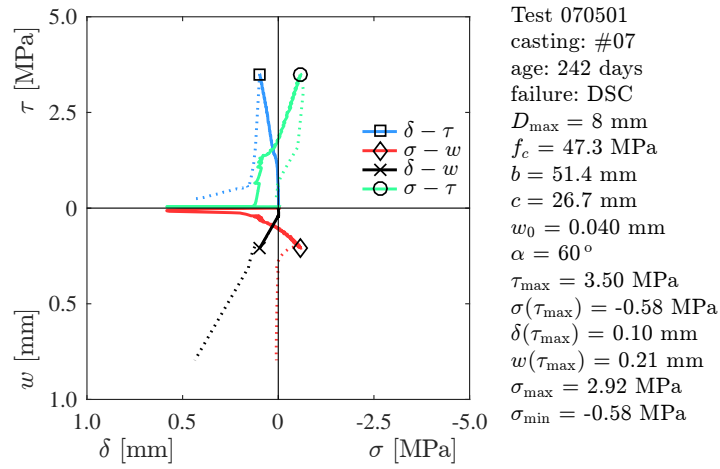


Figure A2.92 – Results for test 070501

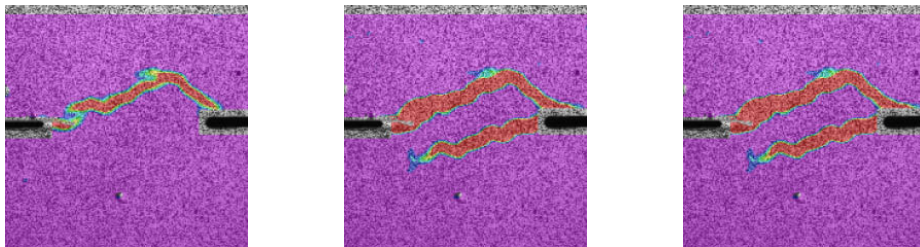
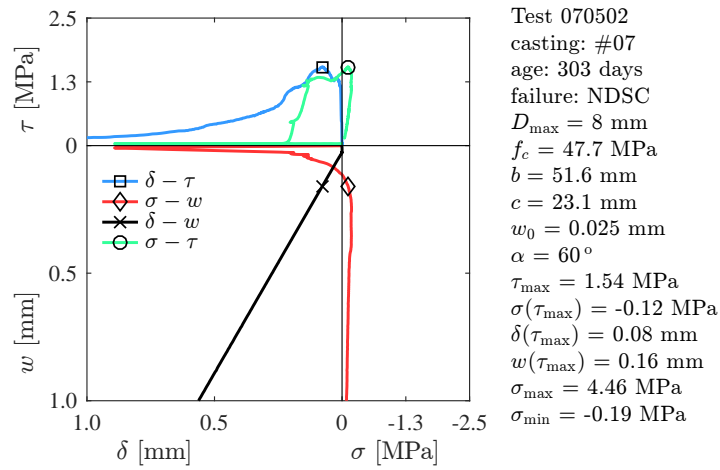


Figure A2.93 – Results for test 070502

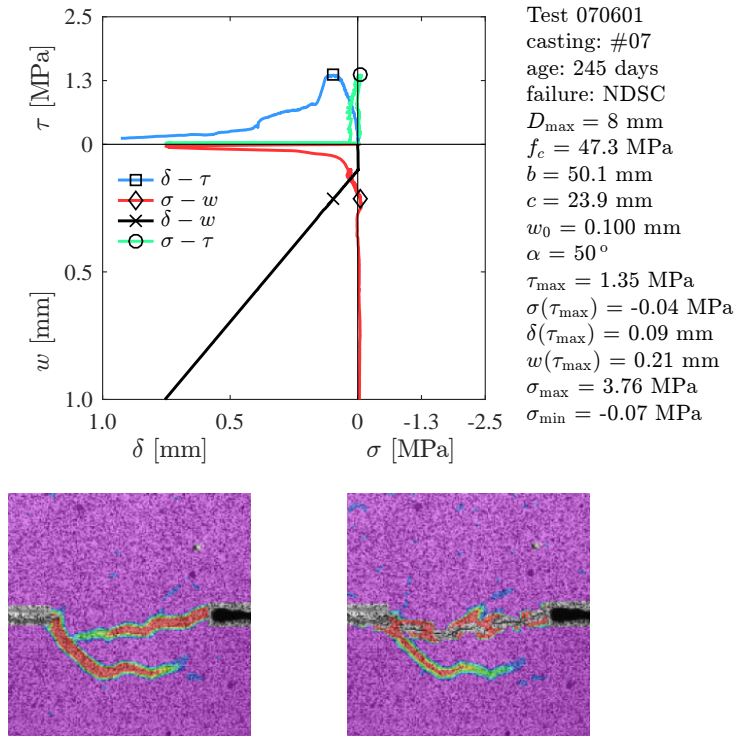


Figure A2.94 – Results for test 070601

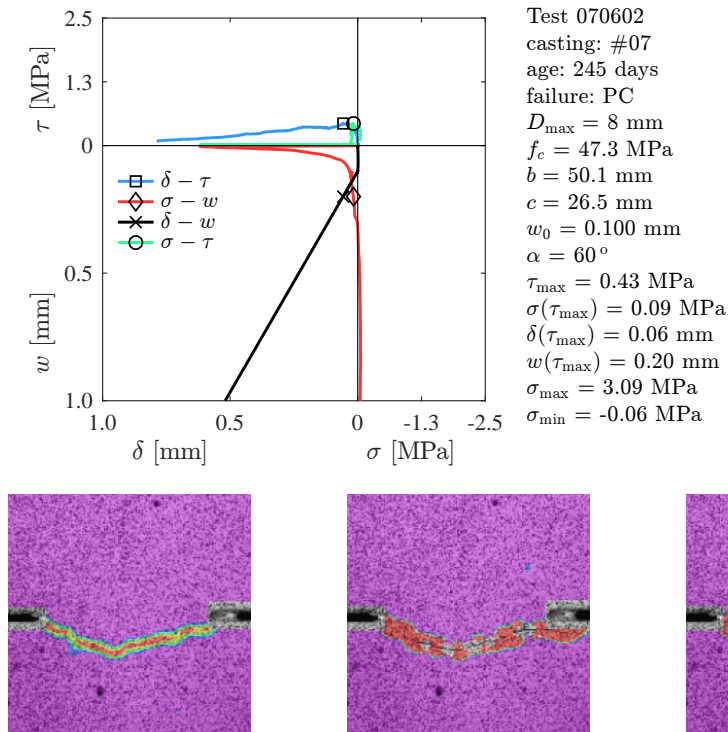


Figure A2.95 – Results for test 070602

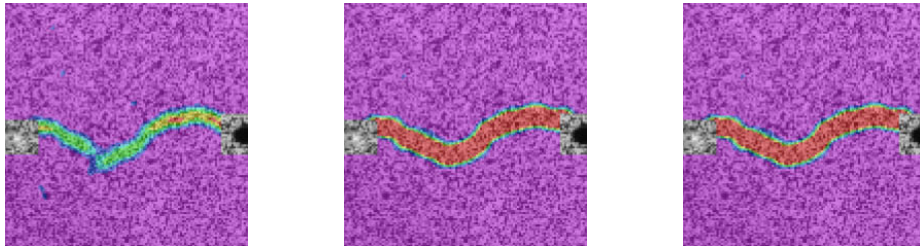
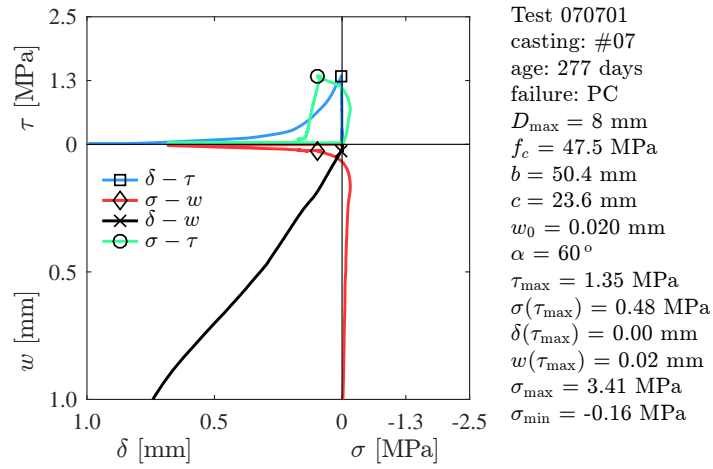


Figure A2.96 – Results for test 070701

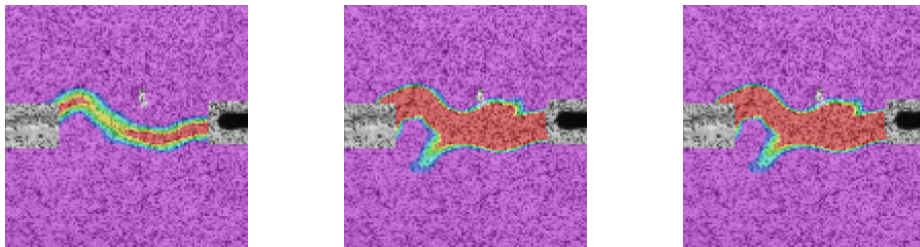
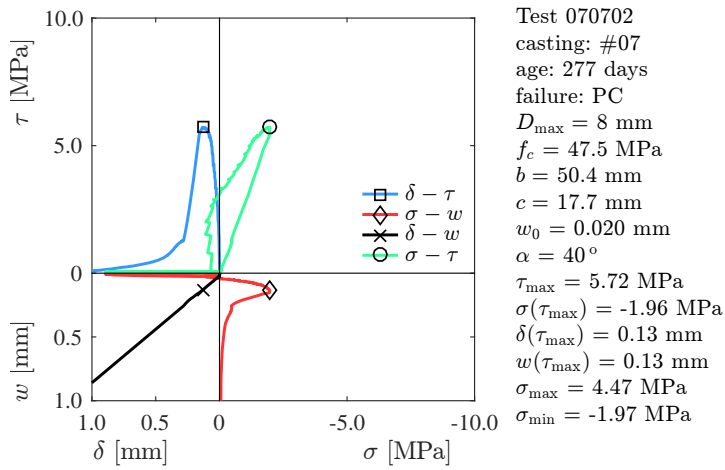


Figure A2.97 – Results for test 070702

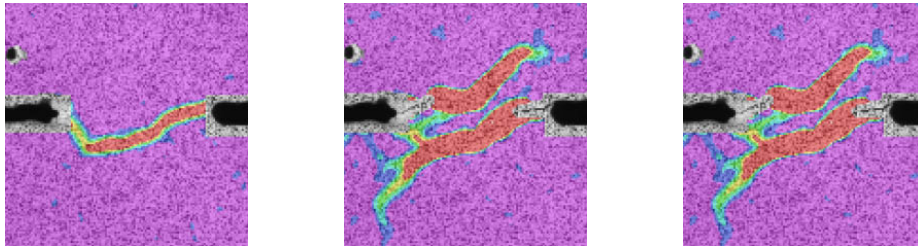
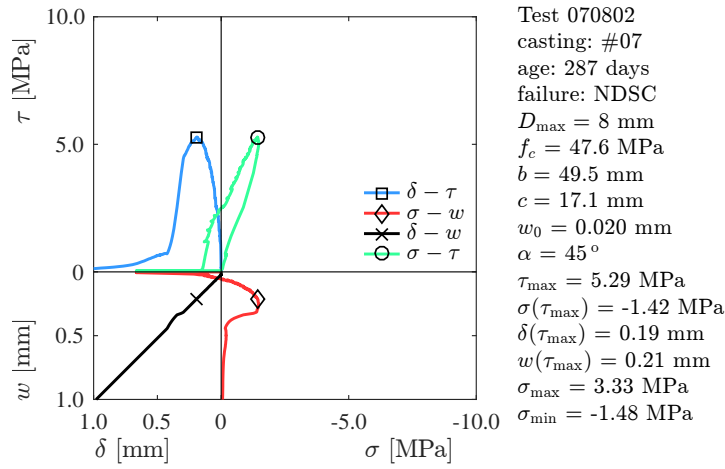


Figure A2.98 – Results for test 070802

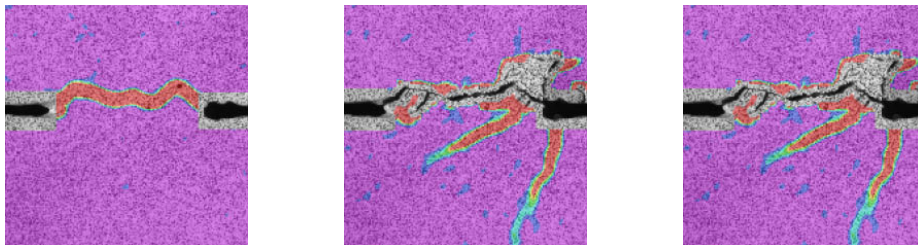
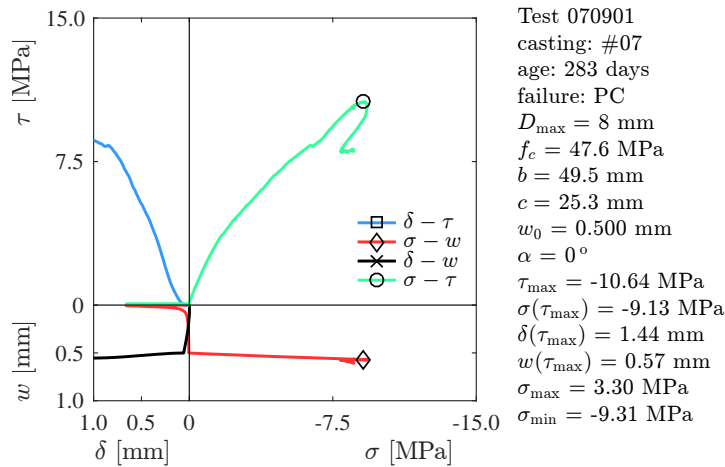


Figure A2.99 – Results for test 070901

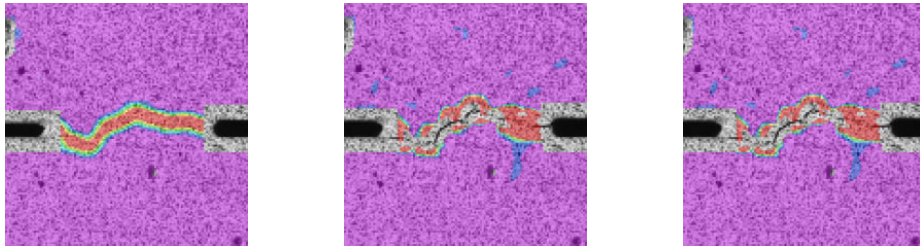
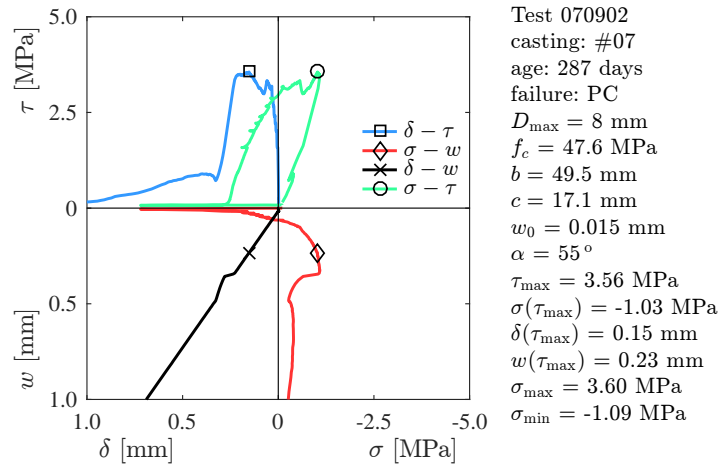


Figure A2.100 – Results for test 070902

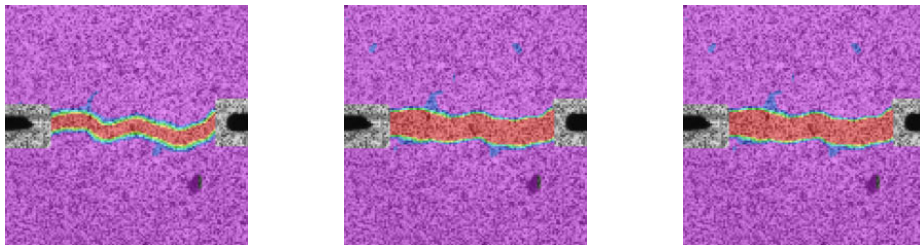
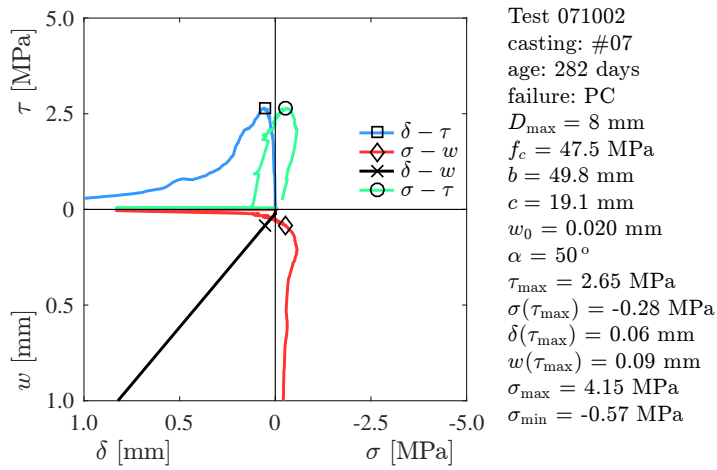


Figure A2.101 – Results for test 071002

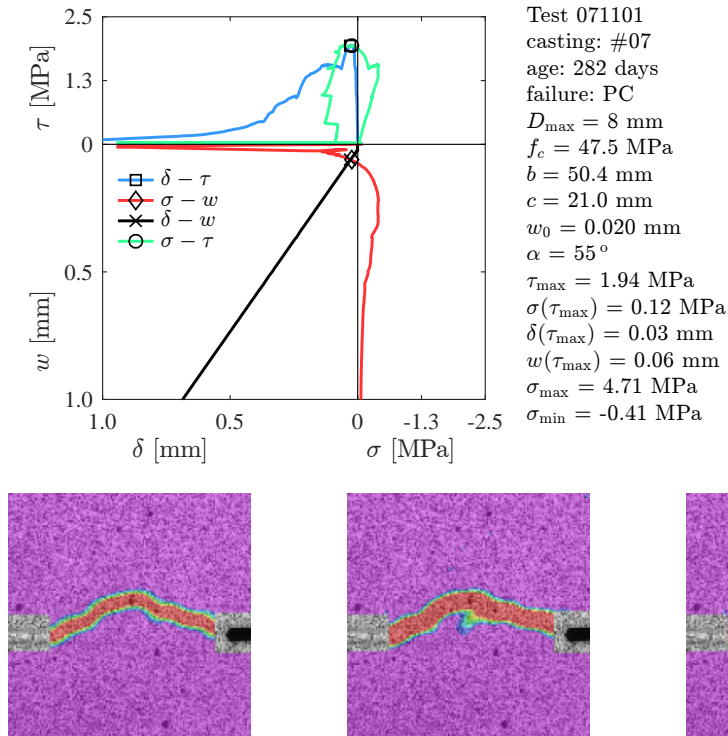


Figure A2.102 – Results for test 071101

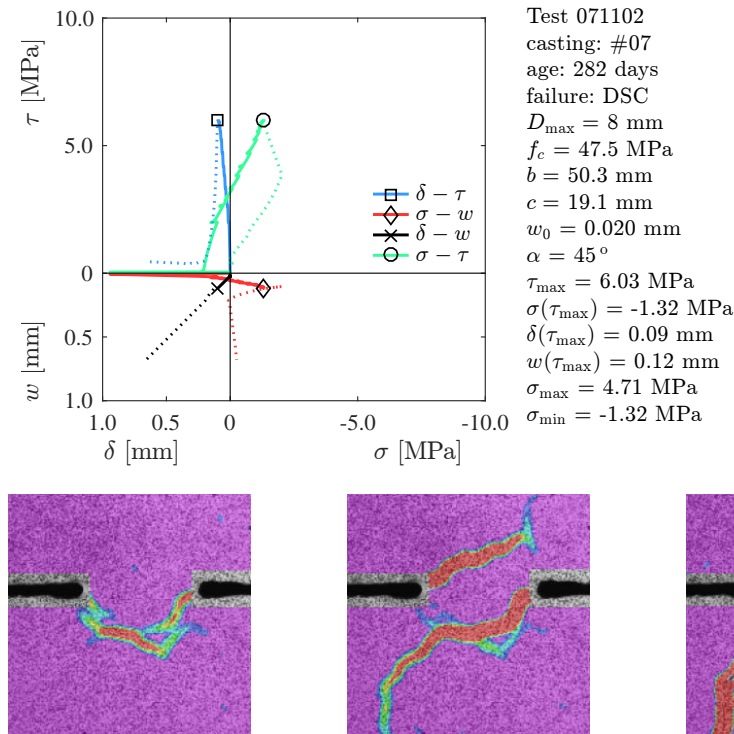


Figure A2.103 – Results for test 071102

Appendix 2

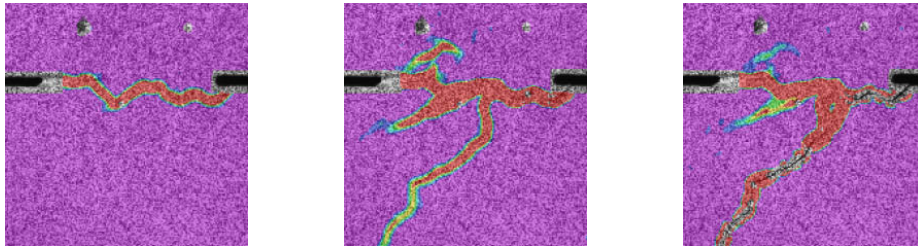
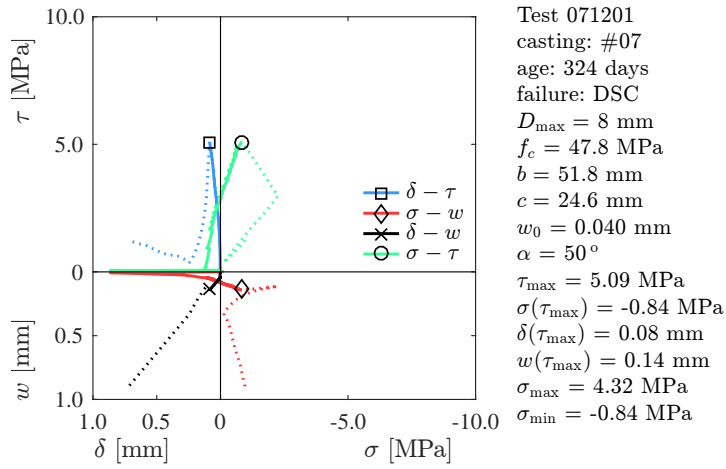


Figure A2.104 – Results for test 071201

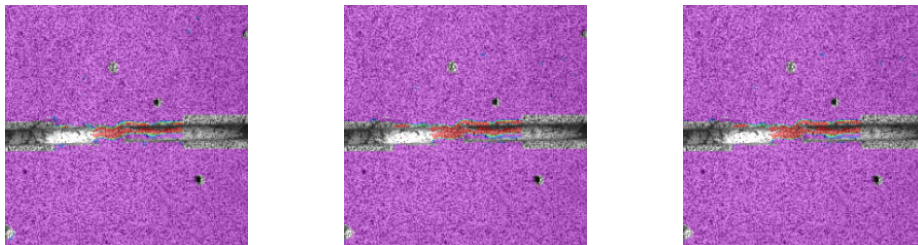
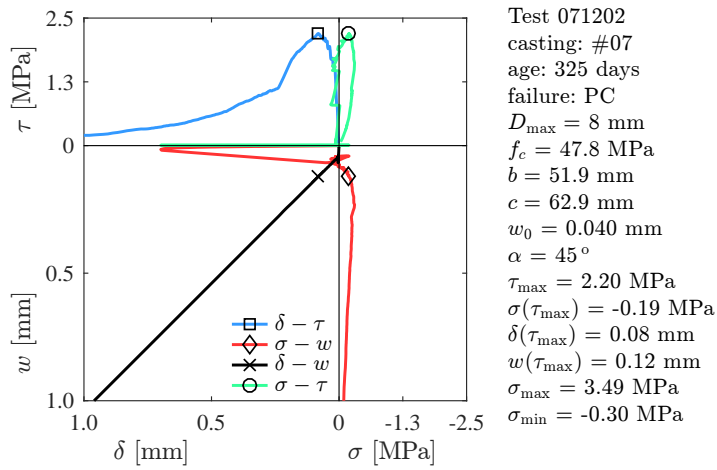


Figure A2.105 – Results for test 071202

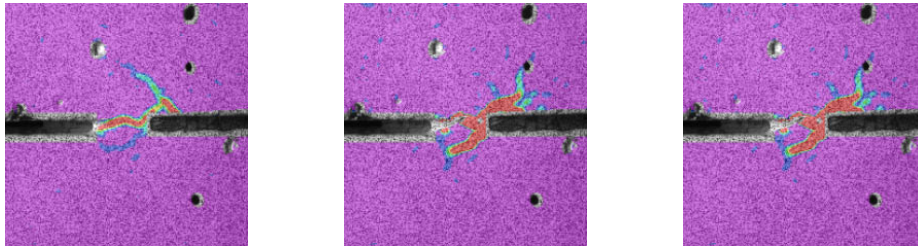
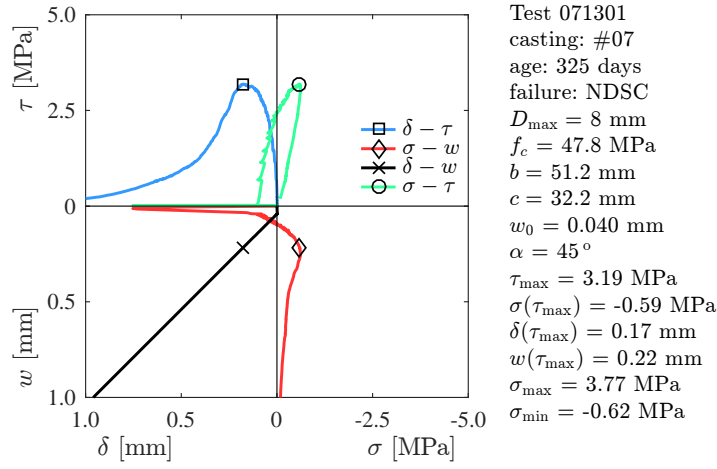


Figure A2.106 – Results for test 071301

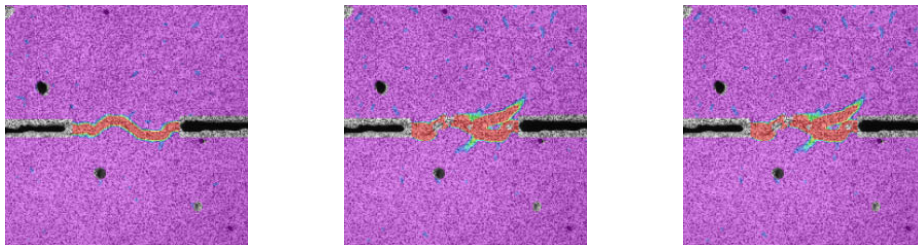
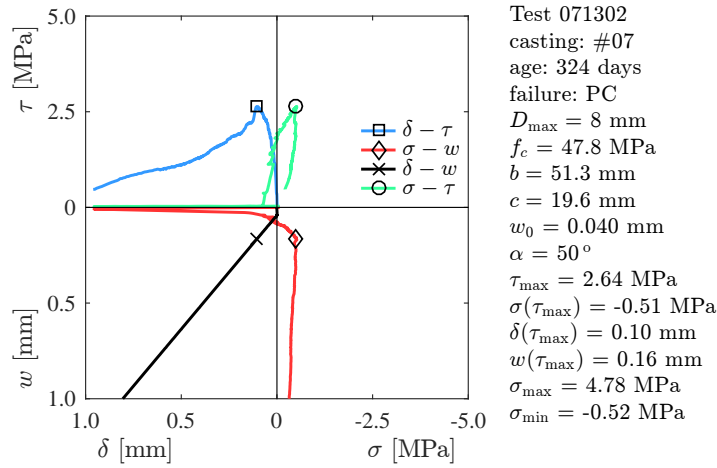


Figure A2.107 – Results for test 071302

Appendix 2

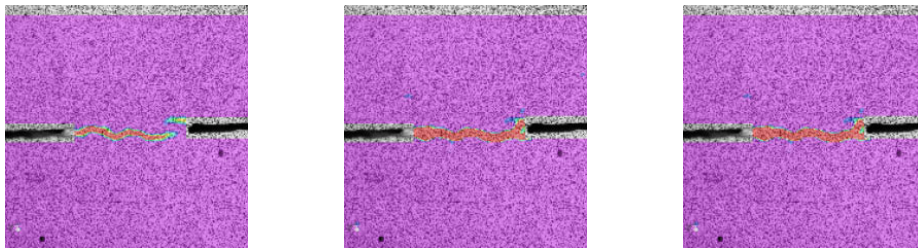
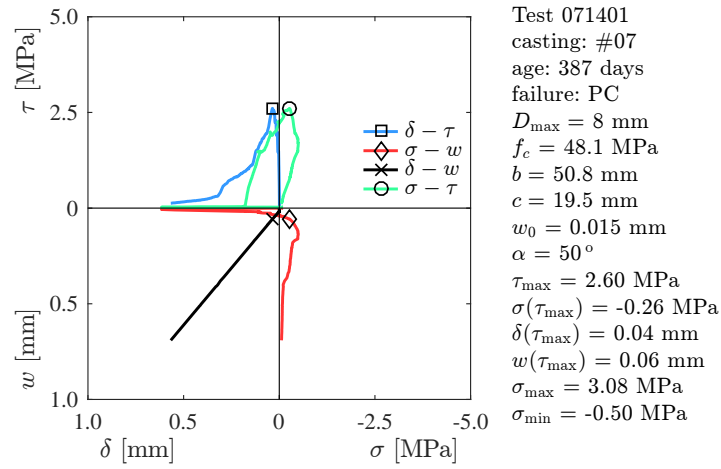


Figure A2.108 – Results for test 071401

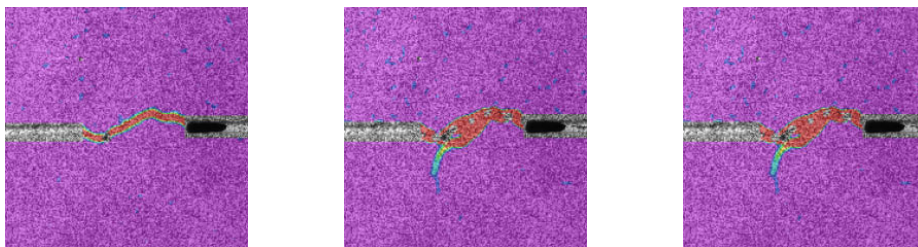
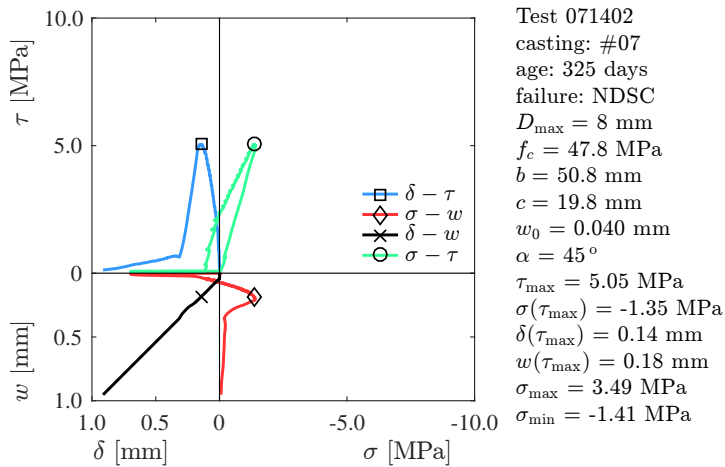


Figure A2.109 – Results for test 071402

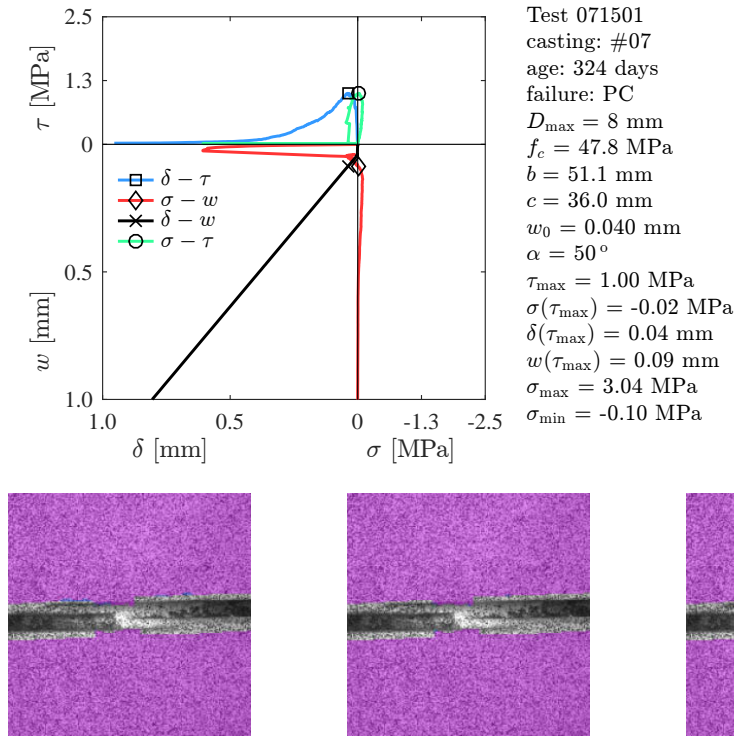


Figure A2.110 – Results for test 071501

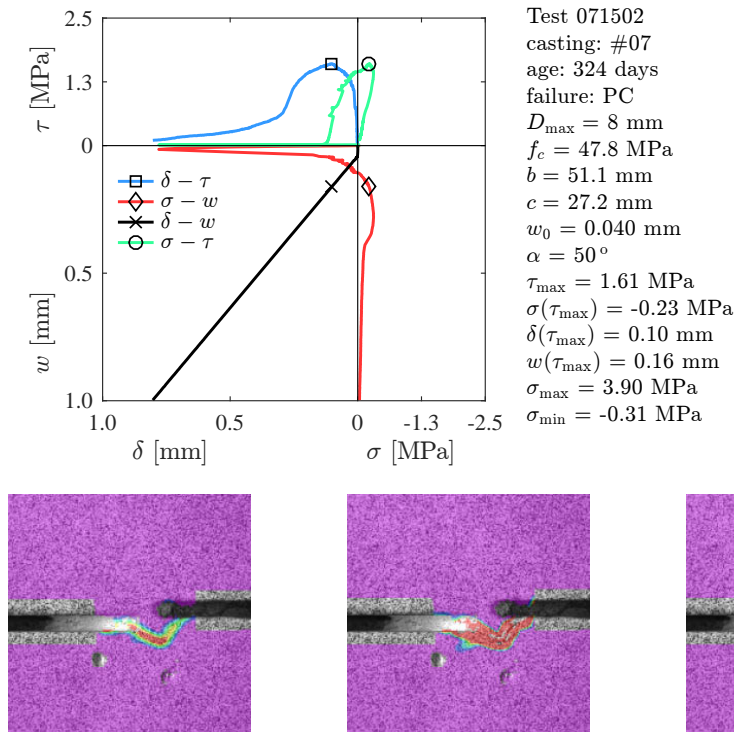


Figure A2.111 – Results for test 071502

Appendix 2

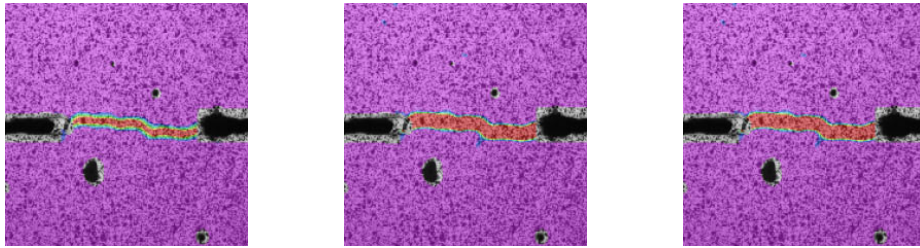
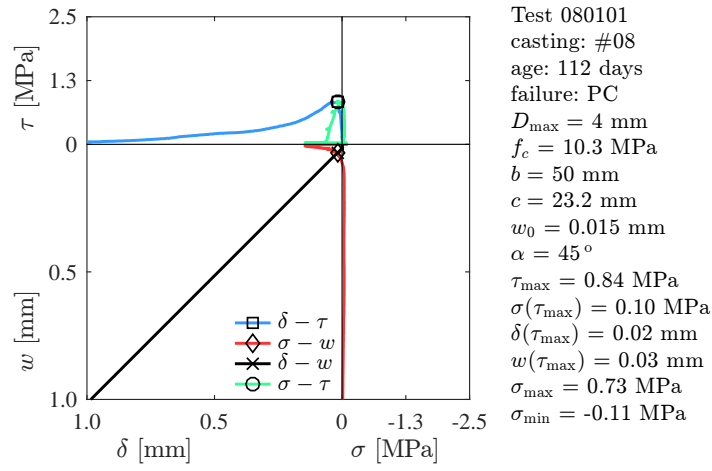


Figure A2.112 – Results for test 080101

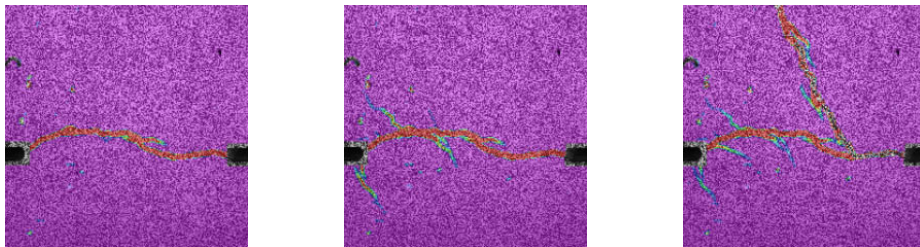
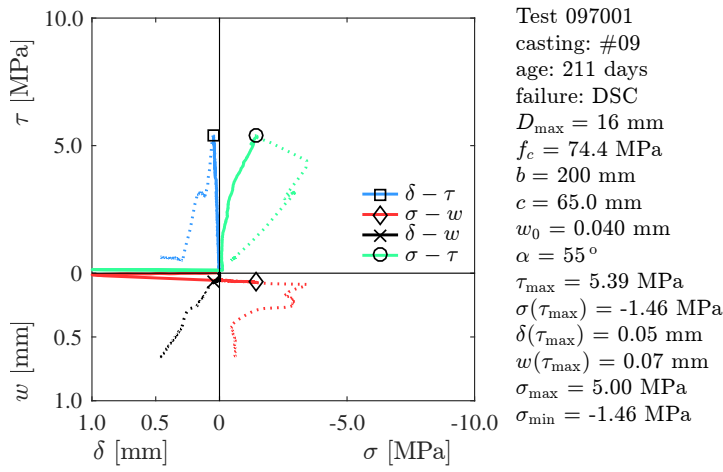


Figure A2.113 – Results for test 097001

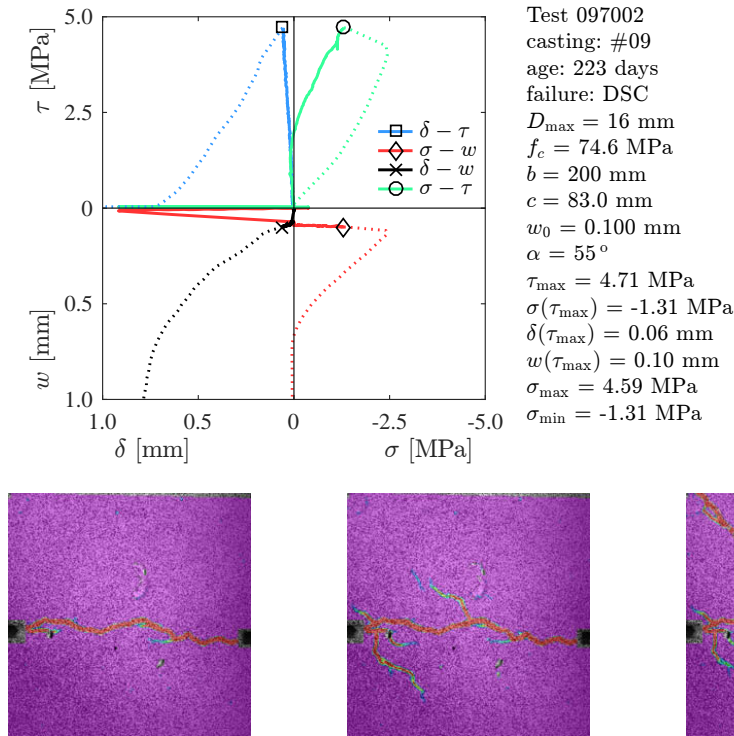


Figure A2.114 – Results for test 097002

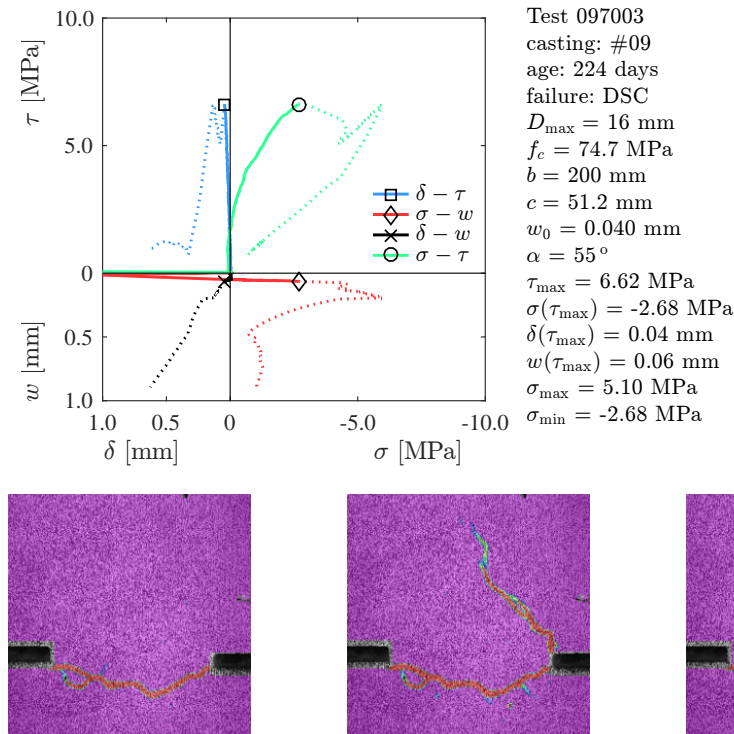


Figure A2.115 – Results for test 097003



## Appendix 3: Detailed results for rebar-to-concrete interfaces

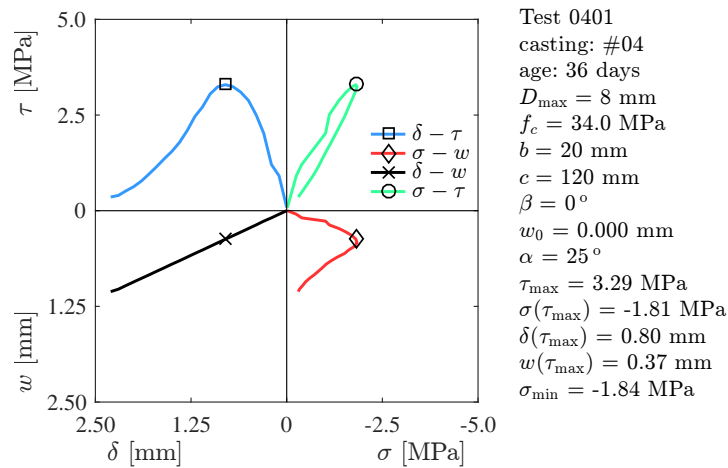


Figure A3.1 – Results for test 0401

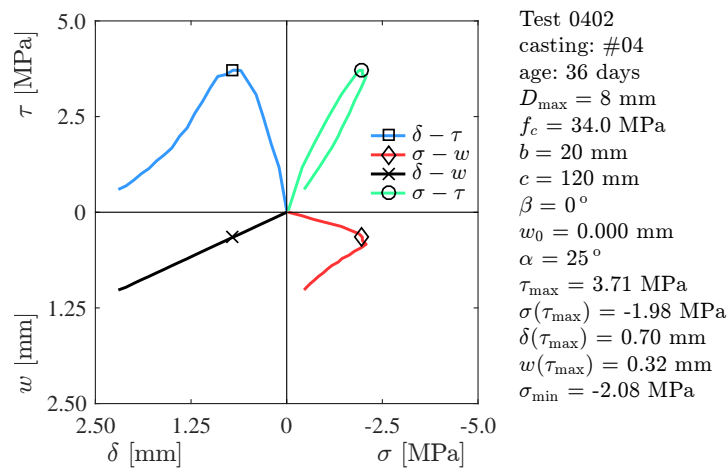


Figure A3.2 – Results for test 0402

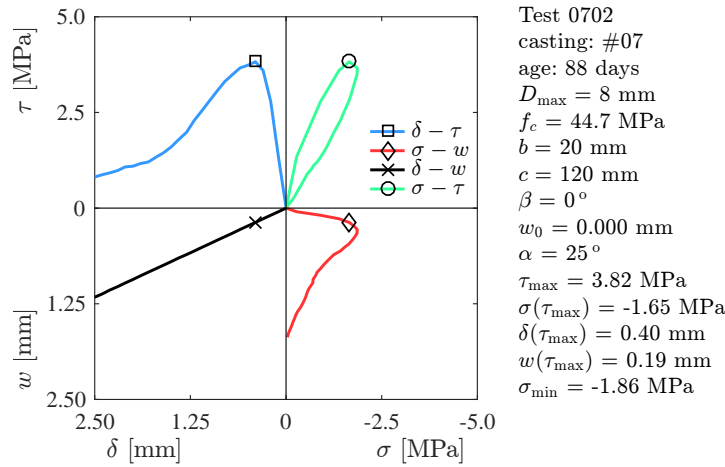


Figure A3.3 – Results for test 0702

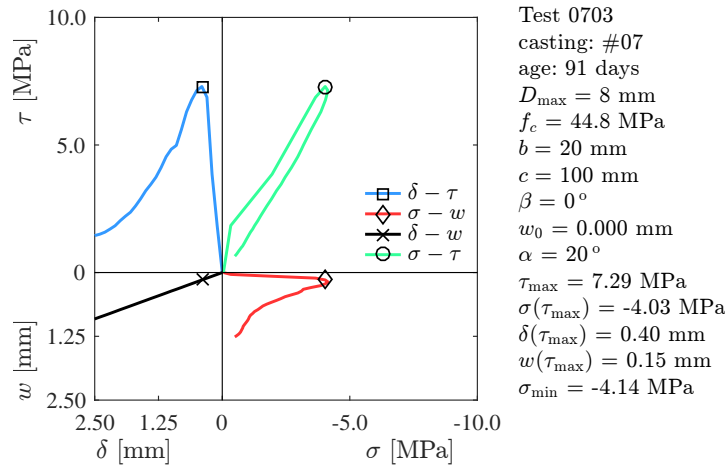


Figure A3.4 – Results for test 0703

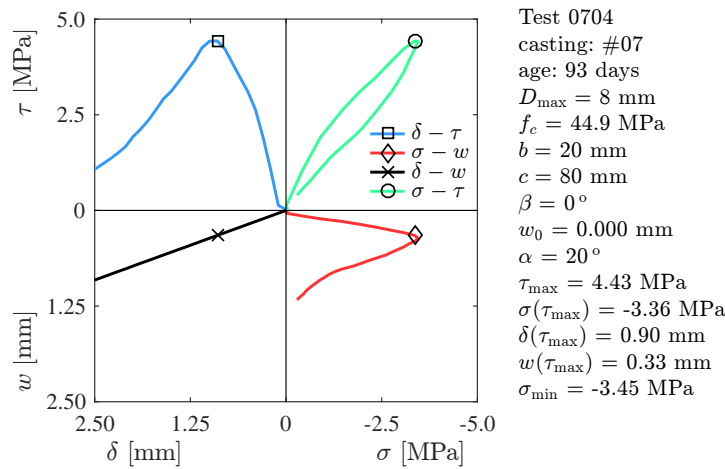


Figure A3.5 – Results for test 0704

Detailed results for rebar-to-concrete interfaces

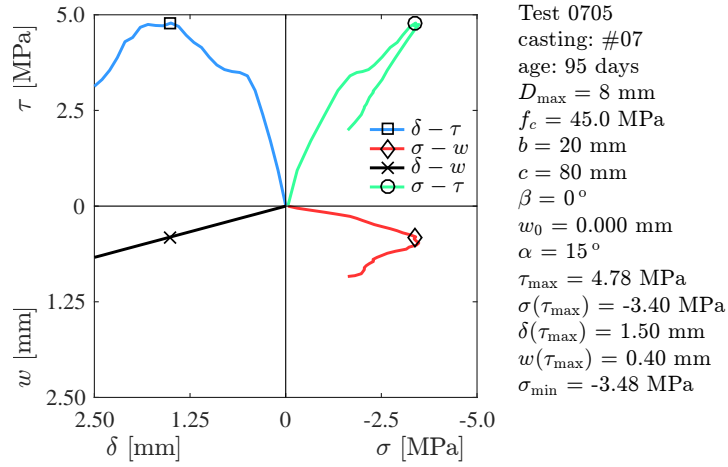


Figure A3.6 – Results for test 0705

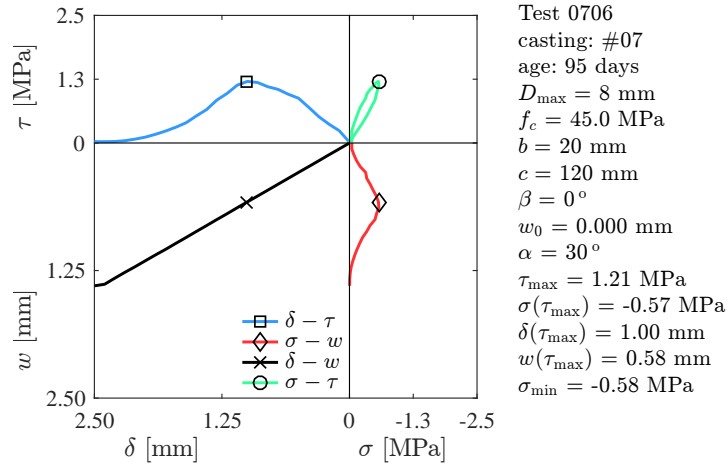


Figure A3.7 – Results for test 0706

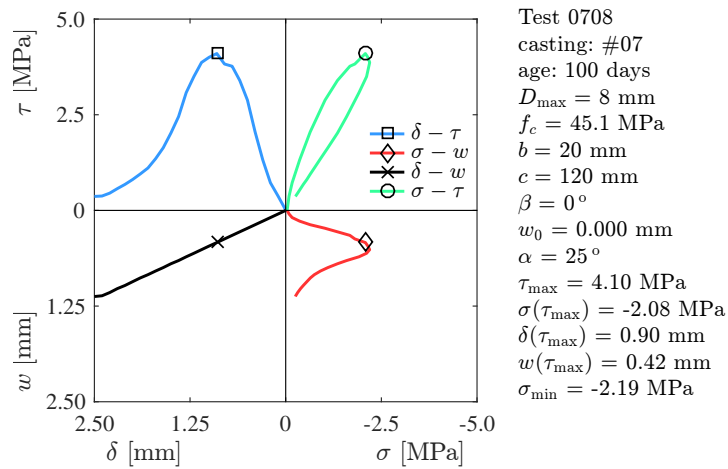


Figure A3.8 – Results for test 0708

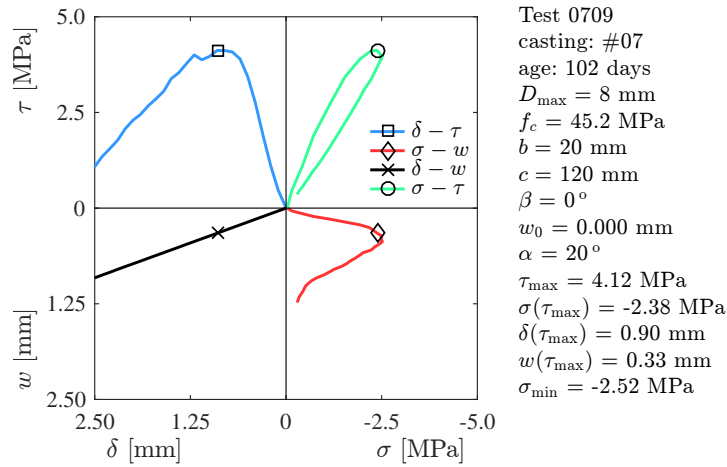


Figure A3.9 – Results for test 0709

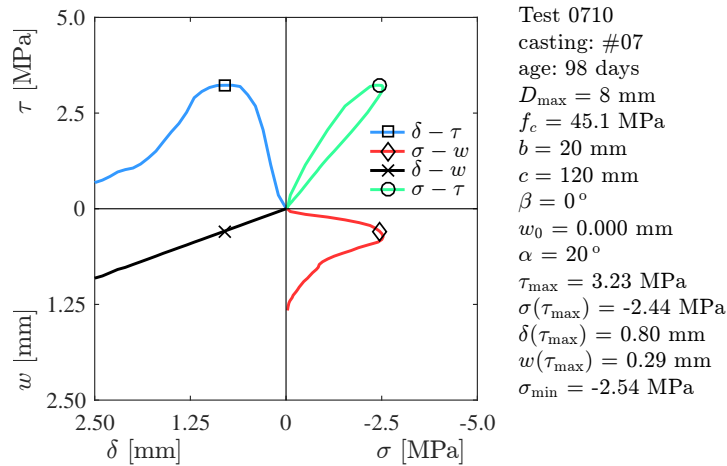


Figure A3.10 – Results for test 0710

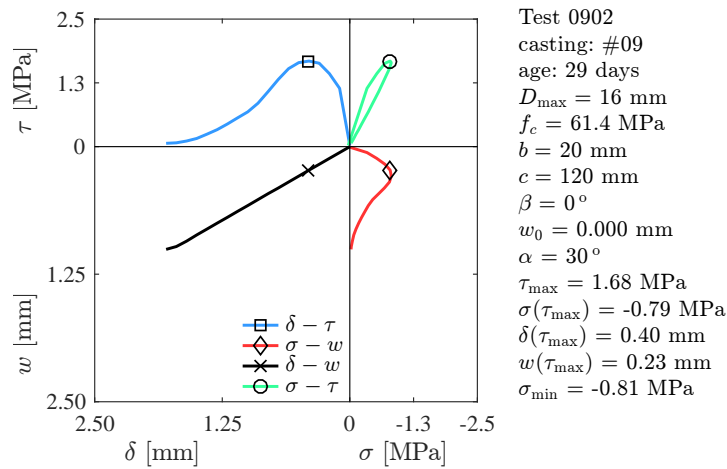


Figure A3.11 – Results for test 0902

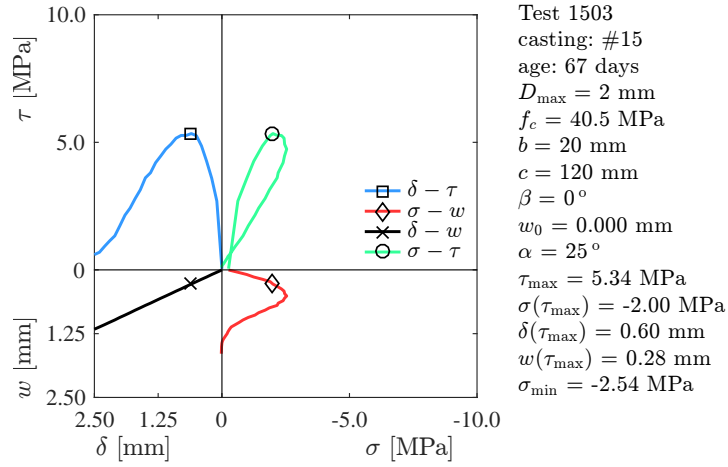


Figure A3.12 – Results for test 1503

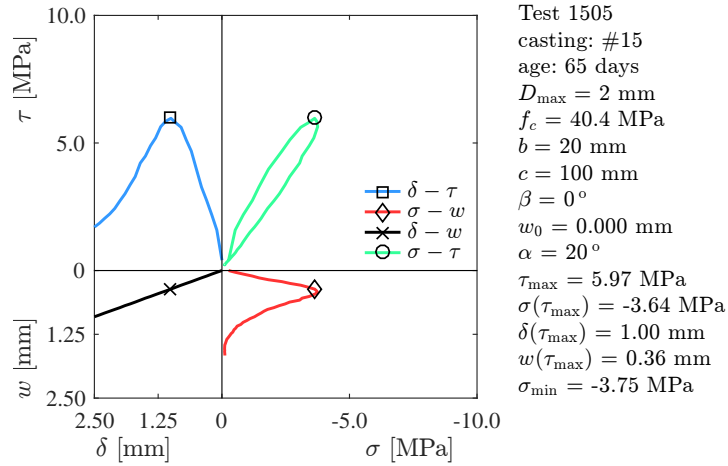


Figure A3.13 – Results for test 1505

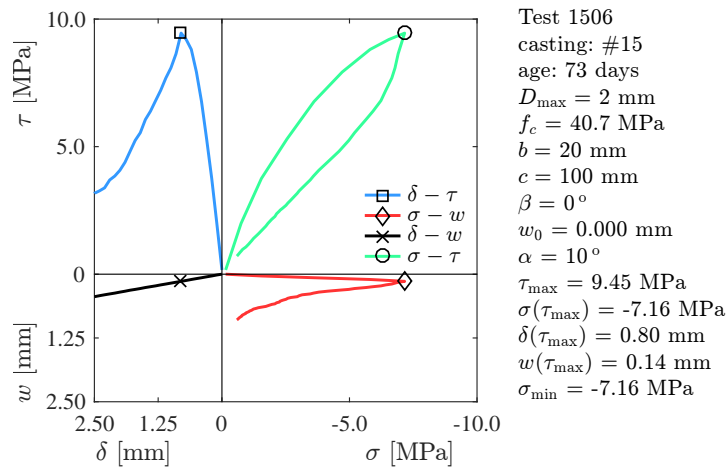


Figure A3.14 – Results for test 1506

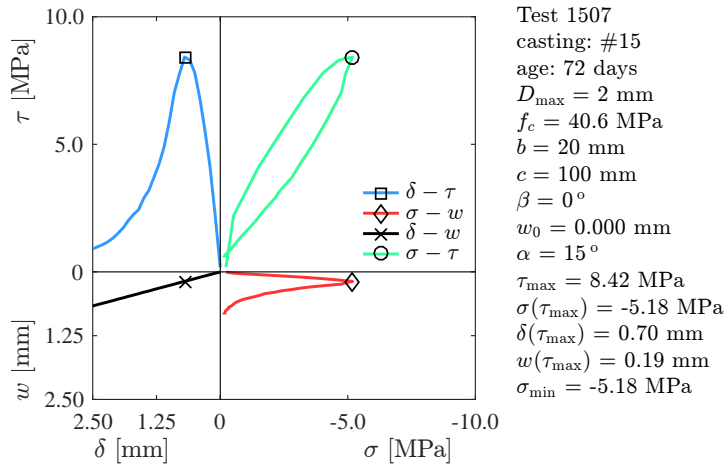


Figure A3.15 – Results for test 1507

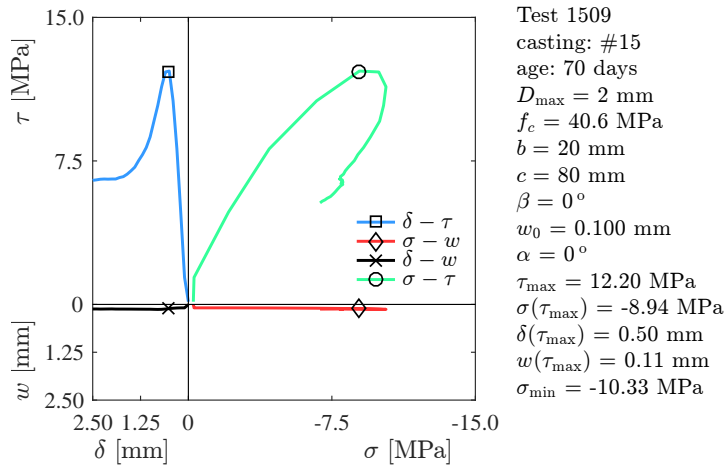


Figure A3.16 – Results for test 1509

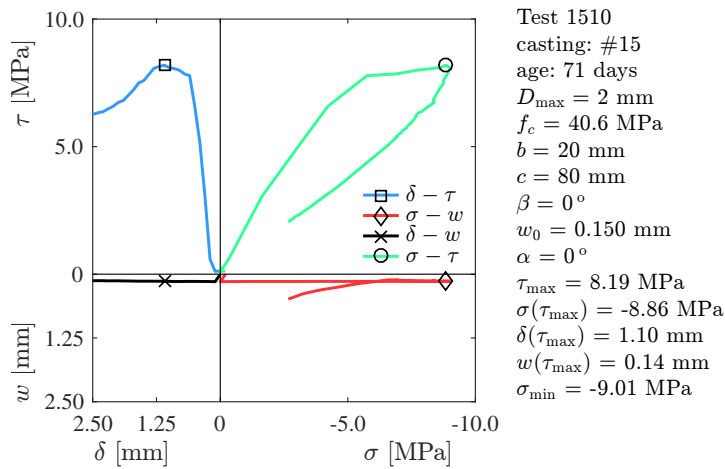


Figure A3.17 – Results for test 1510

Detailed results for rebar-to-concrete interfaces

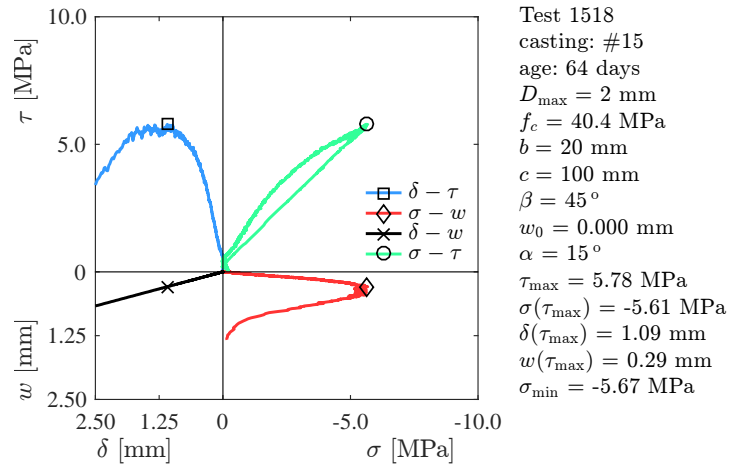


Figure A3.18 – Results for test 1518

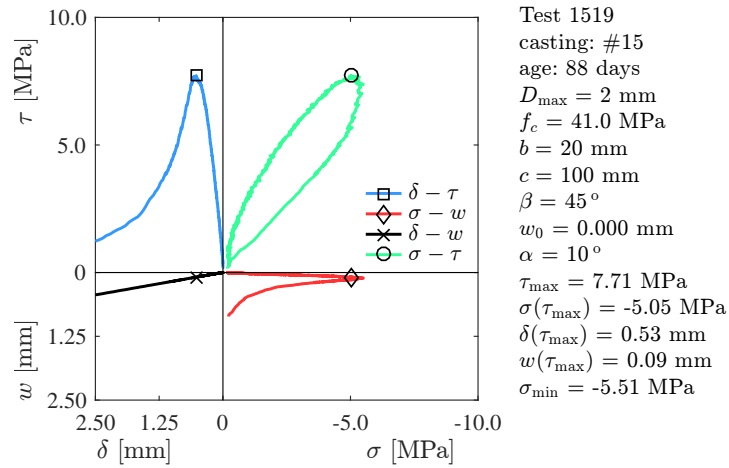


Figure A3.19 – Results for test 1519

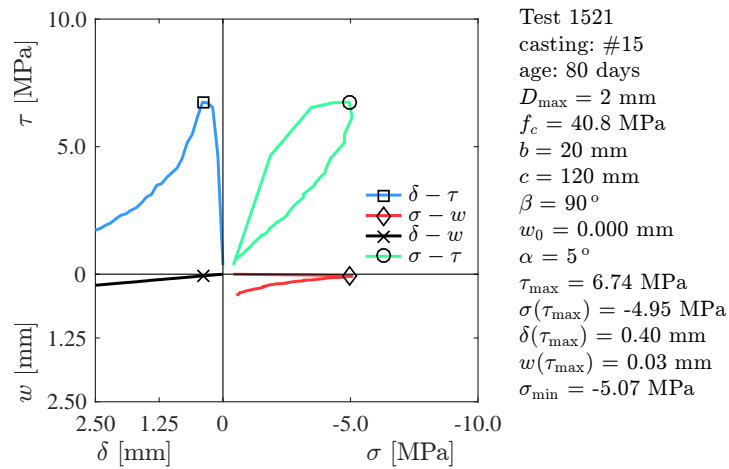


Figure A3.20 – Results for test 1521

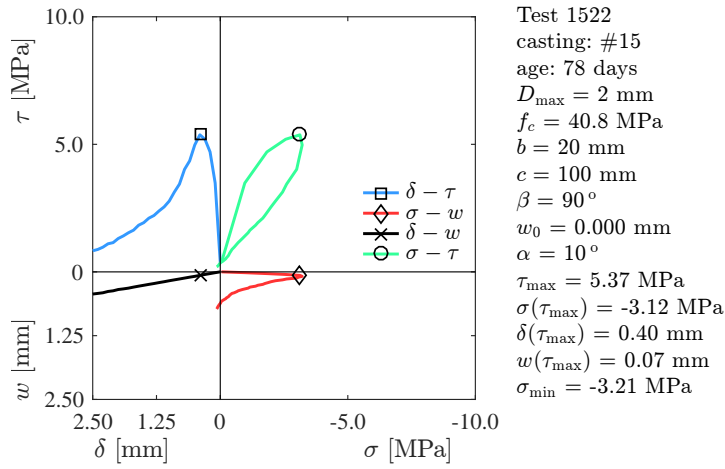


Figure A3.21 – Results for test 1522

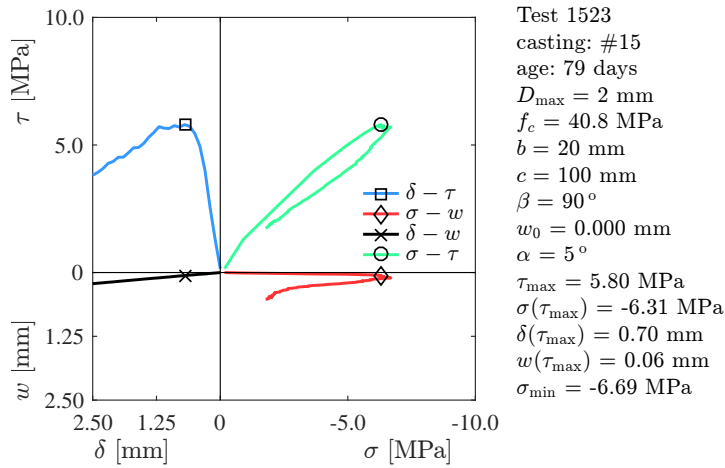


Figure A3.22 – Results for test 1523

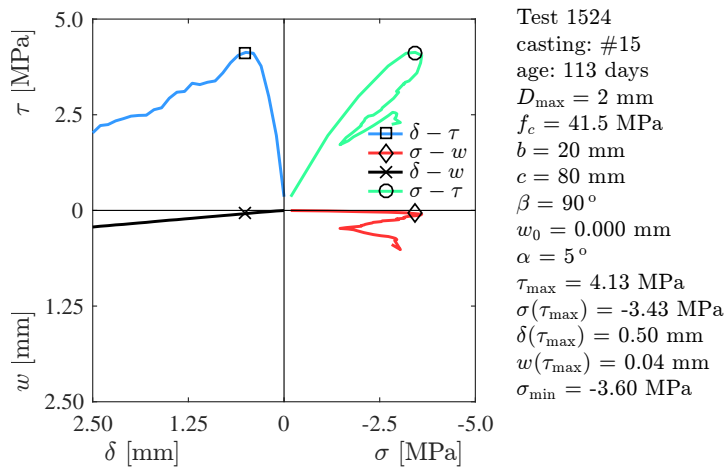


Figure A3.23 – Results for test 1524

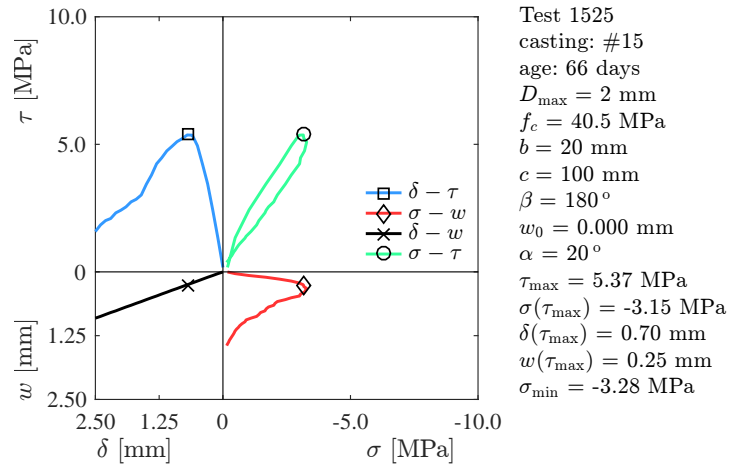


Figure A3.24 – Results for test 1525



## Appendix 4: Results at maximum shear stress from literature

In this appendix, some results at maximum shear stress  $\tau_{\max}$  from the literature are collected and reported. Only a few experimental campaigns are considered, as many investigations do not measure the normal stresses  $\sigma$  or do not report them. For example, this is the case for the extensive campaign conducted by Walraven et al. [10], where the only available information on the normal forces is the amount of reinforcement crossing the crack plane. However, assuming this reinforcement as yielding provides unrealistic values.

The reported results refer to very different specimen geometries and loading conditions, which might not be comparable. Nevertheless, Figure A4.1 shows the values of  $\sigma$  and  $\tau$  at instant  $\tau_{\max}$  for the tests from the literature and the present study [9]. Although subject to considerable scatter, a clear trend is visible, suggesting the presence of a failure curve.

Some outliers can be explained by accounting for a potential influence of particular loading paths. For example, the tests reported by Hassanzadeh [4] (Table A4.3) are plotted differently according to the applied load path. Tests with linear Mixed-Mode kinematics show good agreement with the majority of the other tests, while tests with exponential Mixed-Mode kinematics (and larger initial openings [4]) are characterized by lower values of  $\tau$ .

## Appendix 4

Table A4.1 – Test results from Jacobsen [5] (N.R. – Not Reported)

#	$D_{\max}$ [mm]	$f_c$ [MPa]	$w_0$ [mm]	$\alpha$ [°]	$\tau_{\max}$ [MPa]	$\sigma(\tau_{\max})$ [MPa]	$\delta(\tau_{\max})$ [mm]	$w(\tau_{\max})$ [mm]	$\alpha_{eq}(\tau_{\max})$ [°]	notes
N.R.	8	41.0	0.03	40	6.00	-2.10	0.12	0.12	46.4	
N.R.	8	41.0	0.04	40	3.80	-0.95	0.11	0.13	50.7	
N.R.	8	41.0	0.10	40	1.82	-0.32	0.12	0.20	59.1	
N.R.	8	41.0	0.03	45	3.60	-0.58	0.10	0.13	51.3	
N.R.	8	41.0	0.04	45	2.70	-0.47	0.12	0.16	53.1	
N.R.	8	41.0	0.10	45	1.71	-0.32	0.15	0.25	59.0	
N.R.	8	41.0	0.03	50	3.25	-0.52	0.10	0.14	55.3	
N.R.	8	41.0	0.04	50	2.25	-0.08	0.08	0.14	59.4	
N.R.	8	41.0	0.10	50	1.97	0.00	0.12	0.24	63.7	
N.R.	8	41.0	0.03	55	2.42	-0.45	0.12	0.20	58.6	
N.R.	8	41.0	0.04	55	1.62	0.10	0.04	0.09	68.8	
N.R.	8	41.0	0.02	55	2.92	-0.25	0.09	0.15	58.7	
N.R.	8	41.0	0.03	60	1.60	0.10	0.05	0.10	66.3	
N.R.	8	41.0	0.02	60	2.05	-0.30	0.12	0.23	62.2	

Table A4.2 – Test results from Taylor [8] (note 1: gravel; note 2: rounded gravel; note 3: external reinforcement was added after DSC)

#	$D_{\max}$ [mm]	$f_c$ [MPa]	$w_0$ [mm]	$\alpha$ [°]	$\tau_{\max}$ [MPa]	$\sigma(\tau_{\max})$ [MPa]	$\delta(\tau_{\max})$ [mm]	$w(\tau_{\max})$ [mm]	$\alpha_{eq}(\tau_{\max})$ [°]	notes
5	19	26.7	0	45	1.21	-0.13	1.58	1.58	45.0	1
6	19	26.7	0	25	1.0	-0.27	1.22	0.57	24.99	1
7	19	26.7	0	15	1.11	-0.27	1.22	0.33	15.0	1
8	9	26.4	0	65	0.28	-0.19	0.28	0.6	65.01	1, 3
10	9	26.4	0	15	1.01	-0.3	1.31	0.35	15.0	1
11	9	26.4	0	15	0.81	-0.3	1.59	0.43	15.0	1
12	19	33.8	0	45	1.06	-0.16	1.05	1.05	45.0	1
20	19	42.7	0	45	0.74	-0.15	0.31	0.31	45.0	2

**Results at maximum shear stress from literature**

Table A4.3 – Test results from Hassanzadeh [4] (N.A. – Not Applicable; note 1: exponential loading path; note 2: linear Mixed-Mode loading path)

#	$D_{\max}$ [mm]	$f_c$ [MPa]	$w_0$ [mm]	$\alpha$ [°]	$\tau_{\max}$ [MPa]	$\sigma(\tau_{\max})$ [MPa]	$\delta(\tau_{\max})$ [mm]	$w(\tau_{\max})$ [mm]	$\alpha_{eq}(\tau_{\max})$ [°]	notes
$\beta = 0.9$	8	50	N.A.	N.A.	0.63	-0.31	0.79	0.8	45.27	1
$\beta = 0.8$	8	50.0	N.A.	N.A.	0.63	-0.39	0.8	0.72	41.81	1
$\beta = 0.7$	8	50.0	N.A.	N.A.	1.08	-0.58	0.71	0.59	39.69	1
$\beta = 0.6$	8	50.0	N.A.	N.A.	2.15	-1.53	0.82	0.54	33.52	1
$\beta = 0.5$	8	50.0	N.A.	N.A.	3.14	-2.02	0.62	0.39	32.51	1
$\beta = 0.4$	8	50.0	N.A.	N.A.	4.22	-2.52	0.54	0.29	28.6	1
$\beta = 0.8$	4	50.0	N.A.	N.A.	0.72	-0.43	0.67	0.65	44.42	1
$\beta = 0.7$	4	50.0	N.A.	N.A.	2.2	-1.12	0.72	0.59	39.56	1
$\beta = 0.6$	4	50.0	N.A.	N.A.	1.53	-1.12	0.97	0.59	31.29	1
$\beta = 0.5$	4	50.0	N.A.	N.A.	1.84	-1.53	0.97	0.49	26.86	1
$\beta = 0.4$	4	50.0	N.A.	N.A.	2.06	-1.66	0.53	0.29	28.74	1
$\alpha = 30$	8	50.0	0.0	30	4.0	-2.11	0.06	0.03	30.0	2
$\alpha = 45$	8	50.0	0.0	45	5.21	-1.98	0.05	0.05	45.0	2
$\alpha = 60$	8	50.0	0.0	60	2.69	-0.36	0.08	0.13	60.0	2
$\alpha = 75$	8	50.0	0.0	75	1.88	0.0	0.01	0.02	75.0	2

## Appendix 4

Table A4.4 – Test results from Nooru-Mohamed [7] (N.A. – Not Applicable; note 1: lightweight aggregates; notes 3a, 3b, 6a-1, 6b-2, 6b-3: name of load-path used in [7])

#	$D_{\max}$ [mm]	$f_c$ [MPa]	$w_0$ [mm]	$\alpha$ [°]	$\tau_{\max}$ [MPa]	$\sigma(\tau_{\max})$ [MPa]	$\delta(\tau_{\max})$ [mm]	$w(\tau_{\max})$ [mm]	$\alpha_{eq}(\tau_{\max})$ [°]	notes
29-06	12	49.9	N.A.	N.A.	3.12	0.0	0.09	0.04	23.77	3a, 1
29-01	12	49.9	N.A.	N.A.	1.19	0.0	0.05	0.09	60.3	3a, 1
29-02	12	49.9	N.A.	N.A.	0.62	0.0	0.04	0.14	74.93	3a, 1
29-03	13	49.9	N.A.	N.A.	3.74	-0.13	0.09	0.03	15.72	3b, 1
29-04	14	49.9	N.A.	N.A.	2.91	-0.13	0.1	0.06	34.03	3b, 1
29-05	15	49.9	N.A.	N.A.	2.7	-0.13	0.12	0.09	37.32	3b, 1
46-07	2	41.2	N.A.	N.A.	9.72	-4.11	0.29	0.29	45.0	6a-1
47-15	2	38.3	N.A.	N.A.	11.67	-4.25	0.24	0.24	45.0	6a-1
48-15	2	38.4	N.A.	N.A.	10.56	-5.07	0.21	0.21	45.0	6a-1
48-01	2	38.4	N.A.	N.A.	2.2	0.0	0.18	0.36	63.43	6b-2
47-08	2	38.3	N.A.	N.A.	1.79	0.0	0.08	0.16	63.43	6b-2
46-16	2	41.2	N.A.	N.A.	1.1	0.0	0.02	0.03	63.43	6b-2
46-04	2	41.2	N.A.	N.A.	4.4	0.37	0.08	0.24	71.57	6b-3
48-10	2	38.4	N.A.	N.A.	2.47	0.36	0.06	0.19	71.57	6b-3
47-17	2	38.3	N.A.	N.A.	0.82	0.37	0.04	0.11	71.57	6b-3
28-01	16	41.2	N.A.	N.A.	1.9	-0.13	0.11	0.15	55.15	3b
27-05	16	43.6	N.A.	N.A.	2.17	-0.13	0.13	0.16	52.27	3b
28-03	16	41.2	N.A.	N.A.	1.1	-0.13	0.12	0.25	64.36	3b
27-02	16	43.6	N.A.	N.A.	1.98	-0.13	0.21	0.28	53.56	3b
28-04	16	41.2	N.A.	N.A.	0.82	-0.13	0.23	0.41	60.78	3b

Table A4.5 – Test results from Divakar et al. [3] (N.A. – Not Applicable)

#	$D_{\max}$ [mm]	$f_c$ [MPa]	$w_0$ [mm]	$\alpha$ [°]	$\tau_{\max}$ [MPa]	$\sigma(\tau_{\max})$ [MPa]	$\delta(\tau_{\max})$ [mm]	$w(\tau_{\max})$ [mm]	$\alpha_{eq}(\tau_{\max})$ [°]	notes
C1	12.7	35.5	N.A.	N.A.	3.98	-0.35	0.03	0.01	18.77	
C10	12.7	32.7	N.A.	N.A.	3.71	-0.35	0.04	0.01	11.85	
C11	12.7	34.4	N.A.	N.A.	4.5	-0.69	0.03	0.01	21.05	
C5	12.7	32.9	N.A.	N.A.	4.78	-1.0	0.04	0.01	9.33	
C6	12.7	31.7	N.A.	N.A.	5.97	-1.31	0.05	0.01	7.91	

## Results at maximum shear stress from literature

Table A4.6 – Test results from Millard and Johnson [6] (softening phase not reported, peak values might be higher)

#	$D_{\max}$ [mm]	$f_c$ [MPa]	$w_0$ [mm]	$\alpha$ [°]	$\tau_{\max}$ [MPa]	$\sigma(\tau_{\max})$ [MPa]	$\delta(\tau_{\max})$ [mm]	$w(\tau_{\max})$ [mm]	$\alpha_{eq}(\tau_{\max})$ [°]	notes
2S	10	29.6	0.06	0.0	5.05	-2.66	1.04	0.52	26.57	
9S	10	33.6	0.25	0.0	4.97	-3.2	1.32	0.76	29.95	
11L	10	28.6	0.5	0.0	1.66	-1.19	1.74	1.17	33.85	
12L	10	28.3	0.5	0.0	2.78	-2.25	1.74	1.47	40.13	
13S	10	29.4	0.5	0.0	3.03	-2.01	1.61	1.12	34.85	
15L	10	29.2	0.5	0.0	4.04	-4.02	1.58	0.87	28.73	
16L	10	30.1	0.5	0.0	4.18	-3.76	1.58	0.51	17.8	
19L	10	26.	0.75	0.0	2.38	-2.13	1.55	1.15	36.53	

Table A4.7 – Test results from Bujadham and Maekawa [1] [2] (N.R. – Not Reported; note 1: Lightweight aggregates; note 2: High strength concrete; tests might have been stopped before reaching the ultimate peak load)

#	$D_{\max}$ [mm]	$f_c$ [MPa]	$w_0$ [mm]	$\alpha$ [°]	$\tau_{\max}$ [MPa]	$\sigma(\tau_{\max})$ [MPa]	$\delta(\tau_{\max})$ [mm]	$w(\tau_{\max})$ [mm]	$\alpha_{eq}(\tau_{\max})$ [°]	notes
Fig.12 [2]	N.R.	25.2	0.3	0.0	4.23	-3.38	1.31	0.3	12.87	1
Fig.5 [1]	N.R.	104.0	0.5	0.0	5.87	-4.52	0.78	0.5	32.67	2

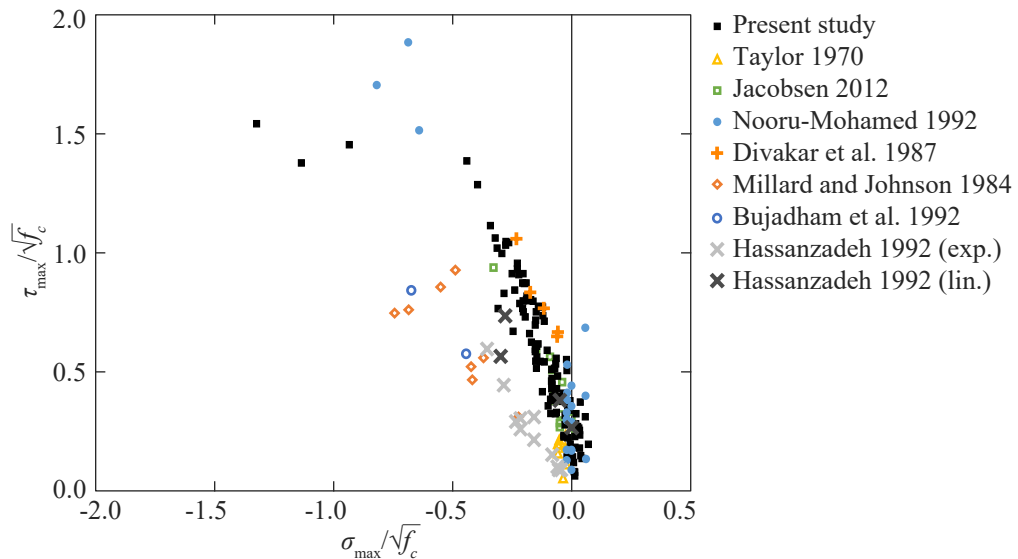


Figure A4.1 – Values of  $\sigma(\tau_{\max})$  and  $\tau_{\max}$  for tests from the present study (Table A1.1) and the literature (Section A1.1)

### Bibliography

- [1] Bujadham, B. and Maekawa, K. (1992). Qualitative studies on mechanisms of stress transfer across cracks in concrete. *Doboku Gakkai Ronbunshu*, (451):265–275.
- [2] Bujadham, B., Mishima, T., and Maekawa, K. (1992). Verification of the universal stress transfer model. *Proc. of JSCE*, 451/V-17:289–300.
- [3] Divakar, M. P., Fafitis, A., and Shah, S. P. (1987). Constitutive Model for Shear Transfer in Cracked Concrete. *Journal of Structural Engineering*, 113(5):1046–1062.
- [4] Hassanzadeh, M. (1992). *Behavior of Fracture Process Zones in Concrete Influenced by Simultaneously Applied Normal and Shear Displacements*. Ph.D. Thesis, Lund University, Sweden.
- [5] Jacobsen, J. S. (2012). *Constitutive Mixed Mode Behavior of Cracks in Concrete: Experimental Investigations of Material Modeling*. Ph.D. Thesis, Technical University of Denmark, Kongens Lyngby, Denmark.
- [6] Millard, S. and Johnson, R. (1984). Shear transfer across cracks in reinforced concrete due to aggregate interlock and to dowel action. *Magazine of Concrete Research*, 36(126):9–21.
- [7] Nooru-Mohamed, M. B. (1992). *Mixed-Mode Fracture of Concrete: An Experimental Approach*. Ph.D. Thesis, Delft University of Technology, Delft, Sweden.
- [8] Taylor, H. P. J. (1970). *Investigation of the Forces Carried Across Cracks in Reinforced Concrete Beams in Shear by Interlock of Aggregate*. Number 42.447 in Technical report (Cement and Concrete Association). London, United Kingdom.
- [9] Tirassa, M. (2020). Experimental data for 'The transfer of forces through rough surface contact in concrete'. type: dataset, doi: 10.5281/zenodo.3894516.
- [10] Walraven, J. C., Vos, E., and Reinhardt, H. W. (1979). Experiments on shear transfer in cracks in concrete. Part I. Technical report, Delft University of Technology, Faculty Civil Engineering and Geosciences.

# Appendix 5: Interface stresses in cracked concrete: testing for review of its fundamentals

Tirassa M., Fernández Ruiz M., Anciaux G., Muttoni A. (2017). Interface Stresses in Cracked Concrete: Testing for Review of Its Fundamentals. In *2017 fib Symposium: High Tech Concrete: Where Technology and Engineering Meet*, pp. 740–748. Maastricht, Netherlands. (doi: [doi.org/10.1007/978-3-319-59471-2\\_87](https://doi.org/10.1007/978-3-319-59471-2_87))

## Abstract

Aggregate interlock is one of the most significant stress transfer actions in cracked concrete and its understanding is fundamental in order to predict the strength of many concrete structures, particularly members failing in shear. Several test programmes focusing on aggregate interlock have been reported in the literature. These programmes, however, often investigate a limited number of parameters and concrete properties, and do not account for different imposed kinematics of the cracked surface.

This paper presents some preliminary results obtained by the authors by using a test setup which allows performing tests on double notched specimens subjected to Mode I, Mode II or Mixed-Mode displacements with imposed kinematics. A series of Mode I tests on small specimens have already been performed and the results are briefly summarized. These tests were categorized depending on the type of the cracked surface (crack through the concrete matrix or at the interface between matrix and aggregates), with results showing a significant dependency on this parameter. A preliminary Mixed-Mode test on a pre-cracked specimen is presented as well and the results are compared to tests from the literature with similar assumed kinematics.

**Keywords:** aggregate interlocking; Mixed-Mode testing; stress transfer in concrete;

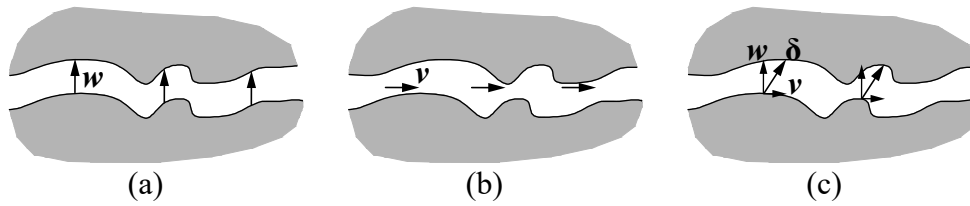


Figure A5.1 – Kinematic modes of cracks: (a) Mode I – opening; (b) Mode II – sliding; (c) Mixed-Mode – opening and sliding

### A5.1 Cracks and Aggregate Interlocking

The transfer of forces through cracks in concrete has been widely investigated in the past. Cracks initiate when the tension in concrete reaches its tensile strength and thereafter the lips of the crack can be subjected to different kinematics, as described for instance by Nooru-Mohamed [3]: In “Mode I” the crack simply opens, and the resultant of the transferred stresses is mostly perpendicular to the crack itself. Simple sliding is defined as “Mode II”. When Mode I and Mode II displacements are acting at the same time, the kinematic modality is called “Mixed-Mode” (Figure A5.1).

Concrete cracks are characterized by being rough because of the non-uniform nature of the composite material. In a displacement controlled Mode I test, the stress normal to the crack increases following an elastic path at first, then it follows a nonlinear path close to the peak and finally the stress decreases gradually. If the crack is subjected to Mode II or Mixed-Mode displacements, protruding parts of the cracks may come into contact and shear stresses can be transferred as well. This phenomenon is called aggregate interlocking. Depending on several factors, like crack roughness, strength of the concrete components (cement paste and aggregate), or the displacement kinematics, the transferred stresses can be large. For this reason, aggregate interlocking is considered as an important action for stress transfer.

One case where the understanding of aggregate interlocking is fundamental refers to concrete members failing in shear. In this case, a critical shear crack develops from the load application zone to the support, as shown in Figure A5.2a. This crack divides the member into two (assumed) rigid bodies. Relative rotation of one part may occur as shown in Figure A5.2b, with the centre of rotation located approximately at the tip of the shear crack. Consequently, for each point of the crack, the components of the relative crack displacement ( $\delta$ ) can be determined (refer to Figure A5.2b where the opening ( $w$ ) and sliding ( $v$ ) of the crack are depicted). If  $|v| > 0$  the crack is subjected to Mixed-Mode and aggregate interlocking allows the transfer of a fraction of the shear load (Taylor [5]), Figure A5.2c.

Many test programmes dedicated to the phenomenon of aggregate interlocking have been performed in the past. The resulting data can be used to find average material parameters which can then be used to perform numerical analyses on different scales.

Paulay and Loeber [4] performed several Mode II tests, finding that the size and type of the aggregates have little effect on the results. Works of Hassanzadeh [1] and Nooru-Mohamed [3]

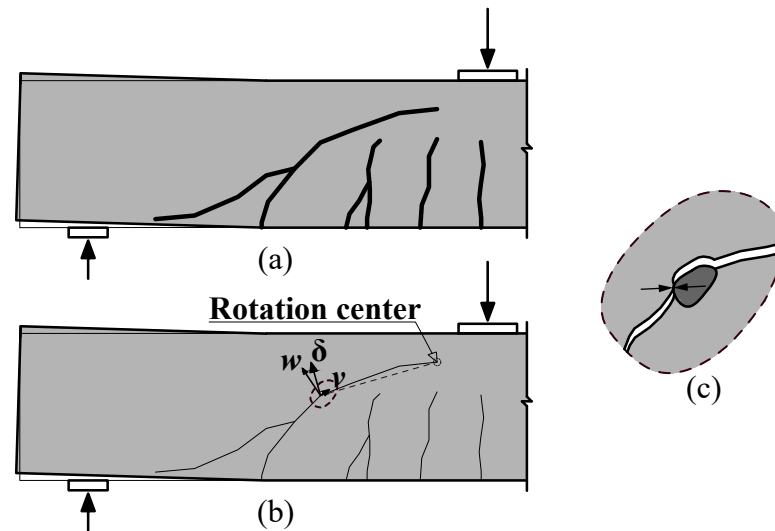


Figure A5.2 – Kinematic modes of cracks: (a) Mode I – opening; (b) Mode II – sliding; (c) Mixed-Mode – opening and sliding

analysed specimens subjected to Mixed-Mode as well as Mode II displacements. They noticed the difficulty in obtaining planar cracks and point out that the stiffness of the test setup is a very important aspect.

An interesting and very rigid test setup was developed by Østergaard et al. [6] at DTU (Denmark). The same setup was then used by Jacobsen [2] to perform 20 Mixed-Mode tests with a realistic imposed cinematic. He used concrete with rather fine aggregates ( $D_{\max} = 8$  mm) for all tests and used the test data to develop an elasto-plastic material model.

The different test programmes are however often difficult to compare with each other (e.g. different setups, materials, imposed kinematics or chosen specimens).

## A5.2 Test Setup

A 500 kN electromechanical machine by the company Zwick has been adapted in order to perform Mixed-Mode tests. A 50 kN hydraulic jack has been added for imposing displacements in the horizontal direction (Figure A5.3).

The specimens were made from a concrete prism measuring 1200 · 240 · 180 mm and horizontally cast with concrete with a compressive strength of 32 MPa after 28 days. Rounded gravel aggregates from the Rhone (Valais, Switzerland) with maximum aggregate size of 16 mm were used. Several slices were cut from this bar using a circular saw. Double notched specimens were then cut out from each slice using a waterjet cutting machine.

Two sizes of specimens have then been tested:

- Group 1: Mode I tests on small 40 · 40 · 10 mm specimens (Figure A5.4a)

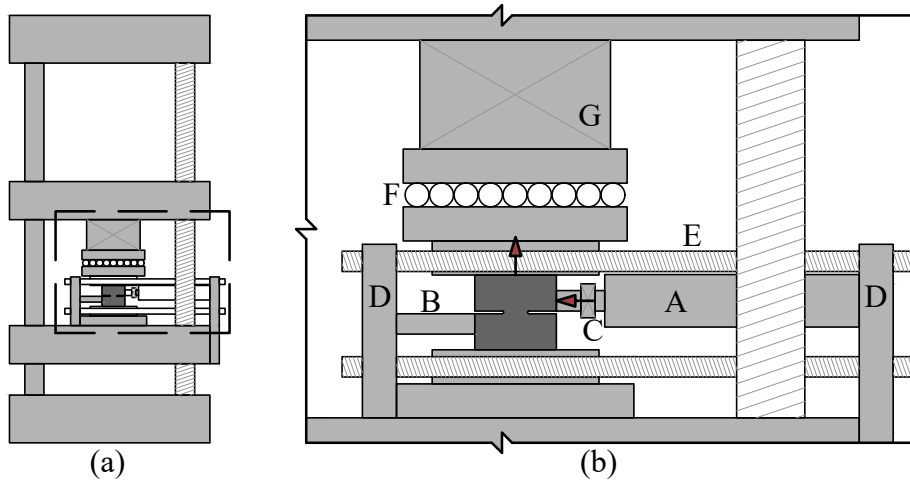


Figure A5.3 – Schematic representation of test setup for Mixed-Mode tests: (a) general overview; (b) detail: A – horizontal jack; B – reaction; C – load cell for horizontal axis; D – steel holding plates; E – stabilizing bars; F – rails for horizontal shifting; G – load cell for vertical axis;

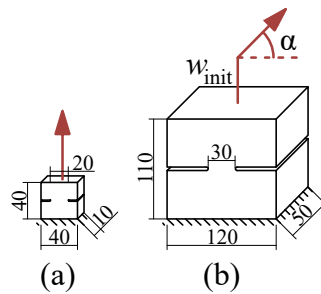


Figure A5.4 – Tested specimens and imposed displacement paths

- Group 2: Mixed-Mode tests on 120 · 110 · 50 mm specimens (Figure A5.4b)

All tests were monitored with the help of two load cells (vertical and horizontal) and a Digital Image Correlation (DIC) measurement system. Tests of group 2 had two custom-made bidirectional gauges. The bidirectional gauges were implemented by connecting two strain gauges perpendicularly, in order to obtain a device capable to measure horizontal and vertical displacements at the same time. The bidirectional gauges were then glued on the back of the specimen, while the front remained completely free for the DIC pictures. All tests were displacement controlled with an initial speed of 0.1  $\mu\text{m/s}$ .

The DIC Analysis was performed using pictures taken with two 4 Megapixel cameras placed in front of the specimen, at about 30 cm of distance. The specimen surface was painted white and a pattern of small black dots was sprayed randomly on the white background. During the test the cameras took pictures at regular time intervals. The pictures were then analysed with the commercial software “Vic3D” in order to obtain data on displacements and strains on the specimen surface. The obtained precision is of about 1/32 of the pixel size (each pixel has a

side length of about 0.0786 mm).

### A5.3 Results of Group 1 - Mode I on small specimens

For group 1, 38 double-notched specimens were prepared. Part of them were randomly cut out of 10 mm thick concrete plates, while some were cut in specified positions in order to obtain single aggregates developing through the critical section. The randomly selected specimens had a critical surface of about 20 · 10 mm, while for the others the depth of the notches was chosen considering the aggregate.

After testing in simple tension, the fracture surfaces were visually inspected in order to determine if a particular mode of fracture (crack through matrix, crack at aggregate interface or crack through aggregate) was predominant. The tests were thus categorized and compared. In 11 cases, the fracture surface developed through the concrete matrix. In 8 cases it mostly developed at the interface of one or several aggregates. In 3 cases the crack went mostly through an aggregate. In the remaining cases, the obtained crack was irregular or the fracture surface did not show a clearly predominant fracture type.

The main results are plotted in Figure A5.5. It shall be noted that the values on the horizontal axis represent the displacement of the testing machine and thus include the deformation of the setup. The small size of the specimen and the low maximum load (about 1 kN) do not allow the use of strain gauges, since their own tensile stiffness and resistance would become important compared to those of the specimen. The stress is calculated dividing the force by the initial surface determined by the notches. The results show that the setup is capable of capturing the different behaviour of cracks in the matrix or at the interface with aggregates. The data can be used to find average material parameters for the different crack types. These parameters can then be used in connection with numerical analyses. It should be noted that in the case of the crack at the aggregate interface the maximum tensile stress  $\sigma_u$  is potentially influenced by the fact that a minor part of the fracture surface develops through the cementitious matrix.

The DIC-Data can be used as an indicator of the crack path evolution during the test. For example, it is notable that there is a high scatter in the 3 tests with the crack going through the aggregate: One test reached a very high tensile strength of about 5 MPa, while the other two broke at about 2 MPa. This is certainly connected to the fact that different aggregate types were concerned, and the different behaviour is visible in the DIC analysis as well. Figure A5.6 and Figure A5.7 compare two of the tests. It can be noted that in test BT12802 (Figure A5.6), the areas with most tensile deformation are those located in zones around the aggregate for most of the test. Only late on the softening branch the crack develops through the aggregate (Figure A5.6c). For specimen BT12702 (Figure A5.7), however, the main strains develop through the aggregate from the beginning.

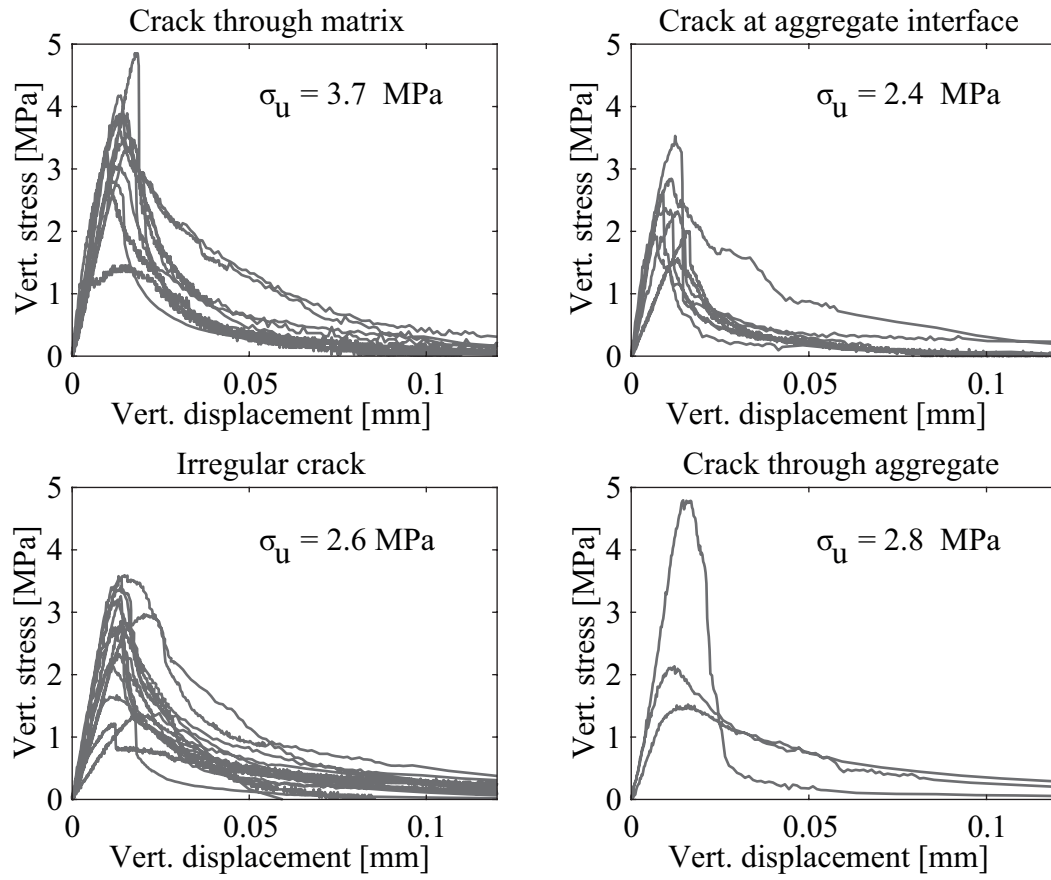


Figure A5.5 – Tested specimens and imposed displacement paths

A5.3. Results of Group 1 - Mode I on small specimens

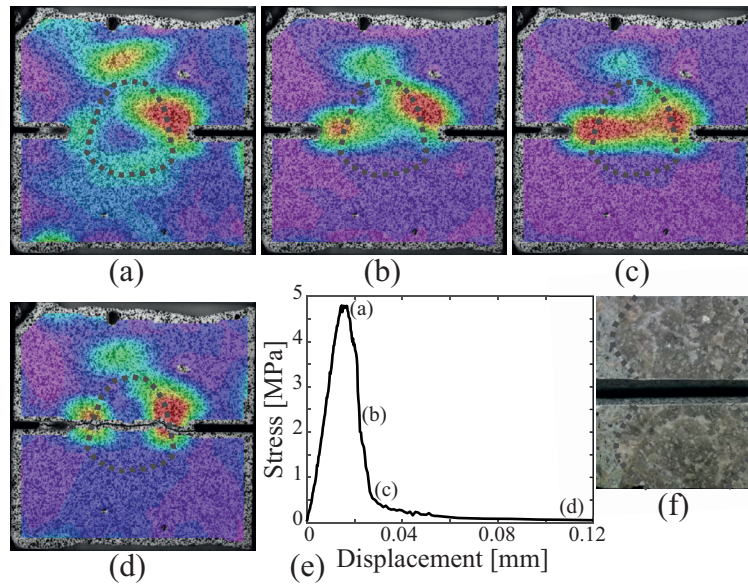


Figure A5.6 – Experiment BT12802, crack through aggregate (approximate shape of aggregate shown dashed): (a)-(d) Principal tensile strains on specimen surface; (e) Displacement-Stress graph; (f) Fracture surface;

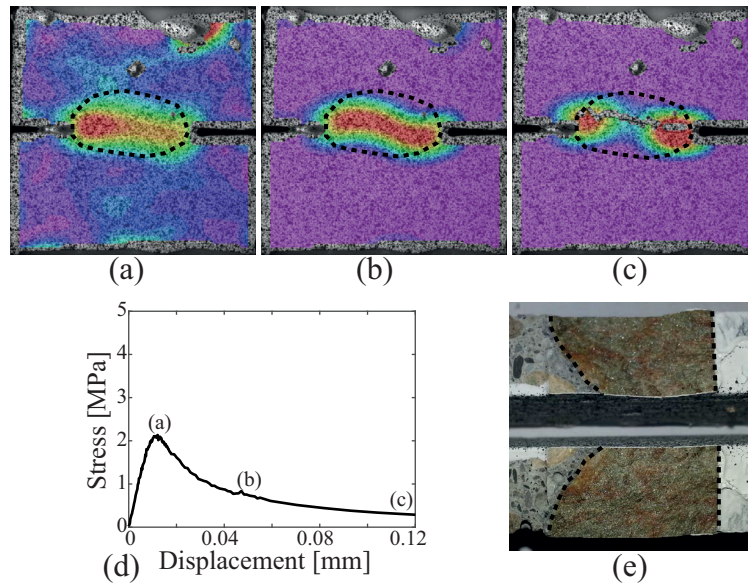


Figure A5.7 – Experiment BT12702, crack through aggregate (approximate shape of aggregate shown dashed): (a)-(c) Principal tensile strains on specimen surface; (d) Displacement-Stress graph; (e) Fracture surface;

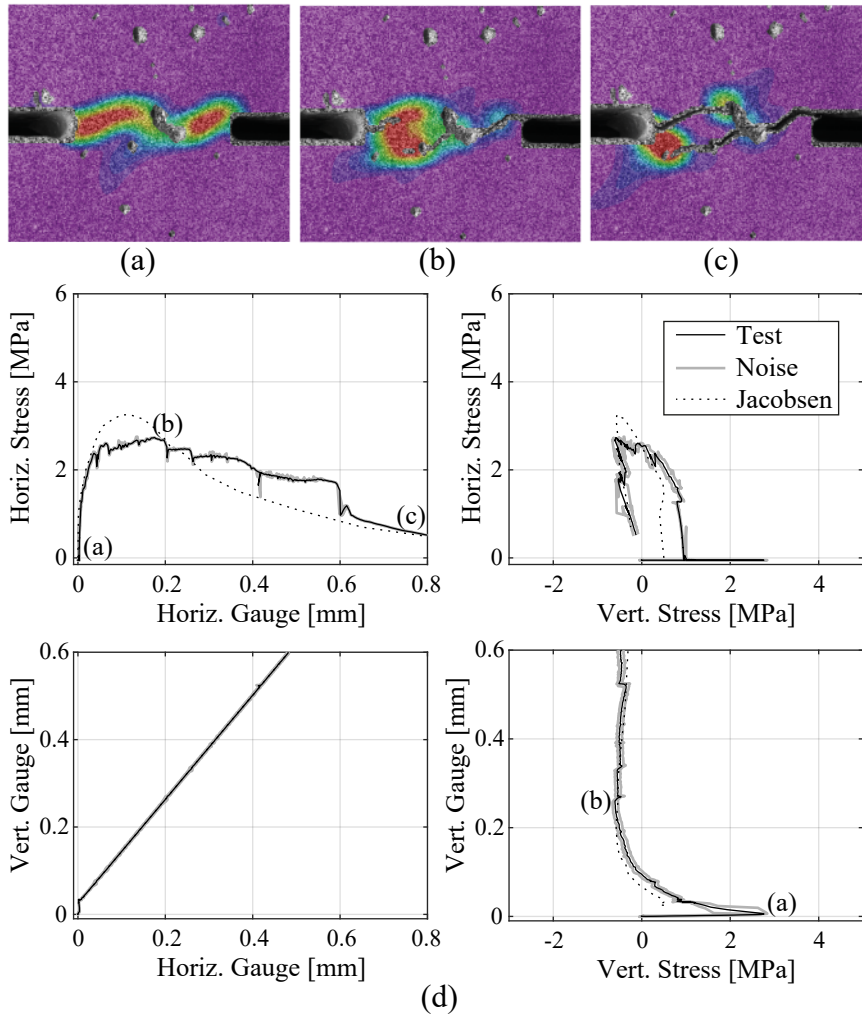


Figure A5.8 – Preliminary Mixed-Mode test BT20102 ( $w_{init} = 0.025$  mm,  $\alpha = 45^\circ$ ): (a)-(c) principal tensile strains on specimen surface; (d) plots of measurements

## **A5.4 Results of Group 2 - Mixed-Mode**

The kinematics for tests of group 2 is imposed in the following manner: first, fracture of the concrete is attained in Mode I; when the average of the two vertical gauges reaches a predefined ( $w_{\text{init}}$ ) value (see Figure A5.4c), the Mixed-Mode phase starts (imposed  $w$  and  $v$  at a given rate) with the horizontal jack moving with a displacement rate of  $0.1 \mu/\text{s}$ .

A preliminary test has been performed and the results are shown in Figure A5.8. It shall be noted that the apparent development of the crack in two branches is only due to an aggregate on the surface which detached from both halves of the specimen.

The results of this specimen are compared to those of Jacobsen [2] on a specimen with almost identical kinematics. The results are shown to be consistent (Figure A5.8d) despite the scatter of the phenomenon.

## **A5.5 Conclusions and Outlook**

This paper presents a new, simple setup for testing double notches specimens with different imposed kinematics. Only few preliminary tests have been performed, but the first results seem promising. The machine seems to be sufficiently stiff for small tensile tests and a first Mixed-Mode test showed a fairly similar behaviour to those reported in the literature.

The setup will undergo some final improvements and then be used for a more extensive testing campaign. The goal is to analyse the influence of different types of concretes and aggregates. Studies on the surface roughness will be performed as well. The results could be useful for the verification and improvement of different theoretical approaches to aggregate interlock.

## **Acknowledgement**

This work has been funded by the Swiss National Science Foundation, research grant 200021\_169649. The authors are very appreciative of the support received.

## **Bibliography**

- [1] Hassanzadeh, M. (1992). *Behavior of Fracture Process Zones in Concrete Influenced by Simultaneously Applied Normal and Shear Displacements*. Ph.D. Thesis, Lund University, Sweden.
- [2] Jacobsen, J. S. (2012). *Constitutive Mixed Mode Behavior of Cracks in Concrete: Experimental Investigations of Material Modeling*. Ph.D. Thesis, Technical University of Denmark, Kongens Lyngby, Denmark.
- [3] Nooru-Mohamed, M. B. (1992). *Mixed-Mode Fracture of Concrete: An Experimental Approach*. Ph.D. Thesis, Delft University of Technology, Sweden.

## Appendix 5

---

- [4] Paulay, T. and Loeber, P. J. (1974). Shear Transfer By Aggregate Interlock. *ACI Special Publication*, 42:1–16.
- [5] Taylor, H. P. J. (1970). *Investigation of the Forces Carried Across Cracks in Reinforced Concrete Beams in Shear by Interlock of Aggregate*. Number 42.447 in Technical report (Cement and Concrete Association). London, United Kingdom.
- [6] Østergaard, Olesen, and Poulsen (2007). Biaxial Testing Machine for Mixed Mode Cracking of Concrete. In *Fracture mechanics of concrete and concrete structures*, volume 1, page 8, Catania, Italy. CRC Press.

# Appendix 6: Modern experimental research techniques for a consistent understanding of aggregate interlocking

Tirassa M., Fernández Ruiz M., Muttoni A. (2018). Modern experimental research techniques for a consistent understanding of aggregate interlocking. In *Proceedings of the 12th fib PhD Symposium in Civil Engineering*, pp. 723–730. Prague, Czech Republic. (url: [infoscience.epfl.ch/record/257222](https://infoscience.epfl.ch/record/257222))

## Abstract

Aggregate interlocking is considered as one of the most important shear transfer actions in cracked concrete members without shear reinforcement. This research project analyses the fundamentals of aggregate interlocking by means of a specific experimental programme. Tests are carried out by precracking notched concrete specimens in pure tension and imposing mixed-mode kinematics (opening and sliding) thereafter. The tests are performed with varying opening and sliding ratios and on various concrete types. The development of cracking is tracked using Digital Image Correlation, which allows also to investigate secondary cracks developing during the mixed-mode phase. The various test results are presented and discussed. They are eventually compared with further tests and analytical models from the literature.

## A6.1 Introduction

Concrete is a quasi-brittle material with limited tensile strength. After cracking, concrete has still the capacity to transfer shear forces by means of a number of shear-transfer actions. One of the actions identified as particularly relevant is aggregate-interlocking [1]. This action develops when cracked concrete slips and this engages contact between the surfaces (due to

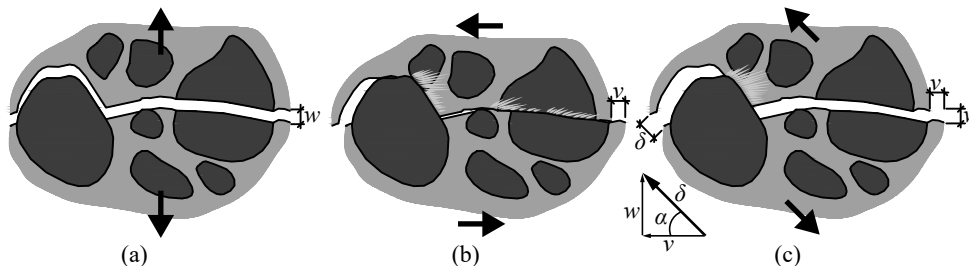


Figure A6.1 – Kinematic of concrete cracks; (a) Mode I opening; (b) Mode II sliding; (c) Mixed-Mode opening with angle  $\alpha$  (aggregates are represented in dark grey, the cement matrix in light grey).

their undulation and potentially protruding aggregates).

The amount of shear force that can be transferred by aggregate interlocking is mostly governed by the material properties of concrete (compressive and tensile strength, aggregate size and petrography) as well as by the kinematics of the crack lips. This latter is usually characterized by the relative opening ( $w$ ) and sliding ( $v$ ) of the lips of the crack. On the basis of these relative movements, several cases can be identified:

- Mode I opening occurs when the crack opens of an amount  $w$  perpendicularly to its global surface (Figure A6.1a)
- Mode II refers to the crack lips sliding relative to each other over a distance  $v$  (Figure A6.1b).
- Mixed-Mode opening refers to the case when Mode I and Mode II are occurring at the same time (Figure A6.1c). In this last case, the global displacement vector is named  $\delta$  and its angle with  $v$  is called  $\alpha$ .

Over the last 50 years, several models for the description and quantification of the forces transferred through aggregate interlocking have been proposed. Many of these theoretical approaches are based on the two-phase concept [10], distinguishing between the cement paste and the aggregates. These models have shown to yield in general to consistent results, although the definition of aggregate and cement paste is subjected to some discussion, as well as the influence of aggregate properties and shape on the aggregate interlocking response. With respect to testing, several test setups have been used in the past [8], incorporating lately refined possibilities to impose kinematics and to perform detailed measurements [6]. Despite these efforts, it exists today still a limited number of tests aimed at investigating the fundamentals of aggregate interlock and particularly of the relationship between the aggregate size and shape, petrography and imposed mixed-mode kinematics.

In order to develop more comprehensive theoretical approaches to the phenomenon, this paper introduces the results of an experimental programme allowing to impose various given crack kinematics. The results are tracked by means of Digital Image Correlation (DIC) and performed for different concrete types. The consistency of the results is checked by

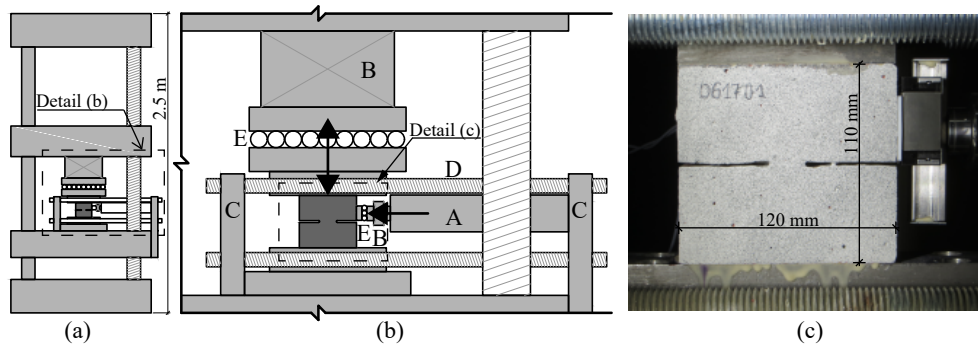


Figure A6.2 – Test setup; (a) general view; (b) detail view; A – horizontal jack; B – load cells for horizontal and vertical load; C – reaction plates; D – threaded bars; E – sliding rails; (c) picture of specimen inside the test setup.

comparison to other experimental programmes and eventually compared to some currently available theoretical models.

## A6.2 Experimental Setup

Similarly to [6], the setup presented in [9] and capable of imposing Mixed-Mode kinematics is used to test double-notched concrete specimens. It consists of a 500 kN electromechanical machine capable of applying normal displacements, to which a 50 kN hydraulic Jack has been incorporated to apply shear forces (Figure A6.2).

As performed by Jacobsen [6], each test starts with a Mode I phase to produce a crack of a predefined opening  $w_{init}$ . Then, the test continues in Mixed-Mode with a constant opening angle  $\alpha$  (Figure A6.3a). The tests are controlled using the average signal of two pairs of devices capable of measuring vertical and horizontal displacements at the same time (Figure A6.3b) and are carried out in displacement control with an initial speed of  $0.1 \mu\text{m/s}$ . The speed is progressively increased once the measured shear force has dropped from its peak value. All tests are monitored using the DIC technology.

The specimens are produced as follows: concrete is cast first in the shape of a prism, cured in sealed conditions for 28 days and then cut into slices using a circular saw. Thereafter, double-notched specimens are obtained from the slices by using a waterjet cutting machine. The specimens are 110 mm high, 120 mm wide and typically 50 mm thick, while the approximately 2 mm deep notches had varying lengths in order to obtain crack widths  $CL$  between 19 and 35 mm (Figure A6.3a).

In the following, the average normal stresses in the region between notches are defined as:

$$\sigma = \frac{F_N}{CL \cdot B} \quad (6.1)$$

where  $F_N$  is the measured normal/vertical load (with tension being positive) and  $B$  the specimen thickness (typically 50 mm). Similarly, the average shear stress is defined as:

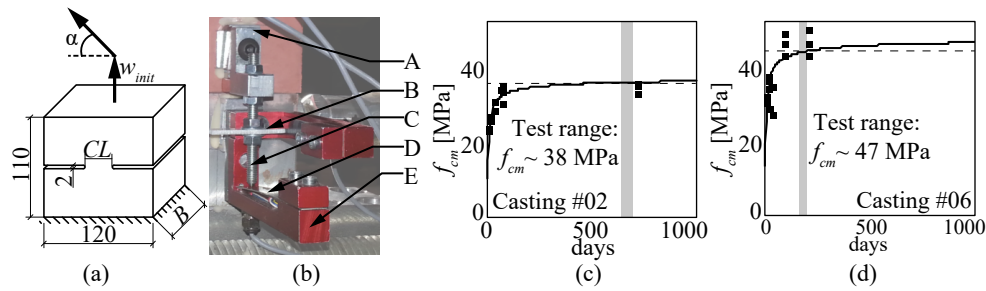


Figure A6.3 – (a) Schematic representation of a specimen and the applied kinematics; (b) Displacement measurement device; A – part I glued to the upper part of the specimen; B – element of part I pushes horizontally against blade of part II; C – element of part I pushes vertically against blade of part II; D – steel blade with strain gauge to measure vertical displacement; E – part II glued to lower part of specimen; (c)  $f_{cm}$  for Casting 02 according to MC 2010 [6]; (d)  $f_{cm}$  for Casting 06 according to MC 2010 [3].

Table A6.1 – Concrete mix properties (the values  $f_{cm}$  are estimated using linear regression according to MC 2010 [3];  $D_{max}$  is the maximum aggregate size).

Concrete Mix #	$D_{max}$ [mm]	Mix Design [kg/m <sup>3</sup> ]			$f_{cm,28}$ [MPa]	$f_{cm,TestDay}$ [MPa]
		Water	Cement	Aggregates		
#02	16	172	310	1955	32	38
			CEMII/A-LL42.5R			
#06 (red pigment added)	8	177	321	1853	40	47
			CEMII/A-LL42.5N			

$$\tau = \frac{F_S}{CL \cdot B} \tag{6.2}$$

where  $F_S$  is the measured shear/horizontal force.

Two different concrete mixes have been used, as described in Table A6.1 and Figure A6.4. The parameters for the applied kinematics have been chosen in accordance to [6], and can be found in Table A6.2.

### A6.3 Experimental programme

#### Types of responses

The Mode I tensile phase ends once the measured value of  $w$  reaches a predefined value  $w_{init}$ . The fracture process zone yields normally a well-defined crack at that moment in-between the notches. During the Mixed-Mode phase, the crack can develop in one of the following ways (see Figure A6.5):

- *Primary/Interface crack*: No additional (significant) cracks develop and strains localize

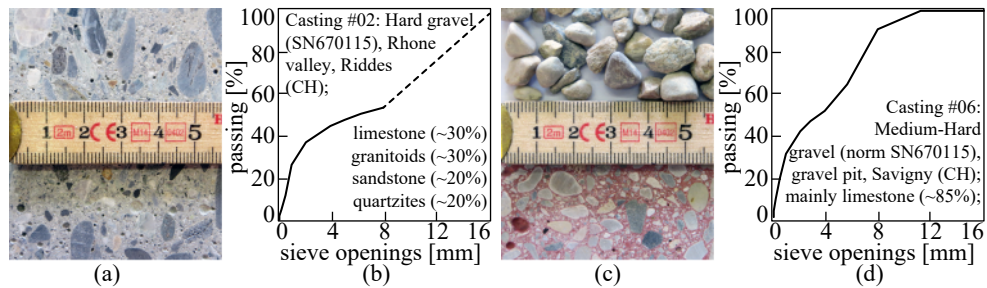


Figure A6.4 – (a) concrete of casting #02; (b) aggregates grading curve; (c) aggregates (top) and concrete (bottom) of casting #06; (d) aggregates grading curve.

in the crack originated in Mode I

- *Non-dominant secondary cracking*: one or several secondary cracks develop, but they do not propagate through the whole specimen. Most of the imposed displacements localize thus on the primary crack.
- *Dominant secondary crack*: a new crack develops, usually starting from the tip of a notch, and progresses in a brittle (unstable) manner

Figure A6.5 shows instances of cracking patterns as determined using DIC. The tests performed with the final version of the setup are reported in Table A6.2.

### Test results

In this section, the average stresses measured during the tests will be presented. Figure A6.6 shows tests for concrete #02 and Figure A6.7 reports the results for specimens of concrete #06. In each plot, one parameter defining the kinematics is set as constant while the other is progressively varied. The plots do not present the initial Mode I phase since  $\nu \approx 0$ . Peak values are marked with a square. As the Mixed-Mode phase starts,  $\nu$  increases and the shear stress  $\tau$  grow notably. At the same time,  $\sigma$  changes from tensile to compressive stresses.

The averages of the maximum tensile strengths reached during the Mode I phases were:

- $f_{ctm,02} = 3.7$  MPa (standard deviation 0.54) for casting #02;
- $f_{ctm,06} = 4.1$  MPa (standard deviation 0.65) for casting #06;

The plots show consistent results between the two concrete types: for the same initial opening, tests with lower displacement angles yield higher normal and shear loads. Similarly, for the same opening angle, tests with lower initial openings develop higher normal and shear loads.

## Appendix 6

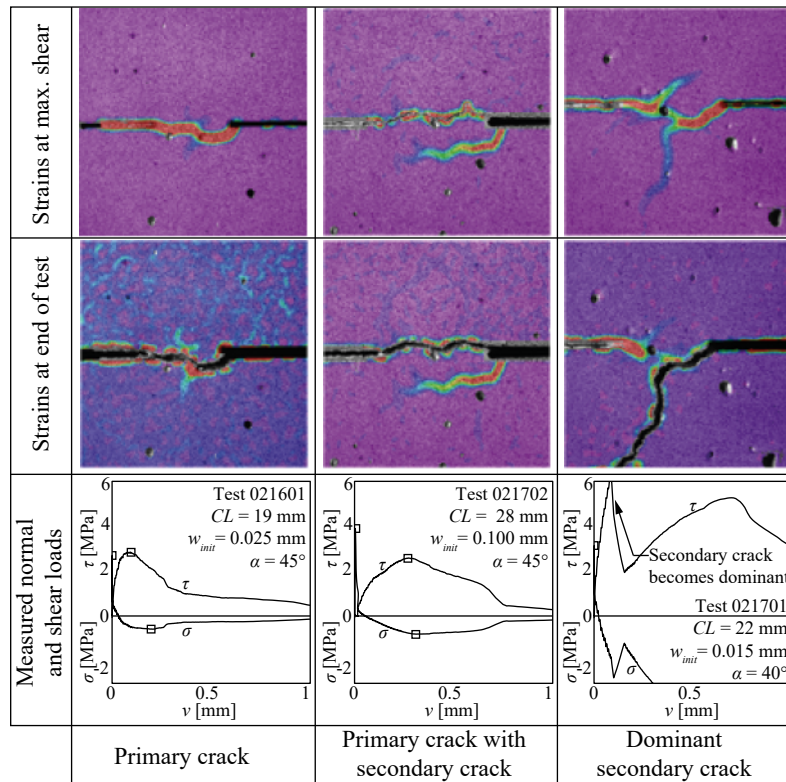


Figure A6.5 – Examples of specimen responses and cracking patterns (based on DIC-analyses).

Table A6.2 – Performed tests, classified by the imposed kinematics; specimens beginning with 02 are made with concrete from casting #02, while specimens beginning with 06 are made with concrete from casting #06; tests marked with \* show non-dominant secondary cracking, tests marked with \*\* show dominant secondary cracking; the width CL is reported in mm in brackets for each test (for definition see Figure A6.3a).

		Initial crack opening $w_{init}$			
		0.015 mm	0.025 mm	0.040 mm	0.100 mm
Mixed-Mode angle $\alpha$	40°	021701 (22.0) **	061501 (19.0) *	061602 (22.0)	061502 (25.0)
		061802 (19.0) *			
	45°	022002 (19.0) *	021601 (19.0) *	061701 (19.0) *	021702 (28.0) *
			061401 (19.5)		060402 (29.5) *
	50°		020804 (34.5) *		
55°		021402 (34.5) *	061801 (25.0)	061601 (28.0) *	
		061402 (25.0) *			
60°	022001 (25.0)	021602 (24.5)			

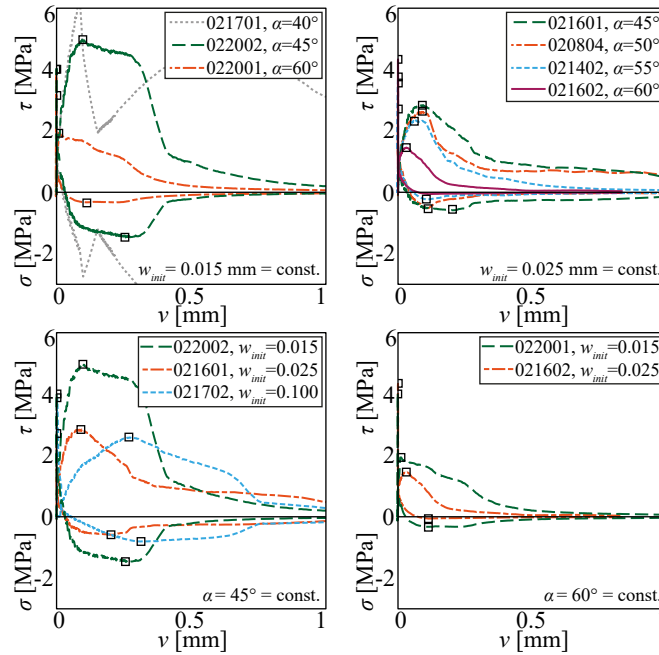


Figure A6.6 – Tests with concrete of casting #02; in each plot one parameter is maintained constant (indicated in the lower right corner) while the other one is progressively varied.

## A6.4 Discussion of test results

### Remarks on notch size and displacement application

#### Notch size

Cutting notches into specimens in order to obtain a single concentrated crack is common practice in these types of tests. Yet, the criteria to select the notch depth and size and the associated parameter CL are not normally homogeneous nor justified. However, this has significant influence on the crack development and therefore on the test results. For example if very small notches are performed (high values of CL), most tests will be characterized by strong secondary cracking [5, 7]. In reference [6] the researcher reports that preliminary testing started with a value of CL which was subsequently decreased in order to reduce the amount of tests dominated by secondary cracking. Once a given notch depth is set, secondary cracking became more dominant for flatter kinematics (small openings and small angles).

For the present study, different notch depths have been investigated. It was noted that if the notches are sufficiently large (low values of CL), it is possible to avoid secondary cracks even for rather flat kinematics. On the other hand, for large values of CL, secondary cracking was occurring even for kinematics with little shear displacement. It seems thus, that the notch depth is an important parameter, which governs the specimen response and the development of secondary cracks.

#### Displacement application

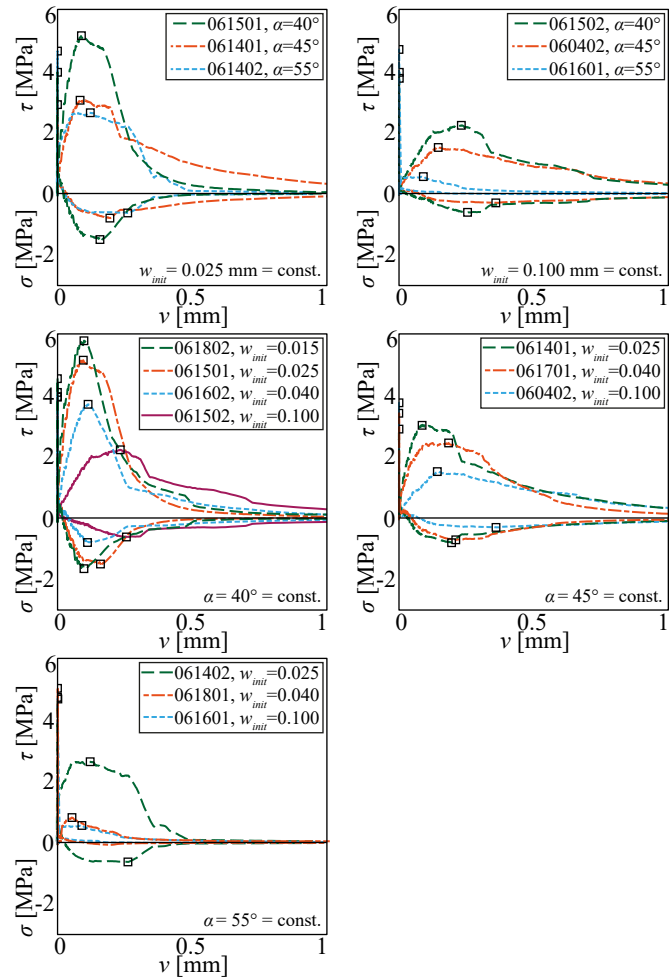


Figure A6.7 – Tests with concrete of casting 06; in each plot one parameter is maintained constant (indicated in lower right corner) while the other one is progressively changed.

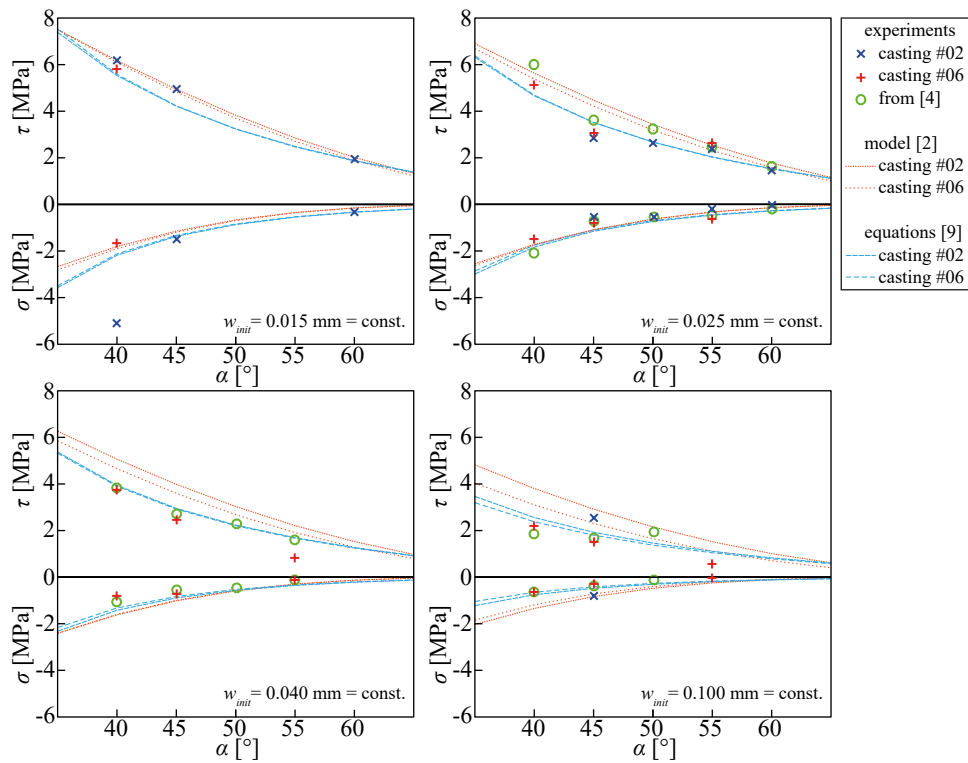


Figure A6.8 – Maximum values of  $\sigma$  and  $\tau$  for all tested concretes as well as tests and models from the literature.

During calibration tests of the experimental setup (not corresponding to the tests discussed here-in), it was noted that when the displacement was not applied in a constantly smooth manner, but with small ramps, secondary cracking developed in a more dominant manner. This may indicate that for testing programmes in the literature with no closed-loop control or where this aspect was not properly addressed, the results and cracking patterns may significantly differ.

### Summary and comparison of experimental results

The maximum values of  $\sigma$  and  $\tau$  obtained for the tests presented are plotted as data points in Figure A6.8. The figure clearly shows that for a given initial opening, the maximum stress progressively decreases for larger opening angles.

No significant difference in behaviour between castings #02 and #06 can be observed despite their very different aggregate size. The results reported in [6] are indicated as well, and their behaviour is consistent to the tests of the present study. In addition to the experiments, the estimates of the strength provided by the following two models are also indicated:

- The two phase model by Walraven [10]; this model only considers Mode I opening followed by pure Mode II sliding. Therefore, the global kinematics (until  $w = 2$  mm)

applied to the specimens has been subdivided into 401 steps to follow the Mixed-Mode kinematics closely;

- The simple closed-form formulas provided in [2], which are based on the two phase model by Walraven as well, but additionally consider modifications to follow Mixed-Mode kinematics more precisely [4];

For each of the models two curves are plotted next to each other in Figure A6.8, as the material parameters were adjusted in accordance to the characteristics of both castings #02 and #06.

### A6.5 Conclusions

This paper presents the results of an experimental investigation on aggregate interlocking. Several tests with two different types of concrete and several different imposed kinematics are presented. The following conclusions can be taken:

- The forces measured during the tests consistently show that specimens subjected to low initial crack openings and to low angles of displacement develop higher aggregate interlocking stresses than specimens with higher initial openings or angles of displacement
- The tests are consistent with similar tests reported in the literature
- The test results are consistent with the two-phase models presented in [10] and [2] despite the various theoretical limitations of such models
- Different cracking patterns have been observed, notably the development of a single primary crack going from notch to notch and the possible additional development of a secondary crack developing diagonally from the primary crack. Some qualitative observations on the influence of the testing procedure on the type of cracking are given, notably that it is easier to obtain primary cracks in specimens with larger notches

### Acknowledgement

This work has been funded by the Swiss National Science Foundation, research grant 200021\_169649. The authors are very appreciative of the support received.

### Bibliography

- [1] Cavagnis, F, Fernández Ruiz, M., and Muttoni, A. (2017). An analysis of the shear-transfer actions in reinforced concrete members without transverse reinforcement based on refined experimental measurements. *Structural Concrete*, 19(1):49–64.

- [2] Cavagnis, F, Fernández Ruiz, M., and Muttoni, A. (2018). A mechanical model for failures in shear of members without transverse reinforcement based on development of a critical shear crack. *Engineering Structures*, 157:300–315.
- [3] fib (International Federation for Structural Concrete) (2013). *fib Model Code for Concrete structures 2010*. Ernst & Sohn, 402 p, Germany.
- [4] Guidotti, R. (2010). *Poinçonnement des planchers-dalles avec colonnes superposées fortement sollicitées*. Ph.D. Thesis, EPFL, Lausanne, Switzerland.
- [5] Hassanzadeh, M. (1992). *Behavior of Fracture Process Zones in Concrete Influenced by Simultaneously Applied Normal and Shear Displacements*. Ph.D. Thesis, Lund University, Sweden.
- [6] Jacobsen, J. S. (2012). *Constitutive Mixed Mode Behavior of Cracks in Concrete: Experimental Investigations of Material Modeling*. Ph.D. Thesis, Technical University of Denmark, Kongens Lyngby, Denmark.
- [7] Nooru-Mohamed, M. B. (1992). *Mixed-Mode Fracture of Concrete: An Experimental Approach*. Ph.D. Thesis, Delft University of Technology, Sweden.
- [8] Paulay, T. and Loeber, P. J. (1974). Shear Transfer By Aggregate Interlock. *ACI Special Publication*, 42:1–16.
- [9] Tirassa, M., Fernández Ruiz, M., Anciaux, G., and Muttoni, A. (2017). Interface Stresses in Cracked Concrete: Testing for Review of Its Fundamentals. In *2017 fib Symposium High Tech Concrete: Where Technology and Engineering Meet*, pages 740–748. Maastricht, Netherlands.
- [10] Walraven, J. C. (1981). Fundamental Analysis of Aggregate Interlock. *ASCE Journal of the Structural Division*, 107(11):2245–2270.



# Max Tirassa

+41 76 401 9339  
max.tirassa@gmail.com  
linkedin.com/in/maxtirassa



---

## Education

- 2016–2020 **EPFL, Swiss Federal Institute of Technology in Lausanne** (CH)  
Doctoral thesis in the Structural Concrete Laboratory
- 2008–2014 **University of Rome ‘Tor Vergata’** (IT)  
M.Sc. with honours in Architecture and Building Engineering
- 2011–2012 Erasmus exchange year at **ENSA Paris ‘La Villette’** (FR)
- 2004–2008 **Scientific secondary diploma**, ‘Blaise Pascal’ high school, Meran (IT)

---

## Professional Experience

- 2016–2020 **EPFL, Structural Concrete Laboratory IBETON**, Prof. A. Muttoni  
Doctoral Thesis on force transfer in concrete interfaces; Execution of experimental campaign; Descriptive model for aggregate interlocking and bond
- 2014–2016 **Suess Staller Schmitt Ingenieure GmbH**, Munich (DE)  
Inspection and assessment of existing structures; Design of residential building in reinforced concrete; Construction site inspections
- 2014 **ARIA Group Architects Inc**, Chicago (USA)  
Three months internship as technical drafter
- until 2014 **Assarit**, Orbetello (IT)  
Sales, production and client assistance in family’s leather shop during holidays

---

## Languages

Italian (native speaker)                      German (native speaker)  
English (proficient user C2)                French (oral C1, writing B2)

---

## Skills

- Drafting Autodesk Autocad, Autodesk Inventor, Nemetschek Allplan, Google SketchUp
- Calculation Cubus, Nemetschek Frilo and Dlubal, elastic-plastic stress fields (JConc)
- Data Data acquisition, management and analysis, Mathworks Matlab
- Graphics Adobe Illustrator, Adobe Photoshop, Adobe Indesign, Gimp
- Management PRINCE2 Foundation certificate in Project Management; goal definition, multi-year planning, management of technical support staff

Procurement	Material and equipment acquisition, cost estimates and evaluation of offers
Communication	Group-working; Public speaking at conferences, meetings and classes
Podcasting	Interviewing, audio processing, HTML, web-design and hosting
Finance	Basic understanding of financial reports and Discounted Cash Flow analysis

---

## Extra-curricular activities

Mountain hiking (Level 1 ASGM certificate on avalanche safety)  
 Interested in architecture, urbanism and cultural heritage; City hiking  
 Disco-Fox dancing, swimming, podcasting

---

## Personal details

Italian nationality	Swiss B permit since 2016
Born 1989 in Meran (IT)	Drivers licence B

---

## Awards and Scholarships

- 2018 **Special Mention** of paper at the *12<sup>th</sup> fib International PhD Symposium in Civil Engineering* (Prague)
- 2015 *AgeQuake Society fellowship* of the ‘International Council for Caring Communities’
- 2014 *Emerge Italy scholarship* of the ‘FederlegnoArredo’  
**Third Team-Prize** (\$2500), student design competition *A society for all ages*; project presentation at the UN headquarters (New York) and the *16<sup>th</sup> China International Real Estate & Architectural Fair* (Beijing)

---

## Publications

- 2020 Tirassa M., Fernández Ruiz M., Muttoni A. (2020). An interlocking approach for the rebar-to-concrete contact in bond. [Submitted for review]  
 Tirassa M., Fernández Ruiz M., Muttoni A. (2020, in press). Influence of cracking and rough surface properties on the transfer of forces in cracked concrete. *Engineering Structures*.
- 2019 Pundir M., Tirassa M., Fernández Ruiz M., Muttoni A., Anciaux G. 2019. Review of fundamental assumptions of the Two-Phase model for aggregate interlocking in cracked concrete using numerical methods and experimental evidence. *Cement and Concrete Research*, 125, 105855. (doi: 10.1016/j.cemconres.2019.105855)
- 2018 Tirassa, M., Fernández Ruiz, M., Muttoni, A., 2018. Modern experimental research techniques for a consistent understanding of aggregate interlocking. *Proceedings of the 12th Fib PhD Symposium in Civil Engineering*. Presented at the 12th fib PhD Symposium in Civil Engineering, Prague, Czech Republic, pp. 723-730. (url: infoscience.epfl.ch/record/257222)
- 2017 Tirassa, M., Fernández Ruiz, M., Anciaux, G., Muttoni, A. 2017. Interface Stresses in Cracked Concrete: Testing for Review of Its Fundamentals. *2017 Fib Symposium High Tech Concrete: Where Technology and Engineering Meet*. Springer, Maastricht, Netherlands, pp. 740-748. (doi: 10.1007/978-3-319-59471-2\_87)
- 2014 Tirassa M., The church of San Giovanni in Palestrina: What to do with a Semi-abandoned minor historical building? 2014. *Proceedings of the 9<sup>th</sup> International Symposium on the Conservation of Monuments in the Mediterranean Basin*, Ankara, Turkey, pp. 965-972